

# The ZEPLIN-III Direct Dark Matter Search: Final Results and Measurements in Support of Next Generation Instruments

*Lea Reichhart*



Doctor of Philosophy  
The University of Edinburgh  
March 2013



# Abstract

Astrophysical observations give convincing evidence for a vast non-baryonic component, the so-called dark matter, accounting for over 20% of the overall content of our Universe. Direct dark matter search experiments explore the possibility of interactions of these dark matter particles with ordinary baryonic matter via elastic scattering resulting in single nuclear recoils. The ZEPLIN-III detector operated on the basis of a dual-phase (liquid/gas) xenon target, recording events in two separate response channels – scintillation and ionisation. These allow discrimination between electron recoils (from background radiation) and the signal expected from Weakly Interacting Massive Particle (WIMP) elastic scatters.

Following a productive first exposure, the detector was upgraded with a new array of ultra-low background photomultiplier tubes, reducing the electron recoil background by over an order of magnitude. A second major upgrade to the detector was the incorporation of a tonne-scale active veto detector system, surrounding the WIMP target. Calibration and science data taken in coincidence with ZEPLIN-III showed rejection of up to 30% of the dominant electron recoil background and over 60% of neutron induced nuclear recoils. Data taking for the second science run finished in May 2011 with a total accrued raw fiducial exposure of 1,344 kg·days. With this extensive data set, from over 300 days of run time, a limit on the spin-independent WIMP-nucleon cross-section of  $4.8 \times 10^{-8}$  pb near 50 GeV/c<sup>2</sup> WIMP mass with 90% confidence was set. This result combined with the first science run of ZEPLIN-III excludes the scalar cross-section above  $3.9 \times 10^{-8}$  pb.

Studying the background data taken by the veto detector allowed a calculation of the neutron yield induced by high energy cosmic-ray muons in lead of  $(5.8 \pm 0.2) \times 10^{-3}$  neutrons/muon/(g/cm<sup>2</sup>) for a mean muon energy of 260 GeV. Measurements of this kind are of great importance for large scale direct dark matter search experiments and future rare event searches in general.

Finally, this work includes a comprehensive measurement of the energy dependent quenching factor for low energy nuclear recoils in a plastic scintillator, such as from the ZEPLIN-III veto detector, increasing accuracy for future simulation packages featuring large scale plastic scintillator detector systems.



# Declaration

Except where otherwise stated, the research undertaken in this thesis was the unaided work of the author. Where the work was done in collaboration with others, a significant contribution was made by the author.

Conducting a reasonably large scale experiment, such as the ZEPLIN–III dark matter search, is only feasible in a collaborative effort. The multi-national ZEPLIN–III collaboration includes the University of Edinburgh, Imperial College London, the STFC Rutherford Appleton Laboratory, LIP–Coimbra and ITEP Moscow. Hence, much of the work presented in this thesis was only possible in collaboration with other team members. A detailed list of contributions in collaborative parts of this work, as well as areas for which the author had sole responsibility, is provided below.

**Chapter 4:** The author made a significant contribution to the physical and analytical work required for deployment, operation, maintenance and monitoring of the detector instrument itself.

**Chapter 5:** The main responsibility for the ZEPLIN–III veto detector lay with the Edinburgh group, hence the author contributed at all stages of setting-up, operating and analysing the data acquired with this instrument. Specifically, the author was responsible for the daily monitoring and long term stability checks, as well as for the gain corrections, equalising the whole PMT array during calibration phase of the detector. Part of the synchronising procedure for coincident events (between ZEPLIN–III and its veto detector) was developed by the author. Furthermore, the author had the leading role in developing the analysis cuts for the tagging of background events as well as in further analysis steps. This work was reported in Ref. [1] and was utilised in the dark matter cross-section limits presented in Ref. [2].

**Chapter 6:** The measurement of the energy dependent quenching factor for a plastic scintillator was performed solely by the author. This work has been published as L. Reichhart *et al.* in Physical Review C, 2012 [3].

---

**Chapter 7:** The estimation of background observed in a dark matter search run, in terms of radioactivity neutrons coming from the rock cavern, was performed by the author. This includes all aspects of this work, starting with constructing and updating the detector setup in CAD, incorporating this more accurate description of the experimental setup into the simulation and the final analysis. Although similar work has been conducted before, this was more comprehensive and independent, considerably reducing the systematic uncertainties associated with such measurements. This work contributed to Ref. [4].

**Chapter 8:** For the analysis of the second science run data the author was heavily involved in the definition of the dark matter signal region and developing the quality cuts for the full dataset. This work contributed to Ref. [2]. Moreover, the revision of the spin-independent cross-section limit from the first science run of ZEPLIN-III was the work of the author, presented in the same publication.

**Chapter 9:** The author performed every element of the muon-induced neutron rate measurement; from analysing the science run dataset acquired with the veto detector for muons and muon-induced neutrons, as well as performing the complementary Monte Carlo simulations. This work has been submitted for publication in Astroparticle Physics [5].

This thesis has been composed by the author and has not been submitted for any other degree or professional qualification.

*L. Reichart*  
March 2013





# Acknowledgements

I wish to thank all of the people who have helped and supported me in the course of this work.

Firstly, I would like to give my honest thanks to Alexander Murphy, a brilliant supervisor and good friend, supporting me in my work as a researcher throughout my PhD studies. His door was always open for questions, discussions and for the occasional life coaching sessions. Furthermore, I want to express my gratitude to my second supervisor, Chamkaur Ghag, who not only gave me support and advice during his postdoctoral position here at the University of Edinburgh, but also after he left to work at other universities in the US and the UK.

The extent of the work presented in this thesis was only made possible through the support and efforts of many people. Foremost, I would like to thank all the members of the ZEPLIN-III collaboration. It was an honour for me to work on an exciting experiment with a driven team of great physicists. My special thanks go to Henrique Araújo for the long and helpful discussions and to my colleagues here at the University of Edinburgh, Paul Scovell and Anthony Hollingsworth, who were a great team to work with. Moreover, I would like to thank Alastair Currie for explaining the essentials of statistical analysis to me. I would also like to acknowledge and thank the whole team at the Boulby Underground Laboratory for the support and good times on site.

I am also grateful to Vitaly Kudryavtsev for his expertise and the fruitful discussions on the muon-induced neutron work.

Finally, I would like to thank my family, friends and partner for supporting me over the last three and a half years. I could always count on their encouragement, especially during those times when the cold and dark winters of the north started to take their toll. I want to especially thank and express my gratitude to my boyfriend Tom, who was by my side at all times, despite my ambitions at work and my numerous and sometimes long stays away from home when on experiments. Your support means the world to me.



# Contents

<b>Abstract</b>	i
<b>Declaration</b>	iii
<b>Acknowledgements</b>	vi
<b>Contents</b>	ix
<b>List of figures</b>	xiii
<b>List of tables</b>	xvii
<b>1 Introduction</b>	1
<b>2 A Review of the Evidence for Dark Matter and Possible Candidates</b>	5
2.1 The standard cosmological model - $\Lambda$ CDM . . . . .	5
2.2 Evidence for dark matter . . . . .	9
2.2.1 Virially bound systems . . . . .	9
2.2.2 Rotation curves of galaxies . . . . .	10
2.2.3 Gravitational lensing . . . . .	10
2.2.4 The cosmic microwave background and large scale structure formation . . . . .	12
2.2.5 Big-Bang nucleosynthesis . . . . .	14
2.3 Dark matter candidates: an overview . . . . .	15
2.3.1 Hot, warm or cold dark matter? . . . . .	16
2.4 Summary . . . . .	21
<b>3 Detection of WIMP Dark Matter</b>	23
3.1 Indirect detection techniques . . . . .	23
3.2 Searching for dark matter at the LHC . . . . .	26
3.3 Direct detection methods . . . . .	28
3.3.1 Cross-sections of WIMP-nucleon interactions . . . . .	30
3.3.2 Detectors and experimental techniques . . . . .	33
<b>4 The ZEPLIN-III Experiment</b>	43
4.1 Detector design . . . . .	44
4.2 Discrimination and the principles of xenon as a detection material . . . . .	49

4.2.1	The primary scintillation signal . . . . .	52
4.2.2	The secondary signal . . . . .	56
4.3	The First Science Run of ZEPLIN-III . . . . .	59
4.4	The Second Science Run of ZEPLIN-III – operations, hardware and software . . . . .	60
4.4.1	Data acquisition . . . . .	61
4.4.2	Pulse parameterisation . . . . .	61
4.4.3	Stability and the slow-control . . . . .	63
4.4.4	Event reconstruction . . . . .	69
4.4.5	Event selection and data structure . . . . .	72
<b>5</b>	<b>The ZEPLIN-III Veto Detector</b>	<b>77</b>
5.1	Design . . . . .	77
5.1.1	Gadolinium concentration . . . . .	80
5.1.2	Material selection and backgrounds . . . . .	82
5.1.3	Acquisition and trigger setup . . . . .	83
5.2	Performance of the veto detector . . . . .	84
5.2.1	Long term stability of the veto detector . . . . .	84
5.2.2	Signal rates . . . . .	88
5.2.3	Tagging of background events . . . . .	90
5.2.4	Implications for signal limits . . . . .	100
<b>6</b>	<b>Quenching Factor for a Plastic Scintillator</b>	<b>103</b>
6.1	Quenching in nuclear recoil interactions . . . . .	104
6.2	Experimental setup . . . . .	105
6.3	Simulations . . . . .	106
6.3.1	Uncertainties in the Monte Carlo simulation . . . . .	107
6.4	$\gamma$ -ray calibrations . . . . .	111
6.5	Neutron exposures . . . . .	111
6.5.1	Nuclear recoils . . . . .	111
6.5.2	Quenching factor . . . . .	112
6.5.3	Impact of systematic errors . . . . .	116
6.5.4	Birks factor, $kB$ . . . . .	120
<b>7</b>	<b>Backgrounds in the ZEPLIN-III Experiment</b>	<b>123</b>
7.1	Background sources . . . . .	123
7.1.1	External background sources . . . . .	124
7.1.2	Internal background sources . . . . .	126
7.2	Shielding against rock neutrons . . . . .	129
7.2.1	GEANT4 simulations with CAD-based geometry modelling . . . . .	129
7.3	Backgrounds in the second science run of ZEPLIN-III . . . . .	132
7.3.1	Electron recoil background . . . . .	132
7.3.2	Nuclear recoil background . . . . .	138

<b>8 The Second Science Run of ZEPLIN-III – Analysis and Results</b>	<b>141</b>
8.1 Analysis . . . . .	141
8.1.1 Defining a signal region . . . . .	142
8.1.2 Selection cuts and efficiencies . . . . .	145
8.1.3 Background estimations . . . . .	152
8.2 WIMP search results from the ZEPLIN-III SSR . . . . .	156
8.3 The final dark matter search result from the ZEPLIN-III project . . . . .	159
8.3.1 Cross-section limit calculations and SSR results . . . . .	160
8.3.2 A revised limit for the first science run of ZEPLIN-III . . . . .	162
8.3.3 Combined cross-section limits . . . . .	164
<b>9 Measurement and Simulation of the Muon-induced Neutron Yield in Lead</b>	<b>169</b>
9.1 Introduction . . . . .	170
9.1.1 Cosmic-rays and muons underground . . . . .	170
9.1.2 Muon-induced neutrons . . . . .	174
9.2 Experimental apparatus . . . . .	175
9.3 Monte Carlo simulations . . . . .	176
9.4 Event selection . . . . .	178
9.5 Muon-induced neutron yield . . . . .	183
9.5.1 Experiment . . . . .	184
9.5.2 Comparison with simulations . . . . .	187
9.5.3 Muon-induced neutron yield in lead . . . . .	193
9.6 Discussion . . . . .	196
<b>10 Conclusions</b>	<b>199</b>
<b>Glossary</b>	<b>203</b>
<b>Bibliography</b>	<b>207</b>
<b>Publications</b>	<b>222</b>

*CONTENTS*

---

# List of Figures

2.1	$\Lambda$ CDM model constraints . . . . .	8
2.2	Rotation curve of spiral galaxy NGC-3198 . . . . .	11
2.3	Merger of two galaxy clusters: the Bullet cluster . . . . .	12
2.4	Temperature power spectrum from the seven-year WMAP data set . . . . .	13
2.5	Measurements of galaxy distribution in comparison to N-body simulations	14
2.6	WIMP freeze out in the early Universe . . . . .	19
3.1	Results from indirect dark matter searches PAMELA, HESS and FERMI	25
3.2	Upper limits on the spin-dependent WIMP-proton cross-section from combined analysis of IceCube and AMANDA-II . . . . .	27
3.3	Preferred regions in the WIMP-mass – spin-independent neutralino-proton cross-section plane in the absence of SUSY signals at the LHC .	28
3.4	Predicted integrated WIMP elastic scattering rates for different target materials . . . . .	32
3.5	Direct dark matter search experiments categorised by utilised energy deposition channel(s) . . . . .	34
3.6	Spin-independent WIMP-nucleon cross-section limits from direct dark matter search experiments . . . . .	36
3.7	Modulation of the residual single hit scintillation event rate from the DAMA/LIBRA experiment . . . . .	40
4.1	Cross-sectional view of the ZEPLIN-III detector . . . . .	45
4.2	Photograph of the ZEPLIN-III instrument without its vacuum jacket .	46
4.3	ZEPLIN-III PMT array . . . . .	46
4.4	Phase diagram of xenon . . . . .	48
4.5	Schematic of the ZEPLIN-III target volume . . . . .	50
4.6	Waveform examples for an electron and nuclear recoil event . . . . .	51
4.7	Xenon scintillation process flowchart . . . . .	52
4.8	Energy dependent relative scintillation yield for nuclear recoils, $L_{eff}$ .	55
4.9	Energy dependent ionisation yield for nuclear recoils . . . . .	58
4.10	Field dependence of scintillation and ionisation yields . . . . .	58
4.11	Spin-independent WIMP-nucleon elastic scattering cross-section result from the first science run of ZEPLIN-III . . . . .	60
4.12	Historical ZEPLIN-III system temperatures . . . . .	64
4.13	ZEPLIN-III system and target pressure correction factors . . . . .	64

---

*LIST OF FIGURES*

---

4.14	$^{57}\text{Co}$ energy spectrum . . . . .	66
4.15	Historical evolution and correction factor of electron life-time . . . . .	66
4.16	Tilt correction factor distribution . . . . .	67
4.17	S2/S1 ratio scatter plot from exposures to a $^{137}\text{Cs}$ and an Am-Be calibration source . . . . .	68
4.18	Copper attenuation grid . . . . .	70
4.19	Iterative event reconstruction process . . . . .	71
5.1	CAD rendering of the veto detector surrounding the ZEPLIN-III dark matter detection instrument . . . . .	78
5.2	Cross-sectional view of the full experimental setup in its second science run configuration . . . . .	79
5.3	Assembly of the veto around ZEPLIN-III . . . . .	80
5.4	Characteristic capture time of tagged neutron events from Monte Carlo simulations . . . . .	81
5.5	Distribution of pulse times in the veto relative to the S1 signal in ZEPLIN-III . . . . .	82
5.6	Evolution of the mean single photoelectron position for all 52 veto detector PMTs over time . . . . .	85
5.7	Centroid position of LED exposure generated peak over time from weekly calibrations . . . . .	86
5.8	Screenshot of the ZE3RA synchronisation display . . . . .	87
5.9	Synchronisation fraction of veto events . . . . .	88
5.10	Cumulative signal rate measured with the veto detector . . . . .	90
5.11	Veto pulse start time distribution . . . . .	91
5.12	$\gamma$ -ray tagging fraction of veto and ZEPLIN-III coincident prompt signals as a function of acceptance window. . . . .	92
5.13	Fraction of accidentally prompt tagged events . . . . .	93
5.14	Prompt tagging efficiency as a function of veto threshold . . . . .	94
5.15	Accidental tagging fraction for the delayed tag . . . . .	96
5.16	Tagging efficiency as a function of pulse multiplicity . . . . .	97
5.17	Neutron tagging efficiency as a function of energy . . . . .	98
5.18	Differential energy spectrum of the electron recoil background in ZEPLIN-III, showing PTAG and DTAG fractions . . . . .	99
5.19	Implications of the tagging efficiency of a veto detector on the evidence for a discovery . . . . .	100
6.1	Experimental setup for plastic scintillator quenching factor measurement	106
6.2	Angular differential cross-section plots for elastic neutron scattering on hydrogen and carbon . . . . .	108
6.3	Angular distribution and nuclear recoil energies of elastic neutron scattering on hydrogen . . . . .	109
6.4	Angular distribution and nuclear recoil energies of elastic neutron scattering on carbon . . . . .	110
6.5	$^{137}\text{Cs}$ calibration spectrum . . . . .	112
6.6	Am-Be source spectrum . . . . .	113

---

6.7	$^{252}\text{Cf}$ source spectrum . . . . .	113
6.8	Energy spectrum originating from irradiation with an Am-Be source . .	114
6.9	Energy spectrum originating from irradiation with a $^{252}\text{Cf}$ source . . .	115
6.10	Energy dependent nuclear recoil quenching factor in a polystyrene plastic scintillator . . . . .	116
6.11	Simulations using an energy-dependent quenching factor in comparison to experimental data . . . . .	117
6.12	Spectra of energy deposits for varying lead shielding thickness from a $^{252}\text{Cf}$ source exposure . . . . .	118
6.13	Spectra of energy deposits for different source positions from a $^{252}\text{Cf}$ source exposure . . . . .	118
6.14	Neutron flux and neutron-induced nuclear recoil spectra from two different Am-Be neutron source input spectra . . . . .	119
6.15	Simulated energy spectrum from irradiation with two different Am-Be neutron source spectra . . . . .	119
6.16	Fraction of energy depositions from carbon nuclei . . . . .	120
6.17	Fit of Birks calculations to the measured quenching factor . . . . .	121
7.1	Muon flux for some of the largest underground facilities . . . . .	125
7.2	ZEPLIN-III veto detector construction used in Monte Carlo simulations with the classical C++ detector construction in comparison to the GDML based geometry . . . . .	131
7.3	Energy differential spectrum of nuclear recoils from single-elastic scatters of rock neutrons within the xenon target . . . . .	132
7.4	Energy differential histogram of the electron recoil background in ZEPLIN-III . . . . .	133
7.5	ZEPLIN-III electron recoil background as a function of radius . . . .	134
7.6	ZEPLIN-III electron recoil background as a function of depth . . . .	134
7.7	Distribution of S1 mean arrival time . . . . .	137
7.8	Schematic of a possible MSSI event . . . . .	138
7.9	Total differential energy spectrum of single-elastic nuclear recoil energy depositions in ZEPLIN-III . . . . .	139
8.1	Gaussian fits to the discrimination parameter $\log_{10}(S_2/S_1)$ of the nuclear recoil band . . . . .	143
8.2	Polynomial fits to the mean and width of the elastic nuclear recoil band	144
8.3	Scatter plot of events recorded from an Am-Be calibration run and representation of the signal acceptance region . . . . .	144
8.4	Quality cut based on spatial RMS of S2 . . . . .	147
8.5	Quality cut based on distance between S1 and S2 position . . . .	147
8.6	Quality cut based on S2 pulse asymmetry . . . . .	148
8.7	Quality cut based on reduced $\chi^2$ of S1 energy reconstruction . . . .	148
8.8	Quality cut based on ML value of reconstructed S1 energy (1) . . . .	149
8.9	Quality cut based on ML value of reconstructed S1 energy (2) . . . .	149
8.10	Quality cut based on the likelihood value of the PMT with the least likely response . . . . .	150

8.11 Quality cut based on a variation of the discrimination parameter: log <sub>10</sub> (s2area/s1area) . . . . .	150
8.12 Nuclear recoil detection efficiencies in the SSR . . . . .	151
8.13 DTAG events in the golden dataset . . . . .	154
8.14 SSR <sup>137</sup> Cs calibration . . . . .	155
8.15 Skew-Gaussian fits to the un-vetoed science data for extrapolation into the WIMP search region . . . . .	156
8.16 Discrimination plot for full SSR exposure from the final non-blind analysis	157
8.17 Distribution of unblinded SSR data in signal acceptance . . . . .	158
8.18 Spatial $\chi^2$ map . . . . .	163
8.19 Discrimination plot for re-analysed FSR data . . . . .	164
8.20 Spin-independent WIMP-nucleon cross-section limit curves from the FSR and SSR of ZEPLIN-III . . . . .	166
8.21 Spin-dependent WIMP-neutron cross-section limit curve for the com- bined FSR and SSR data of ZEPLIN-III . . . . .	167
9.1 Energy spectrum of cosmic-ray nuclei . . . . .	171
9.2 Differential momentum spectrum of atmospheric muons at ground level	172
9.3 Vertical muon intensity as a function of depth . . . . .	173
9.4 Simulated muon-induced neutron yields as a function of atomic (molec- ular) weight . . . . .	175
9.5 Energy spectra of primary/propagated muons . . . . .	177
9.6 Angular distribution of primary/propagated muons . . . . .	177
9.7 Muon event selection in experimental data . . . . .	179
9.8 Simulated summed energy deposition in veto roof modules . . . . .	180
9.9 Muon event selection in simulation . . . . .	180
9.10 Highest energy deposition in barrel scintillator module at trigger time from simulations . . . . .	181
9.11 Comparison between data and simulation of coincident scintillator muon hits . . . . .	182
9.12 Schematic of the veto with scintillator module numbers indicated . . .	182
9.13 Time delay distribution of all pulses from the muon search data set . .	184
9.14 Time delay distribution of single scintillator background . . . . .	185
9.15 Time delay distribution of detected captured muon-induced neutrons .	188
9.16 Channel multiplicities of detected captured muon-induced neutrons .	188
9.17 Energy depositions of detected captured muon-induced neutrons before onset of saturation . . . . .	189
9.18 Relative fraction of neutron multiplicities . . . . .	190
9.19 Muon event associated with an extraordinary number of induced neutrons	192
9.20 Differential energy spectrum of muon-induced neutrons produced in lead	194
9.21 Absolute neutron yields of the most important production processes for muon-induced neutrons . . . . .	196
10.1 Projection of WIMP-nucleon cross-section upper limits for the LUX and LZ experiments . . . . .	201

# List of Tables

2.1	Key events in the history of the Universe . . . . .	6
2.2	$\Lambda$ CDM density parameters . . . . .	7
4.1	List of parameters held by a final golden n-tuple . . . . .	74
5.1	Radiological content of the veto components . . . . .	83
7.1	Component-level contributions to the electron recoil background in ZEPLIN-III . . . . .	135
7.2	Component-level single-elastic nuclear recoil expectations in ZEPLIN-III	140
8.1	Number of observed events and expected backgrounds in the WIMP search region from SSR data . . . . .	157
8.2	Number of observed events and expected backgrounds in the WIMP search region from FSR data . . . . .	164
9.1	Measured and simulated muon-induced neutron rates . . . . .	187
9.2	Fractions of muon-induced neutrons produced in different materials . . .	193
9.3	Fractions of muon-induced neutrons captured on different elements . . .	193
9.4	Muon-induced production yields for neutrons for different versions of GEANT4 and physics lists . . . . .	195

*LIST OF TABLES*

---

# Chapter 1

## Introduction

Understanding the fundamental building blocks of our Universe is one of the great quests of mankind. From comprehensive astronomical observations we infer that less than 5% of the total energy-matter content in our Universe is presently known to us. The rest, the predominant part, comprises two almost equally elusive components: dark energy and dark matter. The existence of dark matter is founded in the observed gravitational interaction with ordinary matter. Furthermore, since dark matter does not seem to interact through any of the standard model forces other than gravity (and possibly via the weak force for certain cases), it plays a crucial role in large scale structure formation. However, the nature of the dark matter (particles) remains unsolved. In the context of recent discoveries, which potentially complete the set of predicted standard model particles, the hunt for the missing dark matter component becomes even more paramount.

Huge experimental efforts are being undertaken to shine light on the nature of the dark matter particle using an array of different experimental techniques including space-, ground- and underground based dark matter searches. A fundamental principle which underlies all of these different searches is to assess/exclude all signals from known sources and look for an excess in the data above background expectations. Therefore, a deep knowledge and insight into background sources originating from interactions of standard model particles is imperative; involving not only an understanding of the nature and origin of the commonly known background sources, but also very precise knowledge of the detector instruments and their environments. As the sensitivities of instruments improve, ‘new’ undiscovered sources of backgrounds arise, challenging the discovery of a clear signal originating from a dark matter particle interaction.

The ZEPLIN-III detector is a direct dark matter search instrument, built to detect single-elastic scatters of dark matter in the form of Weakly Interacting Massive Particles (WIMPs) using a xenon target. This particular instrument was the third in a series of

underground xenon-based rare event search experiments installed at the Boulby mine, UK. At this depth of 1100 m, the background from cosmic-ray muons is reduced by approximately 6 orders of magnitude. Two phases of operation of ZEPLIN-III have produced two competitive cross-section limit results for the WIMP-nucleon interaction.

The topic of this thesis is the second science run of ZEPLIN-III, with an emphasised focus on the incorporated veto system, which was designed to reject signals that might otherwise have been incorrectly identified as a nuclear recoil of a WIMP elastically scattering off a Xe atom. The dark matter detector runs on the principle of a dual-phase time projection chamber, recording two signals from each event. The ratio between the primary scintillation and the secondary electroluminescence signal provides discrimination between electron (*e.g.*  $\gamma$ -rays and electrons) and nuclear (*e.g.* neutrons and WIMPs) recoil interactions. An anti-coincidence device surrounding the dark matter target is an additional important measure to mitigate neutron and  $\gamma$ -ray backgrounds. Radioactivity backgrounds from all components of both detectors and from environmental sources, originating predominantly from trace contaminations, are discussed. The effect of these radioactive sources on the detected signals are manifold and may represent not only a random background of neutrons, electrons and  $\gamma$ -rays, but also could alter the distribution of electron recoil background such that it incorrectly appears as genuine nuclear recoil events.

Rare event searches are constantly pushing the boundaries of achievable sensitivities. Therefore, the necessary detail and precision of background studies for every new experiment must be subject to constant improvement. The knowledge of backgrounds is not only essential for the discovery of a dark matter signal, but also for guiding material selection, location and design for future experiments. For present direct dark matter searches a previously insignificant background becomes one of the dominant sources and may even be a limiting factor for some future searches. Neutrons produced in interactions of high energy cosmic-ray muons with any part of the detector, shielding or the surrounding environment are a great threat. Common shielding constructions are not able to control the muon-induced neutron background due to the high energies (up to several GeV) of generated neutrons. Data from the ZEPLIN-III veto detector provided the unique opportunity to study the muon-induced neutron rate, which in the case of ZEPLIN-III is dominated by the production in lead. The consequences this result has for future deep underground rare event searches are discussed.

The structure of the thesis is as follows. The second chapter summarises first the astronomical observations leading to the postulation of a gravitationally interacting dark matter component and concludes with a discussion of possible dark matter particle candidates arising from independently motivated theories. Chapter 3 gives an overview

---

of the research field in terms of the different experimental techniques pursued and the current results of WIMP-nucleon interaction cross-section limits. In Chapters 4 and 5, details of the ZEPLIN-III and veto instrument designs and performances during the second science run are presented. Chapter 6 subsequently characterises the scintillator plastic of the veto detector with respect to its response to low energy neutron induced nuclear recoils. Backgrounds in the ZEPLIN-III experiment are detailed in Chapter 7. Chapter 8 then focuses on the analysis leading to a final WIMP-nucleon cross-section limit from the second science run of ZEPLIN-III. The measurement of the muon-induced neutron yield in lead, using data taken with the ZEPLIN-III veto detector, is presented in Chapter 9, along with a comparison to comprehensive Monte Carlo simulations. Finally, a short summary and some concluding remarks are given in Chapter 10.



## Chapter 2

# A Review of the Evidence for Dark Matter and Possible Candidates

Modern cosmology presents us with ever increasing evidence about a rather complex composition of our Universe. It concludes on the necessity of components other than visible matter to be able to explain astronomical observations. To agree with our understanding of Newtonian gravity and the laws of physics achieved in centuries of scientific work, non-visible contributors, so-called dark matter and dark energy, need to be considered. Only  $\sim 4\%$  of the total mass-energy content of our Universe is made up from visible baryonic, ‘ordinary’, matter. The remaining part, which constitutes the majority, is split into dark matter ( $\sim 23\%$ ) and dark energy ( $\sim 73\%$ ).

### 2.1 The standard cosmological model - $\Lambda$ CDM

The standard cosmological model,  $\Lambda$ CDM, incorporates our current views and understanding of the Universe. It accommodates two components of unknown nature, dark energy (denoted by  $\Lambda$ ) and Cold Dark Matter (CDM) [6].

The cosmological evolution described by  $\Lambda$ CDM starts with an initial singularity or ‘Big-Bang’ event and subsequent expansion of the first occurrence of space-time. Table 2.1 summarises the key events in the history of the Universe following the Big-Bang. Stages of force unifications are followed by Big-Bang nucleosynthesis and the change over from a radiation to a matter dominated Universe ( $\sim 10^{4.7}$  years after the Big-Bang). Recombination of protons and electrons, and thus decoupling of the photons resulting in a transparent Universe, occurs  $\sim 380,000$  years after the Big-Bang. More recent observations of distant type Ia supernovae indicated an accelerating recession

Table 2.1: Key events in the history of the Universe with their approximate time scales, assuming a flat Universe. Nucleon and electron pair thresholds denote the times when expansion cooled the hot photon plasma to energies below the rest mass of the given matter particle pair, preventing further creation. For further details see text. This table was adapted from Ref. [8, 9].

Event	Temperature	Energy scale	Time
Now	2.73 K	0.0002 eV	13 Gyr
Distant galaxy	16 K	0.001 eV	1 Gyr
Recombination	3000 K	0.3 eV	$10^{5.6}$ years
Radiation domination	9500 K	0.8 eV	$10^{4.7}$ years
Electron pair threshold	$10^{9.7}$ K	0.5 MeV	3 s
Nucleosynthesis	$10^{10}$ K	1 MeV	1 s
Nucleon pair threshold	$10^{13}$ K	1 GeV	$10^{-6.6}$ s
Electroweak unification	$10^{15.5}$ K	250 GeV	$10^{-12}$ s
Grand unification	$10^{28}$ K	$10^{15}$ GeV	$10^{-36}$ s
Quantum gravity	$10^{32}$ K	$10^{19}$ GeV	$10^{-43}$ s

(recently awarded with the Nobel prize in Physics, 2011, going to S. Perlmutter, B.P. Schmidt and A.G. Riess “for the discovery of the accelerating expansion of the Universe through observations of distant supernovae” [7]), leading to the postulation of a dominating dark energy component in our Universe. The implication is that our Universe is in yet another phase, a state of dark energy domination. A similar scalar field may also have been the force behind an inflationary period occurring at approximately the time of grand unification. Inflation theory has been postulated to solve the ‘horizon’ problem, which describes the improbability of non-causally connected patches of the Universe to take the same properties, by stretching a small region to a size large enough to cover the whole observable Universe.

$\Lambda$ CDM is characterised by the Friedmann equations, which describe the expansion of space in the context of General Relativity. Based on the Copernican cosmological principle of a homogeneous and isotropic Universe a scale factor,  $a(t)$ , relating a position vector at time  $t$  to its value at reference time  $t_0$ , can be defined, *i.e.* the new position vector is a scaled representation of its original. Consequently, the expansion rate,  $H(t)$ , can be expressed as:

$$H(t) = \frac{\dot{a}(t)}{a(t)}. \quad (2.1)$$

By taking the reciprocal of Eq. (2.1) we obtain the characteristic time of the expansion. Assuming no decelerated expansion of the Universe,  $H(t)$  would become a constant,  $H_0$ , the so-called Hubble ‘constant’ ( $H_0 = 70.4_{-1.4}^{+1.3}$  km/s/Mpc [10]).  $H_0^{-1}$  then represents the ‘Hubble time’, which would, in case of constant expansion, be a measure for the

Table 2.2:  $\Lambda$ CDM density parameters as published in Ref. [10].

Parameter	Symbol	Value
Baryon density	$\Omega_b$	$0.0456 \pm 0.0016$
Dark matter density	$\Omega_c$	$0.227 \pm 0.014$
Dark energy density	$\Omega_\Lambda$	$0.728^{+0.015}_{-0.016}$

exact age of the Universe. However, including expansion effects, the current estimate of the real age is  $13.75 \pm 0.11$  Gyr [10]. The Friedmann equation is then the equation of motion for the scale factor:

$$H^2 + \frac{\kappa c^2}{a^2} = \frac{8\pi G}{3}\rho + \frac{\Lambda}{3}, \quad (2.2)$$

with the gravitational constant  $G$  and the energy-mass density  $\rho$ , including both baryonic and non-baryonic components and radiation. The last term in the equation,  $\frac{\Lambda}{3}$ , governs the vacuum energy; an invariant property of empty space with  $\Lambda$  denoting the cosmological constant as first introduced by Einstein's Field equation of General Relativity. This so-called dark energy acts as a negative pressure forcing an expansion of space at an increasing rate.  $\kappa$  represents the curvature parameter of space-time taking the value 0, +1 or -1 for a flat, closed or open Universe, respectively. Incorporating the cosmological constant into the mass-energy density allows the Friedmann equation to be simplified by losing the extra vacuum energy term. For the case of a flat Universe ( $\kappa=0$ ), a critical density  $\rho_c$ , using the modified form of Eq. (2.2), can be defined, which normalises the dimensionless density parameter  $\Omega$  according to Eq. (2.3):

$$\Omega \equiv \frac{\rho}{\rho_c} = \frac{8\pi G}{3H^2}\rho. \quad (2.3)$$

Presently the value of  $\Omega$  is near unity, and as such describes a flat Universe. It can be divided into sub-components: dark energy,  $\Omega_\Lambda$ , and matter,  $\Omega_m$ . The latter term consists of two parts, baryonic,  $\Omega_b$ , and non-baryonic (dark) matter,  $\Omega_c$ , respectively. Cosmological and astronomical observation put constraints on these values, such as shown in Fig. 2.1, restricting the parameter space of  $\Omega_\Lambda$  and  $\Omega_m$ .

Table 2.2 summarises the most recently published parameters by the WMAP (Wilkinson Microwave Anisotropy Probe) collaboration based on measurements of the Cosmic Microwave Background (CMB), Baryonic Acoustic Oscillations (BAO) and the Hubble constant, a quantitative measure of the expansion rate of the Universe.

The dark energy fraction,  $\Omega_\Lambda$ , is not only supported by induction from space curvature constraints in the CMB but its effects can also be directly observed through the accelerated expansion of the Universe. Redshift measurements of distant type Ia

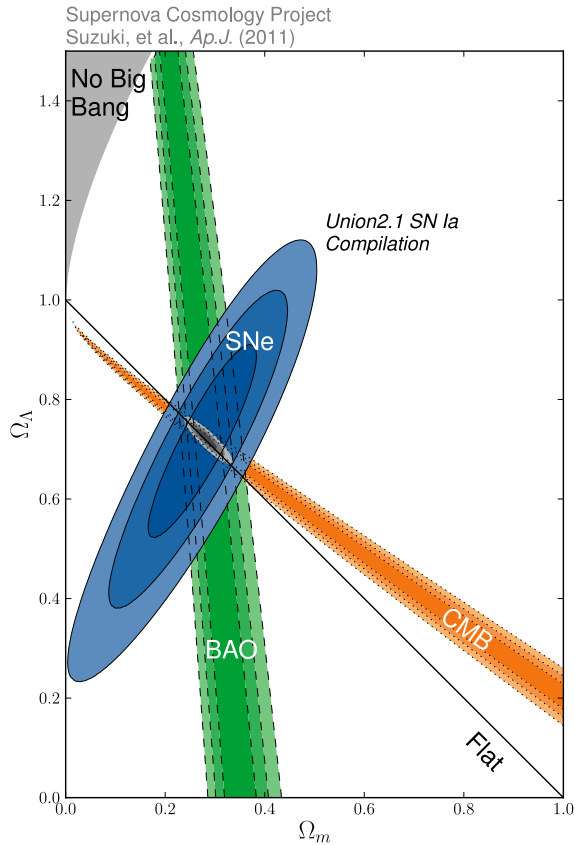


Figure 2.1: Constraints of the  $\Omega_\Lambda$  -  $\Omega_m$  plane in the  $\Lambda$ CDM model by combination of type Ia supernovae (SNe), Cosmic Microwave Background (CMB) and Baryonic Acoustic Oscillations (BAO) measurements. The shaded areas represent 68.3%, 95.4% and 99.7% confidence regions. The line indicates the division between an open and a closed Universe [11].

supernovae, as performed for example by the Supernova Cosmology Project (SCP) [11], conclude on a non-zero dark energy contribution (see Fig. 2.1). Type Ia supernovae are thermo-nuclear explosions of white dwarfs, which have aggregated sufficient mass from a companion star, exceeding the Chandrasekhar limit of 1.4 solar masses. The mass requirement implies similar intensity and luminosity for all supernovae of this type, and as such are frequently referred to as ‘standard candles’.

The dark matter component,  $\Omega_c$ , manifest itself through the gravitational impact at large scales and is supported by numerous astronomical observations. It successfully complies with the  $\Lambda$ CDM cold dark matter paradigm, of dark matter seeding and gravitationally driving structure formations. Evidence is provided, for example, by the effects imprinted in the CMB and by direct observations of mass distributions and dynamics in galaxies and clusters.

The following section will outline the cosmological observations leading to the postulation of a non-baryonic dark component, dominating the matter content of our Universe.

## 2.2 Evidence for dark matter

### 2.2.1 Virially bound systems

The first reference to dark matter in the literature dates back to 1933 by F. Zwicky [12]. By using not only the common method of calculating the apparent mass of a galaxy cluster by the mass to luminosity ratio of the observed stars, but also the virial theorem, led Zwicky to conclude that dark matter must be present in far greater amounts than luminous matter.

In a simplified dynamical framework, galaxy clusters can be treated as statistically stable spheres of radius  $r$ , consisting of  $N$  objects of mass  $m$  and average velocity  $v$ , bound by gravitational forces. For such a system the virial theorem states:

$$\begin{aligned} E &= -U/2 \\ \frac{1}{2}Nm v^2 &= -\frac{1}{2} \left( -\frac{N(N-1)}{2} \frac{Gm^2}{r} \right), \end{aligned} \tag{2.4}$$

where  $E$  and  $U$  denote the kinetic and potential energy of the system, respectively, and  $G$  is the gravitational constant. Consequently, the dynamic mass,  $M$ , can be calculated as shown in Eq. (2.5):

$$M = Nm \simeq \frac{2rv^2}{G}. \quad (2.5)$$

Zwicky's redshift measurements of the radial velocity distribution of member galaxies of the Coma cluster were almost a factor of 10 larger than expected from the summed masses of the individual galaxies (equal to a mass inequality of factor  $\sim 400$ ). This factor has since been revised down based on measurements in the x-ray and infrared spectrum, revealing that luminous stars represent only a minor fraction of the total cluster mass. Instead, hot Intra Cluster Medium (ICM), in the form of x-ray emitting gas, dominates the baryonic mass component. The Coma cluster and clusters of a similar size are typically composed of  $\sim 85\%$  dark matter,  $\sim 13\%$  ICM, and only  $\sim 2\%$  stars [13].

### 2.2.2 Rotation curves of galaxies

Further evidence for a missing mass component arises when looking more closely at the rotational behaviour of spiral galaxies. Galaxies of this type consist of a central bulge and a thin disk, stabilised by angular momentum conservation. Hence, the orbital velocities,  $v(r)$ , of stars outside the central bulge are expected to follow Eq. (2.6), determined by the exerted centripetal force due to the gravitational pull.

$$v(r) = \sqrt{\frac{GM(r)}{r}}, \quad (2.6)$$

where  $M(r)$  is the central mass of the galaxy contained within a radius  $r$ . However, redshift measurements of the orbital velocities in these type of galaxies show no evidence of a decrease at greater radii. Instead, the observed rotation curves are almost flat in this region, inferring a linear increase in mass with radius;  $M(r) \propto r$ . An example, highlighting the discrepancy between expectation and measurement, is shown in Fig. 2.2. To obtain the necessary mass, with the correct properties and distribution, the galaxy may be placed in a spherical halo of dark matter, gravitationally acting upon the system (see Fig. 2.2).

### 2.2.3 Gravitational lensing

Space-time experiences deformation around the gravitational field of mass, as described in the theory of General Relativity. Following the geodesics of curved space, light travelling through the Universe is subject to distortion when passing nearby a massive object. Thus, celestial bodies can serve as an intermediate object forming a gravitational lens which bends the images of distant astronomical background sources. The gravitational field of the intermediate object can be probed, without distinction

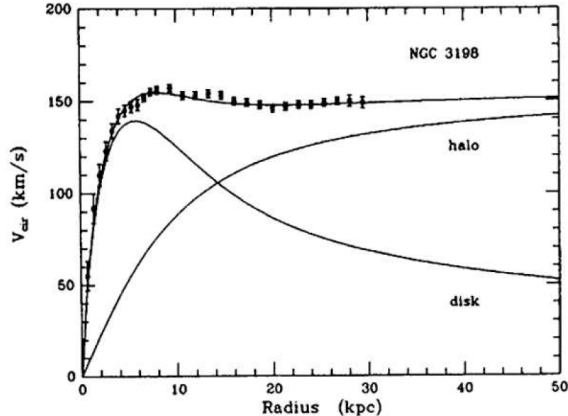


Figure 2.2: Rotation curve of spiral galaxy NGC-3198. The sum of disk and expected dark matter halo contributions match the observations [14].

between baryonic or dark origin. In fact, gravitational lensing was first suggested by Zwicky as a viable technique to measure the mass distribution in our Universe [15].

We distinguish between three different classes of gravitational lensing: strong, weak and micro lensing. Strong lensing distorts the images of the lensed objects to great extent, resulting in clearly visible arcs and multiple images of the same source. On the contrary, micro-lensing imposes no visible distortion on the shape, but the amount of light detected from a background source changes over time.

The weak lensing technique is based on the statistical analysis of numerous weakly lensed sources and is most commonly used for large sky surveys. When observing a preferred direction in the distortion of the intrinsic shape of captured galaxies, mass distributions in the area may be reconstructed. Recent advances in this technique, utilising the redshift dependence (higher redshift galaxies experience stronger shear distortion), enable the recovery of the full three-dimensional gravitational potential of the matter density, resolving large scale structures in both angle and time. This was achieved, for example, by studying the weak lensing data from the Hubble Space Telescope (HST)/Space Telescope A901/902 Galaxy Evolution Survey (STAGES) [16].

A very prominent example, demonstrating the presence of dark matter using the technique of weak gravitational lensing, is the observation of the Bullet cluster [17], a merger of two galaxy clusters. When the two clusters collided, the fluid-like x-ray emitting hot gas or ICM was spatially separated from the visible stellar components, which simply passed through each other. However, the gravitational potential does not trace the ICM, the dominant baryonic mass fraction, but, rather approximately,

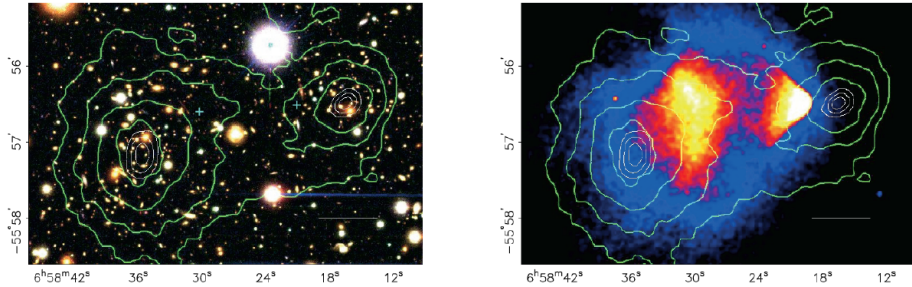


Figure 2.3: Observations from the Bullet cluster (a merger of two galaxy clusters) showing the visible spectrum (left) and the measurements in the x-ray range (right). The green contours visualise the gravitational potential mapped by weak gravitational lensing [17].

the distribution of the galaxies observed in the visible spectrum (see Fig. 2.3). In other words, gravitational lensing measurements reveal the shape of the underlying dark matter mass distribution of the two galaxies.

#### 2.2.4 The cosmic microwave background and large scale structure formation

The cosmic microwave background is a relic of the blackbody radiation at the time of recombination approximately 380,000 years after the Big-Bang. The early Universe was dominated by a hot dense plasma, where matter and radiation were in thermal equilibrium, emitting blackbody radiation. At this stage the high temperatures ( $>3000$  K) supported dissociation of electrons from atomic nuclei. Photons were subject to continuous Thomson scattering from the free electrons, and thus created an opaque Universe. As the Universe expanded, adiabatic cooling caused temperatures to fall below an energy threshold, favouring electrons to combine with protons to form neutral hydrogen atoms. This recombination event decoupled radiation from matter, resulting in free streaming photons in a transparent Universe. Further expansion and cooling led to the highly red-shifted thermal radiation we observe today of  $2.72548 \pm 0.00057$  K [18]. The isotropy of the CMB across the whole observable Universe is striking and provides direct empirical evidence for a Big-Bang scenario.

Despite the apparent homogeneity of the CMB, our Universe evidently consists of very distinct regions of matter over densities in the form of stars and galaxies. To allow for the formation of large scale structures through gravitational attraction, tiny quantum fluctuations in the primordial soup of the early Universe are stretched by inflation to perturbations of the order 1 in 100,000. The gravitational wells of these

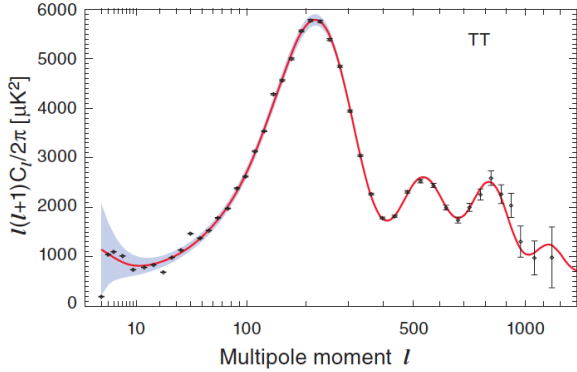


Figure 2.4: Temperature power spectrum from the seven-year WMAP data set. The solid line shows the predicted spectrum for the best-fit flat  $\Lambda$ CDM model [10].

density fluctuations induce baryonic acoustic oscillation in the hot photon-baryon fluid at times before recombination, arising from counteracting radiation pressure rarefying the gravitationally compressed medium. The spatial inhomogeneities at decoupling, the surface of last scattering, are imprinted as angular anisotropies in the CMB as observed today. These are best represented in the form of a power spectrum (an example measurement (from 7-year WMAP observations) is given in Fig. 2.4) showing the acoustic modes caught at their extrema in the form of clearly visible peaks.

The shape of the obtained power spectrum is in excellent agreement with fits from the  $\Lambda$ CDM model, where the positions and amplitudes of the peaks provide constraints on the cosmological parameters as presented previously in Table 2.2. The first peak position is consistent with a flat Universe, indicating a total energy density close to critical. Following observations of a sub-critical dark matter density, a dark energy component needs to provide the missing energy. The relative suppression of the second peak is a measure for the strength of compression and as such the amount of baryonic matter present in our Universe. The series of higher acoustic peaks are sensitive to the dark matter to radiation density ratio, whereby the latter is fixed by CMB temperature measurements. A decrease in the dark matter density increases the amplitude of all peaks and, by not providing gravitational potential wells in the first place, simultaneously eradicates the baryonic compression. The rise in amplitude comes then from a driving effect of the oscillation amplitude, when oscillation modes occur whilst the Universe is still dominated by radiation. At this stage gravitational potential wells are subject to decay, due to the lack of matter domination, boosting the amplitude at rarefaction. A third peak, comparable to or exceeding the amplitude of the second peak, indicates dark matter domination before recombination.

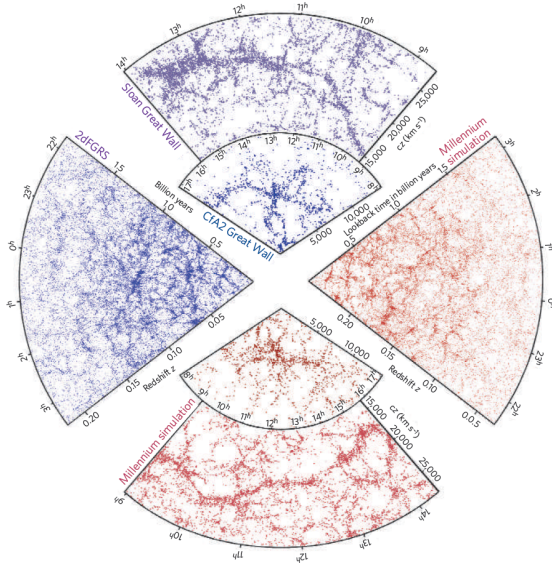


Figure 2.5: Galaxy distribution from spectroscopic redshift surveys (blue) [20, 21, 22] in comparison to data obtained from cosmological N-body simulations (red) [23]. As presented in Ref. [19].

All of the structures imprinted in the CMB help to constrain the fraction of each individual constituent contributing to the overall mass-energy density of the Universe. Extensive N-body simulations probe these parameter constraints, by studying the formation of large scale structures via gravitational interaction of dark matter under the  $\Lambda$ CDM paradigm. Figure 2.5 shows a comparison (for a selected part of the sky) of results obtained from the Millennium simulation [19] to experimentally measured galaxy distributions such as from the Two Degree Field Galaxy Redshift Survey (2dFGRS) [20] and the Sloan Digital Sky Survey (SDSS) [21]. The observed features are strikingly similar, backing a cold dark matter framework leading to the formation of large scale structures visible today.

### 2.2.5 Big-Bang nucleosynthesis

An indirect determination of the dark matter mass fraction in the Universe comes from the measurement of light element abundances. These light elements are produced in the early Universe through Big-Bang Nucleosynthesis (BBN), constraining the baryon to photon ratio observed today.

The early Universe ( $t < 1$  s) was dominated by relativistic particles in thermal equilibrium supporting continuous weak and electromagnetic interactions. At  $t \simeq 1$  s

weak interaction rates fell below the expansion rate of the Universe and the neutron to proton ratio froze out, *i.e.* neutrinos decoupled from the baryons. The resulting neutron to proton ratio of  $\simeq 1/6$  was determined by their mass difference. Subsequent decay of the heavier neutrons into protons altered the ratio to a value of  $\simeq 1/7$  before the short period of primordial nucleosynthesis occurred. BBN is responsible for the preservation of neutrons, forming deuteron through the fusion reaction  $p + n \rightarrow d + \gamma$ . Only when temperatures fell below  $\sim 0.1$  MeV did deuterons become stable against photodissociation and the production proceeded. Once created, further fusion reactions followed, producing predominantly the stable  $^4\text{He}$  isotope, but also in smaller fractions some  $^3\text{H}$  and  $^3\text{He}$ . The deficiency in free neutrons finally stopped the production of new deuterons, which in turn were burned to get to complex nuclei, until eventually the temperature got so low that the electrostatic repulsion of the deuterons caused the reaction to stop, yielding a  $^4\text{He}$  mass fraction of approximately 0.25 (from simply counting the abundance of free neutrons) [24].

The abundances of these early formed light elements can be determined using measurements of light absorption lines in the spectra of distant quasars. Based upon the fact that the amount of deuterium observed was formed during BBN, together with the relative abundances of the other light elements, constraints on the baryonic density can be set. The results are fully compatible with CMB observations.

## 2.3 Dark matter candidates: an overview

So far we have discussed the evidence pointing towards the existence of a dark component, leaving the nature of this elusive substance unanswered. To comply with observations from the CMB and the dynamics of galaxies and clusters, as well as being consistent with BBN and stellar evolution, a viable dark matter candidate has to fulfil a number of fundamental conditions: it must be stable on a cosmological time scale; it must be neutral; interactions other than gravitation must be very weak; and it must match the appropriate relic density.

Additionally, as a secondary condition, the postulated dark matter needs to be consistent with observations and limits set from direct and in-direct searches (see Chapter 3). A thorough discussion of all of the listed constraints is given in Ref. [25]. The list of theorised dark matter candidates to date is extensive. Comprehensive descriptions of Standard Model (SM) and non-SM particles with potential dark matter properties are published in Ref. [26]. The following sections will outline the currently most favoured particle dark matter candidates.

### 2.3.1 Hot, warm or cold dark matter?

Inline with the  $\Lambda$ CDM model paradigm we have thus far only considered the case for cold dark matter (particles). But what are the implications of a warm or even hot dark matter component and how are they defined?

Hot Dark Matter (HDM) describes particles that decouple when relativistic, with a number density roughly equal to that of photons. The prototypical examples of HDM are standard model neutrinos, thermally produced in the early Universe and with a relic abundance today that scales linearly with the masses of the flavours  $m_{\nu_i}$  [25]:

$$\Omega_\nu h^2 = \frac{\sum m_{\nu_i}}{90 \text{ eV}} < 0.0062 \text{ (95\% CL)}, \quad (2.7)$$

where  $h$  is the reduced Hubble parameter, for which the current best limit is taken from Ref. [10]. Consequently, the combined neutrino mass is constrained to  $\sum m_{\nu_i} < 0.58 \text{ eV}$  (95% CL (Confidence Level)) [10]. Due to the free streaming behaviour of such relativistic particles any growth of density perturbations at early times would be severely damped, leading to less clumpiness of galaxy clusters than observed today. As such, the amount that any hot dark matter component would contribute to the total mass-energy density of the Universe is extremely limited.

Thus, to comply with the standard theory of structure formation, CDM particles, which decouple while non-relativistic (*i.e.* become non-relativistic well before the matter dominated era), need to be considered. The most prominent candidate among the CDM particles is the weakly interacting WIMP, a heavy thermal relic. Comprehensive N-body simulations of a CDM scenario (as previously presented in Section 2.2.4) agree very well with observations of galaxy distributions. However, a very light species, which is non-thermally produced, the axion, may still be a viable contender (see below).

Measurements of the CMB anisotropies and galaxy clustering on large scales [27] confirm a Universe with a substantial CDM component. Although these observation probe a large range of scales, probing the  $\Lambda$ CDM model on the very small scale proved to be more difficult. On this scale the dark matter distributions are strongly non-linear due to the added complexity of galaxy formation. N-body simulations suggest that a finite number of sub-haloes are expected for a Milky Way (MW) sized dark matter halo. The absence of luminous satellites, aggregating in these sub-haloes, challenges the successful CDM paradigm. One solution is to assume a sharp drop in galaxy formation efficiency with decreasing halo mass [28]. In this scenario only a small number of sub-haloes are massive enough to host potential luminous dwarf galaxies. Another problem arises from the internal dynamics of these satellites, with greater velocities expected from simulations than measured. One possible explanation for these observations, postulated by M.R. Lovell *et al.* [29], is to replace CDM with Warm Dark Matter (WDM), the

mass of which would be between  $1\text{--}10 \text{ keV}/c^2$ . Using this WDM the formation of haloes that may host satellites is suppressed, and as a result, the dynamics of the sub-haloes are reconciled with the observed data. On the other hand, a more recent publication suggests, based on extensive N-body simulations (Millennium simulation series), that the MW may be less massive than commonly thought, resulting in a reduction in the number of massive sub-haloes. A mass of  $\sim 10^{12}$  solar masses, yielding the required result, would be well within the range of masses allowed. However, this mass supports a virial velocity of only  $\sim 150 \text{ kms}^{-1}$ , well below the rotation speed of the MW disk – usually assumed to be  $220 \text{ kms}^{-1}$  [30].

Despite some minor problems, the  $\Lambda\text{CDM}$  model provides the most robust theory fitting the majority of observations to date. As such, the two CDM candidates that withstand all of the constraints put forward so far are discussed in some more detail.

## Axions

The independently motivated hypothetical axion is a scalar particle arising from physics beyond the standard model, as a solution to the strong CP-problem. The Lagrangian of quantum chromodynamics (QCD) naturally includes a term resulting in CP violation, which depends on the free parameter  $\bar{\theta}$  and with values expected close to unity. This term predicts an electric dipole moment of the neutron. Experimentally, however, no CP violations in strong interactions have been found; the best constraints have been established through measurement of the neutron electric dipole moment, yielding  $\bar{\theta} < 10^{-9}$  [31]. Therefore, the missing CP violating behaviour, implying a very small value for  $\bar{\theta}$ , is one of the fine-tuning problems in the SM. A solution to the CP-problem was proposed by Peccei and Quinn [32, 33] who introduced a new symmetry, which must be spontaneously broken at a temperature  $T_{PQ}$ , during a Peccei-Quinn ( $PQ$ ) phase transition. Thus, the  $PQ$  symmetry invokes an effective potential  $V(\bar{\theta})$ , with a minimum at  $\bar{\theta}=0$ . The associated particle arising from the dynamically restored CP symmetry is the axion, a pseudo-Goldstone boson.

The potential mass of an axion is limited from laboratory searches and astrophysical constraints, from which a mass region above approximately  $3\times 10^{-3} \text{ eV}/c^2$  has been ruled out (see Ref. [34] and references therein). Accelerator searches exclude masses above  $\sim 50 \text{ keV}/c^2$  by looking at axion production from couplings to two photons and to two gluons or the couplings to quarks and gluons. Astrophysics constrains the mass to less than  $0.5 \text{ eV}/c^2$ . Weakly coupled axions accelerate the stellar evolution, allowing stars to lose energy in a very efficient way without re-scattering. Observations of the long lifespans of red giants rule out the higher mass range. Finally, measurements

of the neutrino burst duration from Supernova 1987a are consistent with theoretical predictions, assuming the collapsed supernova core cooled by the emission of neutrinos. Additional cooling through axions would severely decrease this duration, and thus implies an upper limit to the axion mass of  $3 \times 10^{-3}$  eV/c<sup>2</sup>. Despite their very small mass, axions may be a viable CDM candidate due to their non-thermal production in the early Universe. At QCD energy scales, the axion field settles to the CP-conserving minimum and the axion acquires mass during the QCD phase transition. Theoretical models for the production of cold axions are summarised in Ref. [34].

Experiments which search for direct evidence for axions exploit, amongst others, the predicted axion to photon coupling. Dark matter halo axions may be detected by their conversion into microwave photons when passing through a cavity immersed in a static, high magnetic field. When the cavity is tuned precisely to the axion mass, resonances may occur [35]. To date only negative results are reported.

### Weakly interacting massive particles

The WIMP class holds a variety of possible dark matter particle candidates, all of which share a thermal creation process in the early Universe. Whilst in thermal equilibrium at very high temperatures, the number density of CDM was roughly equal to the number density of photons, decreasing together as the Universe expanded. At temperatures below the WIMP mass, production of WIMP particles would drop exponentially due to continuing annihilation. Further cooling, *i.e.* further expansion of the Universe, led to WIMP densities low enough to mitigate further annihilation and the current number of WIMPs ‘froze out’. The relic density today for a generic WIMP,  $\chi$ , can be approximated as [36]:

$$\Omega_\chi h^2 \simeq \frac{3 \times 10^{-27} \text{cm}^3 \text{s}^{-1}}{\langle \sigma_A v \rangle}, \quad (2.8)$$

where  $\langle \sigma_A v \rangle$  is the thermally averaged cross-section for WIMP annihilation into ordinary particles. Although not directly affecting the relic density, the annihilation cross-section is dependent on the WIMP mass,  $m_\chi$ , through [37]

$$\sigma_A v \simeq \frac{g_{\text{weak}}^4}{16\pi^2 m_\chi^2}. \quad (2.9)$$

The weak interaction gauge coupling is denoted by  $g_{\text{weak}} \simeq 0.65$ . For P-wave annihilation, an additional suppression factor needs to be added. By requiring a relic dark matter density, yielding  $\Omega_{\text{total}} \approx 1$ , the annihilation cross-section for any thermally created particle is just as predicted for particles with weak scale interactions and a mass range of approximately 10 GeV/c<sup>2</sup> to 1 TeV/c<sup>2</sup>. Figure 2.6 visualises the freeze-out

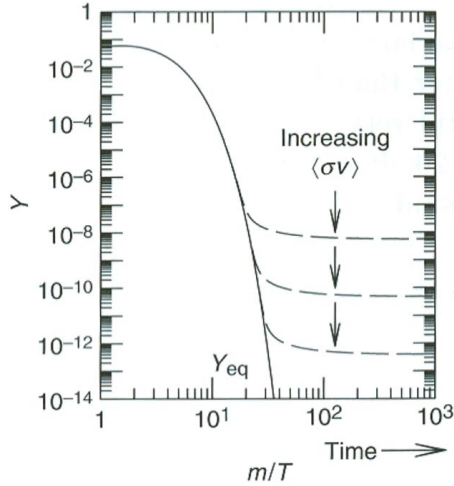


Figure 2.6: Co-moving WIMP density,  $Y$  (the WIMP number density divided by the entropy), as a function of time in the early Universe, showing the decoupling (freeze out) of WIMPs dependent on the annihilation cross-section. The continuing line labeled with  $Y_{eq}$  shows the case when equilibrium would be maintained [38].

scenario in terms of co-moving WIMP number density as a function of time, showing the dependency on the annihilation cross-section.

To find a suitable WIMP candidate one may look into physics beyond the SM on the electroweak scale. One of the best studied extensions to the SM is that of supersymmetry (SUSY), which naturally provides a neutral and stable particle with just the right properties required for a CDM candidate.

The SM of particle physics is one of the most tested theories in physics. Recent detection of what is most likely the Higgs boson by the ATLAS and CMS groups at the Large Hadron Collider (LHC) [39, 40] completes the success story of this theory. However, some details, such as the ‘Hierarchy Problem’, remain unsolved in the SM. The observed Higgs boson mass is  $\sim 125$  GeV/c $^2$ . Although not inconsistent with the SM itself, as it does not predict the mass, one may assume that the Higgs mass would be at the level of the Planck scale (grand unification energy; reduced Planck mass  $m_P = \sqrt{\frac{\hbar c}{8\pi G}} \simeq 2.4 \times 10^{18}$  GeVc $^{-2}$ ) due to large quantum corrections. How can the mass scale of electroweak symmetry breaking be stabilised without requiring an unnatural level of fine tuning? Experimental efforts to date are only able to explore the territory near the electroweak scale, some 16 orders of magnitude below the Planck scale, where quantum gravitational effects would become important. It may seem

natural to assume that some physics beyond the SM occurs at these energies. A symmetry introducing super-partners to the SM particle would cancel the quadratic divergences in the radiative corrections to the mass squared of the Higgs boson. In SUSY a transformation turns a bosonic state into a fermionic state, providing fermion cancelation of quantum corrections due to scalars, and vice versa. The super-partners are subject to the same couplings as their SM counterparts, but with a spin difference of  $\Delta s=1/2$ , *i.e.* leptons and gauge bosons are complemented by a set of SUSY sleptons with spin 0 and a set of gauginos with spin  $s=1/2$ , respectively. Motivated by the ‘Hierarchy Problem’, the SUSY particles are expected to have a mass of about 1 TeV or less, with a residual fine-tuning that increases the more massive the particles are [41]. Furthermore, SUSY provides a mechanism for the unification of the three SM forces (strong, weak and electromagnetic) at high energies and forms together with string theory part of the hypothesised M-theory, a consistent model for a quantum description of gravity.

The Minimal Supersymmetric Standard Model (MSSM) attempts to extend the SM with as few additional parameters as possible. However, without any supplementary conserved quantum number, the MSSM leads to falsified predictions, *e.g.* a significant reduction of the proton lifetime. Thus, as a consequence of lepton and baryon number conservation in the SM, an extra symmetry is required, the so-called R-parity:

$$R = (-1)^{3B+L+2s}, \quad (2.10)$$

where  $s$  denotes the spin and  $B$  and  $L$  are the baryon and lepton number, respectively. Following the definition in Eq. (2.10), all known SM particles are associated with  $R = +1$  and all superpartners with  $R = -1$ . As a direct consequence of R-parity conservation, SUSY particles can only be produced in pairs from SM particle collisions and the heavier superpartners are only allowed to decay into lighter SUSY particles. As a result there are no allowed decay modes for the Lightest Supersymmetric Particle (LSP) and it must be stable. Provided the LSP is neutral and it only interacts via the weak force (next to gravitation) it becomes a viable dark matter candidate. The particles within the MSSM fulfilling these criteria are the neutralino with  $s = 1/2$ , the gravitino with  $s = 3/2$  and the sneutrino with  $s = 0$ . The latter has been experimentally excluded for most of the feasible energy range [42]. The gravitino, the superpartner to the hypothetical graviton, interacts only gravitationally. It is not expected that it was in thermal equilibrium in the early Universe, but rather produced in high-energy particle collisions or in the decays of heavier SUSY particles. As such only a metastable Next-to-Lightest Supersymmetric Particle (NLSP), decaying into the LSP, would have possible detection potential.

The best motivated WIMP candidate is the lightest ( $\tilde{\chi}_1^0$ ) of the four neutralinos, each of which is composed from a linear combination of SUSY fermion fields:

$$\tilde{\chi}_{1,2,3,4}^0 = \alpha \tilde{B} + \beta \tilde{W}^3 + \gamma \tilde{H}_1 + \delta \tilde{H}_2. \quad (2.11)$$

In Eq. (2.11)  $\tilde{B}$ ,  $\tilde{W}^3$  and  $\tilde{H}_{1,2}$  denote a bino (superpartner of the U(1) gauge field corresponding to the weak hyper charge), a neutral wino and neutral higgsinos, respectively, and  $\alpha$ ,  $\beta$ ,  $\gamma$ ,  $\delta$  are the mixing coefficients.

Even the simplest extension to the SM, the previously introduced MSSM, adds over a 100 new free parameters to the theory making it very difficult to set experimental constraints. As such, constrained models, assuming partial unification of parameters at some high energy scale, provide a more accessible way of exploring the allowed parameter space. The two most commonly used SUSY extensions are the minimal SUper GRAvity model (mSUGRA) [43], unifying the SUSY parameters into five universal constants at the grand unification scale, and the lighter version of it, the constrained MSSM (cMSSM) [44], which does not force the gravitino mass to unify at the same energy as the other gaugino masses. Thence, these are also the models predominately used in this thesis when comparing experimentally measured WIMP-nucleon interaction cross-section exclusion curves to the theoretically calculated allowed parameter space [45].

In light of ongoing research at the LHC, in which no evidence has (yet) been found to support a SUSY scenario, it is worth noting that the number of hypothetical dark matter particles, arising from a multitude of theories in this fast progressing area of research, is plentiful. These are either independently motivated theories on the electroweak scale (in an analogous manner to SUSY, naturally providing a dark matter candidate) or self-motivated, with the sole purpose to solve the dark matter puzzle. An overview of most of these particles can be found in Ref. [26]. For example, other WIMP (non-SUSY) candidates are stipulated in the Little Higgs theory or in models with extra dimensions. Each of these theories introduces a new symmetry — for example, T-parity and Kaluza-Klein parity for the two models mentioned — leading to a stable particle and, as such, an excellent WIMP-like dark matter candidate [46].

## 2.4 Summary

Astrophysical evidence for a Universe dominated by the dark sector has been presented. A scenario of non-relativistic cold dark matter agrees well with current observations. From independently motivated theories a number of cold dark matter candidates can

be found. The WIMP shows the greatest discovery potential to date and is sought after using a number of different experimental approaches outlined in the next chapter. This includes the direct search for WIMP-nucleon interactions pursued in experiments located in deep underground mines the main focus of this thesis.

## Chapter 3

# Detection of WIMP Dark Matter

Having established the need for a dark matter component to explain cosmological and astrophysical observations, this chapter will focus on the possible detection methods used to search for this elusive particle. The currently favoured and well motivated cold dark matter candidate, the WIMP, is sought after through a variety of different detection methods. These include space-, ground- and underground-based experiments and can be categorised into three main classes: indirect, particle acceleration and direct searches. It is vital for an exclusive discovery that signals measured with different detection techniques complement one another. Discovery claims based on the result of one measurement alone may lead to controversy and unreliable predictions concerning the exact nature of dark matter.

### 3.1 Indirect detection techniques

Assuming a Majorana type (or Dirac type with no matter-antimatter asymmetry) WIMP, SM particles created in WIMP self-annihilation provide an observable indirect signature of the dark matter in our Universe. In theory, provided kinematic constraints are obeyed, any annihilation products may, potentially, be created. Final particle species being observed by experiments are expected to be dominated by positrons, antiprotons, neutrinos and  $\gamma$ -rays, with the resulting spectra exhibiting a dependence on the WIMP mass. The amount of radiation produced scales with the square of the dark matter density. Experiments utilising this indirect signal thus focus on areas of high dark matter concentration, such as the Galactic Centre, the Sun or nearby galaxies. The hypothesised accumulation of dark matter around the central black hole would provide large fluxes, especially for neutrino searches. In addition to the Galactic Centre, the existence of over dense dark matter regions within galactic haloes (clumps) are discussed, enhancing the expected annihilation rate. Accumulation of dark matter

within celestial bodies of great mass is proposed for any WIMP-like particle due to weak interaction. Although very weak, a WIMP colliding with a star or planet may lose some of its velocity, with a finite probability of getting gravitationally trapped within the core of the body.

The range of indirect dark matter search experiments ranges from ground- and underground-based Cherenkov telescopes to satellites and balloons. A good overview of indirect search experiments and an interpretation of historical and current results is given in Ref. [47] (and references therein). This work will only focus on the most recent and controversial measurements and results.

Data on spectral excess in the antimatter (positron, antiproton) rate over the expected background from cosmic-ray flux are accrued by satellite or balloon mounted experiments in the high atmosphere and above. Although interactions of cosmic-rays with the Interstellar Medium (ISM) generally generate antiparticles, the positron and antiproton fractions are very low ( $e^+/e^- \approx 10^{-1}$ , with  $e^-$  representing only 1-2% of the overall cosmic-ray flux and  $\bar{p}/p \approx 10^{-5}$  at 1 GeV [47]).

Measurements from the space-based PAMELA [48] experiment showed an excess over the expected positron fraction above  $\sim 10$  GeV which cannot be easily explained by secondary production from SM particles. This anomaly was complemented by the more recent measurements of  $e^+ + e^-$  rates using the Fermi satellite [49]. The latter observation was confirmed by data from the ground-based HESS Cherenkov telescope, which can extract the electron component from cosmic-rays by identifying the initial electromagnetic nature of the atmospheric cascade [50, 51]. Results from all these experiments are shown in Fig. 3.1.

Interpretations of the observed excess are plentiful. Figure 3.1 shows a fit from possible dark matter annihilations or decays in full agreement with the increased positron fraction and measured  $e^+ + e^-$  rates [52]. As such, a dark matter contribution to the spectrum cannot be excluded. Nevertheless, the same excess may be explained by the simple assumption that unaccounted but ‘ordinary’ astrophysical sources, such as pulsars or supernova remnants, are adding a significant flux of primary positrons and electrons to the spectrum. Two additional arguments opposing a dark matter interpretation of the results can be found in Ref. [53]. Firstly, the antiproton fraction also measured by PAMELA sets very stringent limits on the dark matter annihilation and rules out most of the parameter space for a common dark matter candidate such as the WIMP (unless exhibiting ‘leptophilic’ behaviour). Secondly, assuming the freeze-out process of the WIMP in the early Universe was subject to the same annihilation cross-section as todays dark matter, the rate of annihilation in the Galaxy would be approximately two orders of magnitude too small to make up for the divergence observed. However, clumpy dark matter density profiles in the Galaxy may provide

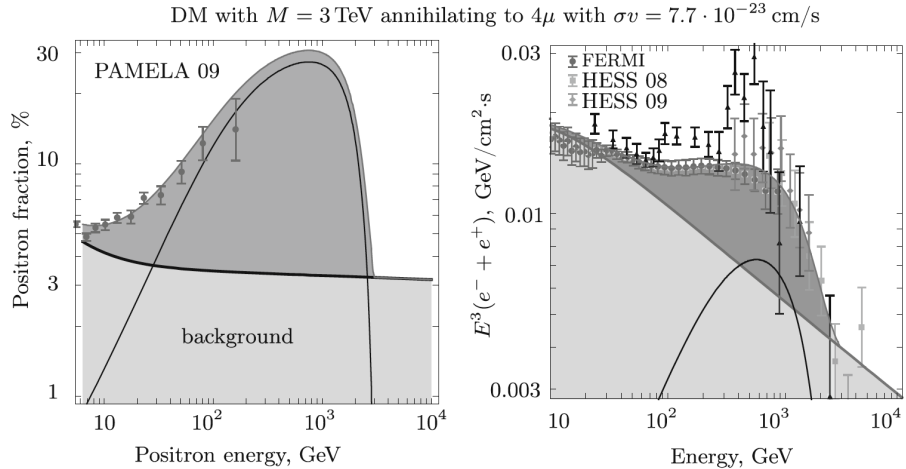


Figure 3.1: Results from the PAMELA experiment, showing an excess in the observed positron fraction above background expectations (left hand side) and collected  $e^+ + e^-$  rates from the Fermi and HESS experiments, exhibiting a similar anomaly (right hand side). The lines (empty histograms) indicate the possible contributions from annihilations of dark matter adding to the background (light grey) to fit the observed data (dark grey) [52].

sufficient enhancement of the annihilation rate.

In contrast to charged particles, neutrinos and  $\gamma$ -rays are not affected by galactic magnetic turbulences. Instead, their propagation is direct with alteration to the spectrum arising only from absorption or oscillation in the case of neutrinos. As such, searches can be directed at discrete locations like the Sun or galaxies beyond the Milky Way. Nevertheless, contributions to the observed rates from common backgrounds need to be carefully assessed. Similarly to secondary production of antimatter,  $\gamma$ -rays are produced when cosmic rays interact with the ISM, predominately producing pions which consequently decay into pairs of photons. Additional sources for  $\gamma$ -ray backgrounds include electron bremsstrahlung in the ISM and inverse Compton scattering. The most recent  $\gamma$ -ray measurements come from the Fermi Large Area Telescope (Fermi-LAT), which looks for  $\gamma$ -rays from dark matter annihilation in dwarf spheroidal galaxies [54]. These low luminosity satellite galaxies around the Milky Way are (expected to be) dark matter dominated systems with only a small interstellar gas component and no current or recent star formation, providing an excellent source to look for dark matter annihilation products. Even more recently, an additional search for pure dark matter satellite galaxies from the same collaboration was published [55]. Based on N-body simulations of a  $\Lambda$ CDM scenario, these are expected to be abundant in the periphery of

our Milky Way. Both searches report a null result. The latter sets a limit for the WIMP annihilation cross-section of  $1.95 \times 10^{-24} \text{ cm}^3 \text{s}^{-1}$  for a WIMP mass of  $100 \text{ GeV}/c^2$  at 95% confidence when annihilating through the  $b\bar{b}$  channel. Cross-section limits from the dwarf spheroidal galaxy search are even lower at  $\sim 10^{-26} \text{ cm}^3 \text{s}^{-1}$  below  $10 \text{ GeV}/c^2$  WIMP mass.

More controversial than the above are results from an analysis of Fermi-LAT data, reporting an enhanced  $\gamma$ -ray rate within a few degrees of the Galactic Centre [56]. A  $7\text{--}10 \text{ GeV}/c^2$  dark matter particle, which primarily annihilates to tau leptons ( $\langle\sigma_A v\rangle = 4.6 \times 10^{-27} \text{ to } 5.3 \times 10^{-26} \text{ cm}^3 \text{s}^{-1}$ ) provides a good fit to the spectrum. Similar to the anti-matter case, it is reasonable to consider alternative explanations. Viable candidates include an extra population of unresolved pulsars towards the Galactic Centre [57], or the secondary production of  $\gamma$ -rays in ISM collisions with high energetic cosmic-ray protons generated by the massive black hole at the centre of the Galaxy [58].

Neutrinos, the only SM annihilation products escaping the Sun, are studied by the currently world leading experiment IceCube [59], a neutrino telescope consisting of an array of over 5,000 photomultiplier tubes (PMTs) installed at a depth of 1–2 km in the Antarctic ice. The Cherenkov light produced from high-energetic muons, generated by interaction of neutrinos in the surrounding ice mass, would provide a detectable signal. Directionality measurements allow the rejection of backgrounds from atmospheric muons. To date no excess over background has been observed. Limits extracted for the WIMP-proton interaction cross-section from a combined analysis with the predecessor experiment AMANDA [60] are shown in Fig. 3.2.

In summary, indirect searches for dark matter based on the detection of SM annihilation products have not shown any conclusive evidence yet. Some experiments have seen anomalies in certain detection channels, but SM explanations are equally convincing and consistency between the different results is not easy to come by.

## 3.2 Searching for dark matter at the LHC

Another powerful tool to ‘indirectly’ measure the existence of particles beyond the SM is provided by accelerator physics, particularly by the LHC. With compelling evidence for the presence of a very light Higgs particle, studies of new physics providing solutions to the ‘Hierarchy Problem’ (discussed in the previous chapter, Section 2.3.1) are of great interest. SUSY theory, which naturally encompasses a dark matter candidate, the LSP, is a role model for such exercises, but analyses are inclusive.

Squarks,  $\tilde{q}$ , and gluinos,  $\tilde{g}$ , are predicted to have the greatest SUSY production cross-section at the LHC. The generation proceeds via  $pp \rightarrow \tilde{q}\tilde{q}, \tilde{q}\tilde{q}^*, \tilde{q}\tilde{g}, \tilde{g}\tilde{g}$  processes in the  $pp$  collisions. Subsequently, squarks and gluinos decay in the most simplified

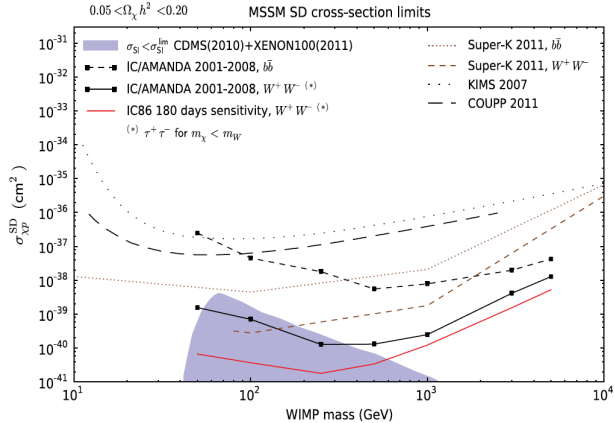


Figure 3.2: Upper limits on the spin-dependent WIMP-proton cross-section (90% CL) from the combined analysis of the IceCube and AMANDA-II data, as well as a projection for the completed IceCube detector (red line). Also shown are results from the indirect DM search Super-K [61] and from the direct search experiments KIMS [62] and COUPP [63]. The shaded area represents the allowed MSSM parameter space, accounting for current constraints from cosmology, accelerator and direct dark matter searches [59].

models via  $\tilde{g} \rightarrow q\bar{q}\tilde{\chi}_i^0, q\bar{q}'\tilde{\chi}_i^\pm$  and  $\tilde{q} \rightarrow q\tilde{\chi}_i^0, q'\tilde{\chi}_1^\pm$  [64]. The most inclusive searches for SUSY are thus concentrated on the presence of multiple jets (with the addition of one or more leptons) and missing transverse momentum, *i.e.* SUSY particles cannot be detected directly. A summary of all individual SUSY searches from the ATLAS detector can be found in Ref. [64]; similarly, results from the squark and gluino search using the CMS detector are presented in Ref. [65]. Searches for rare B meson decays to muon pairs, performed by the LHCb collaboration, show consistency of the number of observed events with background expectations and standard model signal predictions [66]. This result puts another strong constraint on standard SUSY models; however, alternative SUSY constructions can be found which are fully consistent with the measured limit [67].

No evidence for SUSY has been seen to date. The absence of a significant departure from the expected standard model backgrounds allows model dependent constraints for the direct detection parameter space of the WIMP mass,  $m_{\tilde{\chi}_1^0}$ , as a function of neutralino-proton interaction cross-section,  $\sigma_p^{SI}$ , to be calculated. Figure 3.3 shows predictions for  $\sigma_p^{SI}$  using the cMSSM with boundaries being pushed to high WIMP masses and very low cross-section values from the assumption of a measured Higgs mass of  $125 \pm 1$  GeV/c<sup>2</sup> [68].

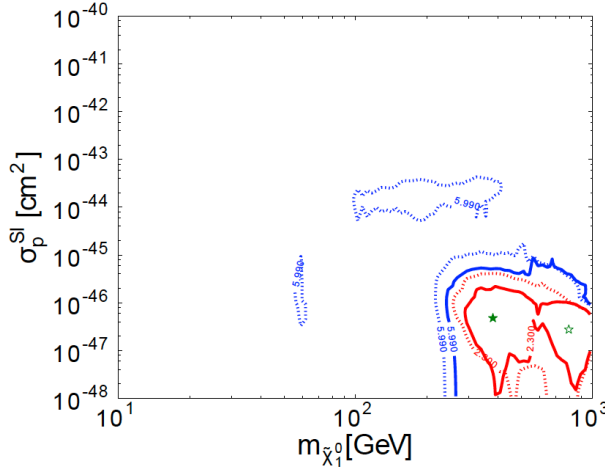


Figure 3.3: Preferred regions in the WIMP mass – spin-independent neutralino-proton cross-section plane, based on calculations in the cMSSM, are presented. Constraints imposed by the cosmological dark matter density, results from ATLAS and CMS  $\sim 5/\text{fb}$  7 TeV LHC data (solid, dashed lines uses  $1/\text{fb}$  LHC data), precision electro-weak measurements and the 225-live days of XENON100 data results on spin-independent dark matter scattering [69] are used (see Ref. [68, 70, 71] and references therein for details). Red and blue lines correspond to the 68% and 95% confidence regions, respectively. The best-fit points are denoted by the green stars [68].

Despite current negative results for physics beyond the SM, the LHC remains a powerful instrument with high discovery potential, especially given the planned upgrade to 14 TeV collision energy in the near future. Nevertheless, accelerator searches will always be more model dependent than direct searches, and absolute exclusion of the existence of a dark matter particle, even in the event of continuing null results, is unattainable. On the other hand, if accelerator searches successfully identify a new particle, direct detection experiments are still required to confirm it is stable on a cosmological time-scale, and to verify that it is indeed the solution to the missing matter component of our Universe.

### 3.3 Direct detection methods

Assuming a weakly interacting dark matter particle, a small but finite probability exists for a WIMP from the galactic halo to elastically scatter off a target nucleus in a dedicated low background experiment. The aim of direct dark matter searches is the detection of WIMP-nucleon interactions in the form of single nuclear recoils, similar to the signal signature of neutron elastic scatters. On the contrary, the dominant

backgrounds, such as  $\gamma$ -rays and  $\beta$  particles, produce electron recoils in the target through interactions with the electrons of the target atoms.

In the absence of any SUSY particles seen by the LHC, it should be emphasised that direct searches, such as the ZEPLIN-III dark matter experiment (the main topic of this thesis), are searching for any WIMP-like dark matter candidate from the galactic halo, *i.e.* conducting broadband sweeps of the electroweak parameter space, such that the experiments are model independent.

The event rate in direct WIMP detection depends both on astrophysical and particle physics parameters. The Standard Halo Model (SHM) describes an isotropic and isothermal sphere of dark matter extending much further than the visible baryonic disc, with a density profile  $\rho(r) \propto r^{-2}$  and a mean particle speed of  $\sim 270$  km/s. The SHM is very much a simplified picture in comparison to complex galaxy dynamics, studied for example using N-body simulations, in which a density profile with a significant level of lumpiness is generated, and also suggesting the possibility that the dark matter haloes may be co-rotating with the galaxy discs to some degree [72]. However, to allow comparison between different experiments, it is customary and reasonable to adopt SHM parameters for cross-section or event rate calculations. The standard values are: the local dark matter density,  $\rho_0 = 0.3$  GeV/cm<sup>3</sup>; the local circular speed of the solar system moving through the halo (it is usually assumed that the rotation curve has already reached its asymptotic value at the Solar radius),  $v_c = 220$  km/s; and the local escape speed of the dark matter particles,  $v_{esc} = 544$  km/s [73] (and references therein).

The WIMP-nucleus scattering rate is governed by the astrophysical factors given above, but is also strongly dependent on the properties of the target nucleus. The following event rate and cross-section calculations are based predominately on the very good overviews given in Refs. [73, 74]. The nuclear recoil energy differential event rate expressed in terms of events/kg/day/keV (also called differential rate or dru) is given by

$$\frac{dR}{dE_R} = \frac{\rho_0}{m_N m_\chi} \int_{v_{min}}^{\infty} v f(v) \frac{d\sigma}{dE_R}(v, E_R) dv. \quad (3.1)$$

In Eq. (3.1)  $m_N$  and  $m_\chi$  are the masses of the nucleus and the WIMP, respectively,  $\frac{d\sigma}{dE_R}$  is the differential cross-section for the WIMP-nucleus elastic scattering and  $f(v)$  is the WIMP speed distribution in the detector frame. The lower integration limit,  $v_{min}$ , is the minimum WIMP speed causing a recoil energy,  $E_R$ , and is described by kinematics of non-relativistic scattering:

$$v_{min} = \sqrt{\frac{m_N E_R}{2\mu_N^2}}, \quad (3.2)$$

where  $\mu_N = (m_\chi m_N)/(m_\chi + m_N)$  is the reduced mass of the WIMP-nucleus system. The upper integration bound is formally infinity, but the local escape speed,  $v_{esc}$ , is normally taken as the maximum speed for gravitationally bound WIMPs. An idealised SHM dark matter sphere extends infinitely, and thus so too does the velocity distribution which takes the form of a solution to the collision-less Boltzmann equation (Maxwellian distribution), given by Eq. (3.3), where  $\sigma_v = \sqrt{(3/2)} \cdot v_c$  is the dark matter velocity dispersion in the halo and  $N$  is a normalisation constant:

$$f(\mathbf{v}) = N \exp\left(-\frac{3|\mathbf{v}|^2}{2\sigma_v^2}\right). \quad (3.3)$$

However, in reality the Milky Way halo is finite and the velocity distribution will be limited by the local escape speed. A more realistic but still ad hoc approach is provided in Eq. (3.4), whereby  $f(\mathbf{v})$  is subject to a smooth truncation at speed  $v_{esc}$ :

$$f(\mathbf{v}) = \begin{cases} N \left[ \exp\left(-\frac{3|\mathbf{v}|^2}{2\sigma_v^2}\right) \exp\left(-\frac{3v_{esc}^2}{2\sigma_v^2}\right) \right], & |\mathbf{v}| < v_{esc}, \\ 0, & |\mathbf{v}| \geq v_{esc}. \end{cases} \quad (3.4)$$

For a full description of the velocity distribution of WIMPs streaming through the detector in the experiment's frame of reference, the Earth's rotation around the Sun with a speed of  $\sim 30$  km/s needs to be considered. This additional velocity component leads to a seasonal variation in the expected WIMP event rate, which may be utilised as a signature for dark matter detection (see subsection "Other detection techniques" in Section 3.3.2 for more details). A complete parameterisation including the detectors motion in the halo frame, where velocity  $v_e(t)$  describes the summed velocity of the Sun in the halo frame and that of the Earth relative to the Sun, and the result of the integral over the velocity distribution

$$\int_{v>v_{min}} \frac{f(v)}{v} dv, \quad (3.5)$$

is given in Ref. [75].

### 3.3.1 Cross-sections of WIMP-nucleon interactions

The final part of Eq. (3.1) left to discuss is the WIMP-nucleus cross-section, which can be split into spin-independent (SI) and spin-dependent (SD) components. The finite size of the target nucleus implies that, with increasing nuclear recoil energy,  $E_R$ ,

there is a loss of coherence, which ultimately leads to a suppression in the event rate for heavy target nuclei. This is accounted for by the nuclear form factor,  $F(E_R)$ , a Fourier transform of the nucleon density, also sometimes parameterised in terms of the momentum transfer  $q = \sqrt{2m_N E_R}$ . By introducing a zero momentum transfer cross-section,  $\sigma_0$ , the form factor can be decoupled and the differential cross-section expressed as

$$\frac{d\sigma}{dE_R} = \frac{m_N}{2\mu_N^2 v^2} (\sigma_0^{SI} F_{SI}^2(E_R) + \sigma_0^{SD} F_{SD}^2(E_R)) . \quad (3.6)$$

The contributions to the SI cross-section arise from scalar and vector couplings to quarks and takes the form

$$\sigma_0^{SI} = \frac{4\mu_N^2}{\pi} \left( [Zf_p + (A-Z)f_n]^2 + \frac{B_N^2}{256} \right) , \quad (3.7)$$

where  $Z$  and  $A$  are the atomic and mass number, respectively, and  $f_{p,n}$  represent the effective scalar coupling to the proton and the neutron, respectively. The last term in Eq. (3.7) describes the vector coupling contributions with  $B_N$  as defined in Eq. (3.8):

$$B_N \equiv \alpha_u^V(A+Z) + \alpha_d^V(2A-Z) . \quad (3.8)$$

Only valence quarks contribute to the coupling, and the parameters  $\alpha_{q=u,d}^V$  determine the vector coupling strength.

For general comparison to theory and other experiments (with different target materials) cross-section limits are commonly calculated in the form of the scalar WIMP-nucleon cross-section,  $\sigma_n$ , related to  $\sigma_0^{SI}$  as given in Eq. (3.9), where  $\mu_n = (m_\chi m_n)/(m_\chi + m_n)$  is the WIMP-nucleon reduced mass:

$$\sigma_0^{SI} = A^2 \left( \frac{\mu_N}{\mu_n} \right)^2 \sigma_n . \quad (3.9)$$

In this case WIMP coupling to neutrons and protons is assumed to be very similar, and thus  $f_p = f_n$ . Additionally, when studying Majorana type particles,  $B_N$  vanishes.

The form factor for the SI contributions,  $F_{SI}^2(q)$ , is determined from electron-nucleus scattering data [76] and may be parameterised as follows:

$$F_{SI}^2(q) = \left( \frac{3j_1(qR_1)}{qR_1} \right)^2 \exp[-q^2 s^2] , \quad (3.10)$$

where  $j_1$  is a spherical Bessel function,  $s \approx 1$  fm is the thickness of the nuclear skin and  $R_1 = \sqrt{R^2 - 5s^2}$  with  $R \approx 1.2 A^{1/2}$  fm. For zero momentum transfer, the form factor

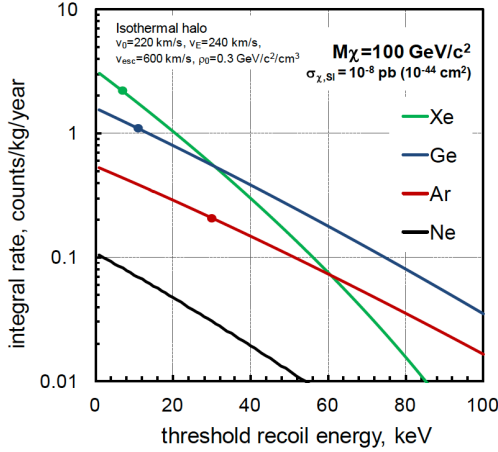


Figure 3.4: Predicted integrated WIMP elastic scattering rates as a function of energy threshold for a number of different targets (Xe, Ge, Ar, Ne), assuming perfect energy resolution and detection efficiency. Calculations are followed through from [77] with the halo parameter used as shown in the figure and assuming a  $100 \text{ GeV}/c^2$  WIMP mass as well as an interaction cross-section per nucleon of  $10^{-8} \text{ pb}$ . The dots indicate reasonable detection thresholds for the various technologies utilising a specific target material [72].

is normalised to unity,  $F(0) = 1$ . As previously mentioned, the nuclear form factor decreases as a function of transferred momentum much more rapidly for heavier target nuclei. In fact, for xenon the first characteristic diffraction minimum is observed at 100 keV nuclear recoil energy. Nevertheless, the energy spectrum of nuclear recoils due to WIMP interactions with a target material is approximately exponential with most recoil energies expected well below 100 keV (despite the dependence on the WIMP mass) [77]. A low detector energy threshold is crucial for boosting the WIMP count rate. Despite the negative influence of the form factor on the event rate for heavier target materials, the  $A^2$  dependence of  $\sigma_0^{SI}$  (as shown in Eq. (3.9)) will (in total) favour heavier nuclei. The effect on the event rate is demonstrated in Fig. 3.4, showing the integrated rate as a function of threshold energy for different target materials. The greatest interaction rates at low thresholds are expected for Xe. Further advantages of Xe as a target material are discussed in the next chapter, Section 4.2.

The spin-dependent contributions to the total WIMP-nucleus cross-section originate from axial-vector coupling to quarks. For a fermionic WIMP the SD zero momentum cross-section is given by

$$\sigma_0^{SD} = \frac{32G_F^2\mu_N^2}{\pi} \frac{J+1}{J} [a_p\langle S_p \rangle + a_n\langle S_n \rangle]^2, \quad (3.11)$$

where  $J$  is the total angular momentum of the nucleus,  $G_F$  is the Fermi coupling constant and  $\langle S_{p,n} \rangle$  are the expectation values for the spin content of the proton or neutron group in the nucleus. An approximation of these quantities can be found from simple shell model calculations assuming that the nuclear spin only depends on the single unpaired proton or neutron, and, as such, vanishes for even nuclei. The effective WIMP-nucleon coupling constants  $a_{p,n}$  are the sum of the WIMP-quark couplings coming from each quark flavour multiplied by the proton or neutron spin fraction each of these quarks carries and are dependent on the WIMP particle content. An explicit definition can be found in Ref. [74].

The form factor for the SD part,  $F_{SD}(q)$ , is defined as:

$$F_{SD}^2(q) = \frac{S(q)}{S(0)}. \quad (3.12)$$

$S(q)$  is a sum composed of three independent functions, an isoscalar, an isovector and an interference term (with coefficients determined by the WIMP-nucleon couplings). A complete definition of the so-called spin structure functions can be found in Ref. [78].

In contrast to the SI case, heavier target materials may not necessarily yield greater interaction rates than target species with a favourable spin factor, such as  $^{19}\text{F}$  or  $^{127}\text{I}$ . For example, in ZEPLIN–III the relatively low value of  $\langle S_p \rangle$  results in a strongly reduced sensitivity to WIMP-proton interactions. Only the WIMP-neutron channel, *i.e.* by setting  $a_p = 0$ , allows a competitive result for the SD cross-section to be obtained.

### 3.3.2 Detectors and experimental techniques

A number of different approaches are pursued in trying to detect a direct interaction in the form of a nuclear recoil of a galactic halo WIMP (expected flux on Earth of order  $\sim 10^5$  (100  $\text{GeVc}^{-2}/\text{m}_\chi$ )  $\text{cm}^{-2}\text{s}^{-1}$ ) with a given target material. Energy depositions may produce a signal via three different channels: the generation of heat (phonons), excitation (resulting in scintillation) and ionisation. Most experiments use two of these detection channels simultaneously in various combinations to exploit different relative yields for electron and nuclear recoils, enhancing background rejection. The two signal channels affected by a lower (quenched) yield for nuclear recoils are scintillation and ionisation. Phonon signals are not observed to be significantly quenched [79]. A compilation of completed, current and near future direct dark matter search experiments is shown in Fig. 3.5, highlighting the different detection signals used for each detector. It should be once more emphasised that a potential discovery

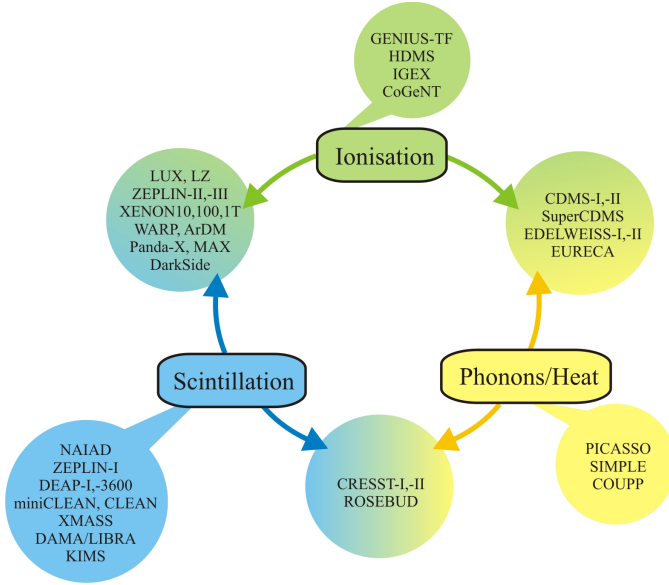


Figure 3.5: Direct dark matter search experiments categorised by energy deposition channel(s) used. The author acknowledges that there may be some dark matter searches missing in this diagram.

would highly benefit from dark matter signals detected with different target materials and technologies in terms of characterising the newly discovered particle and for the mitigation of systematic errors.

The following subsections will briefly discuss the two leading general detection techniques: liquid noble gas and cryogenic crystal detectors. Comprehensive reviews of searches for the direct detection of dark matter can be found in Refs. [80, 81, 82], and specifically for liquid noble gas detectors in Refs. [72, 83]. Similarly to previously discussed detection methods, I will concentrate on the most recent experiments and cross-section results and conclude by giving a short review of alternative detection technologies, utilising for example the expected seasonal event rate variations or changing directionality.

### Noble gas detectors

Liquid noble gas targets show a number of favourable properties for applications in direct dark matter search experiments. Whilst acting as the scintillation medium, liquid noble gas targets also provide the possibility to detect ionisation signals from the primary interactions (when operated with a dual-phase liquid-gas target). Freed electrons can drift through the medium and are extracted into a gas layer of the

given detection material through the application of electric fields, amplifying the ionisation signal through secondary scintillation (electroluminescence). Moreover, the generally large scintillation yields and low radioactive contamination levels are advantageous. Contaminants such as Kr, Rn, Ar and O<sub>2</sub> (or other electronegative impurities) are relatively easy to remove with dedicated purification systems. Another favourable property for low-background experiments, attempting to achieve the greatest sensitivity, is self-shielding. It has been demonstrated in two-phase systems that by selecting only the most central region of the target volume, peripheral parts of the liquid may act as a shield protecting the central region from ambient radioactivity.

Xe and Ar are the most commonly used noble gas elements. Despite the general advantages of these two noble gases, specific properties apply. Ar is relatively abundant in the atmosphere and therefore easier to source than Xe. Nevertheless, to achieve the necessary levels of low background, <sup>39</sup>Ar depletion is imperative (due to its  $\beta$ -decay with an endpoint energy of 565 keV, at a rate of 1 s<sup>-1</sup>kg<sup>-1</sup> [84]). Underground natural gas reservoirs were found to store argon with an <sup>39</sup>Ar component of less than 5% of the atmospheric value [85]. However, using these underground sources is significantly more cost extensive. Liquid xenon shows better self-shielding properties, higher scintillation and ionisation yields and the Vacuum Ultraviolet (VUV) scintillation light can be detected with quartz-window PMTs without additional wavelength shifting (necessary for Ar). A more detailed discussion of liquid/gaseous xenon as a detection medium is given in the next chapter, Section 4.2.

In the case of single-phase (liquid) detectors, scintillation is the only signal observed by an array of PMTs viewing the target volume. Discrimination between electron recoil background and nuclear recoils is achieved to some degree with pulse-shape discrimination from the difference between the two effective decay time constants. Here, liquid argon shows great potential, with significantly different time scales of  $\sim$ 1,600 ns to  $\sim$ 7 ns for electron and nuclear recoils, respectively, in comparison to  $\sim$ 32 ns and  $\sim$ 18 ns in liquid xenon (measured in an energy range of 10–20 keV) [72]. Currently installed and built detectors which use this technology are XMASS [86], featuring a  $\sim$ 800-kg Xe target contained within a spherical shell, the future DEAP-3600 (3600 kg) [87] detector and its partner experiment MiniCLEAN (360 kg) [88], both of which utilise liquid argon. The XMASS experiment predicts a sensitivity to spin-independent WIMP-nucleon cross-sections of order 10<sup>-9</sup> pb to be feasible. However, a recently published light WIMP search analysis ( $<20$  MeV/c<sup>2</sup>) only reached a cross-section limit at the level of 10<sup>-5</sup> pb [89]. The two liquid argon detectors are currently being installed in the SNOLAB underground laboratory in Canada and projected sensitivities to the SI cross-section are  $2\times 10^{-9}$  pb and 10<sup>-10</sup> pb for MiniClean and DEAP-3600, respectively. The former is also designed to hold a liquid neon target, which, in the case of a positive

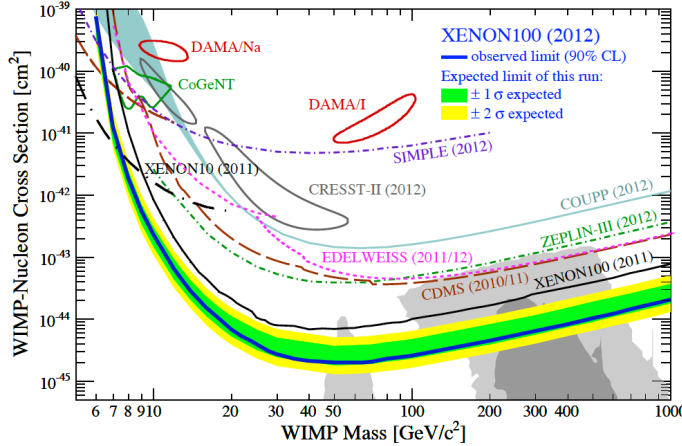


Figure 3.6: Spin-independent WIMP-nucleon cross-section limits as a function of WIMP mass from direct dark matter search experiments [91, 75, 92, 93, 94, 95, 96, 97, 98], including the most current (status February 2013) results: the SSR of ZEPLIN-III and the 225-live-day data of the XENON100 experiment. The grey shaded areas represent the  $1\sigma/2\sigma$  regions preferred by cMSSM [69].

result, provides the opportunity to independently verify backgrounds and the observed WIMP signals with a different target material by exploiting the  $A^2$  dependency in  $\sigma_0^{SI}$  given in Eq. (3.7).

Current world leading experiments, however, use the advantages of dual-phase technology, allowing much higher discrimination efficiencies to be achieved. ZEPLIN-II was the first dark matter detector operated underground to simultaneously measure scintillation and ionisation (through secondary scintillation) signals [90]. ZEPLIN-III reported in its second science run a spin-independent WIMP-nucleon cross-section limit of  $3.9 \times 10^{-8}$  pb (90% CL) [2]. The present world-leading 90% confidence SI cross-section limit comes from the 225-live-day data of the XENON100 experiment (34 kg of Xe fiducial target mass) at  $2.0 \times 10^{-9}$  pb (both minima are near 50 GeV/c $^2$  WIMP mass), surpassing all previous cross-section limits for WIMP masses above  $\sim 8$  GeV/c $^2$  [69]. Cross-section limit curves for these and previous results are shown in Fig. 3.6.

Dual-phase detectors utilising argon as a detector material are the DarkSide-50 experiment [99] with a target mass of 50 kg, currently constructed at the Gran Sasso National Laboratory (LNGS) and the 1-tonne ArDM detector [100], ready to be installed in an underground location. Projected sensitivities for these experiments are  $\sim 10^{-9}$  pb in both instances. The DarkSide collaboration is currently operating a 10-kg prototype detector (DarkSide-10) at LNGS [99].

Cross-section limits as low as  $2 \times 10^{-10}$  pb are expected to be reached in the near future with the LUX detector [101], very recently installed in the Sanford Underground Laboratory in South Dakota, USA. The 370-kg (100 kg fiducial) dual-phase liquid/gas xenon detector is expected to start operation early this year (2013) and will further prove the scalability of liquid noble gas detectors.

Plans for building tonne-scale xenon detectors are pursued by the XENON1T [102] and the LUX-ZEPLIN (LZ) [103] collaborations, expected to reach sensitivities at the level of  $10^{-11}$  pb in the next  $\sim 5$  years. The two-phase LZ detector features a 7-tonne xenon target with a fiducial volume of  $\sim 5$  tonnes. The dimensions of the water tank (8 m in diameter and 6 m in height) currently used by the LUX experiment also allow for the installation of the larger LZ detector following the completion of the former. The water tank provides shielding from ambient  $\gamma$ -ray and neutron backgrounds and doubles as an active muon veto. Similarly to the LUX detector, the 2.2-tonne dual-phase XENON1T detector ( $\sim 1.1$  tonne fiducial volume) also utilises a water Cherenkov muon veto in the form of a water tank surrounding the detector (4 m thick water shield on all sides), which will be installed at LNGS.

### **Cryogenic crystal detectors**

Cryogenic crystal direct dark matter detectors excel in terms of discrimination, energy resolution and thresholds. Elastic scattering WIMPs may be detected via an induced temperature increase (of order  $\mu\text{K}$ ) in the crystals, which are cooled to tens of mK. The fraction of the energy deposited by a particle that is transferred to the crystal to create the measured phonons is practically independent of the particle type. As such, quenching does not affect nuclear recoils in this channel and excellent energy resolution and low thresholds can be achieved. For electron recoil discrimination, a second channel, which is subject to quenching, is read out simultaneously.

The CDMS-II experiment based at the Soudan Underground Laboratory, USA, uses an array of germanium (and silicon) crystals with a combined phonon and scintillation readout. Their present WIMP-nucleon cross-section limits are derived from the nineteen 230-g germanium detector modules. Ionisation charges drift through the modules, due to the application of a weak electric field, to electrodes on the surfaces of the  $\sim 10$  mm thick wafers. In this case, using ionisation yield measurements to discriminate between particle species, rare signal signatures arising from electron recoil background mimicking nuclear recoils, are potentially very damaging. Electron recoils occurring very close to the surface of the detector (electrodes) may suffer from reduced ionisation collection due to trapping in crystal defects or diffusion to the wrong electrodes. To overcome this problem, the CDMS-II experiment exploits the difference

in arrival time of the phonon signals between surface and bulk events. Combining the signal channel ratio and a minimum timing threshold, a discrimination of less than 1 in  $10^6$  was achieved. A spin-independent WIMP-nucleon cross-section limit at 90% confidence of  $3.8 \times 10^{-8}$  pb for a WIMP mass of  $70 \text{ GeV}/c^2$  was reported by the CDMS-II collaboration [93] (see Fig. 3.6).

The EDELWEISS II WIMP search, operated at the Laboratoire Souterrain de Modane, uses a similar approach; in this instance, phonon and ionisation signals are simultaneously detected using an array of 400-g germanium cryogenic crystals. Here, surface events are identified and rejected through an interleaved electrode geometry on the surface of the crystals, whereby charges from bulk recoils are drifted to one set of ‘fiducial’ electrodes. Electron recoils occurring close to the surface, on the other hand, may produce signals in both alternating ‘fiducial’ and ‘veto’ electrodes. A cross-section of  $4.4 \times 10^{-8}$  pb at 90% confidence level for a WIMP mass of  $85 \text{ GeV}/c^2$  was excluded [94] (see Fig. 3.6).

On the contrary, the CRESST-II experiment utilises energy depositions in the form of excitations followed by subsequent scintillation together with the common phonon signal readout. Each detector module is made from the combination of a  $\text{CaWO}_4$  target and a separate small silicon or silicon-on-sapphire wafer for recording of the scintillation light emitted by the target. Eight modules are operated with a total target mass of  $\sim 10 \text{ kg}$ . In their most recent publication, the CRESST-II collaboration reports the detection of 67 events in the WIMP signal acceptance region. Evaluating background events, contributing to the measured signal, they find two allowed regions with  $> 4\sigma$  statistical significance in the standard spin-independent WIMP-nucleon cross-section – WIMP-mass parameter space. The regions are centred around a WIMP mass of  $25.3 \text{ GeV}/c^2$  and  $11.6 \text{ GeV}/c^2$ , with a cross-section of  $1.6 \times 10^{-6}$  pb and  $3.7 \times 10^{-5}$  pb, respectively [92]. Clearly these regions have long been excluded by other experiments (see Fig. 3.6). Moreover, motivated by the recent interest in light WIMPs, an extended analysis of the CRESST-II commissioning run data (2007) to lower WIMP masses was conducted [104]. Observed upper limits of the SI WIMP-nucleon cross-section result in mild tension with the allowed WIMP elastic scattering regions published from the CRESST-II science run data [92]. It remains unclear if unaccounted background sources/signals are responsible for the apparent excess or if more exotic dark matter scenarios need to be considered.

Despite all of the favourable properties associated with using cryogenic crystals as a target material in direct dark matter searches, one major disadvantage in comparison to liquid noble gas detectors remains – scalability. High-purity cryogenic crystals are limited to comparably small sizes and are very cost extensive to produce. Large scale

detectors are thus based on modular technology, combining lots of small individual crystal detector modules together. The amount of instrumentation needed to support every individual structure may also have a negative impact on the background. Projects to scale up to one tonne, currently under consideration, are the SuperCDMS experiment [105], based on CDMS technology, and EURECA [106], a joint venture from the CRESST and EDELWEISS collaborations.

### Other detection techniques

For an exact determination of the expected energy differential event rate, the Earth’s orbit around the Sun needs to be considered. Depending on the orbital velocity component in the direction of solar motion, the Earth’s velocity can either add or subtract to the total Earth’s speed with respect to the galactic rest frame. The resulting annual modulation, *i.e.* a cosine function with a period of one year, shows a peak in the summer around the 2<sup>nd</sup> of June and a minimum in the winter around the 2<sup>nd</sup> of December. Since the Sun’s circular speed in the Galaxy is significantly larger than the Earth’s orbital speed, the amplitude of the modulation is very small and expected to be of order 1–10%.

This ‘model-independent’ annual modulation signature in the WIMP event rate has been tested for over a decade now by the DAMA/LIBRA collaboration. The experiment based at LNGS consists of 25 ~10-kg NaI(Tl) crystals with a PMT readout for the induced scintillation signals. From a total exposure of 1.17 ton·years (in conjunction with its predecessor experiment DAMA/NaI) DAMA/LIBRA presents evidence for a modulating signal with statistical significance of  $8.9\sigma$  and over 13 measured annual cycles. Not only is the measured period ( $0.999 \pm 0.2$  years) and phase ( $146 \pm 7$  days) compatible with expectations of dark matter particles from the galactic halo, the modulation is as expected for dark matter interactions only present in the low energy region of single hit events [107]. The measured amplitude of the signal from the plot of residuals is  $0.0116 \pm 0.0013$  counts/day/kg/keV (see Fig. 3.7). This very consistent modulation is subject to controversy in the field of dark matter research, since other direct dark matter experiments very clearly exclude the possibility that the results obtained by DAMA/LIBRA could have originated from standard single-elastic nuclear recoils (see Fig. 3.6). However, speculation of backgrounds with similar periodical behaviour, such as cosmic-ray muons, giving rise to this sort of variation in the event rate were found to be incompatible with the observed phase [108]. Alternative WIMP interaction models may need to be considered to resolve the apparent incompatibility between the results discussed here. An inelastic dark matter model may offer a possible resolution. Here, it is assumed that WIMPs scattering off baryonic matter

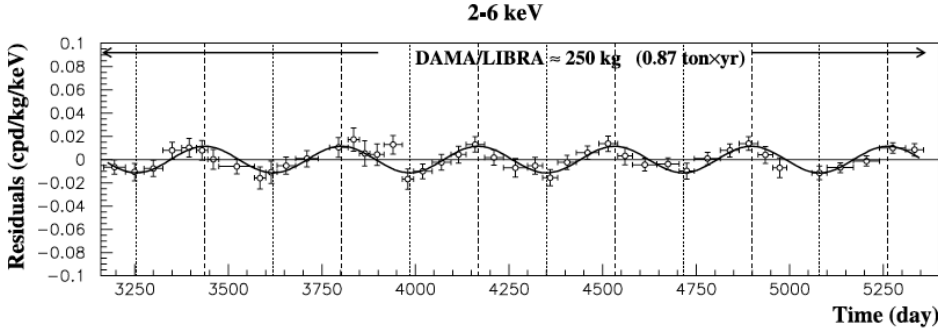


Figure 3.7: Modulation of the residual single hit scintillation event rate in DAMA/LIBRA from the 2–6 keV energy interval. Here, only the data collected over six annual cycles (0.87 ton×year) from the DAMA/LIBRA experiment are shown. The curve indicates the best fit (cosinusoidal function) to data from the full exposure. Maximum and minimum from the expected dark matter interaction rates are indicated by the dashed and dotted vertical lines, respectively [107].

simultaneously transfer to an excited state, while elastic scattering is forbidden or highly suppressed. However, most of the favoured parameter space was excluded by ZEPLIN–III [109] and shortly after fully ruled out by XENON100 [110].

More recently, the CoGeNT collaboration also reported an annual modulation in the rate of low-energy events consistent with a WIMP mass of 7–9 GeV/c<sup>2</sup> and a cross-section of  $\sim 10^{-4}$  pb [91]. However, the statistical significance was only  $2.8\sigma$ . Additionally, a search for annual modulation in low-energy CDMS-II data yielded a negative result and therefore disfavours the elastic WIMP scattering origin of the signal observed in the CoGeNT experiment at >98% confidence [111]. A conclusive explanation of the observed annual modulation signals remains unclear and may involve even more exotic dark matter models (*e.g.* [112]).

A second unambiguous characteristic of the WIMP flux from the galactic halo is directionality, arising from the detector’s motion with respect to the Galaxy. Two effects need to be considered here. Firstly, the WIMP flux in the detector’s lab frame will be sharply increased in the direction of the Earth’s motion through the Galaxy, resulting in a similar peak in the recoil spectrum. Mostly dominated by the Sun’s motion, the event rate in the forward direction (relative to the mean direction of the motion of the Sun) is expected to be roughly an order of magnitude larger than in the backward direction. Being able to measure the general incoming direction of a WIMP would allow to distinguish a genuine dark matter signal from isotropic background with only  $\sim 10$  detected events [74]. Secondly, due to the Earth’s rotation around it’s

own axis, a change in the mean recoil direction in the lab frame of the detector may, over a sidereal day, produce an observable signature for full directional reconstructing detectors. Here, the change in directionality observed depends directly on the latitude of the detector's location on Earth. Research in this field is currently limited to R&D programmes only. Experimental efforts are based on gaseous targets in Time Projection Chambers (TPCs) attempting to detect a directional signal on an event to event basis. The DRIFT detector is the first of its kind and is still in operation in the Boulby Mine, UK [113]. Nevertheless, the sensitivities achieved by detectors using this type of technology are, to date, inadequate for providing any real discovery potential, due to the minimal target masses achieved in any reasonably sized detectors.

A completely different approach is used by a set of experiments, for example, PICASSO [114], SIMPLE [96] or COUPP [97], which operate on the principle of a bubble chamber. Metastable superheated droplets are dispersed in viscous materials. Upon interaction with radiation the droplets undergo a phase transition. Each bubble nucleation of the gas phase is accompanied by an acoustic signal, which then can be detected by piezoelectric transducers. This detection technique provides excellent rejection of signals from electron recoils, when choosing the right chamber pressure and temperature. Competitive limits on the spin-dependent WIMP-proton cross-section are reported from these types of experiments.

An overview of the most recent searches for WIMP dark matter using a multitude of different approaches has been presented. The variety of detection methods and target materials used is of utmost importance for the discovery of a new particle in the first instance and, in the long term, for studying its properties. The growing number of experiments and current results reflects the momentum of this fast progressing field. The ZEPLIN project has delivered valuable contributions to the field of direct dark matter search and has had a leading role in the development of dual-phase xenon scintillation detectors. In the subsequent chapters, I will concentrate on the ZEPLIN–III experiment, focussing in particular on a thorough characterisation of instrument components and background signals; furthermore the final cross-section results obtained from the second science run data will be presented.



## Chapter 4

# The ZEPLIN–III Experiment

ZEPLIN–III (ZonEd Proportional scintillation in LIquid Noble gases) was the last instrument deployed within the ZEPLIN programme, each of which was designed to have a competitive sensitivity at the time of its deployment [115].

The first detector, ZEPLIN–I, was based on a single liquid phase scintillation technique. Discrimination between nuclear and electron recoils was established by using pulse shape analysis, looking for the statistical difference in the time constants of event species. The  $\sim$ 5-kg liquid xenon detector set a world leading limit (at the time) for the spin-independent WIMP-nucleon cross-section of  $1.1 \times 10^{-6}$  pb at 80 GeV/c<sup>2</sup> WIMP mass [116].

The next experiment, ZEPLIN–II, was the first detector to exploit the technology of dual-phase liquid/gas xenon for discrimination. In each recoil interaction two signals were produced: a primary scintillation within the liquid xenon; and a secondary delayed electroluminescence signal from the gas-phase following the extraction of electrons freed by ionisation generated by the recoil. The dual-phase discrimination methodology will be explained in more detail in Section 4.2. In this case the 31-kg xenon target was viewed from above (*i.e.* in the gas phase) by 7 PMTs recording both signals. During the run, an unexpected contamination from radon progeny compromised the results. Nevertheless, a competitive limit of  $6.6 \times 10^{-7}$  pb at a WIMP mass of 65 GeV/c<sup>2</sup> was obtained [90].

The final project, ZEPLIN–III, operated in a similar manner to ZEPLIN–II albeit much improved, with a dual-phase xenon target. Two successive science runs were exploited: a short initial First Science Run (FSR) and a longer Second Science Run (SSR), following significant upgrades.

The following sections will give an overview of the design of the detector (a very detailed description of the detector construction is given in Ref. [117]) and summarise

the configuration and results of the FSR. The author joined the project in between the two science runs, and thus the description of the ZEPLIN–III experiment in this thesis will predominantly concentrate on the SSR, including all procedures and analysis steps needed to extract a comprehensive dark matter interaction cross-section limit.

## 4.1 Detector design

The ZEPLIN–III detector was designed as a two phase liquid/gas TPC operating with xenon as a target material. It was operated in the Boulby Underground Laboratory at a vertical depth of 1100 m (2850 m water equivalent (w.e.)), significantly reducing background from atmospheric cosmic-rays. A cross-sectional view of the detector construction is given in Fig. 4.1 and a photograph of the assembled detector without its vacuum jacket is shown in Fig. 4.2. The instrument consisted of two main parts. Firstly, the target volume, composed of the PMT array immersed in the liquid xenon, the liquid xenon disc above it (the actual target volume) and the xenon gas layer on top, all enclosed in a target dome made from oxygen-free copper. Secondly, the cooling unit, sitting below the target volume with the liquid nitrogen vessel as its main part. Both entities were then sealed in by a vacuum jacket, also made from low-background copper. In its main dimensions the ZEPLIN–III instrument stood 1100 mm tall with a diameter of 760 mm.

Inside the target dome, an array of 31 PMTs immersed in liquid xenon viewed the  $\sim$ 40 mm thick target volume from below. They were arranged in a hexagonal pattern with a pitch spacing of 54 mm, as shown in the photograph of Fig. 4.3. The PMTs were placed in holes 53 mm in diameter manufactured into a pure copper screen, providing both light screening and electrical isolation between the PMTs. The screen was 128 mm in height and had a diameter of 340 mm. The holes in the top layer of the screen, also dubbed the ‘PMT mirror’, were finished with highly polished conical sections to improve light collection (see Fig. 4.3). In order to minimise the number of electrical feed throughs needed (in total 465 if all 15 pins of each PMT would be connected separately), a common high voltage supply and a system to distribute the appropriate voltage to each dynode was used, reducing the total number of connectors to only 47. A stack of 16 thin copper plates interspaced with quartz connected each pin to the right voltage. At the same time, a set of holes gave clearance to pins which needed to pass through to a lower level plate. The 2 mm thick plates are visible in the cross-sectional view of Fig. 4.1, just below the PMTs.

For a detector operating in dual-phase mode constant high electric fields in three distinct regions are necessary. Firstly, the drift field, a directed field applied across the liquid xenon volume to drift the electrons produced in the ionisation process of

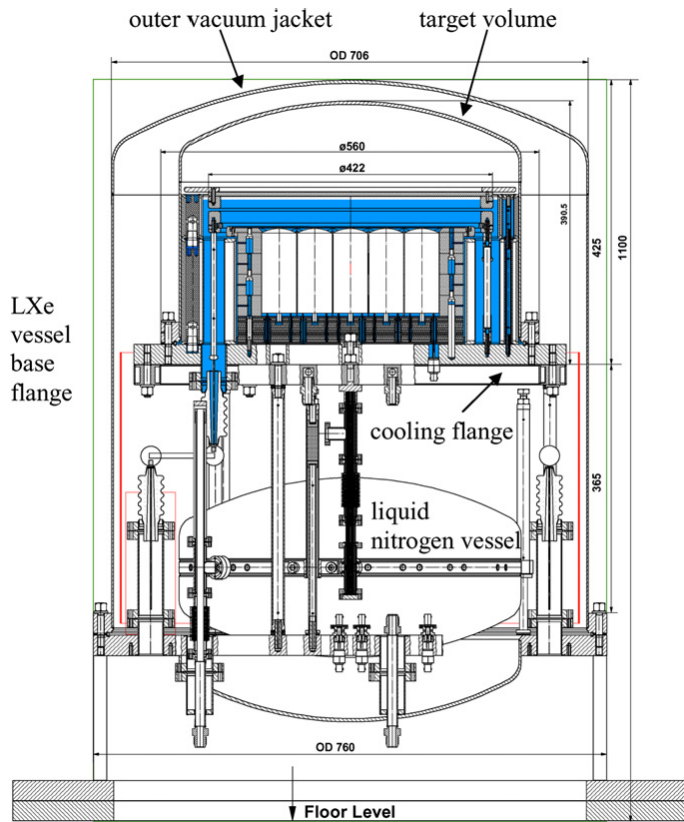


Figure 4.1: Cross-sectional view of the ZEPLIN-III detector, showing the key subsystem components [117].



Figure 4.2: Photograph of the ZEPLIN–III instrument without its vacuum jacket. The two main vessels, the target dome at the top and the liquid nitrogen reservoir below, are shown. Both are covered with thermal insulation. One of the two levelling wheels is visible at the bottom right of the photograph (see Section 4.4.3).



Figure 4.3: Photograph of the PMT array fitted into the copper screen with the PMT wire grid placed on top of it.

the recoil towards the liquid surface. Secondly, an extraction field, to extract the electrons into the gas phase. Finally, an electroluminescence field needs to be applied across the gas gap of the xenon; it must be high enough for the accelerated electrons to produce excited gas atoms. These then form excimers which relax by dissociative radiative emission – electroluminescence. Unlike other liquid xenon TPCs, ZEPLIN-III was unique in adopting a planar geometry with only a single pair of outer electrodes (a cathode wire grid at the bottom of the target volume and an anode plate above the gas phase), providing all three field regions, thus avoiding the need for additional physical components in the liquid volume. The anode plate was made from solid polished copper and acted not only as an electrode, but also as a mirror for the produced light to be reflected back to the bottom PMT array, recording both of the signals produced. Using this specific electrode structure has a significant advantage. Despite the necessity of applying a single much higher electric field and the sacrifice of independently controllable field regions, it produces very uniform electric field lines. This is a very favourable property as it ensures constant symmetric shapes of the secondary signals, influencing directly the precision of a dual-phase system. The electric field across the liquid,  $E_l$ , and the gas,  $E_g$ , can be calculated using Eq. (4.1) and Eq. (4.2), respectively:

$$E_l = \frac{V}{\left(\frac{\epsilon_l}{\epsilon_g} \times d_g\right) + d_l}, \quad (4.1)$$

$$E_g = \frac{\epsilon_l}{\epsilon_g} \times E_l. \quad (4.2)$$

$\epsilon_l = 1.96$  and  $\epsilon_g = 1.00126$  are the dielectric constants of the liquid and the gas, and  $d_l$  and  $d_g$  are the thickness of the liquid and gas layer, respectively.  $V$  denotes the potential difference between the cathode and the anode. Using these two equations and the values from the SSR configuration ( $V = 15$  kV,  $d_l \simeq 36$  mm,  $d_g \simeq 4$  mm), the resulting electric fields are  $\sim 3.4$  kV/cm in the liquid and  $\sim 6.7$  kV/cm in the gas phase. During the FSR, ZEPLIN-III operated with slightly higher electric fields, 3.9 kV/cm and 7.8 kV/cm in the liquid and gas phase, respectively.

A second wire grid was inserted just above the PMT array and 5 mm below the cathode grid. It was held at the same voltage as the PMTs and provided a reverse electric field to prevent ionisation electrons produced in interactions below the cathode grid (dominated by the radioactive background of the PMTs) to be extracted into the gas phase. Thus, no secondary signal was produced. This feature allowed for better rejection of this type of background. Moreover, it protected the PMTs from the high electric field.

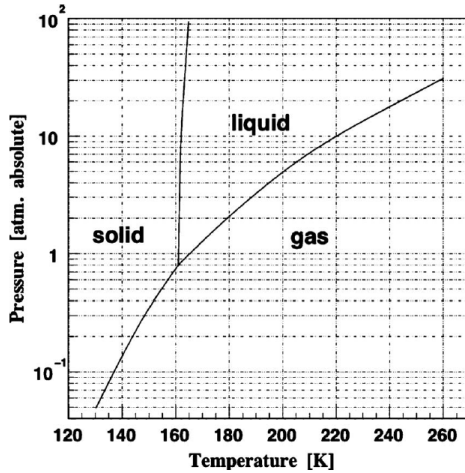


Figure 4.4: Phase diagram of xenon [118].

A comprehensive cooling system was needed to keep the noble gas in a stable liquid state, with the nominal operating temperature around -100 °C. At atmospheric pressure the liquid phase of xenon only extends over a very narrow range from about 162 K to 165 K (see phase diagram in Fig. 4.4). To keep the xenon at this temperature, liquid nitrogen (LN2), stored in a 40-l reservoir below the target dome, was used. There were two connections between the cooling reservoir and the target vessel. Firstly, a conduction path was provided by a bundle of thick copper wires connected to a cooling flange attached to the underside of the target vessel. The other side of the copper wires was then dipped into the LN2 bath. The second thermal path was established by keeping boil-off gas in direct contact with the hollow cooling flange. The LN2 reservoir needed to be refilled on a daily basis.

The inlets and outlets of the xenon into the target volume were independent from the cooling system. The xenon was only filled once before the start of a dedicated run and was not subject to active recirculation as is the case for many currently running or starting up dark matter experiments, *e.g.* [119, 120]. Large volumes and the subsequent increased contact of the xenon with surrounding structure materials (*e.g.* PTFE) demand constant purification. On the contrary, the inner parts of the ZEPLIN-III detector were predominantly made from pure copper. The purification of the xenon prior to filling was accomplished through an external getter removing electronegative contaminations from the gas. These would prevent ionisation electron drift, and thus suppress the production of secondary signals. Xenon impurities were required to be below the ppb level of O<sub>2</sub> equivalent substances to ensure no attachment during the

maximum drift time in the ZEPLIN-III TPC of  $\sim 17\ \mu\text{s}$ . This time corresponds to the length that ionisation electrons would have to travel to reach the surface of the liquid if an event occurred at the very bottom of the target chamber. Additionally, levels of radioactive  $^{85}\text{Kr}$  needed to be kept as low as possible to prevent  $\beta$ -decays from this element contributing to the low energy background (see also Section 7.1.2 in Chapter 7).

Essential for the design of such a complex instrument are complementary Monte Carlo simulations guiding construction details and the selection of building materials. Moreover, the creation of ‘realistic’ datasets assists with the planning of electronics, data acquisition and data analysis software. Finally, a Monte Carlo simulation is essential for assessing expected backgrounds, in particular for neutrons. A full comprehensive Monte Carlo GEANT4 [121] based simulation package for the final instrument was developed [122]. If not otherwise indicated, Monte Carlo simulations throughout this thesis are based on this established and well tested simulation framework (with adaptation and upgrades according to use).

The ZEPLIN-III instrument was designed to push the boundaries of the dual-phase xenon detection technique. Immersing the PMTs in the liquid xenon removed two interfaces with large refractive index mismatches. On the other hand, a refractive index mismatch at the liquid gas interface significantly improved light collection for the primary scintillation signal, due to total internal reflection. The flat planar geometry of the xenon target provided large solid angle acceptance and decreased the dependency on reflective surfaces. High electric fields provided low thresholds for the electroluminescence signal and good 3D-position reconstruction was established through the array of PMTs in the x-y plane and through the drift time of the electrons in the z-direction, giving information concerning the depth of the recoil within the liquid xenon.

## **4.2 Discrimination and the principles of xenon as a detection material**

ZEPLIN-III used two signals from one interaction to discriminate between the dominant electron recoil background and nuclear recoils. When a particle interaction occurs within the liquid part of a target prompt scintillation light is produced. At the same time, ionisation takes place. By the application of a sufficiently strong electric field across the target volume, the freed ionisation electrons are drifted to the surface of the liquid and extracted into the gas phase. Through a second electric field in the gas the electrons are sufficiently accelerated to induce electroluminescence. In ZEPLIN-III

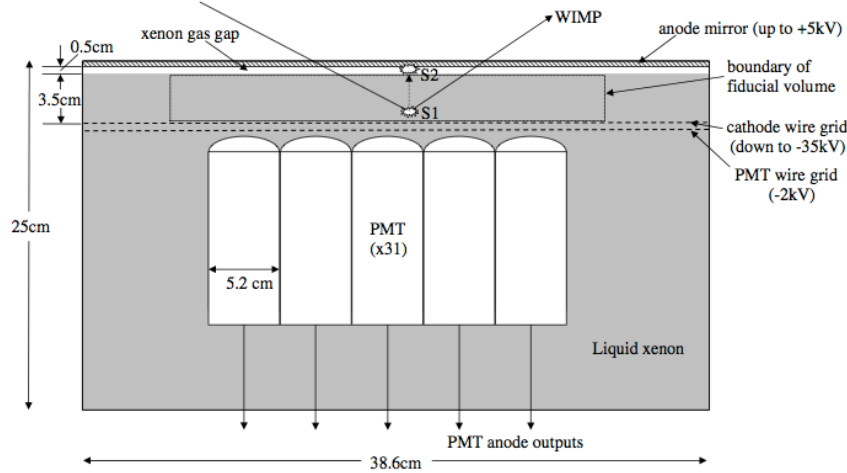


Figure 4.5: Schematic of the target volume of ZEPLIN-III. The 5 middle PMTs shown are immersed in the liquid xenon. The PMT wire grid, the cathode wire grid and the anode mirror on top of the gas gap are also shown in the figure. A possible WIMP interaction, producing both an S1 and an S2 signal, is indicated with arrows [117].

both signals were recorded with the same array of PMTs. A schematic of the target volume depicting an interaction which produces a prompt scintillation signal (S1) and a delayed electroluminescence signal (S2) is shown in Fig. 4.5.

Electron recoil type events (*e.g.*  $\gamma$ -rays or electrons) give rise to a different signal signature in comparison to nuclear recoil events (*e.g.* neutrons and also the expected signature for WIMP interactions). The interaction mechanism for nuclear recoils involves, besides the energy loss to the atomic electrons, energy transfer to the atomic nuclei. Moreover, charge recombination along the particle track is different for the two particle types. The fraction of electrons escaping recombination is higher for electron than nuclear recoils. Therefore, relatively speaking, more energy will be observed in the secondary ionisation signal (via electroluminescence) in electron recoil events. Typical waveforms from an electron and a neutron recoil event of equal apparent energy are displayed in Fig. 4.6. Consequently, from the ratio between the two signals (S2/S1), a high level of discrimination between electron and nuclear recoils can be established [123] (see S2/S1 discrimination plot presented later on in this chapter, Fig. 4.17).

The chosen detection medium, xenon, has a number of advantages over other target materials utilised for dark matter detection. Firstly, its intrinsic properties such as its mass and density allow for a very high efficiency in stopping penetrating radiation,

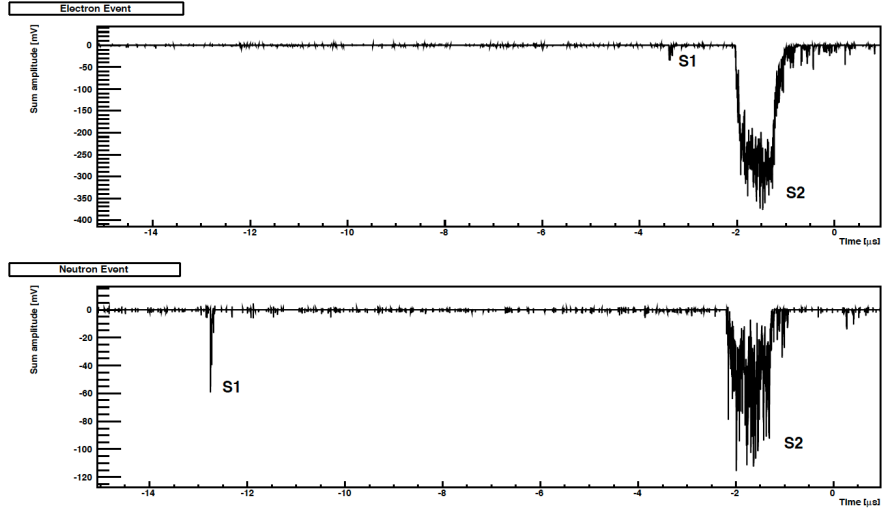


Figure 4.6: Parts of the summed waveform for an electron recoil event (top) and a single-elastic neutron scattering event (bottom) with the same apparent S1 energy of 10 keV<sub>ee</sub>. In both cases, a small primary pulse (S1) precedes a large secondary pulse (S2), but with a clearly different S2/S1 ratio for each of the primary interaction particle species [124].

making it advantageous for WIMP detection. The xenon nucleus mass number ( $A \approx 131$ ; it consists of several natural occurring isotopes) is a good kinematic match to the currently favoured WIMP mass, and therefore enhances interaction rates at low energies by up to an order of magnitude in comparison to other detection mediums such as argon or germanium. Additionally, the presence of odd-neutron isotopes with non-zero nuclear spin also makes xenon detectors sensitive to spin-dependent interactions. The high density of xenon ( $\sim 3 \text{ g/cm}^3$  at 195 K) allows one to build relatively small detectors with large target masses. Another intrinsic property is the very good radio-purity of xenon, with no long-lived radioactive isotopes. The only known problematic contaminant is anthropogenic  $^{85}\text{Kr}$  (a  $\beta$ -emitter with  $T_{1/2} = 10.8$  years); see Section 7.1.2, Chapter 7 for more details. Scintillation output and sensitivity in the ionisation channel are also favourable in xenon. It features a very high scintillation yield with a wavelength of 178 nm [125] and it is transparent to its own scintillation light. The scintillation wavelength can be detected by PMTs with high quantum efficiencies in this range without the need for wavelength shifting materials. Another striking property of xenon as a detection medium, used in many of the recently developed dark matter detectors (*e.g.* [86, 119, 120]), is the feature of self-shielding. Confined fiducial volumes can be chosen within the full liquid xenon volumes to achieve extremely low-background

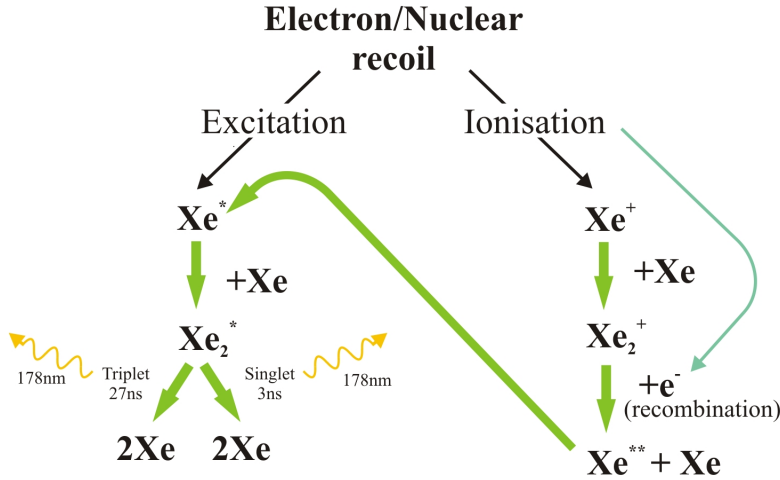


Figure 4.7: Flowchart of the two processes creating a primary scintillation signal in an elastic recoil in liquid xenon. In the primary interaction both excited and ionised Xe atoms are created. The two branches produce, in their final stages, excited dimer states responsible for the typical scintillation light of the noble gas ( $\lambda = 178$  nm). Transparency of the medium to its own scintillation light, *i.e.* the energy of the emitted photons is less than the energy difference between the ground state (of the two separated atoms) and the first atomic excited state, ensures good light collection.

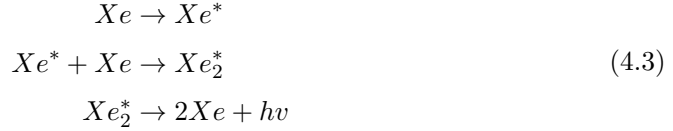
regions without the need for any physical barriers. Comprehensive overviews of the properties of liquid xenon and its utilisation in noble gas detectors are given in Refs. [72, 83].

#### 4.2.1 The primary scintillation signal

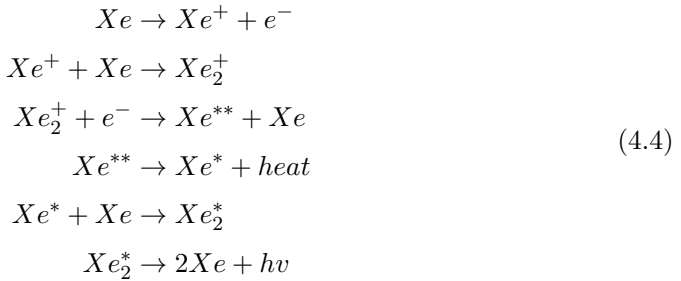
The scintillation light produced in a particle interaction within the liquid xenon is attributed to two separate processes involving excited atoms and ions. A flow chart of the individual processes, both resulting in the production of VUV scintillation photons and their interconnection, is shown in Fig. 4.7 [126, 127].

Firstly, direct excitation takes place resulting in excitation luminescence by the de-excitation of singlet and triplet states of the created excimer  $Xe_2^*$ , see Eq. (4.3). The transition of the excited states occurs at short interatomic distance, where the ground state potential is repulsive and the molecule becomes dissociated. The two possible de-excitations from the lowest electronic excited states are quite different in their characteristic decay time due to the forbidden direct transition of the triplet to the ground state. The latter becomes possible through spin-orbital coupling and the

mixing of states [128], resulting in a decay time of  $\sim 27$  ns for the triplet and  $\sim 3$  ns for the singlet state [129].



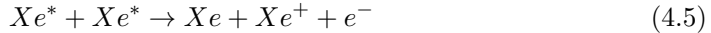
The second process, so-called recombination luminescence, produces the same VUV photons but proceeds via indirect excitation. Xe atoms get ionised in the interaction and subsequently produce excited dimer states by recombination, see Eq. (4.4). The final stage of this sequence is similar to that of direct excitation, with the same wavelengths and decay times expected. Nevertheless, the population of the two different excimer states is not necessarily the same. Moreover, the ratio of these states is also dependent on the primary interacting particle species. In the case of nuclear recoils, recombination is fast and consequently de-excitation is dominated by excitation luminescence. On the other hand, for electron recoils, with a longer recoil track topology, the time needed for the recombination process can slow down the observed decay times, with measured apparent time constants of 34 ns to 45 ns (at zero field) [127, 128]. Measurements, applying high electric fields, *i.e.* prohibiting full recombination of ionisation electrons with Xe ions, concluded that only  $\sim 1/3$  of the scintillation light is associated with direct excitation. The remaining  $\sim 2/3$  result from recombination [126, 130]. The difference in the observed time constant of the scintillation signals allows moderate particle discrimination via pulse-shape analysis, with best results at zero field [129]. This technique is utilised in single-phase xenon detectors, such as [86].



Reported scintillation yields for electrons in the energy region between 10 to 100 keV reach values of  $\sim 70$  to  $\sim 80$  scintillation photons per keV (a comprehensive analysis of existing data for liquid xenon is given in Ref. [131]).

## Nuclear recoil scintillation yield

The different track topologies of electron and nuclear recoils also result in a significantly quenched scintillation yield for interactions of neutrons and WIMPs with the Xe atoms. In the case of a nuclear recoil, a significant amount of the incident particle’s energy is dissipated to the kinetic energy of the target atom (heat), and thus is not visible as direct scintillation light or as a consequence of freed charge. Only a fraction of the energy transferred in the recoil goes directly into electronic excitation or ionisation. Consequently, the observed energy is quenched in comparison to electron recoils. This mechanism of energy transfer to atomic motion is commonly referred to as nuclear quenching and was quantified by Lindhard [132] with the so-called Lindhard factor. Additionally, Hitachi [133] proposed quenching of scintillation light by bi-excitonic collisions to explain the lower relative scintillation light yield observed for nuclear recoils than expected from nuclear quenching alone. When the density of excited species along the particle track becomes high enough collisions between them become possible. In such a collision an electron is emitted, auto-inoising one of the two colliding free excitons (see Eq. (4.5)). The resulting ion can recombine with an electron and subsequently produce an excited state. However, in this case only one photon from each initially created exciton is emitted at the final stage instead of two.



A more recent paper on beam measurements also provides an empirical model, in reasonable agreement with experimental measurements, for the relative scintillation light yield [134]. The authors found that the relative scintillation efficiency,  $L_{eff}$ , can be best modelled via the product of three components: nuclear quenching,  $q_{ncl}$ ; bi-excitonic quenching or electronic quenching,  $q_{el}$ ; and the addition of a non-negligible electron escape probability for nuclear recoil tracks,  $q_{esc}$ ; see Eq. (4.6):

$$L_{eff} = q_{ncl} \times q_{esc} \times q_{el}. \quad (4.6)$$

In this case the bi-excitonic quenching part includes an extension proposed by Mei *et al.* [135]. It considers the changed quenching as a result of different stopping powers for recoils of different energy, as quantified by Birks’ Law [136]. The final term,  $q_{esc}$ , represents the reduction of the scintillation light yield resulting from escaping electrons. Even at zero field, electrons produced in ionisation may thermalise outside of the Onsager radius (escape radius) and consequently evade recombination [137].

It is paramount for all direct dark matter experiments to assess the scintillation yield of neutron induced nuclear recoils, due to the expected similarity of WIMP to neutron

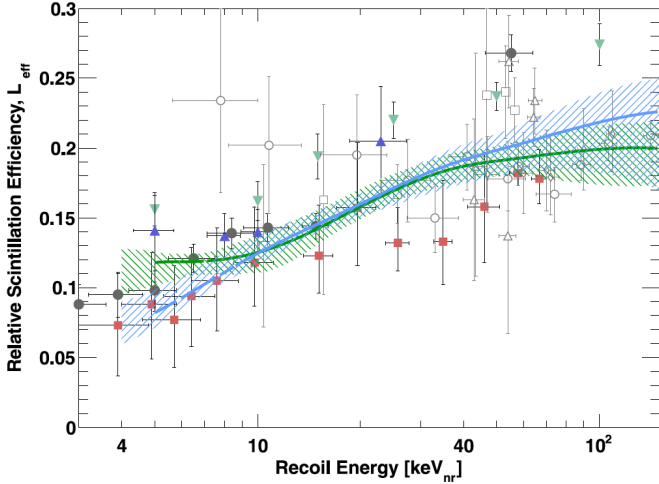


Figure 4.8: Relative scintillation yield for nuclear recoils,  $L_{eff}$ , as a function of recoil energy in  $\text{keV}_{nr}$  as measured from the two ZEPLIN-III datasets, including the relevant 68% confidence limit bands, using the Monte-Carlo approach (FSR: green, SSR: blue). Also shown are previous measurements with mono-energetic neutron beams ( $\bullet$  [138],  $\blacksquare$  [134],  $\blacktriangle$  [139],  $\circ$  [140],  $\triangle$  [141],  $\nabla$  [142],  $\diamond$  [143]) and measurements using a similar Monte Carlo matching technique ( $\blacktriangledown$  [144]) [145].

interactions. Conventionally,  $L_{eff}$  is given as a relative factor comparing the true nuclear recoil energy in  $\text{keV}_{nr}$  to the response to a 122 keV  $\gamma$ -ray. Energy depositions in liquid xenon are generally expressed in electron-equivalent units,  $\text{keV}_{ee}$ , calibrated by 122 keV  $\gamma$ -rays (typically from a  $^{57}\text{Co}$  source), or in  $\text{keV}_{nr}$  when referring to nuclear recoil energies. Kinematic determinations of the energy transfer from neutrons to the xenon atoms are performed with mono-energetic neutron beams elastically scattering off liquid xenon targets [139, 140, 141, 142, 146]. An alternative, more recently adopted, indirect method has been made possible through the precision of modern Monte Carlo codes, modelling the elastic scattering of neutrons as well as the detector response very accurately. As such, the relative scintillation yield can be directly extracted from real dark matter experiment data using broad-band neutron sources (*e.g.* Am-Be – for more on calibration sources used for the ZEPLIN-III experiment see Section 4.4.3) and comparing experimentally measured energy deposition spectra to simulations. (Note: this technique is very similar to that described in Chapter 6 on the quenching factor for a plastic scintillator). Only (comparatively) recently has it been found, in contrast to the previously established constant value [142] for  $L_{eff}(E)$ , that the relative scintillation yield exhibits an energy dependent decrease at lower energies [139]. Generating great interest in the community, this has since been confirmed by numerous experimental

measurements.

The reconstructed energy of the primary scintillation signal S1 in keV<sub>ee</sub> for a given nuclear recoil energy deposit, E, in keV<sub>nr</sub> can be related to  $L_{eff}(E)$  using Eq. (4.7).

$$S1 = \frac{S_{nr}}{S_{ee}} L_{eff}(E) E, \quad (4.7)$$

where S<sub>nr</sub> and S<sub>ee</sub> correspond to the electric field suppression factors (defined as unity at zero electric field) for nuclear recoils of energy E and electron recoils, respectively.

Figure 4.8 shows the  $L_{eff}$  measurements from the ZEPLIN–III experiment, both from the FSR (green) and the SSR (blue), in comparison to previously published measurements using mono-energetic neutron beams and similar Monte Carlo matching methods [145].

#### 4.2.2 The secondary signal

The secondary signal, S2, originates from the primary ionisation in an electron or nuclear recoil. The ionisation yield is defined as the number of electron-ion pairs produced per unit absorbed energy. This is quantified using the  $W$ -value, the average energy required to produce one electron-ion pair, which can be expressed using the Platzman equation for rare gases [147]:

$$W = E_0/N_i = E_i + E_{ex}(N_{ex}/N_i) + \epsilon, \quad (4.8)$$

where  $E_0$  is the energy transferred by a particle to the medium creating a mean number of ionised,  $N_i$ , and excited,  $N_{ex}$ , atoms, respectively.  $E_i$  and  $E_{ex}$  are the mean energy expenditures for ionising or exciting an atom, respectively, and  $\epsilon$  is the mean energy of sub-excitation electrons. Up to and including these energies, free electrons will only scatter elastically, and thus increase the temperature of the medium. Liquid xenon has the smallest  $W$ -value measured ( $W = 16.5 \pm 0.8$  eV [145]) of all liquid rare gases, and therefore the greatest ionisation yield.

To utilise this high ionisation yield in a dual-phase detector technology, high electric fields are applied across the target volume, prohibiting the (full) recombination of freed electrons. The drift velocity of these free negative charge carriers is relatively quick in heavy noble liquids. At a field of 1 kV/cm, a speed of 2.25 mm/μs has been measured in xenon [148]. Upon reaching the surface (boundary between liquid and gas phase) the electrons may, with a high enough electric field, be extracted into the gas. Once in the gas phase, the electrons are accelerated, through another electric field, to energies large enough to excite the Xe gas atoms; thus producing a secondary scintillation (electroluminescence) signal (S2). A single electron extracted into the

gas can create hundreds of scintillation photons along its track. For the ZEPLIN-III configuration (FSR) one extracted electron produced approximately 300 VUV photons, which resulted in an observed signal of  $\sim 30$  photoelectrons (phe) in a dedicated single electron emission study [149]. This fact demonstrates the power of the ionisation channel in allowing extremely low energy thresholds to be achieved. The observed spectrum from electroluminescence is, except for a small difference in the peak position of the emitted wavelength to  $\lambda = 171$  nm [150], very similar to that of the primary scintillation signal in the liquid. The change in wavelength is due to a slight downwards shift of the exciton energy levels in the liquid in comparison to the excimer levels in the gas.

### Nuclear recoil ionisation yield

Due to the dense track of low energy Xe ions in nuclear recoils, a stronger recombination rate along the path is to be expected, resulting in a much smaller number of electron-ion pairs produced in comparison to electron recoils of the same energy. Unexpectedly however, it has been observed that there is an increasing number of charge carriers with decreasing energy. Using a similar Monte Carlo matching approach, the ionisation yield for nuclear recoils,  $Q_y$ , at low energies can be measured. Moreover, using the reconstructed energy of the S2 signal, the energy dependent  $Q_y(E)$  value can be linked as follows:

$$\frac{S2}{W q_0/q(|\mathbf{E}|)} = Q_y(E)E, \quad (4.9)$$

where  $q(|\mathbf{E}|)/q_0$  denotes the relative fraction of charge collection at a finite electric field. The ionisation yield as measured by the ZEPLIN-III collaboration [145] is given in Fig. 4.9 alongside results using a similar approach and measurements at various electric fields and nuclear recoil energies from neutron scattering experiments.

Another, rather unexpected, property of nuclear recoils is the observation of a largely unaffected scintillation yield following the application of an electric field. Figure 4.10 shows the field dependence for both scintillation and ionisation yields for 56.5 keV<sub>nr</sub> nuclear recoils and 122 keV  $\gamma$ -ray electron recoils (and also for alpha recoils at 5.5 MeV from  $^{241}\text{Am}$ ) [143]. Electron recoils show, as expected, an indirect proportionality of charge and scintillation light output with a changing drift field. In nuclear recoils, although a similar dependency is recorded, the field suppression factors are considerably lower and changes from the varying electric field are very small. The fact that electron recoils, unlike nuclear recoils, are affected very strongly represents the basis for event species discrimination at high electric fields; the higher the applied electric field the better the achievable event species discrimination.

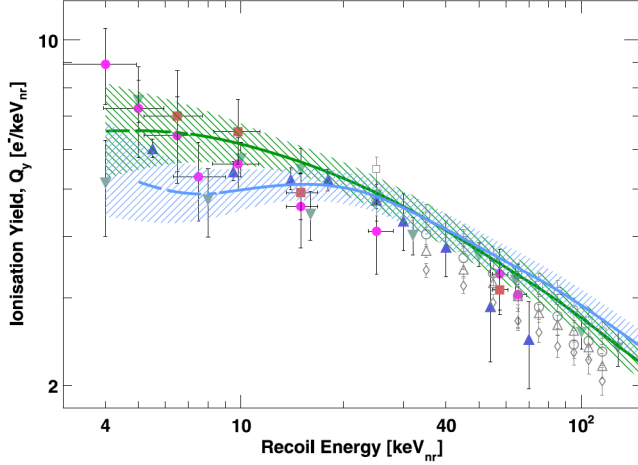


Figure 4.9: Ionisation yield for nuclear recoils as a function of recoil energy in  $\text{keV}_{nr}$  as measured from the two ZEPLIN-III datasets, including the relevant 68% confidence limit bands, using the Monte-Carlo approach (FSR: green, SSR: blue). These are compared to previously performed measurements at 1.0 kV/cm (●) and 4.0 kV/cm (■) from Ref. [134], at 2 kV/cm (□, △), 0.3 kV/cm (○) and 0.1 kV/cm (◇) from Ref. [143] and at 0.73 kV/cm using the same Monte Carlo matching technique (▲ [144], ▼ [151]) [145].

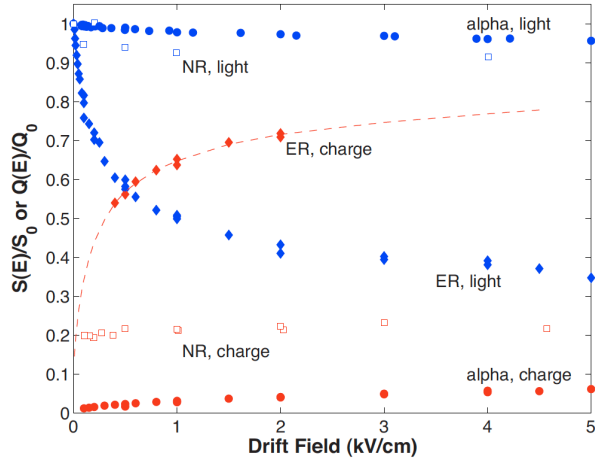


Figure 4.10: Field dependence of the scintillation and the ionisation yield for electron and nuclear recoils at 122 keV and 56.5  $\text{keV}_{nr}$ , respectively.  $S(E)/S_0$  and  $Q(E)/Q_0$  are the relative scintillation and ionisation yields in comparison to their corresponding zero field values [143].

### 4.3 The First Science Run of ZEPLIN-III

Between February the 27<sup>th</sup> and May the 20<sup>th</sup>, 2008 ZEPLIN-III performed its first science run (84% live time), collecting 847 kg·days of WIMP search data in 83 days. The set of PMTs employed during the FSR were taken from the batch of the primary model developed for ZEPLIN-III (ETL D730/9829Q) [152]. A fiducial volume of 150 mm in radius and ∼30 mm in height was defined, constraining the xenon target to ∼6.5 kg of xenon as the physical WIMP search region.

In this run the shielding was composed of a 30 cm thick polypropylene plastic box surrounding the detector on all sides. Subsequently, the whole structure was enclosed by a 20 cm thick lead castle (smelted and boxed in stainless steel for stacking), both reducing the external neutron and  $\gamma$ -ray fluxes by a factor of  $\sim 10^5$ .

A 10% portion of the accrued science data was used for developing initial data analysis and selection cuts, establishing the level of electron recoil background, and to define a WIMP search region. The remaining data set was kept blind in the first instance for a ‘blind’ non-biased analysis, but had to be completely revealed before the final analysis stage to refine data selection cuts. An unexpected background population of events with a multiple-scintillation single-ionisation event topology, predominantly originating from  $\gamma$ -rays emitted from the PMTs, proved to be very challenging (for more information on so-called MSSI events see Section 7.3.1 in Chapter 7).

Due to an exemplary discrimination of 1:7800, defined as the relative number of events from the electron-recoil band and events that leak into the acceptance region of the signal, a very respectable spin-independent WIMP-nucleon cross-section limit of  $8.1 \times 10^{-8}$  pb at 60 GeV/c<sup>2</sup> WIMP mass (at 90% confidence) was published from this first test run of the ZEPLIN-III experiment (see Fig. 4.11) [153]. Seven events were observed within the WIMP search box; fully consistent with the expected leakage from the electron recoil band. ZEPLIN-III remains the detector with the highest electric field applied in any liquid xenon TPC dark matter detector, and consequently shows the best discrimination achieved to date. Spin-dependent cross-section limits and WIMP-nucleon cross-section limits for an inelastic dark matter case are published in Ref. [154] and Ref. [109], respectively. During the SSR analysis, an inefficiency at low energies was found in the selection cuts of the FSR data analysis. Implementing corrections raised the achieved limit marginally to a minimum of  $8.4 \times 10^{-8}$  pb at 55 GeV/c<sup>2</sup> [2] (more details to this correction and the re-analysis of the FSR data are given in Chapter 8, Section 8.3.2).

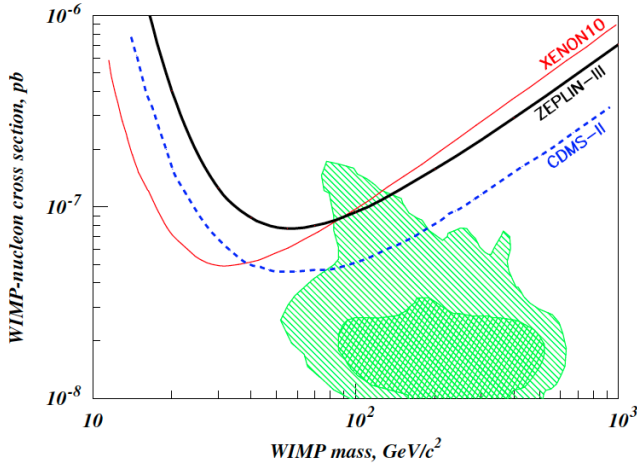


Figure 4.11: Spin-independent WIMP-nucleon elastic scattering cross-section result from the first science run of ZEPLIN–III, as published in Ref. [153] (prior to the re-analysis), with comparison to results from the XENON10 [155] and CDMS–II [156] experiments. The hatched areas show the 68% and 95% confidence regions of the neutralino-proton scattering cross-section as calculated in the cMSSM [157] [153].

#### 4.4 The Second Science Run of ZEPLIN–III – operations, hardware and software

The second science run of ZEPLIN–III lasted for a period of 319 days between the 24<sup>th</sup> of June 2010 and the 7<sup>th</sup> of May 2011, acquiring 1344 kg·days in fiducial exposure [2]. To improve the performance of the instrument two major upgrades had been implemented prior to the SSR. Firstly, a significant reduction in background radiation – by a factor of  $\sim 20$  – was achieved by replacing the PMT array from the FSR with a batch of new PMTs (ETEL D766Q [158]). Improvements of the observed background in the SSR, in comparison to the FSR, are discussed in more detail in Chapter 7. The second major upgrade was the retrofitting of a tonne-scale polystyrene-based plastic scintillator active veto detector system around the ZEPLIN–III instrument. Surrounding an extra layer of 15 cm thick polypropylene shielding, the veto system replaced the FSR hydrocarbon shielding configuration. To reduce environmental  $\gamma$ -ray background the FSR lead castle was re-used in the SSR. The modular veto system provided event species identification and allowed rejection of signals that might have otherwise been identified as a possible WIMP interaction. 60.5% of neutron elastic recoils and up to 28% of the  $\gamma$ -ray background were tagged by this anti-coincidence system. The design and the performance of the veto detector during the SSR is covered in great detail in Chapter 5.

Additional minor upgrades, such as the automation of calibration, monitoring and liquid nitrogen refill, significantly increased the achievable duty cycle and ensured stable conditions throughout the data taking run.

The following sections outline the measures taken to ensure stable operation to achieve a good quality dataset. Furthermore, the first analysis steps including pulse parameterisation and first pass selection cuts as well as the 3D-position reconstruction of the selected events are discussed.

#### 4.4.1 Data acquisition

As described earlier, the full PMT array was powered by a single high voltage supply (at 900 V), and as such all PMT signal outputs were first attenuated (attenuator Phillips Scientific 804) to normalise their individual gains. Subsequently, the signals were split into two channels for high and low sensitivity (HS/LS) and were each digitised with a 8-bit ACQUIRIS DC256 flash ADC. The 10 times gain difference of the high sensitivity channel was provided by fast amplifiers (Phillips Scientific 770). These two different readouts allowed for a wide dynamic range of the output signal to be covered. The waveforms were digitised at 500 MS/s (2 ns sampling) for  $\pm 18 \mu\text{s}$  around the trigger point. The length of the waveforms was defined by the maximum drift time of the TPC and by the requirement that both signals (primary and secondary) were recorded, irrespective of whether the system was triggered by an S1 or an S2. The trigger was derived from the shaped sum signal of all 31 PMTs from the high sensitivity channel, triggering both the ZEPLIN-III and the veto detector Data Acquisitions (DAQ). After each trigger, the system was inhibited for 1 ms to control dead time. The hardware threshold in the SSR corresponded to an electroluminescence signal of  $\approx 5$  extracted electrons, translating to  $\approx 10$  ionisation electrons created in the liquid, accounting for an electron lifetime and emission probability at the surface of 66%. A single emitted electron generated a mean response of  $11.8 \pm 0.4$  phe [2]. The shaped sum of events with S1 energy  $\lesssim 50 \text{ keV}_{ee}$  were too small to activate the hardware trigger. In this case, the delayed S2 signal may have triggered the system; as such the S1 signal was recorded in the pre-trigger region of the waveform.

#### 4.4.2 Pulse parameterisation

A bespoke pulse parameterisation software package for processing and reducing all raw data accrued with the ZEPLIN-III detector, dubbed ZE3RA (ZEPLIN-III Reduction and Analysis), was developed by collaborators from the University of Coimbra [159]. The processing steps, such as data filtering, pulse finding and correct clustering

of pulses, were tuned using calibration data to maximise electron-nuclear recoil discrimination near the detection threshold, where WIMP elastic scatter signals are predominantly expected. ZE3RA was the first important link of the analysis chain, reducing the huge amount of data recorded by the acquisition system to a set of relevant physical parameters with implying only minimal knowledge of the physics underlying the specific experiment. As such, the developed software package is also easily transferable to other systems and, more importantly, allows an unbiased analysis of experimental data.

In the first processing step, the baseline of each event, for both sensitivity channels separately, was characterised. From a  $2\ \mu\text{s}$  sample, extracted from the beginning of each waveform, the mean of the baseline,  $\mu_{bas}$ , and the noise,  $\sigma_{bas}$ , were determined. Relative delays from the differences in the signal processing chains (*e.g.* cabling and amplifiers) were observed with a typical range of  $\pm 10\ \text{ns}$  between the individual channels. Following the correct alignment of channels, pulse finding algorithms were applied to identify all real pulses in any given waveform. The procedure was based on a search for excursions of the signal amplitude above a defined threshold,  $V_{thr}$ :

$$V_{thr} = \mu_{bas} + 3 \sigma_{bas}. \quad (4.10)$$

This software threshold is equivalent to an energy threshold of  $1.67\ \text{keV}_{ee}$  in S1. Excursions above this threshold were primarily searched for in shaped waveforms with smoothing data filters applied, due to possible spread of a number of individual photoelectrons over significant time periods (of up to  $\sim 1\ \mu\text{s}$  in the case of an S2 signal). Some of the finer structures may have therefore been lost. Consequently, the original data buffer was also used for identifying amplitudes above threshold, and the final set of pulses available for any subsequent analysis was a union of pulses collected from the smoothed and from the unmodified data together.

Paramount for correct and accurate pulse parameterisation is the determination of pulse start and especially pulse end times for identified pulses. Deciding when to stop to add small signal excursions above threshold to a given pulse cluster is non-trivial, but the choice is important as it has significant consequences for the detection efficiency of small signals. For the SSR analysis a time gap algorithm was adopted, measuring the time difference,  $t_{gap}$ , between pulses. An iterative process recursively merged consecutive pulses into a single cluster if  $t_{gap} < 20\ \text{ns}$  for S1-like pulses and  $t_{gap} < 100\ \text{ns}$  for S2-like pulses. Finally, identified pulses were parameterised and the 10 largest by area of each individual channel were written into a n-tuple file for further analysis. The individual parameters extracted from the raw data buffers are given in Table 4.1 in Section 4.4.5. In addition to a complementary graphical interface,

ZE3RA also provides a built-in ‘blind manager’, which is a very important tool for a signal-blind analysis. With a set of simple rules defined events can be excluded from both reduction and visualisation.

#### 4.4.3 Stability and the slow-control

A very important step towards improving stability was the implementation of a fully automated daily operation procedure. Minor upgrades such as a motorised source delivery device enabled the system to be fully computer controlled. A slow-control server handled the automated cooling (*i.e.* opening and closing of valves) as well as the daily routine procedures for stand alone operation underground. As a result, a consistent 96% duty cycle was achieved with one hour per day reserved for the daily  $^{57}\text{Co}$  calibration and refilling of the cryogenic reservoir. The periodicity of the liquid nitrogen refill is demonstrated in Fig. 4.12 (right hand side), showing the temperature at the end of the liquid nitrogen delivery line for a full month. Thermal stability is of the utmost importance for the quality of the data produced. Crucially, a stable target temperature, directly influencing the pressure, the liquid level and the thickness of the gas phase, needs to be maintained at all times. The liquid nitrogen input braid temperature was held constant by the system within a temperature range of 1 K, relative to the temperature set point. As shown in Fig. 4.12 (left hand side), the opening and closing of the valve, allowing nitrogen boil-off gas to reach the cooling flange, is reflected in the oscillating braid temperature with a period of  $\sim$ 30 min. The reaction time of the target pressure was very long in comparison to these relatively quick periodical temperature changes. As such, the pressure remained at a constant value of 1.61 bar with a 13 mbar RMS variability within the full dataset (see Fig. 4.13, right hand side), keeping the gas layer at a thickness of  $\sim$ 3.5 mm. A snapshot from the monitoring server of the target pressure (labelled TARC) is shown on the left hand side in Fig. 4.13. The final science data set was corrected for the remaining small pressure variations. Moreover, the importance of slow-control meta-data in such rare event search experiments should be emphasised. All sources that may affect the data, including slowly varying environmental parameters, need to be taken into account.

#### Calibrations

A number of different  $\gamma$ -ray and neutron sources were utilised for calibrating the system. Firstly, a  $\sim$ 15-min run with an exposure to a  $^{57}\text{Co}$  source was performed each day to ensure constant data calibration and quality control throughout the science run.  $^{57}\text{Co}$  undergoes electron capture and populates an excited state of  $^{57}\text{Fe}$ . The two dominant  $\gamma$ -rays observed in this radioactive decay are at 122.1 keV and 136.5 keV with a relative

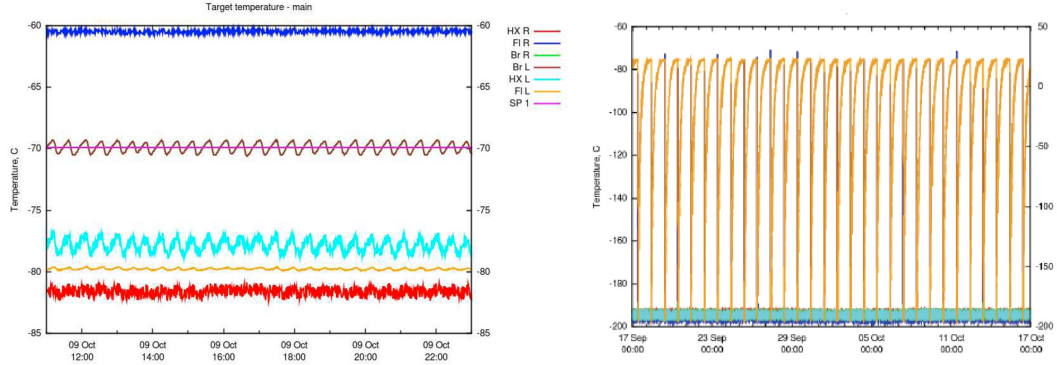


Figure 4.12: Temperatures of the ZEPLIN-III system as monitored by the slow-control. Left: Snapshot of a 12 hour period of the target temperature with the set point temperature, SP 1, shown in pink and the periodic oscillation of the braid temperature, BR L, in brown [160]. Right: Historical one month view of the temperature measured at the end of the liquid nitrogen delivery line (orange), showing excellent reproducibility [124].

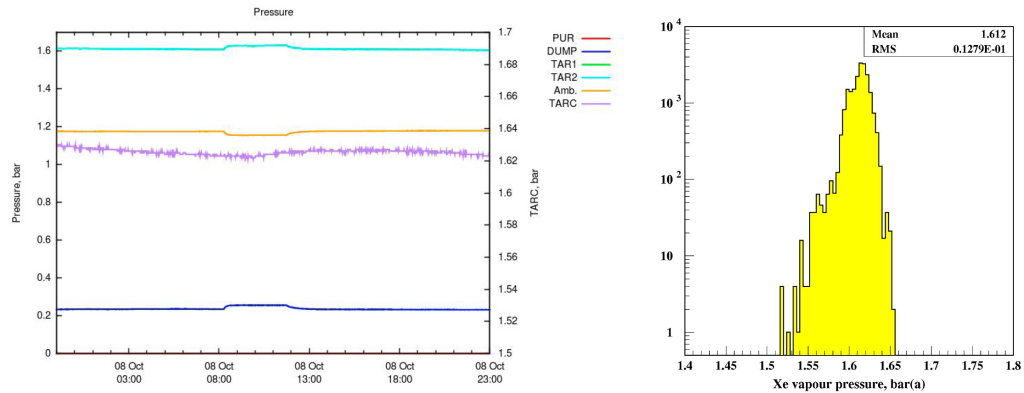


Figure 4.13: Left: The target (TAR 2, light blue line) and the ambient (Amb., yellow line) pressures as measured by the ZEPLIN-III slow-control system from a 12 hour period. Observed changes in the target pressure at this scale (referring to the left hand scale of this plot) are mirrored in the ambient pressure, and thus are a consequence of pressure changes within the laboratory itself. The ambient pressure corrected target pressure (TARC, purple line) remains approximately flat (measured with the scale indicated on the right hand axis) [160]. Right: Distribution of recorded target pressures in the SSR [124].

intensity of 85.6% and 10.6%, respectively [161]. The two  $\gamma$ -rays are rapidly absorbed in the liquid xenon predominantly via the photoelectric process. Xe demonstrates an attenuation length of less than 4 mm at these energies. An energy spectrum using a linear combination of S1 and S2, yielding the best energy resolution, from a  $^{57}\text{Co}$  exposure is shown in Fig. 4.14. The runs were fully automated and controlled by the slow-control system. A newly motorised source delivery system inserted the source via a copper tube line inside the shielding and placed the source just above the centre of the detector on top of the vacuum jacket,  $\sim$ 190 mm above the liquid surface. A separate copper tube offered the possibility for inserting other sources manually (*e.g.* the Am-Be neutron source).

An additional check of the PMT performance was provided by a weekly calibration run with a newly installed fibre-coupled LED light gun at a pulse rate of 100 Hz and a pulse duration of 1  $\mu\text{s}$ . In addition to the flat fielding properties of the event reconstruction code ‘Mercury’ (see Section 4.4.4), it also regularly provided information about the single photoelectron (SPE) response. In general it is of great interest to keep the array equalised at all times to ensure event position independent triggering of the system. The second factor that may cause a bias of the trigger towards individual PMTs is the quantum efficiency of the tubes. Variations over the full array were relatively small with a mean quantum efficiency of  $0.26 \pm 0.06$ . Only minor contributions to the trigger variability are expected.

To ensure a consistent dataset over very long time periods, such as demanded by the search for very rare events, the system needs to be calibrated on a day-to-day basis and parameters continuously corrected. The daily  $^{57}\text{Co}$  calibration allowed to access the evolution of some of the most significant parameters throughout the entire science run: electron life-time, detector tilt and gain.

Firstly, the electron life-time, the time before an ionisation freed electron becomes captured, is determined by the purity of the liquid xenon. It directly influences the number of ionisation electrons able to reach the surface dependent on the interaction depth within the liquid xenon target, and thus the size of the observed corresponding electroluminescence signal. It is obtained from the exponential depth dependence of the relative contributions from the S2 and the S1 area (S2/S1 ratio). The free electron life-time measured at the start of the SSR was  $\sim$ 14  $\mu\text{s}$ , achieved by prior purification of the xenon with a hot getter. Despite the fact that no active recirculation took place, it was observed that the purity of the liquid xenon improved over time. One possible explanation may be the constant application of an electric field, removing electro negative impurities. The electron life-time, increasing steadily over the course of the SSR, reached a maximum of  $\sim$ 45  $\mu\text{s}$  at the end of the run (see Fig. 4.15).

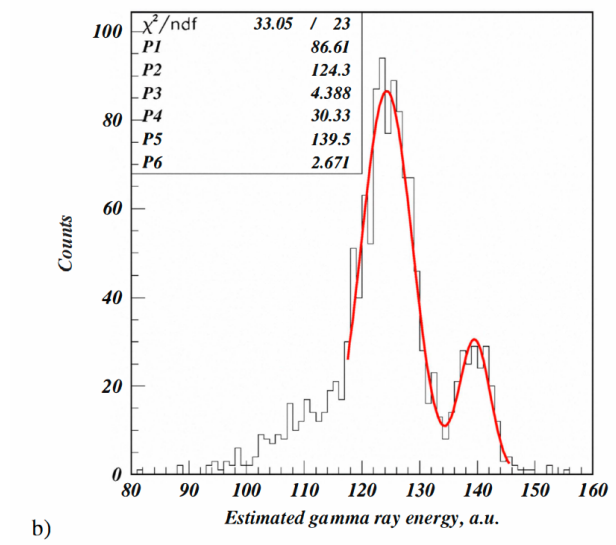


Figure 4.14:  $^{57}\text{Co}$  energy spectrum using a linear combination of S1 and S2 light yields restricted to a central spot of the target volume ( $R < 50$  mm). The two  $\gamma$ -ray lines at 122 keV and 136 keV are well separated [162].

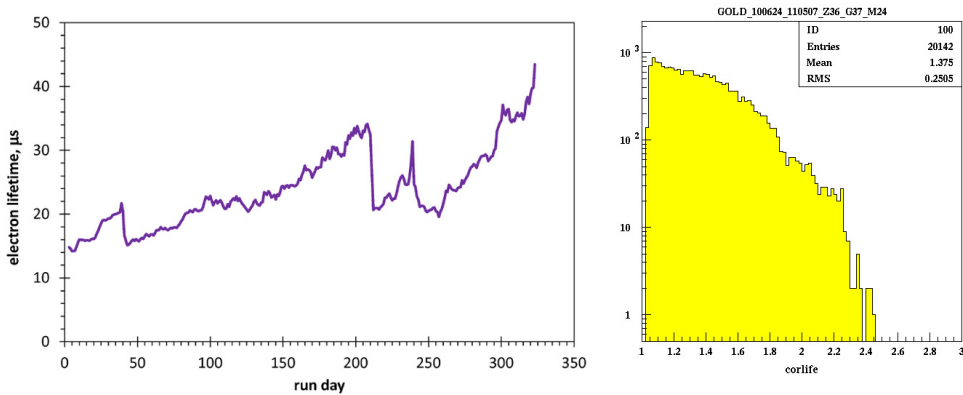


Figure 4.15: Left: Historical evolution of the electron life-time over the full length of the SSR [124]. Steep degradation in electron life-time are correlated with power failures at the underground laboratory. Right: Correction factor for the electron life-time with a mean value of 37%.

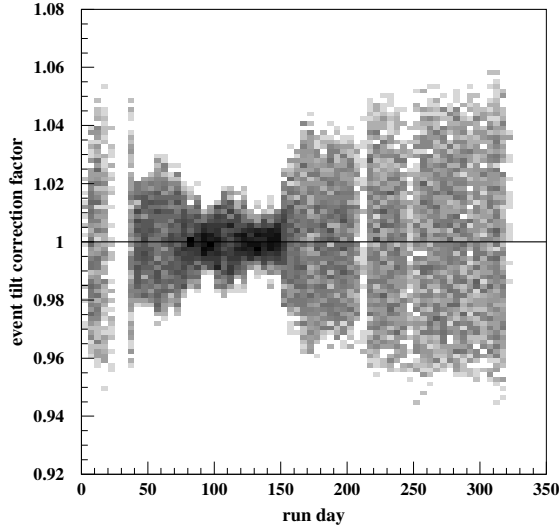


Figure 4.16: Distribution of tilt correction factors for S2 pulse areas, calculated from position dependent width of S2 signals [124].

Secondly, due to the local geological topology, tilts of the physical experimental setup are expected over long time frames and, thus, need to be corrected for. The tilt of the instrument can be probed by the polar dependence of the S2 width distribution, measuring the thickness of the gas layer. To first order, any movements of the detector were mitigated on a weekly basis by manually re-adjusting the tilt via an externally accessible levelling system. The whole detector was balanced on three threaded rods, of which two were connected to a steel cable pulley system. One of the copper wheel pulleys is visible in the photograph of Fig. 4.2. The final data were corrected for any residual variation in the tilt of the detector (see Fig. 4.16).

Thirdly, by fitting the S1 pulse areas, resulting from a response to a known electron recoil energy, gain variations of each individual channel can be measured. The responses may be built up from a number of factors, such as internal gain drifts of the data acquisition or in the electronic chains, but also variability in parameters specific to the PMT and the scintillation light produced in the first place. The correction over all pulses in the SSR data equals 4.7% (RMS).

To calibrate the system for the nuclear recoil response, three separate exposures to an Am-Be neutron source, totalling  $\sim$ 10 hours, were performed. Neutrons populating the nuclear recoil band are mimicking the signal expected from a WIMP elastic scatter in the liquid xenon target, and thus are used for defining the WIMP signal search region (see Chapter 8, Section 8.1.1).  $^{241}\text{Am}$  is an alpha emitter inducing an  $(\alpha, n)$  process

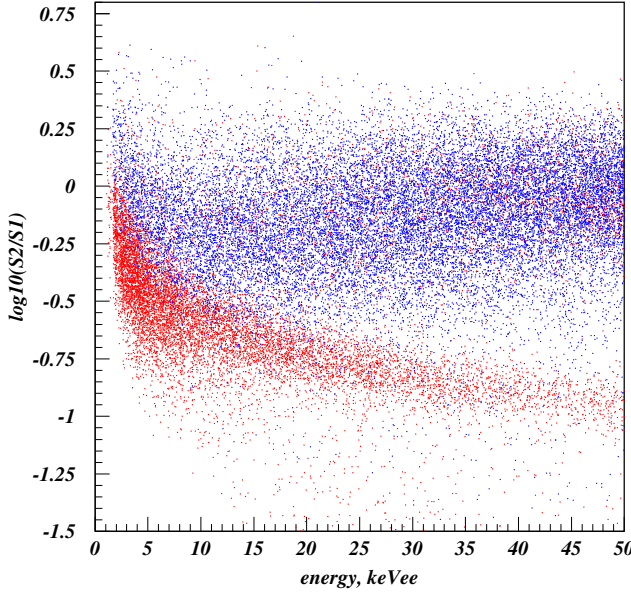


Figure 4.17: S2/S1 ratio scatter plot as a function of energy in keV<sub>ee</sub>. The two extended calibration runs to populate the electron recoil band from a <sup>137</sup>Cs exposure (blue) and the nuclear recoil band from an exposure to an Am-Be neutron source (red) are shown. Event selection includes fiducialisation only, no other quality cuts are applied.

in the <sup>9</sup>Be isotopes. A continuous spectrum of neutrons up to 10 MeV in energy are emitted with a count rate of  $1321 \pm 14$  neutrons/s for the source used in the SSR [2].

For calibrating the electron recoil band the target was exposed to a <sup>137</sup>Cs source with a strength of 4.6 kBq, producing a rate of  $\sim 150$  counts/s in the detector. Following the  $\beta^-$ -decay of <sup>137</sup>Cs a  $\gamma$ -ray at 661.7 keV with a relative intensity of 85.104% is emitted [163]. The calibration run time was adjusted to yield a similar exposure time in terms of the total number of observed events in the recorded WIMP search data. Thus, it can be used to study the leakage of electron recoil events into the nuclear recoil band. Figure 4.17 shows the S2/S1 ratio as a function of energy in keV<sub>ee</sub> for the two extended dedicated neutron and  $\gamma$ -ray calibration runs, populating the nuclear and electron recoil band, respectively.

#### 4.4.4 Event reconstruction

To use the self-shielding properties of xenon, and thus increase the WIMP sensitivity by reducing unwanted background events, accurate position reconstruction is needed to define an enclosed fiducial volume without any physical separating surfaces. While the interaction depth of events can be measured very accurately by the electron drift time (tens of  $\mu\text{m}$  precision), the evaluation of the position in the horizontal plane depends on reconstruction algorithms based on the light distribution pattern across the PMT array. In addition to the determination of the position, a comprehensive event reconstruction code also estimates the energy given a set of corresponding PMT output signals from the array.

The probability of the  $i^{\text{th}}$  PMT detecting  $n_i$  photons is well approximated by a Poisson distribution:

$$P_i(n_i) = \frac{\mu_i^{n_i} e^{-\mu_i}}{n_i!}, \quad (4.11)$$

where  $\mu_i = N\eta_i(\mathbf{r})$ , with  $N$  being the total number of photons produced in a given event and  $\eta_i(\mathbf{r})$  being the Light Response Function (LRF). LRFs are defined as the fraction of detectable signal produced by a light source in the  $i^{\text{th}}$  PMT. As such,  $\mu_i$  represents the expectation of number of photons detected by the  $i^{\text{th}}$  PMT.

The event reconstruction code developed for the ZEPLIN-III experiment, dubbed ‘Mercury’ [162], calculates the interaction location,  $r$ , and the total number of initial photons of an event by using a Maximum Likelihood (ML) fit to the S1 response and a Weighted Least Square (WLS) method for the S2 channel. The former, the maximum likelihood approach, is a method for finding the set of parameters that maximises the likelihood of obtaining an experimentally measured outcome. The likelihood function can be calculated from the Poisson distribution (Eq. (4.11)) and takes the form

$$\ln L(r, N) = \sum_i (n_i \ln(N\eta_i(r)) - N\eta_i(r)) + C. \quad (4.12)$$

Although this technique is most viable for small signals, where statistical variations obey a Poisson distribution, such as the S1 with 1–2 phe/keV total collected charge from the entire PMT array, pulses which are attributed to a greater light output, and as such are normally distributed, may be preferentially reconstructed with a more flexible weighted least square method. This affects a genuine S2 signal, where a single electron extracted into the gas phase produces on average  $\sim 12$  phe in the form of electroluminescence.

In the case of a weighted least square method, the parameter estimates are found from minimisation of the weighted sum of squared residuals:

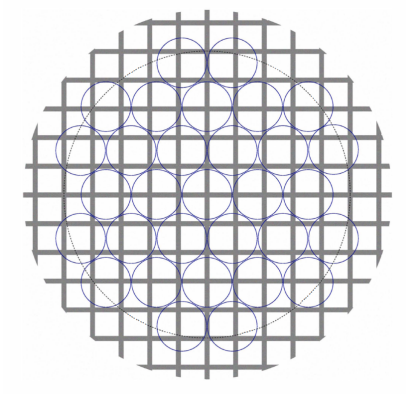


Figure 4.18: Schematic view from the top showing the PMT array and the copper grid. The dotted line indicates a 150 mm radius [162].

$$\chi^2 = \sum_i w_i (A_{ei} - A_i)^2, \quad (4.13)$$

where  $A_i$  and  $A_{ei}$  are the measured and expected output signals of the  $i^{th}$  PMT, respectively, with  $A_{ei} = N\eta_i(r)q_{si}$ .  $q_{si}$  denotes the average single photoelectron response of a given PMT and  $w_i$  is the weighting factor, the reciprocal of the variance of  $(A_{ei} - A_i)$ .

Both reconstruction algorithms require knowledge of the light response functions, which in the case of ZEPLIN–III were obtained *in-situ* from  $^{57}\text{Co}$  calibration data. An iterative process was used to find a converging value for the LRF of each individual PMT, simultaneously flat-fielding the array. To test the power of the reconstruction, *i.e.* the quality of the LRFs, a copper grid was inserted just above the anode mirror for the SSR. The void pitch was 30 mm, the grid thickness was 5 mm and it was arranged as shown in Fig. 4.18. The thickness of the copper plate (5.1 mm) was chosen such that it would sufficiently attenuate the  $\gamma$ -ray flux from the  $^{57}\text{Co}$  calibration source to create a shadow image in an event distribution plot in the x-y plane.

In case of a circular photocathode it is reasonable to assume axial symmetry of the LRF, *i.e.* it can be simplified as a function of distance,  $r$ , from the centre of a given PMT. The first step in an iterative reconstruction process uses a centroid method to produce a first approximation for the LRFs. The positions are found simply by the weighted average of the PMT coordinates, with the weights representing the light distribution across the PMT array. By fitting the obtained light response distribution as a function of  $r$ , a first estimate for the LRFs can be found and used in the next step of reconstruction with either a ML or WLS method, producing yet another set of LRFs for

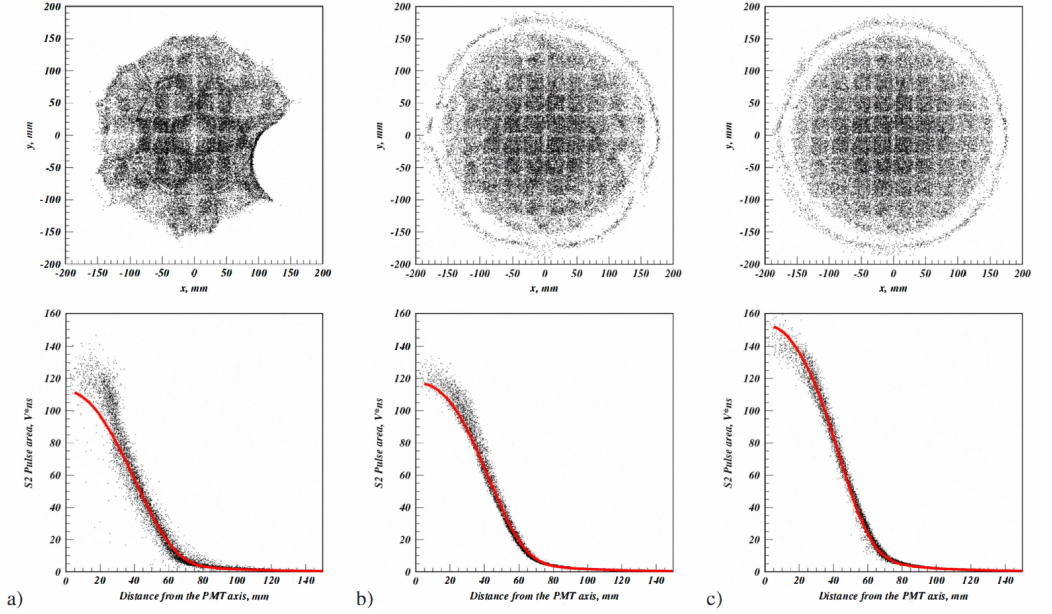


Figure 4.19: Iterative event reconstruction process from left to right showing the initial position estimates using the centroid method (a), the first iteration with a WLS fit (b) and the final (5<sup>th</sup>) WLS iteration (c). Top: Estimated event positions from S2 pulses. The first estimate (top left) shows that events are preferably reconstructed towards the centre of the PMT array. This is most obvious for the bottom right corner, where one PMT was not working. After the last iteration, a clear shadow image of the copper grid is visible (top right). Bottom: Response of PMT 11 as a function of distance,  $r$ , from its centre and the corresponding S2 LRF fits [162].

further iterations of the latter. Figure 4.19 shows an example of the iterative process to find the LRFs and the reconstructed event position of the S2 signal. The imprecision of the first estimate of event positions from the centroid method is emphasised by the non-functional PMT at the bottom right corner of the ZEPLIN-III SSR array (see Fig. 4.19 a). Despite the initial significant distortion of event positions, after 5 iterations using the WLS method, the LRFs converged and a clear shadow image of the copper grid is visible.

The spatial resolution achieved from this reconstruction process was 13 mm for the S1 and 1.6 mm in the case of the S2 signal (FWHM) for the inner 100 mm radius. In addition, Mercury allows to produce two dimensional spatial maps of the likelihood and  $\chi^2$  distribution for each event separately for S1 and S2. This can be a very helpful tool in identifying multiple vertices (see Section 8.3.2 in Chapter 8 for an example application).

A much greater precision in the position reconstruction was achieved for S2 signals. Consequently, the S1 energy variable was calculated by fits to the S1 response assuming the corresponding S2 position (mercury parameter name: *s1emlm*). This type of energy reconstruction is also favourable due to the requirement that genuine ‘good’ events show only small differences between the true positions of the S1 and S2. Events with large distances were rejected by data analysis quality cuts. The final definitions of the energy variables are:

$$\begin{aligned} S1 \text{ energy} &= (0.96 * s1emlm / (1. - 1.068E - 5 * \text{drift time})) , \\ S2 \text{ energy} &= (1.11 * s2em) , \end{aligned} \quad (4.14)$$

where *s2em* is the reconstructed S2 energy at S2 position. For the best estimate of energy resolution one may, due to the anti-correlation of the light and charge outputs in a dual-phase detector, employ a linear combination of S1 and S2 signals. The ionisation electrons may contribute either to the S2 signal, if they have been extracted from the interaction track by the high voltage field applied across the liquid, or to the S1 signal, when luminescence occurred due to recombination. As such, a combination of both signals allows for a better representation of the energy than from either channel independently. For ZEPLIN–III the best energy resolution was achieved at

$$E = S2 \times 0.715 + S1 \times 0.285 , \quad (4.15)$$

with 10.6% FWHM obtained at 122 keV for events with a radius less than 100 mm in the SSR. 8.1% FWHM was achieved using only the inner most events with a radius of < 50 mm. Here, the two  $\gamma$ -ray lines from  $^{57}\text{Co}$  are clearly resolved as shown in Fig. 4.14. The better performance of the PMTs in the FSR allowed to achieve an impressive resolution of 4.5% using the same analysis codes. Very similarly affected was the measured average light yield at 122 keV $_{ee}$ , at full electric field, in the SSR recording only 1.3 phe/keV $_{ee}$  compared to a value of 1.8 phe/keV $_{ee}$  obtained in the FSR.

#### 4.4.5 Event selection and data structure

Following the reduction of the waveforms with ZE3RA, the dataset was searched for single-elastic scatter events with the so-called ‘golden’ code. It is reasonable to assume that a genuine WIMP would only scatter once within the target volume given the very small interaction cross-section. A single-elastic scatter event was defined by the occurrence of one single S1 followed by one single S2 pulse. The golden code can be split

into two main sections. The first pass cuts include the golden rule (single S1 and S2), voltage and waveform cuts. Following the calculation of the output parameters from the golden rule, a set of second pass cuts were applied to refine the event selection. All previously mentioned correction factors were applied at this stage of data processing.

The event selection procedure in the golden code started by iterating through all pulses to select possible S2 candidates, meeting a minimum mean charge arrival time ( $s2tau > 300$  ns) and integrated area ( $s2area > 5$  Vns) requirement to distinguish them from the S1 population. The width of the S2 signal was determined by the gas gap properties and, as such, the mean charge arrival time was well defined. Subsequently, this process was repeated to identify preceding S1 signals for events with only one S2 found in a given summed waveform for an event. The necessary condition to pass the S1 selection was, next to a maximum mean signal arrival time and a minimum energy threshold of 1 phe, that at least 3 PMTs were contributing to the area of the given S1 pulse (3-fold coincidence). The latter cut rejects signals associated with PMT afterpulses, where electrons are emitted somewhere along the dynode chain of the PMT and accelerated to produce a viable signal. Events satisfying the golden rule were then subject to voltage and waveform checks, rejecting data with spurious anode, cathode or PMT voltages and currents, and irregular waveforms. At this stage a new set of variables was calculated for the selected events (for a list of the most important parameters see Table 4.1) followed by a final set of cuts refining the selection. This included a more stringent threshold on the S2 pulse area and amplitude as well as a maximum and minimum restriction on the S2 pulse width, S1 and S2 tau parameters and the drift time. The final product was written into data n-tuples, dubbed ‘golden-n-tuples’, holding a set of golden events. Subsequently, the mercury event reconstruction code, accessing the provided variables, processed the selected dataset and extended the n-tuple by a block containing the final energy variables and event positions (see Table 4.1). Finally, selected events were completed using information from the pulses recorded with the veto instrument for synchronised data (see Chapter 5).

Various stages of the golden dataset accommodated blind rules, necessary for a non-biased analysis and compulsory for rare event searches. Up to the final stage of the analysis blind rules applied to the nuclear recoil band, with the exception of vetoed events.

Table 4.1: The list of parameters held by a final golden n-tuple. It includes seven main blocks holding in total 138 different variables, some of which are in the form of arrays. Only the most important parameters are listed here. The parameter blocks are ordered by the occurrence in the data handling process and the corresponding processing codes are indicated in bold letters.

Parameter block	Parameters
Event	Event number, time and synchronisation timestamp
Slow Control	System temperatures and pressures Environmental temperatures and pressures Detector vacuum High voltage and current
<b>ZE3RA</b>	
Channel	Baseline mean and RMS noise
(66 channels in total: 32HS+32LS+2Sum)	Time interval used to evaluate baseline noise Total number of pulses
Pulse (10 largest/channel)	Number of saturated samples Pulse start time, amplitude and width at 10% and 50% maximum Integrated pulse area total and above threshold Pulse area with constant integration Mean charge arrival time Area fraction in first half-width of pulse
<b>Golden code</b>	
Gold	Number of saturated samples, start time, mean charge arrival time, FWHM, area fraction in first half-width and flat-fielded summed area of the selected S1 and S2 pulses Drift time (time between S1 and S2) Energy calculated from S1 Energy calculated from S1-S2 anti-correlation Number of triggers in S1 (S1 fold) Correction factors for: electron life-time, pressure (to correct S2 area), diffusion (to correct S2 width and charge arrival time), DAQ gain and detector tilt (to correct S2 area) x-y position from centroid reconstruction

*Continued on next page*

Table 4.1 – *Continued from previous page*

Parameter block	Parameters
<b>Mercury</b>	ML estimator for S1 x-y coordinates S1 energy reconstructed with ML/WLS for S1/S2 position and ML/ $\chi^2$ values Number of PMTs with exactly 1 phe/2 phe in S1 WLS estimator for S2 x-y coordinates S2 energy reconstructed with WLS and $\chi^2$ Spatial RMS for S1 and S2 signals Horizontal distance between S1 and S2
<b>RaVen</b>	
Veto (first 100 pulses)	Event number, time and synchronisation timestamp Total number of pulses Pulse channel, start time, height, baseline, area, and width



## Chapter 5

# The ZEPLIN-III Veto Detector

As previously mentioned in Section 4.4, one of the major upgrades prior to the SSR of ZEPLIN-III was the incorporation of a 1-tonne scale plastic scintillator detector, acting as an anti-coincidence device for the main dark matter instrument. The modular system of 52 individual polystyrene based scintillator bars, coupled with gadolinium-loaded polypropylene shielding, provided tagging of  $\gamma$ -ray and neutron events in coincidence with ZEPLIN-III. In addition, the veto was also utilised for independent diagnostics of environmental radioactivity background and provided a tool for measuring production yields of high energy cosmic-ray muon-induced neutrons (see Chapter 9).

This chapter summarises the design of the veto detector (see Section 5.1), covered in Ref. [164], and gives a detailed description of its performance during the SSR of ZEPLIN-III (see Section 5.2). Most of the work discussed here was previously presented in Ref. [1] to which the author contributed heavily.

### 5.1 Design

The ZEPLIN-III veto system consisted of 52 individual plastic scintillator modules surrounding a 15 cm thick Gd-loaded polypropylene shielding, which encircled the ZEPLIN-III dark matter detection instrument. A CAD rendering and a cross-sectional view of the full experimental setup is shown in Fig. 5.1 and Fig. 5.2, respectively. The structure formed by assembling the individual modules can be described by two main geometrical shapes: a circular barrel composed of 32 scintillator bars and a roof constructed from 20 individual scintillators. These shapes provided  $>3\pi$  sr coverage around ZEPLIN-III. Each barrel module had the form of a parallelepiped of length 1 m, width 15 cm, and a trapezoidal cross-section with parallel sides of length 15 cm and 12 cm. The roof sections were of four different lengths (80, 75, 67 and 51 cm) to form

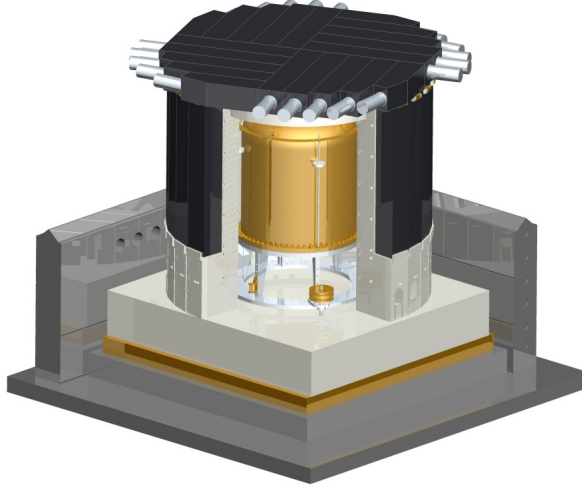


Figure 5.1: CAD rendering of the veto system surrounding the ZEPLIN-III dark matter detection instrument. The veto setup consists of 32 Gd-loaded polypropylene pieces (white) surrounded by the same number of active scintillator modules (black) with PMTs housed in cups and recessed into the lower polypropylene structure. The roof of the veto detector is composed of 20 scintillator modules, which are placed on top of a roof plug. The lower polypropylene structure contains no Gd and rests on a copper and lead base. Finally, a lead castle (only the first view lead blocks are indicated on the sides facing the back) envelops the entire assembly. For display purposes only, a quarter of the scintillator bars from the barrel are not drawn to reveal the ZEPLIN-III detector.

a pseudo-circular shape divided into quadrants and were of rectangular cross-section with side lengths of  $15\text{ cm} \times 16\text{ cm}$ .

The individual detector modules were made from polystyrene based plastic scintillator, UPS-923A (p-terphenyl 2%, POPOP 0.02%), produced by Amcrys-H, Kharkov, Ukraine [165]. The plastic material had a density of  $1.06\text{ g/cm}^3$  and a refractive index of 1.52 for blue light. The nominal average light output for electron recoils was measured to be  $\sim 5500$  photons/MeV. The scintillation light showed a peak intensity at 420 nm, a rise time of 0.9 ns and a decay time of 3.3 ns. The average bulk attenuation length for the 52 modules has been experimentally measured and was found to be approximately 1 m [164].

A single 3-inch PMT (ETEL-9302 KB) with an average quantum efficiency of  $\sim 30\%$  was optically coupled to one end of each individual scintillator bar. Due to the increased radioactivity from within the PMTs, their position had been chosen to provide maximum distance to the xenon target, *i.e.* on the lower face of the barrel modules and

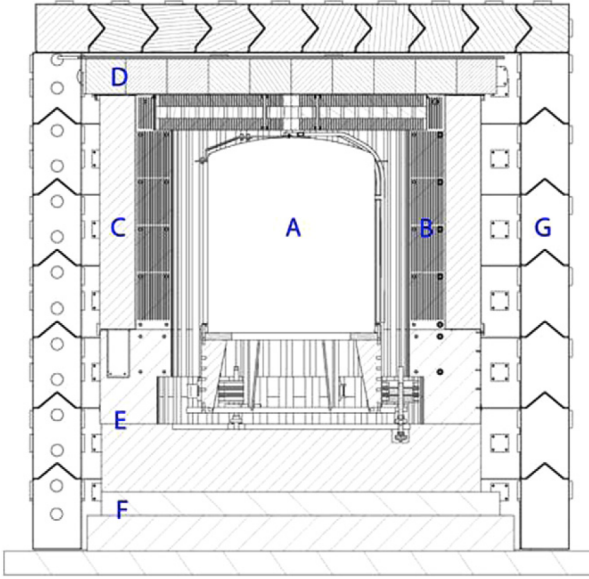


Figure 5.2: Cross-sectional view of the full experimental setup in its second science run configuration. The main components are the ZEPLIN-III detector (labelled A), the Gd-polypropylene shielding (B), the plastic scintillator barrel modules (C) with the PMTs housed in cups and recessed into the lower polypropylene structure, the plastic scintillator roof modules (D), the polypropylene base containing no Gd (E), a lead and copper fundament (F) and the lead castle (G) enclosing the entire assembly [164].

on the outside face of the roof modules. The cups, which also accommodated a custom built preamplifier, housing the 20 roof PMTs can be seen in Fig. 5.1 (grey). The PMT cups of the barrel modules are obscured by the polypropylene shielding in which the PMTs were embedded. Additionally, all modules were wrapped in PTFE sheet of high diffuse reflectivity and a highly-specular reflective aluminised Mylar film was located at the end opposite to the PMT, to increase light collection. Finally, the bars were covered with opaque PVC foil for light tightness and sealed with copper tape.

Inside the shell of plastic scintillator modules an additional 15 cm of polypropylene based plastic added to create a 30 cm thick hydrocarbon shielding construction; again, designed in the shape of a segmented barrel with a roof plug, clearly visible in Fig. 5.2 as the dark hatched regions. The 32 polypropylene bars were slightly rotated with respect to the plastic scintillator sitting on the outside to avoid line-of-sight gaps between the individual modules. The polypropylene shielding was loaded with  $\sim 0.4\%$  Gd by weight in the form of  $\text{Gd}_2\text{O}_3$  mixed into an epoxy and filled into 2 mm wide slots, with a pitch of 10 mm cutting through the full depth of the polypropylene slabs and the roof plug.



Figure 5.3: Photographs documenting the progression during the assembly of the veto around the ZEPLIN–III detector, starting with the installation of the Gd-loaded polypropylene around the instrument, followed by the insertion of the roof plug and the arrangement of the polystyrene scintillator bars, wrapped in black opaque PVC, around the polypropylene barrel. Finally, the start on the construction of an additional layer of 6 cm of polypropylene shielding between the lead castle and the veto detector is visible.

Figure 5.3 shows a compilation of photographs taken during the installation phase of the veto detector around the ZEPLIN–III instrument. It shows the individual steps of the assembly procedure of all major parts.

The comprehensive construction provided active rejection of background events through the detection of  $\gamma$ -rays following radiative neutron capture on, predominantly,  $^{157}\text{Gd}$  after thermalisation via hydrogen scattering. Utilising the very high  $^{157}\text{Gd}$  neutron capture cross-section of  $2.4 \times 10^5$  barn [166] has two major advantages for detecting and identifying neutrons in coincidence with an internally enclosed detector. Firstly, the time between the initial and the delayed signal is greatly reduced in contrast to neutron captures on hydrogen. It is very desirable in an experimental environment to keep capture times to a minimum in order to reduce the data volume and false-coincidence rates. Secondly, the emission of 3–4  $\gamma$ -rays, totalling  $\sim 8$  MeV after capture on  $^{157}\text{Gd}$ , provides a clear signal to observe, *i.e.* it increases the probability of detection. In the case of a pure hydrogen system, the radiative neutron capture would only produce a single  $\gamma$ -ray with an energy of  $\sim 2.2$  MeV.

### 5.1.1 Gadolinium concentration

To optimise the tagging efficiency for neutron events, *i.e.* the identification and subsequent rejection of neutron events that otherwise might have been identified as a WIMP, simulations calculating the correlation between gadolinium concentration and tagging fraction have been performed during the design phase of the veto. Figure 5.4

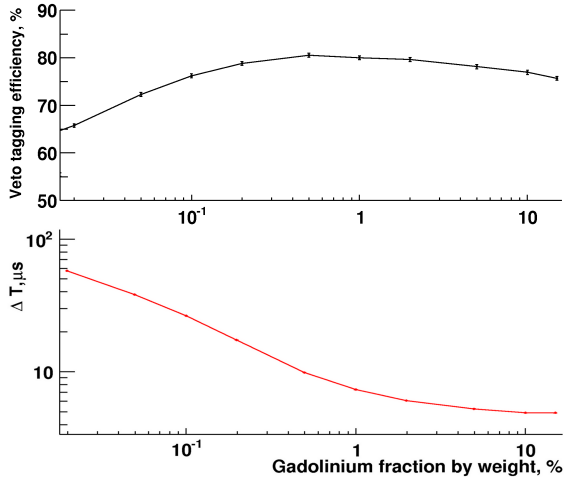


Figure 5.4: Monte Carlo simulation of the full setup with different concentrations of gadolinium loading by weight in the polypropylene parts of the veto. Upper panel: Ideal tagging efficiency of neutron events for background rejection [164]. Lower panel: Characteristic capture time of tagged neutron events, *i.e.* characteristic time delay between nuclear recoil signals observed in ZEPLIN-III and the signals in the veto. The lines indicated are to guide the eye only.

shows that a maximum tagging efficiency of  $\sim 80\%$  is reached at a gadolinium fraction by weight of  $\sim 0.5\%$  using an idealised simulation, omitting any thresholds that would be necessary in the real data to reduce accidental tagging of uncorrelated background events.

To calculate the exact gadolinium concentration, achieved in the production process of the polypropylene parts of the veto, an *in-situ* calibration run with an Am-Be ( $\alpha, n$ ) source was performed. A population of single-elastic neutron scatters was defined by selecting a nuclear recoil band within two standard deviations of the median from coincidence data of the ZEPLIN-III instrument (see, for example, Fig. 8.3 in Chapter 8). The same calibration data set was utilised later for the evaluation and optimisation of the neutron tagging efficiency for the SSR (see Section 5.2.3).

Figure 5.5 shows the delayed arrival times of signals in the veto relative to the S1 signal observed in ZEPLIN-III for the selected data, alongside Monte Carlo simulations for comparison. A fit to the time delay distribution resulted in a characteristic neutron capture time of  $10.7 \pm 0.5 \mu s$ , which corresponds to a gadolinium concentration of  $0.42 \pm 0.03\%$  Gd by weight using the results shown in the lower panel of Fig. 5.4. The gadolinium concentration found satisfies design specification since variations of up to  $\pm 0.1\%$  do not change the tagging efficiency by more than 1%.

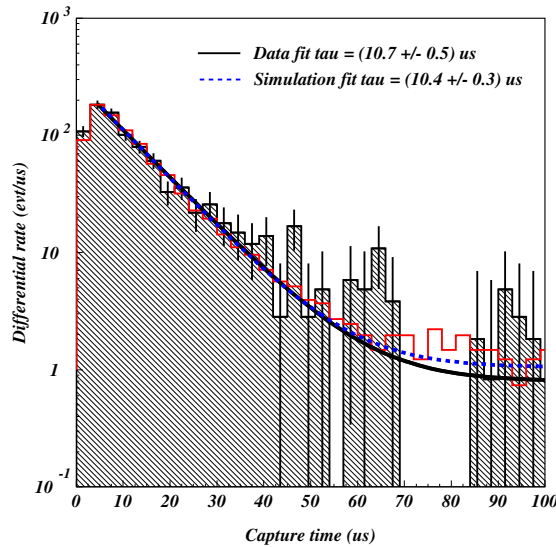


Figure 5.5: Pulse time distribution in the veto relative to the S1 signal in ZEPLIN-III from a selected dataset of single-elastic neutron scatters (black hatched histogram) in comparison to Monte Carlo simulations (red open histogram). The fit to the data, resulting in a characteristic capture time of  $10.7 \pm 0.5 \mu\text{s}$ , is in excellent agreement with the trend line of the simulation [1].

### 5.1.2 Material selection and backgrounds

The selection of materials for each individual part of the veto detector was based on component-level radio-assays. Evaluations of the radiological contamination for all construction materials were performed in order to keep additional contributions to the background within the ZEPLIN-III xenon target to a minimum, *i.e.* the gain for the experiment from event tagging by the veto must outweigh the addition in expected background. The contaminations from  $^{235}\text{U}$ ,  $^{238}\text{U}$ ,  $^{232}\text{Th}$  and  $^{40}\text{K}$  were determined, using a High-Purity Germanium (HPGe) detector setup in the low background count facility of the Boulby Underground Laboratory, by direct observation of  $\gamma$ -ray emissions, complemented by Inductively Coupled Plasma Mass Spectrometry (ICP-MS) and Optical Emission Spectrometry (ICP-OES) measurements for some of the samples. It is essential to not rely on measurements from one technique alone. For example, the direct observation of  $\gamma$ -rays is predominantly limited to the late chain decays, and as such secular equilibrium was assumed to infer contamination levels with complementary Monte Carlo simulations. On the contrary, complementary

Table 5.1: Radiological content of the veto components as measured by direct observation of  $\gamma$ -rays (HPGe) or through mass-spectrometry techniques (ICP-MS/OES) [164].

Component	Mass (kg)	Radiological content		
		U (ppb)	Th (ppb)	K (ppm)
<i>HPGe measurements</i>				
Plastic scintillator	1057.0	0.2±0.3	0.1±0.7	0.2±0.6
PTFE inner wrap	8.8	1.3±0.2	0.2±0.5	1.2±0.4
Silicone	0.1	2.9±0.4	0.5±0.8	5.7±1.1
PTFE tape	3.1	3.2±1.3	6.1±1.1	3.9±1.0
Veto PMTs	6.2	38.0±0.8	21.1±1.2	65.5±2.4
PMT preamplifiers	0.7	8.4±1.7	13.2±2.2	10.1±1.7
PMT base	5.5	12.7±1.4	14.8±2.4	20.2±2.4
Epoxy	70.0	2.5±0.6	0.9±0.3	0.6±0.1
Gd oxide	8.0	0.9±0.1	1.2±0.3	1.7±1.1
<i>ICP-MS/OES</i>				
Copper tape	26.0	1.9±0.2	2.9±0.4	14.0±2.0
PTFE inner wrap	8.8	2.0±1.0	5.0±1.0	<4
Veto PMTs	6.2	30.2±2.2	30.0±3.7	60±2.2
PMT preamplifiers	0.7	10.3±0.5	29.7±3.2	24±3.7
PMT base	5.5	13.0±3.4	19.0±2.0	21.0±3.0
Polypropylene	510.0	<1	<1	<5
PMT mounting	15.8	30.0±7.8	<10	<10
Cabling	30.2	110.0±5.4	20.0±3.2	29.0±7.3
Connectors	2.1	<10	<10	<4
Optical gel	0.3	<1	<1	<1
Gd oxide	8.0	2.5±0.5	3.4±0.7	<4

ICP-/MS/OES measurements are ideal to cover the early chain activities, due to the direct measurements of isotope abundances. Table 5.1 lists the measured radiological contents of all veto components. In all cases, the upper limits from either set of measurements have been used as inputs for the simulations, which estimated the background contributions to ZEPLIN-III and the veto detector itself.

### 5.1.3 Acquisition and trigger setup

Data were accrued with a dedicated data acquisition system (CAEN model V1724), digitising waveforms with a 14-bit resolution, an input range of 2.25 V, 40 MHz bandwidth and a sampling rate of 10 MS/s. The timelines of recorded events were 320  $\mu$ s in length. Waveforms were parameterised using a bespoke data

reduction software, dubbed ‘RaVen’, adapted from that developed for the ZEPLIN–III instrument [159].

The veto detector was operated in ‘slave’ and ‘master’ mode simultaneously. In slave mode the veto acquisition system was triggered by an external trigger generated by ZEPLIN–III. The trigger point and waveform lengths were tailored to enable quasi dead time free recording of coincident events with the dark matter instrument, *i.e.* 200 pre-trigger samples and 3000 post-trigger samples with a sample length of  $0.1\ \mu\text{s}$ . This finite recorded pre-trigger time ensured that dead time free recording also held true when the system was triggered by an S2 signal, where the drift time between the earlier occurring S1 signal and the S2 signal needs to be considered. The master mode allowed for independent triggering of the veto system when certain requirements were met. One of these conditions was the sum of simultaneously occurring pulses of the roof modules exceeding a set threshold. This particular trigger setup enabled the study of muon-induced neutrons. At this depth, most cosmic-ray muons have an arrival direction which is close to vertical, and thus such a trigger condition provided a high efficiency for the detection of cosmic-ray muons, but added little to the total data storage or rate implied for the experiment. Measurements of the muon-induced background are presented in Chapter 9.

## 5.2 Performance of the veto detector

The veto showed excellent and reliant performance during the full runtime of the SSR. The following sections give details on the stability and signal rates in the veto during the SSR, as well as a detailed description on the optimisation of tagging efficiencies of background events in coincidence with ZEPLIN–III.

### 5.2.1 Long term stability of the veto detector

Important for a long running experiment is the stability of the detector system over time. Therefore, a number of parameters, including electronic gains (single photoelectron response of the PMTs), coincidence rates, background rates, tagging efficiencies of electron recoil events and environmental parameters were monitored throughout the course of the experiment. For this purpose, a set of scripts, automatically generating plots and fits of the desired monitoring parameters, were created and included in the daily ZEPLIN–III project system checks and calibration procedures. Thus, the veto allowed for an independent monitoring and stability check on a daily basis, not only for the veto detector itself, but for the full ZEPLIN–III system, *e.g.* by looking at slave-triggered signal rates. Figure 5.6 shows the position of

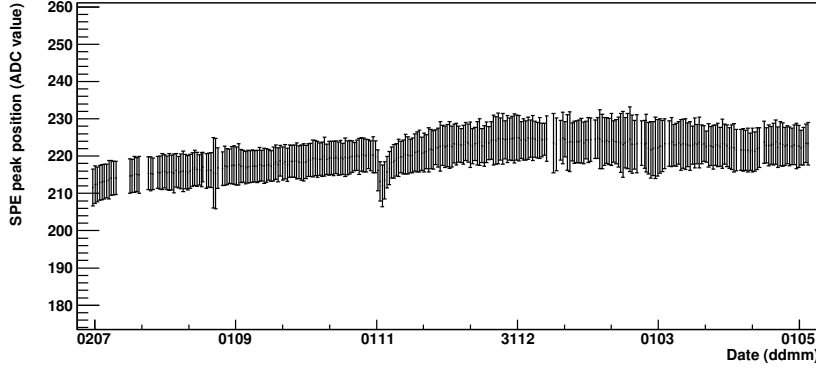


Figure 5.6: Evolution of the mean single photoelectron position for all 52 veto detector PMTs over time. The given error bars represent the RMS of the 52 mean SPE peak positions.

the SPE peak averaged over all 52 scintillator bars for each day of the SSR. The peak positions are defined by the centroids of the Gaussian fits to the pulse height parameter. This analysis of the SPE positions not only monitored the stability of the gains, but also provided calibration of each individual module on a day to day basis with no interruption to the dark matter search run. Moreover, the same methodology was used to normalise the gains of the PMTs in the first place. Variations of less than  $\sim 10\%$  between the individual channels have been achieved. Only a very small but steady change of  $\sim 0.6\%/\text{month}$  in the SPE position was observed (see Fig. 5.6). Despite the small change, implementation of these corrections are important for experiments with long time scales, such as the SSR of ZEPLIN-III. A single photoelectron is equivalent to an approximate energy deposition of 20 keV at the far end of the plastic slab. Limitation to a single PMT per scintillator bar prevented position reconstruction along the slab, and as such the far end of the scintillator bar is referred to as a conservative energy estimator.

Additionally, a dedicated calibration run with a pulsed blue LED (at  $\sim 30$  Hz for  $\sim 300$  s), coupled via fibre optic cable to each individual scintillator bar at the end opposite to the PMT, was performed on a weekly basis. Figure 5.7 displays the evolution of the LED generated pulse size (average of 48 phe in each scintillator) for one typical module, showing no change in optical transmission. Monitoring of the location of the SPE peak, and of the centroid of the LED generated peak, over the duration of the experiment, confirmed the system's general stability.

Another very important parameter is the efficiency in synchronising veto to ZEPLIN-III events. For data acquisitions operating at different sampling speeds,

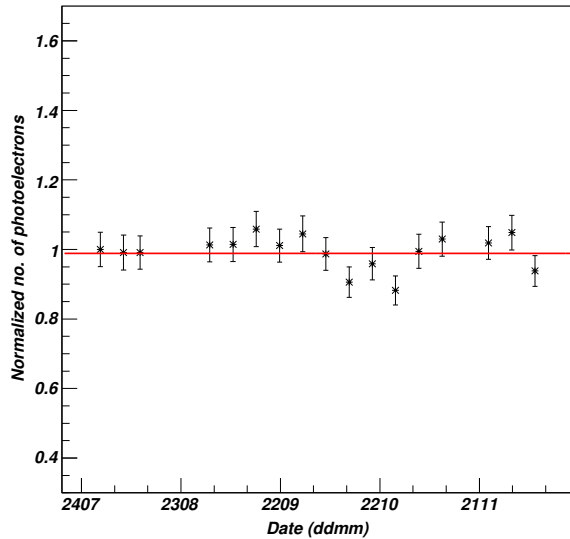


Figure 5.7: Centroid position of LED exposure generated peak over time for weekly LED calibration runs from a typical veto scintillator module. The data points are normalised to the first measurement [1].

digitising waveforms of different lengths with different resolution, comprehensive synchronisation procedures need to be in place to ensure maximum and consistent efficiency. In the first instance, correlated events were assigned by utilising a bespoke synchronisation unit clocked at 1 MHz, sending out a 32-bit digital time stamp to both acquisition systems following a trigger. As a fail-safe, a number of further methods were implemented in the analysis, ensuring correct and continuous synchronisation of events independent from the external synchronisation unit. Firstly, an internet time server was used to match the two data streams within 4 ms. Since the time server synchronisation was subject to slow drifting, a second control sequence was in place, monitoring the time difference between the two DAQ systems and checking that it agrees within 1 ms with the preceding or subsequent event (excluding veto self-triggers). Since the trigger rate was only  $\sim 0.4 \text{ s}^{-1}$ , the time consistency check proved to be a very powerful tool. Finally, using the sum of all PMT responses of ZEPLIN-III, which was also fed into and recorded by the veto data acquisition, allowed pulse parameters from both DAQs to be compared on an event-by-event basis. Since each event was represented by a unique set of variables, such as the number of pulses recorded in each timeline, the start times of pulses and their amplitudes, reliable matching of data was ensured with these off-line synchronisation techniques. Figure 5.8 shows a snapshot of the ZEPLIN-III sum

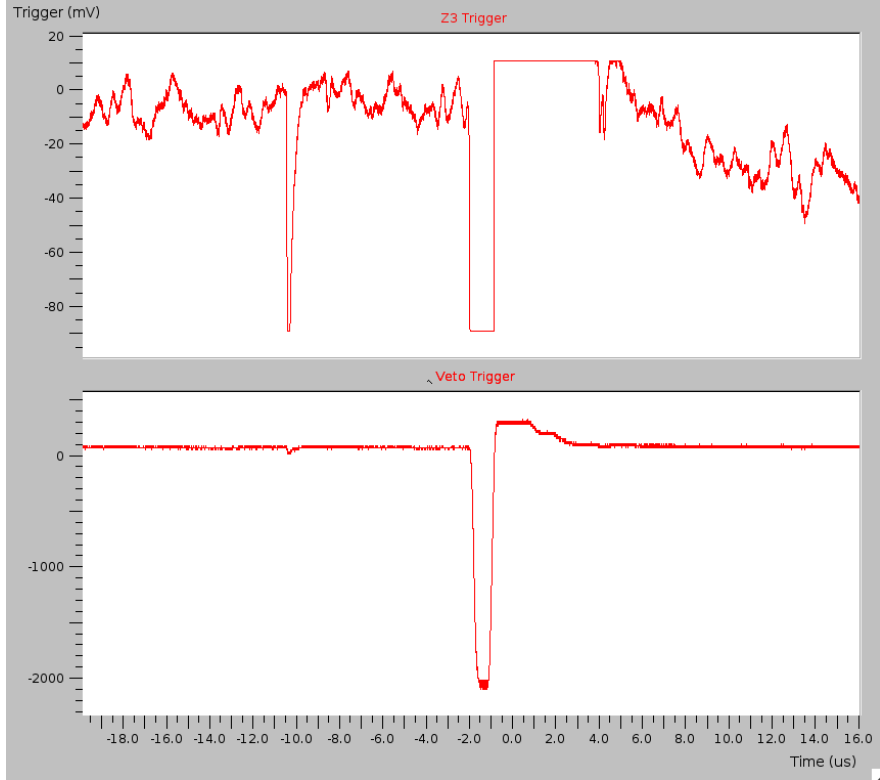


Figure 5.8: Screenshot of the ZE3RA synchronisation display for a successfully matched event, showing the summed signal from ZEPLIN-III as recorded by the ZEPLIN-III DAQ (top panel) and the veto DAQ (bottom panel).

channel as recorded by the ZEPLIN-III DAQ (top panel) and the veto DAQ (bottom panel) for a successfully synchronised event. Despite the difference in resolution and range of the two DAQs, correlated events can be clearly identified. The fraction of matched events for each individual day of the SSR is presented in Figure 5.9. An overall synchronisation efficiency of  $\sim 97\%$  has been achieved for the full dataset of the SSR.

Following the successful synchronisation of the veto data stream to that of ZEPLIN-III, the golden n-tuples were extended by the veto block, containing the pulse parameters extracted with RaVen from the veto detector waveforms of the first 100 occurring pulses in each event (see Table 4.1 in the previous chapter). Due to the array format of the n-tuple data structure, a restriction in the number of pulses had to be implemented to keep the data volume at manageable levels. Nevertheless, the efficiency for golden veto events with all pulses accepted was 99.4%.

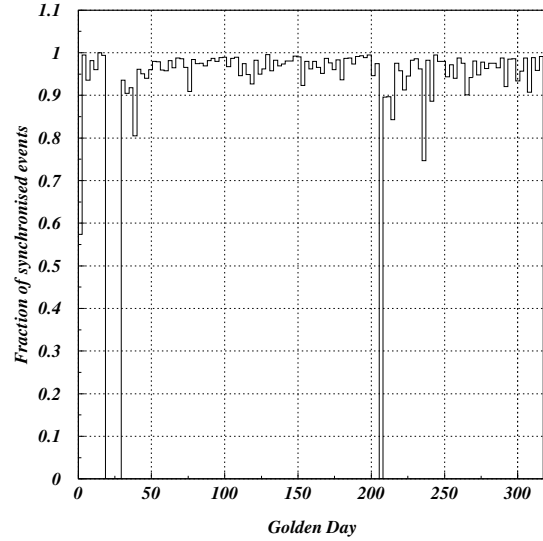


Figure 5.9: Fraction of synchronised events for the entire golden dataset of the SSR. Empty days represent time used for calibration measurements and other operational necessities other than taking WIMP search data, *i.e.* the synchronisation efficiency is not compromised.

### 5.2.2 Signal rates

Figure 5.10 displays the cumulative pulse rate recorded by the veto above a given threshold as indicated on the x-axis. The plot only extends to the onset point of saturation (between 65 and 70 phe), which is due to the range of the ADC in combination with the gain settings of the PMTs. These were chosen to provide excellent resolution down to the single photoelectron level, providing great advantages for a low threshold analysis and as previously mentioned enabled calibration without interruption to science data taking. The shape of the pulse distribution in Fig. 5.10 shows three distinct regions of interest and can be described by a combined fit to the three components. The first feature, the SPE peak up to 2 phe, arising from thermionic emission from the photocathodes and ambient light leakage into the scintillator, can be fit with a semi-Gaussian. The second component, fitted with an exponential, originates from radiological contamination from within the veto PMTs and spans the range from 2–15 phe. The domination at this energy range is related to the decay of  $^{40}\text{K}$  from the potassium generators in the PMTs behind the photocathodes. To reduce the risk of vacuum loss in the production process of a PMT, the glass envelope is made in one piece,

and thus potassium generators are installed for the subsequent evaporation process to sensitise the photocathode surface. The  ${}^{40}\text{K}$  decay has an 89%  $\beta^-$ -decay branching ratio with an endpoint energy of 1.31 MeV [167]. For a refractive index of 1.49 at 400 nm, electrons with energies exceeding 178 keV will produce Cherenkov radiation in the PMT window. In addition to these photons, bremsstrahlung may be produced in the window and direct scintillation in the plastic from interaction of  $\beta^-$ -particles with energies in the tail of the distribution, escaping through the window, may occur. Magnitude and slope of this second feature are consistent with expectations [168]. Finally, the third component is comprised of an exponential fit to the background arising from  $\gamma$ -ray interactions within the scintillators from environmental radioactive sources, such as from the uranium and thorium decay chains and from the  ${}^{40}\text{K}$  contamination within the shielding and other construction and surrounding materials. Despite their low radiological content, this part of the pulse rate spectrum was dominated by the two plastic components of the veto, due to their total combined mass of  $\sim 2$  tonnes. The pulse rate from radiological contamination also agrees well with predictions from Monte Carlo simulations based on the component-level radio-assays previously mentioned (see Table 5.1) [164]. Contributions to the single-elastic neutron scattering rate in the ZEPLIN-III fiducial volume of the xenon target and in an energy range of 5–50 keV<sub>nr</sub> are  $\sim 0.13$  events/year, assuming unity detection efficiency and not including tagging capabilities of the veto itself (see also Section 7.3 in Chapter 7). This rate translates to an expectation of only  $\sim 0.002$  detected neutrons in the WIMP search region for the full duration of the SSR attributed to the veto detector. For efficiencies and the definition of the acceptance region in the SSR see Section 8.1 in Chapter 8. Contributions from the veto to the electron recoil background in ZEPLIN-III arise only from the polypropylene shielding and equal 0.25 dru (at 10 keV<sub>ee</sub>), which is significantly less than contributions from radiological contaminations within the ZEPLIN-III PMTs (see Section 7.3). Backgrounds from radioactive impurities in the plastic scintillator posed a very low risk to ZEPLIN-III since they were tagged with near unity efficiency.

Assessing the pulse rate spectrum of the veto detector is very important for the overall performance of the ZEPLIN-III experiment, as it is of direct consequence to the tagging capability of the veto, *i.e.* it determines the probability of ZEPLIN-III events being accidentally tagged. The following section will discuss the tagging of  $\gamma$ -ray and neutron events with the veto detector, detailing the individual efficiencies and accidental tagging rates.

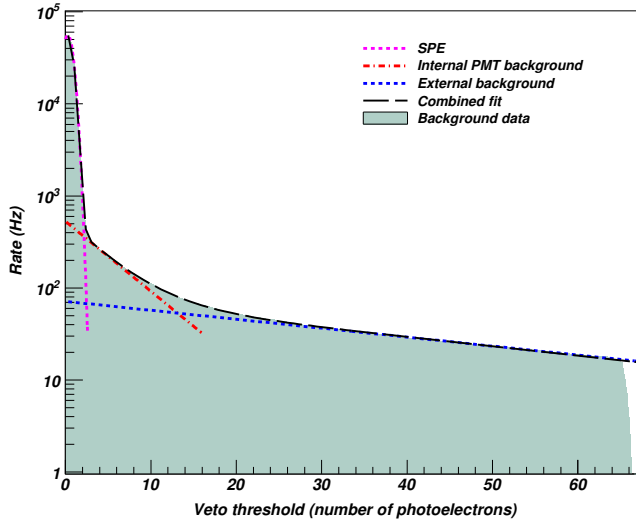


Figure 5.10: Cumulative signal (pulse) rate measured with the whole veto detector array above given thresholds in number of photoelectrons from slave mode triggered events only. Statistical errors are too small to be seen on this plot. The fit to the data (black dashed line) is comprised of three individual components: the SPE peak (pink dashed line), the internal background from the PMTs (red dot-dashed line) and the  $\gamma$ -ray background from radiological contamination within surrounding materials including the veto detector material itself [1].

### 5.2.3 Tagging of background events

ZEPLIN–III discriminated between particle species by recording two signals for each interaction, a prompt scintillation and a delayed signal from electroluminescence in the gas phase from ionisation liberated electrons, and thus allowed efficient rejection of most background events. However, the signature arising from neutron single-elastic scatters are identical to the expectation for a possible WIMP signal. Therefore, active identification and rejection of neutron events with the help of a veto detector is crucial. Furthermore, despite excellent discrimination of electron recoil events (1:7,800 in the FSR [153]), there is always a finite probability for these background events to be misidentified as nuclear recoils (see Section 7.3.1 and Section 8.1.3 in Chapter 7 for more details on rare types of electron recoil events and leakage into the nuclear recoil band, respectively). A tagging efficiency of  $\sim 28\%$  for  $\gamma$ -rays and  $\sim 61\%$  for neutrons by the veto of coincident events in ZEPLIN–III has been achieved. Details are given in the sections to follow.

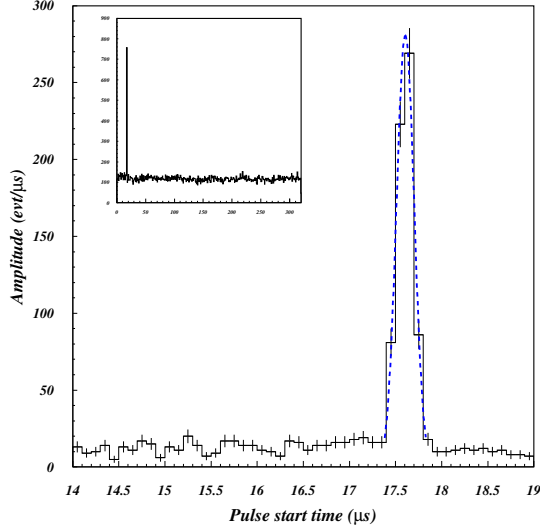


Figure 5.11: Pulse start time distribution as observed by the veto detector array for a small enlarged region around the trigger point and for the full timeline range of  $320\ \mu\text{s}$  in the inset. The peak at  $17.7\ \mu\text{s}$  corresponds to pulses which are in prompt coincidence with an S1 signal in ZEPLIN–III. When the system was triggered by an S2, S1 prompt coincidences in the veto are distributed in the  $16\ \mu\text{s}$  prior to the trigger point. Pulses after the peak are from randomly distributed background events in the veto detector itself [1].

### Prompt tagging

Following a Compton scatter within the xenon target volume of ZEPLIN–III, a  $\gamma$ -ray had a finite probability to interact as well within the plastic scintillators of the veto. Thus, a prompt signal at the time of the S1 signal may have been observed in the veto in coincidence with ZEPLIN–III. Every time an event was triggered in ZEPLIN–III, by the summed signal of all PMTs from either an S1 or S2 signal, a forced trigger signal was sent to the veto. Independent of the original trigger time in ZEPLIN–III, the trigger point in the veto timeline corresponded to  $17.7\ \mu\text{s}$  with sufficient pre-trigger time to accommodate for S2 triggered events. In this case, the prompt signal was shifted by the drift time in the liquid xenon volume to earlier times in the waveform.

Figure 5.11 shows the pulse time distribution recorded in the veto from slave mode triggers. The peak at  $17.7\ \mu\text{s}$  corresponds to prompt signals in coincidence with an S1 trigger. In the inset, the full length of recorded timelines is given. The slightly

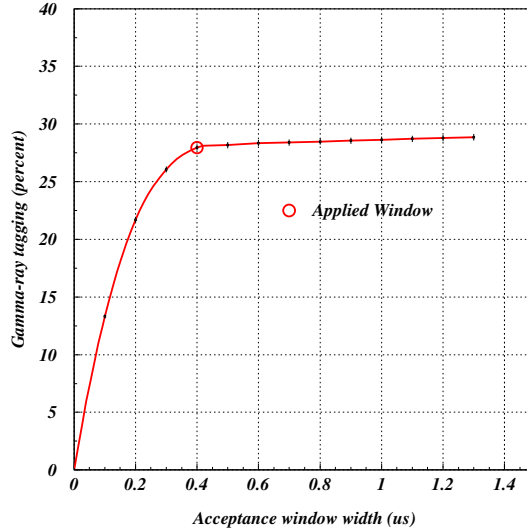


Figure 5.12:  $\gamma$ -ray tagging fraction of veto and ZEPLIN-III coincident prompt signals as a function of acceptance window width around the trigger point (including corrections for S2 triggered events). The efficiency rises rapidly at first until reaching a window size of  $0.4 \mu\text{s}$ . Beyond this point the continuing slow increase corresponds almost exclusively to the inclusion of additional accidental coincidences. The line indicated is to guide the eye only [1].

raised pulse rate at pre-trigger times arises from S2 triggered events, which have a preceding S1 signal. Thus, the coincident prompt signals in the veto are distributed in the region prior to the trigger. Consequently, these shifts in the prompt signal timing were corrected for further analysis. The lower level of pulses occurring after the prompt peak are unrelated randomly distributed background signals in the veto detector, which were useful themselves in quantifying the accidental tagging rate.

The goal when determining selection criteria for a prompt tag is to balance maximum efficiency with an acceptable accidental tagging rate of uncorrelated events. Firstly, a time window for coincidence signals was defined. The timing resolution of the combined veto-ZEPLIN-III system was affected predominantly by the sampling speed of the veto digitisers (100 ns sampling). The contribution from ZEPLIN-III itself was minor (2 ns sampling). Together they determined the arrival time of an S1 and the trigger, as well as the measure of the time between an S2 and an S1 signal in case of S2 triggered events. Taking these factors into account, a window of  $0.4 \mu\text{s}$ , *i.e.*  $\pm 0.2 \mu\text{s}$  around the ZEPLIN-III trigger, had been found to most effectively select

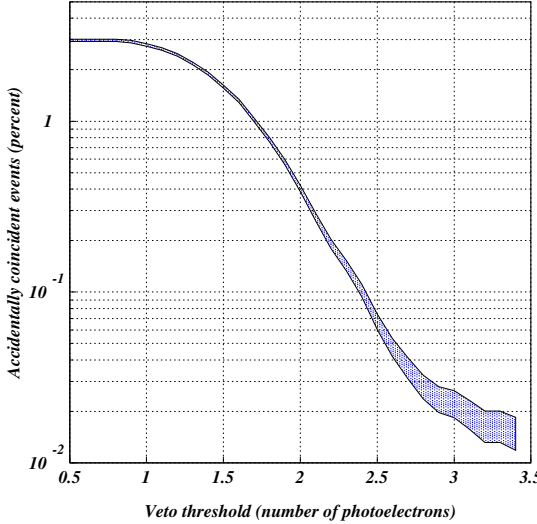


Figure 5.13: Fraction of accidentally tagged events in a  $0.4 \mu\text{s}$  window as a function of veto detector threshold. The hatched area represents the  $1\sigma$  error band. At a threshold of 2 phe the accidental tagging fraction equals 0.4% [1].

prompt coincident signals. In Fig. 5.12, different sizes of acceptance windows are plotted against the prompt tagging efficiency achieved for each window width. It illustrates that the tagging efficiency rises steeply only to the point of the defined window of  $0.4 \mu\text{s}$ , centred around the prompt peak. Above this value, the slow constant increase in the percentage of tagged events is predominantly due to accidental coincidences with randomly distributed background events. Therefore, increasing the window size would have only introduced more accidental coincidences, and thus lowered the effective exposure of the xenon target by unwanted rejection of potential WIMP events.

The accidental tagging rate can be calculated from the product of the event rates in both systems and measured directly by applying the same acceptance window off-coincidence anywhere in the timeline. The rates extracted by the latter method are illustrated in Fig. 5.13 relative to an applied minimum threshold on the total signal size, *i.e.* the sum over all pulses occurring within  $\pm 0.2 \mu\text{s}$  of each other. At a threshold of only 2 phe the accidental tagging rate falls by an order of magnitude to 0.4%, excluding sufficiently the tagging through uncorrelated signals at the single photoelectron level.

A similar plot, shown in Fig. 5.14, can be drawn for the actual prompt tagging efficiency achieved for a given signal threshold, using a dataset of synchronised slave

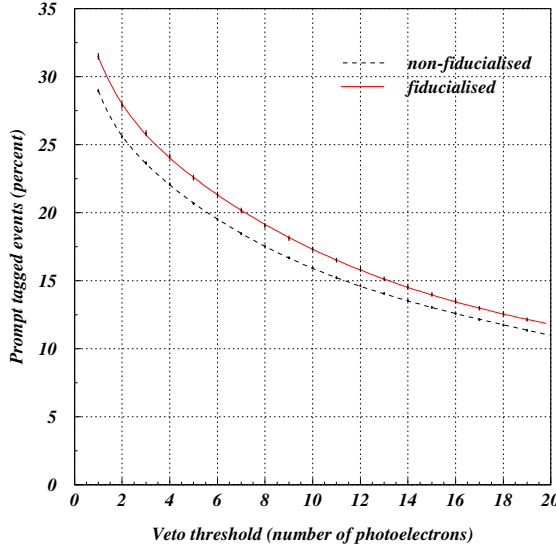


Figure 5.14: Prompt tagging efficiency as a function of veto threshold on summed coincident signals for all synchronised ZEPLIN–III events ( $<100$  keV $_{ee}$ ) in the full xenon volume (black dashed line) and in the fiducialised region of the target (red). At a 2 phe threshold the fraction of prompt tagged events equals  $28.1 \pm 0.2\%$ . The lines indicated are to guide the eye only [1].

mode triggered background events. The prompt tagging fractions are given relative to all triggered events below 100 keV $_{ee}$  energy in ZEPLIN–III (dashed black line) and for those events that occur in the fiducialised volume of the xenon target (red solid line). As expected, the tagging efficiency increased when selecting a central confined region in the liquid xenon volume. In this case, electron recoil events were more likely to be produced by Compton scatter  $\gamma$ -rays, rather than by  $\beta$ -induced background or interactions from  $\alpha$ -particles. At a threshold of  $\geq 2$  phe, the prompt tagging efficiency reads  $28.1 \pm 0.2\%$  for synchronised electron recoil background in the fiducial volume of ZEPLIN–III.

The final selection criteria for a prompt tagged event were comprised by a minimum threshold requirement of  $\geq 2$  phe ( $\sim 40$  keV) on the summed signals distributed in any pattern across the veto detector array, provided that they were themselves within  $\pm 0.2 \mu s$  of one another and by the restriction to an acceptance window for prompt coincidences of  $0.4 \mu s$ . In addition to the valuable identification and rejection of  $\gamma$ -ray background, prompt tagged events provided an independent estimate of the electron

recoil background in the xenon target (see Section 5.2.3). Furthermore, Section 5.2.4 discusses the implications of a veto detector identifying  $\gamma$ -ray backgrounds for a signal limit in case of an observed event population in the signal region.

### Delayed tagging

Signals from neutron single scatters in the fiducial volume of the xenon target are indistinguishable from a signal expected from a WIMP. Thus, explicit tagging of neutron events is crucial for any direct dark matter experiment to mitigate irreducible backgrounds. Neutrons generating a signal within ZEPLIN-III were moderated to thermal energies by the hydro-carbon shielding surrounding the WIMP target. Once thermalised, the neutrons were predominantly captured on the gadolinium enclosed in the veto detector construction and  $\gamma$ -rays from the radiative capture could be detected with the veto scintillators. The emitted  $\gamma$ -rays were delayed by the characteristic capture time of the veto system, depended on the gadolinium concentration within the polypropylene components (described earlier in Section 5.1.1). The same Am-Be calibration dataset used for calculating the Gd concentration was adopted for calculations of the neutron tagging efficiency presented here.

Similarly to the definition of a prompt tag, tagging efficiencies for neutrons should be maximised whilst maintaining a low fraction of accidental coincidences with ZEPLIN-III in the science data. A maximum accidental rate of 1% had been chosen to be an acceptable loss in effective exposure. Therefore, the choice of threshold in number of photoelectrons and multiplicity of simultaneously firing scintillator modules (within  $\pm 0.2 \mu\text{s}$  of each other) was found by lowering the threshold step by step and varying the multiplicity requirement until the accidental rate fell below the set limit. The distribution of pulse times, shown in Fig. 5.5, implies that 99.9% of all pulses arrived within  $70 \mu\text{s}$  after the S1 time. Opening the window beyond this point would increase the tagging efficiency only slowly and predominately due to expected accidental coincidences. Furthermore, the window was restricted to times after the prompt window only. Although a small fraction of neutrons already undergo captures at these short time scales, this part of the timelines was not considered. Despite the apparent under-prediction of neutron tagging efficiencies by this cut, coincident events falling in this category were still rejected due to the previously applied prompt tagging subroutine in the analysis procedure for the ZEPLIN-III science data. For the determination of the ‘true’ delayed tagging efficiency, captures falling in the positive half of the prompt window need to be considered separately and added into the calculation.

Figure 5.15 shows the accidental rate, calculated by looking at the electron recoil band in background data only, as a function of photoelectron threshold with no

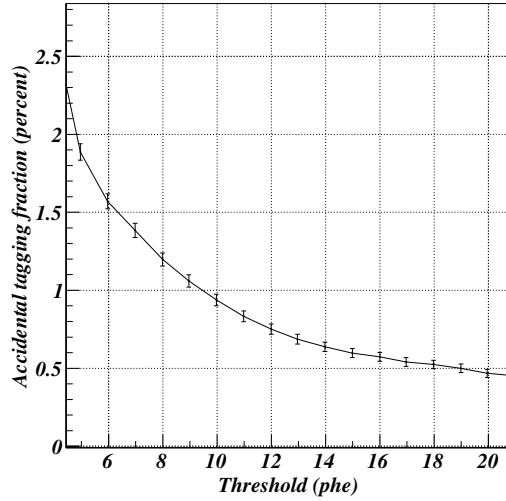


Figure 5.15: Accidental tagging fraction for the delayed tag subroutine as function of threshold with no multiplicity requirement applied. At a threshold of 10 phe the accidental rate falls just below 1%. The line indicated is to guide the eye only.

multiplicity requirement applied, *i.e.* the sum of all coincident pulses independently of their distribution within the veto scintillator array are considered. At a threshold of  $\geq 10$  phe, the accidental rate falls just below 1%. Adopting this threshold, the change in varying the minimum scintillator multiplicity requirement can be explored and is shown in Fig. 5.16. Going from multiplicity 1 to 2 decreases the neutron tagging efficiency by  $\sim 10\%$ . On the other hand, it was found, when requiring a multiplicity of 2, a threshold of 8 phe yielded a similar tagging efficiency for neutrons. Lowering the threshold by simultaneously increasing the multiplicity did not compromise the accidental tagging rate, since a stronger dependency on multiplicity was found for  $\gamma$ -ray background (filled histogram in Fig. 5.16), which makes up the population for delayed accidental coincidences. Combining the two sets of requirements does not lead to an improvement since equivalent distributions are being tagged by both sets of selection criteria, but increases accidental rates due to linear adding of accidentally tagged background events. Thus, a neutron tagged event needed to fulfil no multiplicity requirement, but the summed signal had to add up to a minimum of 10 phe. With these selection criteria laid out, a tagging efficiency for single scatter neutrons in the WIMP acceptance region, *i.e.* nuclear recoils with an energy deposition of less than 20 keV<sub>ee</sub> in the ZEPLIN-III fiducial volume, of  $58.5 \pm 0.5\%$  was achieved. Due to the detection mechanism of recording signals following radiative neutron capture, the fraction of

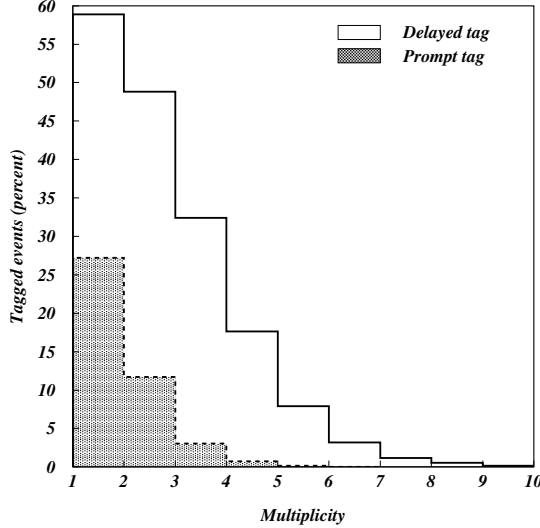


Figure 5.16: Tagging efficiency as a function of simultaneously recorded pulses (within  $\pm 0.2 \mu\text{s}$  of each other) for delayed (empty histogram) and prompt tags (filled histogram), respectively [1].

tagged events stays constant over the full range of nuclear recoil energy deposits in ZEPLIN-III, as shown in Fig. 5.17. The delayed  $\gamma$ -rays from the de-excitation of the excited  $^{158}\text{Gd}$ , following a neutron capture, are independent of the original neutron energy, due to the destruction of the angular distribution through proton recoils in the hydro-carbon shielding (thermalisation) prior to capture.

The delayed tagging requirements were chosen to keep the accidental rate at 1%. However, considering the order of the tagging procedure of background data, the selection of uncorrelated events by the delayed tag subroutine is reduced by 0.28%. The population of electron recoils is lowered prior to delayed tagging by applying the prompt tag selection first. Hence, the accidental tagging rate for the identification of neutrons in the science data equals 0.7%.

As previously mentioned, to calculate the true neutron tagging capability of the veto detector, delayed pulses at very short timescales, *i.e.* those which fall into the first half of the prompt window, also need to be considered. However, it is not feasible to measure this fraction by using the neutron calibration data with an exposure to an Am-Be source. High energy  $\gamma$ -rays are emitted in the Be ( $\alpha, n$ ) reactions, accompanying the neutrons. These  $\gamma$ -rays would fall within the prompt acceptance window, and thus

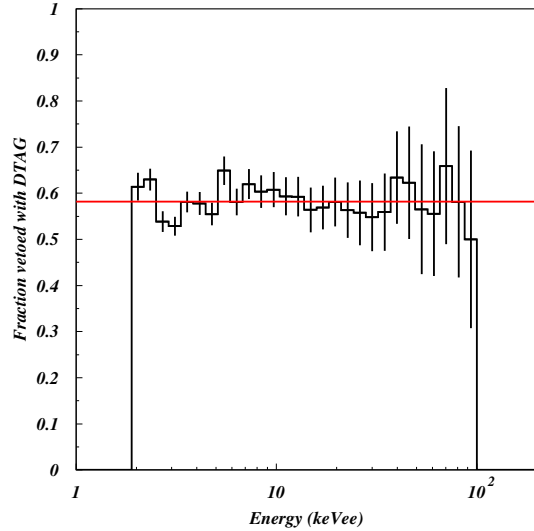


Figure 5.17: Neutron tagging efficiency as a function of energy measured by using data from a neutron calibration run with an Am-Be source. For energy deposits below 20 keV<sub>ee</sub> an effective neutron tagging efficiency of  $58.8 \pm 0.5\%$  is achieved. It stays relatively constant over the full energy range [1].

would increase the tagging fraction for non-neutron events artificially. Furthermore, their high energies (mostly 4.44 MeV) are not representative of a usually observed  $\gamma$ -ray background and are indistinguishable from the high energy  $\gamma$ -rays released in the de-excitation of the <sup>158</sup>Gd isotope. Consequently, instead of a direct measurement, the additional fraction of neutron tagging was calculated by extrapolating the pulse time distribution of delayed signals into the positive half of the prompt window. From this, an additional  $1.7 \pm 0.1\%$  in neutron tagging efficiency is to be expected. Complementary Monte Carlo simulations predicted an additional  $1.5 \pm 0.1\%$  for an equivalent window. As such, the real total neutron tagging efficiency adds up to  $60.5 \pm 0.5\%$  for a 10 phe threshold. This is in reasonable agreement with the design goals set out for the performance of the veto detector presented in Ref. [164]. This rejection capability limits the expected background from neutrons in a WIMP acceptance region of 5–50 keV<sub>nr</sub> and in the fiducial volume of the ZEPLIN-III xenon target (6.5 kg), to a value of  $\sim 0.2$  neutrons/year (incl. efficiency and acceptance).

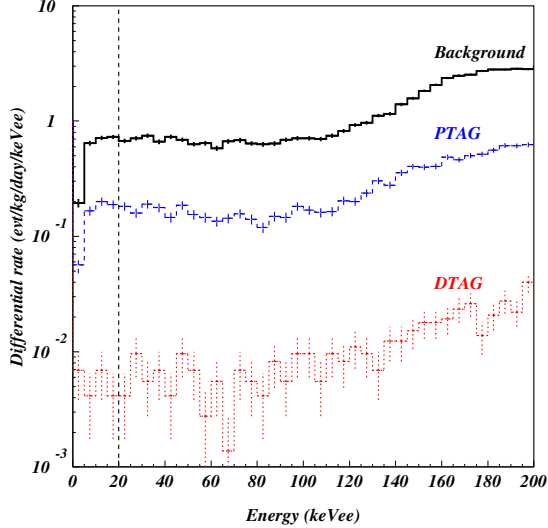


Figure 5.18: Differential energy spectrum of the electron recoil background in ZEPLIN-III (black solid histogram). Also shown are the rate of prompt tagged (PTAG – blue) and delayed tagged (DTAG – red) events. Both are approximately constant with energy. The 0.7% DTAG fraction of the background is consistent with the expected accidental delayed coincidence rate. The dashed line indicates the approximate upper boundary of the WIMP search region [1].

### Tagging of background data

With all subroutines defined to tag prompt and delayed events in coincidence with ZEPLIN-III, the impact on the science data can be explored. Figure 5.18 shows both tagging rates as a function of energy deposits of the coincident signals in ZEPLIN-III and a comparison to the overall rate observed in the science data. The region of interest for WIMPs has been excluded from this plot, so as to not conflict with the procedure of a blind analysis. Hence, only the background from electron recoils has been considered here. The prompt tagging rate, labeled as ‘PTAG’, is approximately a constant fraction of the total differential rate. Importantly, this constant fraction of prompt tagged events provided an unbiased sample of background events, which was utilised for characterisation of data and development of cuts in the blind analysis. Therefore, the sacrifice of possible WIMP data from the full exposure time was avoided (*e.g.* the 10% of the data in the FSR). Similarly, the rate of delayed tagged events, labeled as ‘DTAG’, remains constant over the full energy range and is consistent with

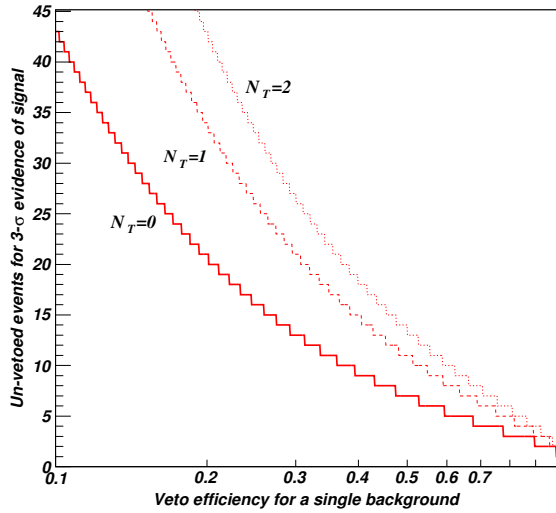


Figure 5.19: Implications of the tagging efficiency of a veto detector on the evidence for the discovery of a signal in a rare event search experiment assuming a single background scenario.  $N_T$  indicates the number of tagged events observed in the signal region [1].

the accidental tagging rate of 0.7% of the electron recoil background. The prompt tagging efficiency of energy deposits below 20 keV<sub>ee</sub> amounts to an average fraction of  $28.2 \pm 0.6\%$ . The combined accidental coincidences from both tags for background events equals 1.1%, from the addition of 0.4% prompt and 0.7% delayed accidentals, respectively. On the other hand the accidental tagging rate for WIMPs remains at 1.4%, since the full accidental coincidence rate for neutron tagging of 1% needs to be considered.

#### 5.2.4 Implications for signal limits

An anti-coincidence device that rejects background signals with a known efficiency can be incorporated in calculating confidence intervals when a population of candidate events is observed in a signal region. Considering the information of the number of vetoed events implies the measure of un-tagged background events with Poisson uncertainty, a relative fraction of vetoed to un-vetoed background samples of  $\frac{\eta}{(1-\eta)}$ , with  $\eta$  representing the tagging efficiency, can be defined. Utilising the profile likelihood ratios [169], as implemented in the ROOT [170] class `TRolke`, confidence intervals can be calculated. Figure 5.19 shows the number of un-tagged events that need to be observed in a pre-defined signal region to constitute 3- $\sigma$  evidence for a genuine signal

as a function of  $\eta$ . For simplification of the statement only a single background case was assumed. Hence, with  $\eta = 0.28$ , only 15 un-vetoed events with no tagged events in the signal region would be sufficient evidence for a discovery, using no other additional discrimination parameters. In ZEPLIN-III and in similar rare event searches, the backgrounds from nuclear and electron recoils must be added up with different veto efficiencies for each type. The use of additional differentiation parameters, such as pulse shapes, energies and S2/S1 discrimination, could lower the number of necessary un-vetoed signal-like events even further than in the simplified case presented in Fig. 5.19.



## Chapter 6

# Quenching Factor for a Plastic Scintillator

The understanding of energy quenching in nuclear recoil interactions is one of the key factors in the analysis of any dark matter experiment looking for direct interactions of WIMP particles with scintillator target materials. The scintillation yield for nuclear recoils is studied extensively for liquid xenon and results from the measurements performed by the ZEPLIN-III collaboration are presented in Chapter 4, Section 4.2. On the contrary, although widely used, not only in the field of dark matter but also in industry and medicine for neutron detection, experimental data on the response of plastic scintillators to low energy nuclear recoils are scarce. Conceptual designs for future, large active neutron rejection systems for dark matter experiments featuring scintillators are under discussion [171], and will require improved knowledge of the low energy response, even when the main neutron detection mechanism is via radiative capture. In the case of polystyrene-based scintillators, little data exist for recoils below  $\sim 1$  MeV, which are produced, for example, by radioactivity neutrons.

This chapter will present a measurement of the energy dependent quenching factor for low energy neutron-induced nuclear recoils, characterising the plastic scintillators used in the ZEPLIN-III veto. In the context of the ZEPLIN-III experiment, the quenching factor was determined to accurately model the veto detector and its response to neutrons. The text and figures in this chapter will follow closely the work reported in Ref. [3] published by the author. In addition, more details of the analysis process as well as a study of systematic effects from the Monte Carlo simulation are presented.

## 6.1 Quenching in nuclear recoil interactions

The response of organic scintillators to particle interactions in terms of the dependence on material, incident particle type and incident particle energy were first discussed by Birks [136, 172]. In general, it is found that the response arising from nuclear recoils (such as when irradiated by neutrons) is significantly diminished in comparison to the light output obtained from electron recoils (such as when irradiated by  $\gamma$ -rays). At higher energies (MeV and above), the scintillation output is generally found to be proportional to the energy deposition but, at lower energies, a strong departure from proportionality has been observed for nuclear recoils. A thorough characterisation and understanding of such effects is essential for accurate low energy calibrations.

The scintillation light yield for a nuclear recoil of a given energy is quenched, *i.e.* reduced in comparison to the scintillation output observed from an electron recoil of the same energy. A significant contribution to this difference may be identified with the heat associated with the atom cascades generated by nuclear recoils as described by Lindhard [132]. A formalism in which the scintillation light yield of highly ionising particles depends not only on the energy of the particle, but also on its stopping power in specific materials, was developed by Birks [136], of which a detailed description is presented in Ref. [173]. The resulting relation may be written as:

$$\frac{dL}{dr} = \frac{S \frac{dE}{dr}}{1 + kB \frac{dE}{dr}}, \quad (6.1)$$

where  $dL/dr$  is the scintillation yield per unit path length  $r$ ,  $S$  is the absolute scintillation factor,  $BdE/dr$  is the density of excitation centres along the recoil ionisation track and  $k$  is a quenching factor. By finding the ratio between the light yield for electron recoils,  $L_e$ , and for ions,  $L_i$ , Eq. (6.1) may be rewritten in terms of the quenching factor for nuclear recoils,  $Q_i$ , in integrated form as:

$$Q_i = \frac{L_i(E)}{L_e(E)} = \frac{\int_0^E \frac{dE}{1+kB(\frac{dE}{dr})_i}}{\int_0^E \frac{dE}{1+kB(\frac{dE}{dr})_e}}. \quad (6.2)$$

From Eqs. 6.1 and 6.2 an energy dependence of the quenching factor is apparent. This is especially significant for the low energy region where the stopping power experiences greatest variation. The majority of the measurements obtained to-date for the quenching factor in plastic scintillators concentrate on neutrons and protons in the energy region above  $\sim 1$  MeV [174, 175, 176, 177, 178]. In recent years, the need for precise knowledge of neutron quenching factors for materials used in the direct search for dark matter has led to significant new measurements at low energies, often

making use of dedicated neutron scattering facilities [179, 180]. However, no recent measurements have been reported for plastic scintillators despite their incorporation into several low energy experiments.

## 6.2 Experimental setup

One of the 52 plastic scintillator modules of the ZEPLIN–III veto detector was used for data taking in the Boulby Underground Laboratory. For any details on the composition and shape of the scintillator material and properties in terms of average light output and attenuation see Chapter 5 (Section 5.1).

Energy spectra were recorded with the dedicated data acquisition system of the veto detector and waveform parameterised with the bespoke data reduction software ‘RaVen’. The trigger was provided by an external pulse generator at a constant frequency. Additionally, during the neutron source measurements, data were taken simultaneously with a multi-channel pulse height analyser (MAESTRO MCA), triggered by an internal discriminator.

To measure the response to nuclear recoils, the scintillator was exposed to neutrons from an  $^{241}\text{Am}$ -Be ( $\alpha, n$ ) source and, separately, to a  $^{252}\text{Cf}$  fission source. The plastic was shielded from  $\gamma$ -ray emission from the sources and the environment by enclosing it in a 20 cm thick castle composed of low-background Cu and Pb in equal parts with an additional 4 cm of lead on the roof. Neutron exposures were performed with the sources placed directly on the castle (~50 cm above the sealed scintillator). A schematic of the setup, as used in the simulation, is shown in Fig. 6.1.

Systematic uncertainties in the setup were explored extensively, which are presented in more detail in Section 6.5.3, from which it was found that variation in neutron source position had negligible effect.

Crucially,  $\gamma$ -ray attenuation and external electron-recoil contamination within the nuclear recoil data have been quantified using Monte Carlo simulations and dedicated measurements (see Section 6.3 for detailed discussion of simulations). In particular, the effect of varying the thickness of the lead component of the castle roof was examined.  $\gamma$ -ray emission spectra from the  $^{252}\text{Cf}$  and Am-Be sources (reconstructed from values given in the NuDat database [181]) have been studied separately. The actual  $\gamma$ -ray activities were  $21,000 \pm 2,100 \text{ } \gamma/\text{s}$  for the  $^{252}\text{Cf}$  source and  $6,300 \pm 400 \text{ } \gamma/\text{s}$  for the Am-Be source (the latter accounts only for the two highest energy  $\gamma$ -rays of 3.21 MeV and 4.44 MeV from de-excitation of  $^{12}\text{C}^*$  populated by the  $\text{Be}(\alpha, n)$  reaction). The simulations indicated that a single  $\gamma$ -ray from the Am-Be source may be transmitted through the shielding along with every 30,000 neutrons (of which  $\sim 600$  deposited energy in the scintillator bar) for the nominal lead thickness in the given configuration, while

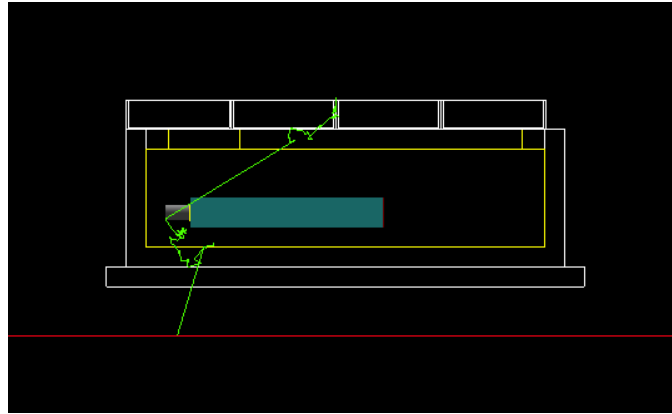


Figure 6.1: Side view of the experimental setup for the quenching factor measurement of a plastic scintillator as used in the Monte Carlo simulations. The scintillator is shown in blue, the copper shield in yellow and the lead shielding in white. A potential track of a neutron fired from the defined source position is drawn in green.

no  $\gamma$ -rays from the  $^{252}\text{Cf}$  source exposure should be observed. Thus, the results showed that the  $\gamma$ -ray fluxes from the sources made no significant contribution to the neutron exposure data. To confirm this conclusion, an extended exposure of the scintillator to a 11-kBq  $^{60}\text{Co}$   $\gamma$ -ray source (1.17 and 1.33 MeV  $\gamma$ -rays), placed externally on the upper surface of the enclosure, was performed. No measurable increase in event rate over background was observed. Given that contributions from the  $\gamma$ -rays coming from the sources themselves were negligible in the neutron measurements, most  $\gamma$ -rays detected during the neutron exposure were generated internally (inelastic scattering and radiative neutron capture). Non source-related backgrounds, arising, for example, from low level activity of shielding components and the plastic scintillator itself, were measurable, but were not significant above a threshold of 2 phe.

### 6.3 Simulations

The methodology used to extract the quenching factor was first applied to liquid argon scintillation by the WArP group [182]; other examples followed [144, 153, 145]. Experimental data were compared to a comprehensive Monte Carlo simulation which included a detailed description of the experiment. The relationship between real energy deposition and resulting scintillation production, *i.e.* the energy-dependent quenching factor, was included as a parameter in the simulation. An iterative process was used to optimise the quenching factor, minimising on  $\chi^2$  in the comparison between data and simulated energy spectra. The simulations have been performed with the

GEANT4 toolkit (version 9.2, with neutron cross-sections from ENDF/B-VI [183]) using standard neutron spectra for the two sources (Am-Be ISO 8529-1 [184],  $^{252}\text{Cf}$  fission spectrum from SOURCES-4C [185]). Emitted neutrons and their secondaries were propagated including all relevant nuclear and electromagnetic physical processes; a set of optical processes described the generation and detection of scintillation light from nuclear and electron recoil interactions in the scintillator. These photons were tracked to the photocathode of the PMT including relevant optical effects (reflection, refraction, attenuation) at which point the production of photoelectrons was simulated. Appropriate random fluctuations were included to model the production of scintillation photons and the production of photoelectrons from the PMT photocathode.

It should be noted that for a full description of neutron scattering in hydrogenous materials the standard GEANT4 elastic scattering process must be supplemented with a model (`G4NeutronHPTermalScattering`) to describe the energy region below 4 eV for the correct treatment of thermal neutron scattering from chemically-bound atoms. In these molecules several temperature-dependent vibrational modes are possible, which alter the scattering cross-section [186]. This is of particular relevance to this study and radiative capture on hydrogen is enhanced by  $\sim 20\%$  over the standard model.

### 6.3.1 Uncertainties in the Monte Carlo simulation

The most important factor shaping the nuclear recoil spectrum is the correct implementation of the angular differential cross-sections for elastic neutron scattering. The relevant cross sections for the scattering of neutrons from protons are well known, and their correct implementation in the present Monte Carlo simulation was confirmed by using a dedicated testing simulation setup. Its simplified geometry consisted of a cube made from hydrogen (or carbon for carbon recoil tests) placed in vacuum. A neutron beam of different energies was focused centrical on to the material. Single-elastic scatters were detected and their nuclear recoil energy depositions as well as the position of interaction recorded and the opening angle of the scattered neutrons determined. Subsequently, these angles, converted into the centre of mass frame, can then be compared to plots retrieved from the ENDF database [187] (see Fig. 6.2, left). The angular distributions coming from the GEANT4 output for different neutron energies are plotted on the right hand side of Fig. 6.3.

The angular distributions for elastic scattering on hydrogen are, as expected from interaction of particles with similar mass, flat over a whole range of energies shown in the plots from the database and confirmed in Fig. 6.3 for the GEANT4 simulation. Due to the more complex nature of the angular distributions for neutron scattering on carbon (see Fig. 6.2, right), data from the CSISRS database [188] were retrieved

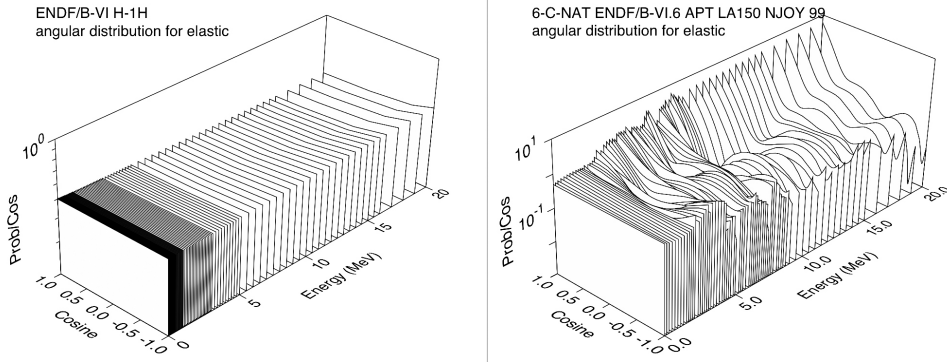


Figure 6.2: Angle differential cross-section plots for elastic neutron scattering on hydrogen (left) and carbon (right) from the ENDF database [187].

for direct comparison of the differential angle cross-sections (green data points on the right hand side of Fig. 6.4). These have been freely scaled in the y-direction to give the best visible agreement with the centre of mass scattering angles determined from the GEANT4 output. For energies of 2 MeV and above good agreement is given. Below this neutron energy, the ENDF plot does not show any visible structure in contrast to the observed spectra and experimental data are sparse. The only available data from the CSISRS database for 1 MeV neutrons on carbon are shown at the top right of Fig. 6.4. Here, both angular distributions are plotted with respect to the laboratory frame and again good agreement is achieved. The possible impact of further uncertainties, due to the scarcity of low-energy experimental data, on the final results of this work was explored in detail, and was shown to also be insignificant. Even in an extreme case of assuming the carbon cross-sections were reduced to zero, the key results produced below remained essentially unchanged. This is in large part due to the relatively small role of scattering from carbon nuclei in the present experiment.

Finally, to ensure that the output of recoil energies generated by GEANT4, given the correct angular distributions, were calculated correctly, the recoil angles in the laboratory frame were independently determined from the recorded momentum directions of the recoiling nuclei. Using a simple 2-body kinematic equation, the nuclear recoil energies in the laboratory frame was then calculated from the energy of the scattered neutron, which, given the correct treatment, are in agreement with the direct output from GEANT4. These comparisons are plotted for different energies on the left hand side of Figs. 6.3 and 6.4 for H and C, respectively.

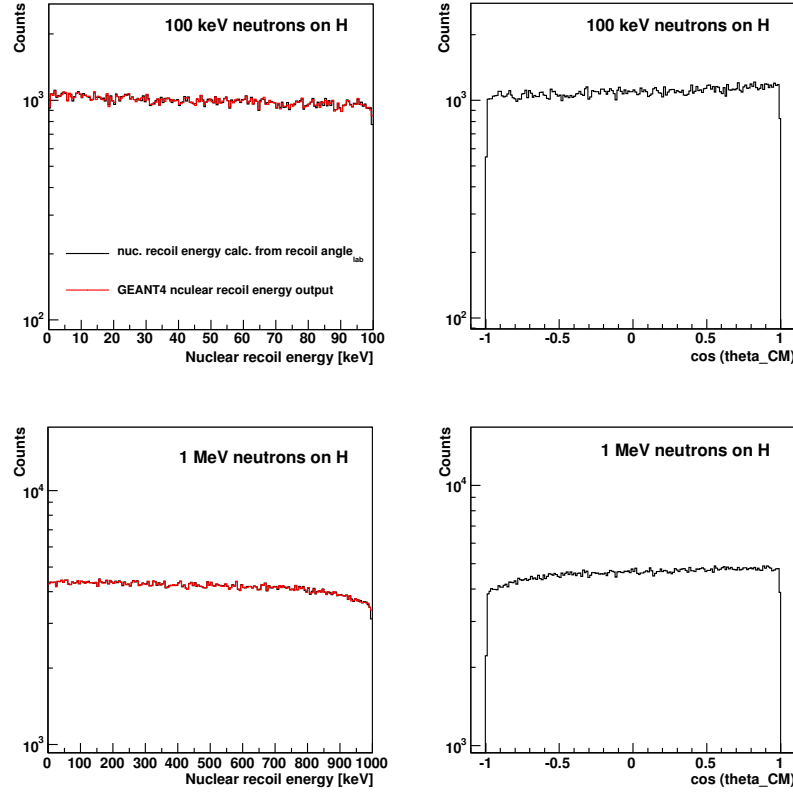


Figure 6.3: Left: Nuclear recoil energies in the laboratory frame calculated from the recoil angles and the neutron energy (black) are shown in comparison to the direct nuclear recoil energy output of GEANT4 (red). Right: Angular distributions of elastic neutron scattering on hydrogen from the GEANT4 output for different primary neutron energies.

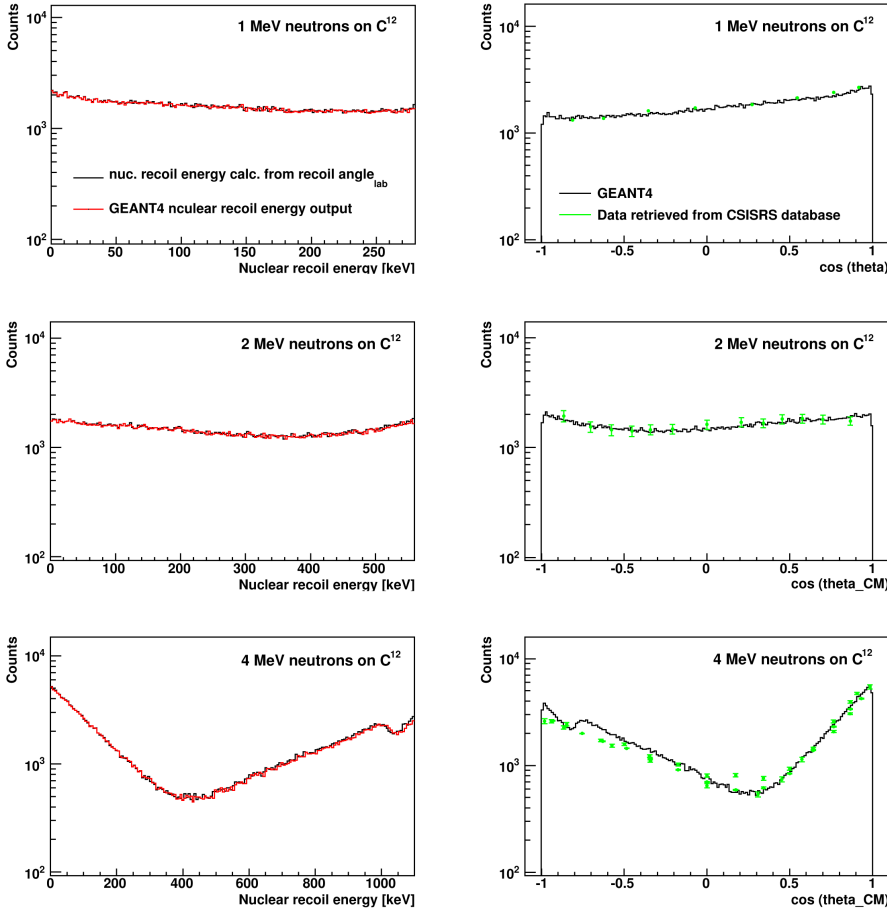


Figure 6.4: Left: Nuclear recoil energies in the laboratory frame calculated from the recoil angles and the neutron energy (black) are shown in comparison to the direct nuclear recoil energy output of GEANT4 (red). Right: Angular distributions of elastic neutron scattering on carbon from the GEANT4 output (black) are plotted in comparison to data from the CSIRS database (green) for given neutron energies.

## 6.4 $\gamma$ -ray calibrations

By definition, the response of the plastic scintillator to  $\gamma$ -rays is unquenched, allowing standard  $\gamma$ -ray sources to be used to determine the overall gain of the system. Moreover, it is expected that the GEANT4 simulations should provide an excellent match to the  $\gamma$ -ray calibration data, validating most processes included in the physics model and the accuracy of the geometry implemented. The PMT gain was set such that both SPE peaks and Compton edge features could be resolved in all spectra, allowing presentation of the data in terms of absolute numbers of photoelectrons.

With the roof of the shielding castle open, calibration measurements with a  $^{137}\text{Cs}$   $\gamma$ -ray source (4.7 kBq) were performed. Figure 6.5 shows the acquired spectrum in comparison to Monte Carlo simulations. Data were acquired with the CAEN acquisition system (solid black spectra) with a trigger provided by an external pulse generator operating at constant frequency. Signal pulses were then extracted from the recorded waveforms. The result of a GEANT4 simulation of this exposure is shown by the dashed red line; excellent agreement across the full energy range is demonstrated. The scintillator module used had an attenuation length of  $\sim$ 80 cm and the photoelectron yield with the calibration source above the centre of the plastic (48.7 cm from the photocathode face) was measured to be  $\sim$ 44 phe/MeV.

The simulations did not include spurious effects such as dark emission from the photocathode, after-pulsing, or  $\beta^-$  radiation from  $^{40}\text{K}$  contamination in the glass PMT envelope. Each of these effects are known to contribute at the single to few photoelectron level with significant rate [1, 4] as shown in the previous chapter, Section 5.2, in the cumulative background signal rate plot of the veto detector (Fig. 5.10). Consequently, a 5 photoelectron analysis threshold was imposed on the  $\gamma$ -ray calibration data, and therefore on the neutron scattering analysis and results.

## 6.5 Neutron exposures

### 6.5.1 Nuclear recoils

Data were accrued for a live time of 600 s from separate exposures to the Am-Be source ( $5,500 \pm 300$  neutrons/s) and the  $^{252}\text{Cf}$  source ( $3,400 \pm 170$  neutrons/s). Placing the sources externally to the copper-lead enclosure attenuated the  $\gamma$ -ray emission from the sources to a negligible level. The impact of the enclosure on the neutron fluxes is illustrated in Figs. 6.6 and 6.7 for the two sources. The figures show Monte Carlo simulations of the neutron emission spectra, the energy spectra as they enter the scintillator (both referring to the y-axis on the left), and the resulting nuclear recoil energy depositions in the polystyrene (y-axis on the right). The spectra at the

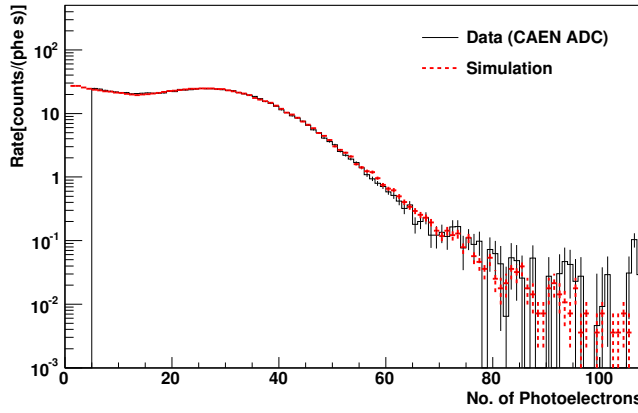


Figure 6.5: Energy spectrum acquired from a  $^{137}\text{Cs}$   $\gamma$ -ray source exposure. The data acquired with the CAEN acquisition (solid black spectrum) with a threshold of 5 phe is shown in comparison to the simulation data (red dashed spectrum).

scintillator interface include single neutrons being recorded multiple times as they are scattered out of the scintillator and re-enter again after interacting with the shielding. The recorded energy depositions are the total integrated signals from each individual neutron-induced recoil event. The shielding attenuated significantly the neutron flux, and scattering reduced the energies of surviving particles. Since this is a large effect, it was of importance to quantify how the uncertainty in the lead thickness affected the neutron spectrum at the scintillator interface. The impact of geometrical changes within the uncertainties of the experimental setup were found to be statistically insignificant (see Section 6.5.3).

Furthermore, the impact of thresholds in the simulated neutron source spectra (50 keV in both instances) has been examined. Reasonable extrapolations down to 0 keV did not change the recoil spectrum above threshold much and the ensuing quenching factor analysis was affected very little.

### 6.5.2 Quenching factor

Where data do not exist for quenching factors at low energies, it is customary to assume an energy-independent quenching as determined at higher energies. Various constant quenching factors have been considered and then compared to the experimental data. Figures 6.8 and 6.9 show the data from the Am-Be and  $^{252}\text{Cf}$  source exposures in comparison to simulations which assumed an energy independent quenching factor, with  $Q_i = 0.1$  yielding, in both cases, the best fit to the measured data. For such a

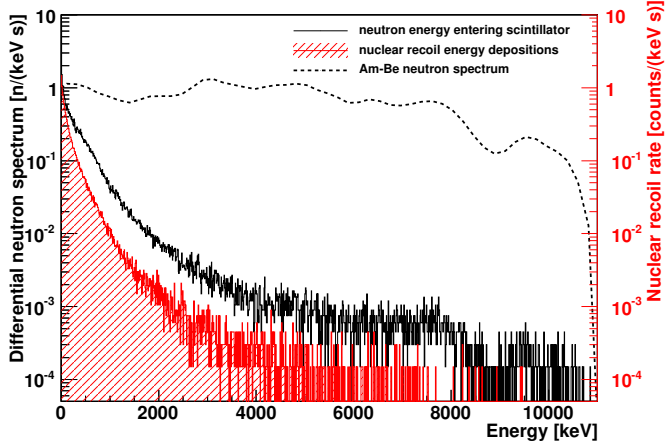


Figure 6.6: Monte Carlo simulated energy depositions in the scintillator from neutron-induced nuclear recoils coming from an Am-Be source (red hatched spectrum – referring to the scale on the right). The y-axis on the left refers to the neutron flux from the source (black dashed spectrum) and the differential neutron spectrum when entering the scintillator bar (black solid spectrum).

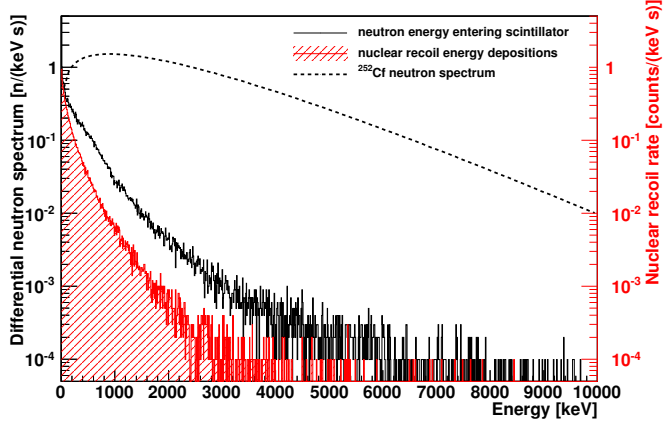


Figure 6.7: Monte Carlo simulated energy depositions in the scintillator from neutron-induced nuclear recoils coming from an  $^{252}\text{Cf}$  source (red hatched spectrum – referring to the right hand scale). The left hand scale refers to the original neutron spectrum (black dashed spectrum) in comparison with the differential rate of neutrons entering the scintillator bar (black solid spectrum).

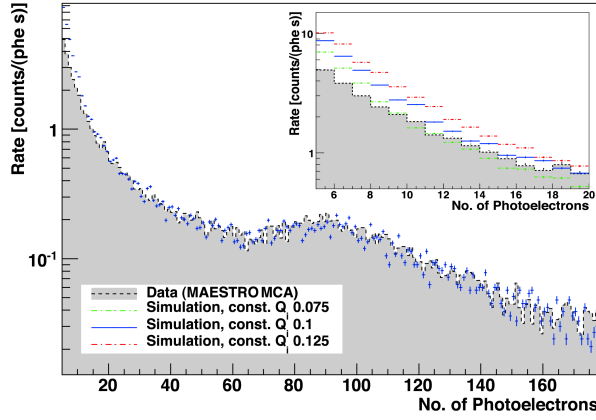


Figure 6.8: Background-corrected energy spectrum originating from irradiation with an Am-Be source (grey shaded area) in comparison with simulations using the quenching factor  $Q_i$  as a constant parameter for the whole energy range. The best agreement with the real data is met by the curve featuring  $Q_i = 0.1$  (blue solid spectrum). The peak at  $\sim 90$  phe represents the 2.2 MeV radiative capture  $\gamma$ -rays from hydrogen. The inset shows the impact of different constant quenching factors at low photoelectron values. A marked discrepancy between simulation and data suggests that an energy-dependent quenching factor may provide a better physical description for low recoil energies.

value, the nuclear recoil spectrum was quenched sufficiently such that the (un-quenched) peak arising from the 2.218 MeV  $\gamma$ -ray emission following radiative capture of neutrons on hydrogen could be resolved. This feature, appearing at  $\sim 90$  phe (with  $\sigma \simeq 30$  phe) was, thus, used to normalise the energy scales of simulated to observed spectra and extract a quenching factor for the nuclear recoils. Both figures show that by adopting energy independent quenching factors, a discrepancy occurs below  $\sim 35$  phe. Above this value the goodness-of-fit was determined by statistical fluctuations only in both cases. The data shown in Figs. 6.8 and 6.9 were recorded with the MAESTRO MCA for the reason of better statistics at the position of the hydrogen capture peak. Subsequent analysis was mainly performed using data acquired with the CAEN system to avoid bias from threshold dependent trigger setups. Aside from counting statistics, the two recordings did not differ from each other at higher energies.

At very low photoelectron values ( $\lesssim 20$ ) greater divergence was observed between the Monte Carlo and the measured data (see insets in Figs. 6.8 and 6.9) indicating an energy dependent behaviour of the quenching factor at low recoil energies. The methodology used to derive this energy dependent behaviour is as follows: a hypothetical  $Q_i(E)$  function was composed from 14 values of recoil energy (125, 150, 175, 200, 225, 250,

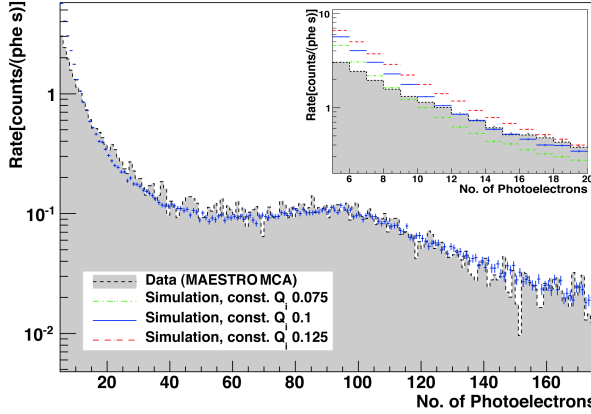


Figure 6.9: Background-corrected energy spectrum originating from irradiation with a  $^{252}\text{Cf}$  source (grey shaded area) in comparison with simulations using the quenching factor  $Q_i$  as a constant parameter for the whole energy range and a close up of the very low energy part of the spectrum as an inset at the top right.

300, 350, 400, 450, 550, 650, 750, 850 keV) and interpolated linearly between these points; a constant behaviour was assumed below and above this range. Above 1 MeV, low statistics and the decreasing gradient of the quenching factor precluded more in-depth analysis. For each combination of  $Q_i(E)$  parameters (from a limited grid, guided to cover reasonable ranges), the full simulation was performed and  $\chi^2$  calculated for the resulting match to the data. Below 5 phe, spontaneous SPE emission and other effects mentioned previously can make a significant contribution to the experimental data, and therefore this region was excluded from the minimisation. The  $Q_i(E)$  parameters were modified for each iteration until no significant improvement in  $\chi^2$  could be obtained.

Figure 6.10 shows the resulting energy-dependent quenching factor from minimising the overall  $\chi^2$  for both datasets. Here the 5 phe analysis threshold allowed measurements down to a nuclear recoil energy of approximately 125 keV. In the sub-threshold region below 5 phe an even stronger decrease in the quenching factor with energy would be inferred from uncorrected data. The 68% confidence intervals shown are determined by the envelope of regions built up from quenching factor model curves which fulfil the criterion of  $\chi^2_{model} < \chi^2_{min} + Q_y$ , where  $Q_y = 15.89$  for 14 free parameters [189]. These were produced by changing each interpolation point randomly, scanning a reasonable area of the parameter space. Subsequently, new model histograms were produced by multiplying these quenching factor test curves with the nuclear recoil energy depositions recorded from simulations, the attenuated mean light

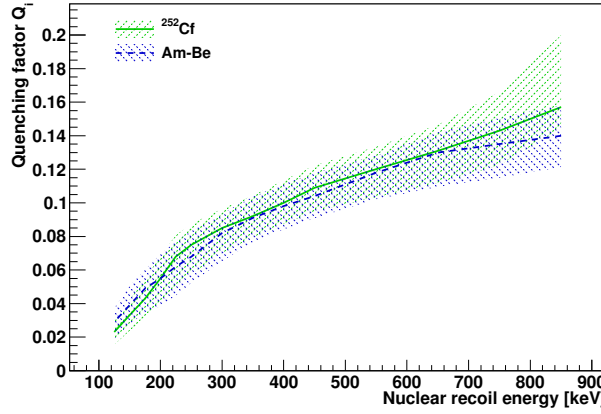


Figure 6.10: The nuclear recoil quenching factor in a polystyrene plastic scintillator UPS-923A as a function of recoil energy deposition extracted by mean of  $\chi^2$  minimisation from comparison of simulations to data from a  $^{252}\text{Cf}$  (solid green) and an Am-Be (dashed blue) exposure, respectively. The hatched areas represent the 68% CL bands.

yield and the quantum efficiency of the PMT. In the following, appropriate smearing of the calculated energy deposition in photoelectrons was applied and the unchanged contribution from electron recoil events added. In addition to the selection cut of using a  $\chi^2$  test, the model curves had to pass a so-called ‘Run test’, which analyses the sequence of positive or negative residuals from comparing a model (simulation) to experimental data points [190]. This is a useful method to asses the goodness of fit, for example, if statistics are low, and thus error bars are large, resulting in an underestimated  $\chi^2$  value. The average number of expected runs,  $\langle r \rangle$ , for a given number of bins,  $N$ , equals  $1 + \frac{2N_A N_B}{N}$ , where  $N_A$  and  $N_B$  are the number of positive and negative residuals, respectively.

Figure 6.11 compares the  $^{252}\text{Cf}$  data (black hatched histogram) with the best fit of the energy-dependent (red solid) and the best fit of the energy-independent simulation (blue dashed), respectively. The inset provides the same comparison but for the Am-Be study.

### 6.5.3 Impact of systematic errors

In addition to the previously discussed uncertainties in the Monte Carlo in terms of correct treatment of the angular differential cross-section for elastic neutron scattering, geometrical changes within the uncertainties of the experimental setup as well as the

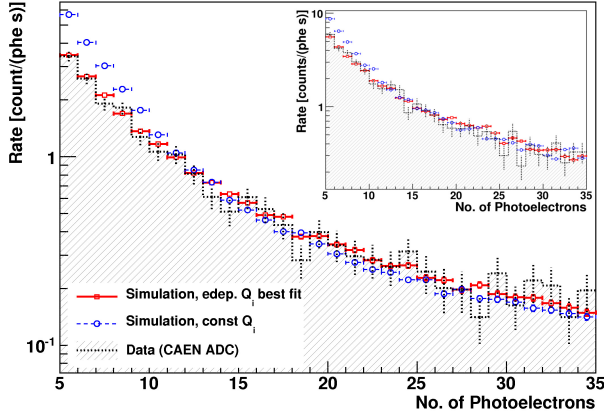


Figure 6.11: Simulations using an energy-dependent value for  $Q_i(E)$  in comparison with background corrected data acquired with the CAEN ADC (black hatched spectrum) from irradiation of the scintillator with a  $^{252}\text{Cf}$  and Am-Be source (inset), respectively. The best fit using  $\chi^2$  minimisation is shown by the red solid histogram ( $\square$ ). For comparison, the blue dot-dash spectrum ( $\circ$ ) shows the use of a constant quenching factor (from best fit to data).

choice of the neutron input spectrum may affect the final result of an energy dependent quenching factor. Firstly, the impact of varying the thickness of the lead shielding,  $t_{\text{lead}}$ , on the roof of the box by  $\pm 1$  cm on the neutron energies entering the scintillator, and thus on the final spectrum of recorded energy depositions (see Fig. 6.12), was studied. The figure only shows the spectra produced by using a  $^{252}\text{Cf}$  source as a representative example; very similar results were obtained when using an Am-Be source. Changes from varying the shielding composition are noticeable in both plots, but uncertainties are clearly covered by the given error bars as the reduced  $\chi^2$  values do not exceed changes greater than 1.

Secondly, variation in the neutron source position,  $pos_{\text{source}}$ , on top of the shielding box were considered. Changes of up to  $\pm 3$  cm did not show any significant impact on the final result. Figure 6.13 shows the simulated final energy deposition spectra arising from irradiation with a  $^{252}\text{Cf}$  source placed at different positions.

Thirdly and finally, uncertainties in the neutron input spectrum of the Monte Carlo simulation were studied. It is known that there are uncertainties connected with the neutron spectrum of an Am-Be source due to source grain size as well as the degree of uniformity of the Am-Be mixture itself. Additionally to the neutron source spectrum used for this work (Am-Be ISO 8529-1 [184]), the spectrum given by Marsh *et al.* [191] has been studied and plotted in Fig. 6.14. The effects on the nuclear recoils, and thus

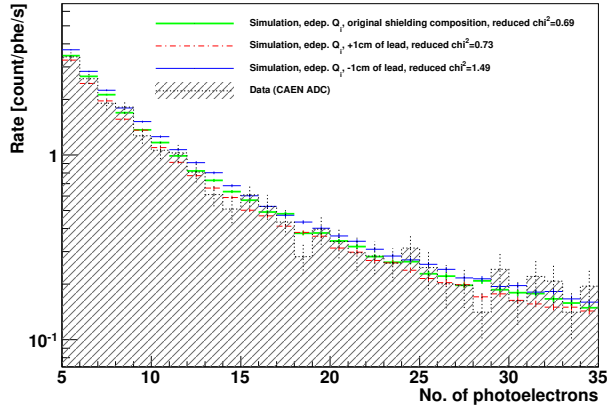


Figure 6.12: Comparison of simulated energy spectra with varying shielding thickness (solid green =  $t_{lead}$ , dashed-dotted red =  $t_{lead} + 1$  cm, solid blue =  $t_{lead} - 1$  cm) to experimental data (hatched, black dotted spectrum) from irradiation with a  $^{252}\text{Cf}$  source.

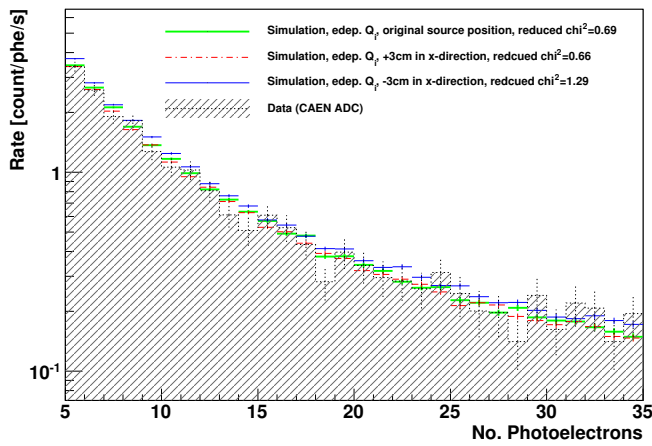


Figure 6.13: Comparison of simulated energy spectra of varying source position (solid green =  $pos_{source}$ , dashed-dotted red =  $pos_{source} + 3$  cm, solid blue =  $pos_{source} - 3$  cm) to experimental data (hatched, black dotted spectrum) from irradiation with a  $^{252}\text{Cf}$  source.

on the final energy spectrum (see Fig. 6.15) were marginal.

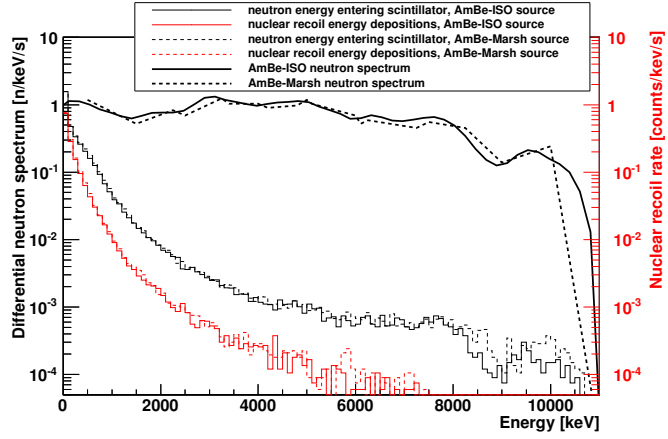


Figure 6.14: Right hand scale (red): Simulated energy depositions in the scintillator from neutron induced nuclear recoils from two different Am-Be neutron source input spectra (solid - ISO-8529-1, dashed - Marsh). Left hand scale (black): Neutron fluxes coming directly from the sources (thick solid - ISO-8529-1, thick dashed - Marsh) and neutron energies when entering the scintillator bar (thin solid - ISO-8529-1, thin dashed - Marsh).

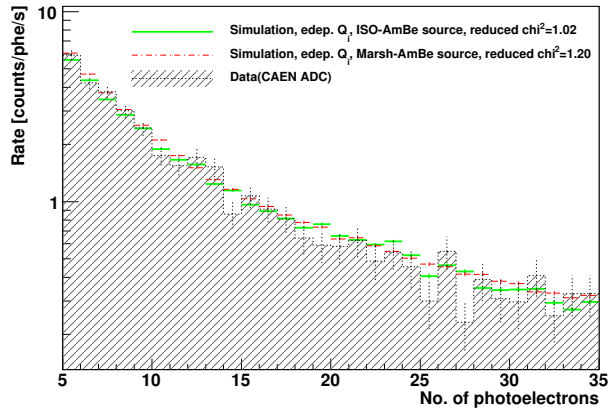


Figure 6.15: Simulated energy spectra using tow different Am-Be neutron source spectra (solid green - ISO-8529-1, dashed-dotted red - Marsh) are shown in comparison to the experimental data (hatched black dotted spectrum).

### 6.5.4 Birks factor, $kB$

Following the discussion in Ref. [173], the absolute value of the quenching factor for specific materials is expected to depend only on the so-called ‘Birks factor’,  $kB$ , independently of the particle type. Consequently, the relative scintillation yield curve may be estimated by incorporating the appropriate energy-dependent stopping power for the specific particle species. The  $kB$  factor is then determined by fitting Eq. (6.2) to experimental data.

At higher energies, contributions to the observed energy depositions came predominately from the scattering of protons in the plastic scintillator. For lower energy depositions, it was found that carbon nuclei (99%  $^{12}\text{C}$ ) contribute over 30% of the overall nuclear recoil energy depositions. As shown in Fig. 6.16, this relative fraction rises almost linearly in the lower energy region reaching  $\sim 50\%$  below 20 keV.

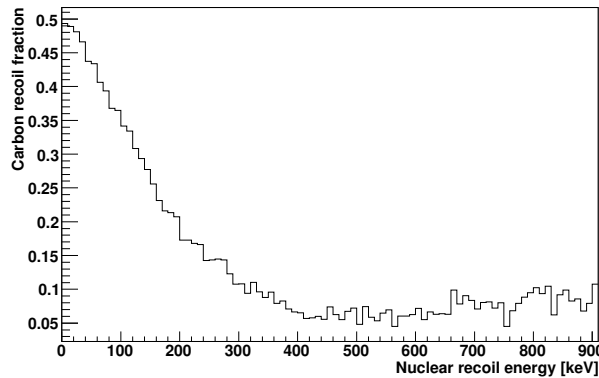


Figure 6.16: Fraction of nuclear recoil energy depositions coming from carbon nuclei relative to the proton recoil contributions in the plastic scintillator averaged from exposures to both Am-Be and  $^{252}\text{Cf}$  neutron sources.

The energy-dependent quenching factors derived here from the two neutron sources are in good agreement with each other and may therefore be combined. This is significant, since the neutron spectrum from an Am-Be source is somewhat uncertain below a few hundred keV as mentioned earlier, although this is especially so for stronger sources than the one used here [191]. The  $^{252}\text{Cf}$  fission spectrum, which is known more precisely, yielded very similar results. A combination of the two results, following the prescription for asymmetric errors in Ref. [192], is presented in Fig. 6.17 as the black solid line, with the uncertainty represented by the shaded band. The quenching factor is seen to have a significant energy dependence, increasing in gradient towards low energies. In general, the observed dependence is reasonably similar to that expected

from the Birks formalism above about 300 keV, but it departs from the expected behaviour at lower energies. Fitting the present quenching factor values in the range of 300 keV to 850 keV resulted in a  $kB$  factor of  $0.014 \pm 0.002 \text{ g MeV}^{-1}\text{cm}^{-2}$ . The error given is statistical only. This is also shown in Fig. 6.17, with the contributions from protons, from carbon ions and the sum shown separately. Stopping powers for protons and carbon have been taken from NIST [193] and the SRIM Stopping Range Tables [194], respectively.

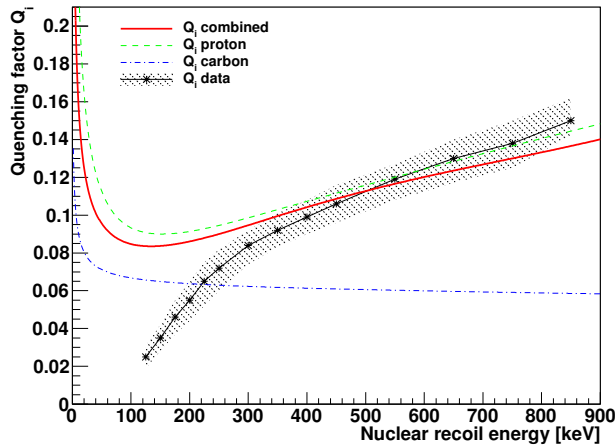


Figure 6.17: A fit of semi-empirical calculations of Birks for combined proton and carbon stopping powers from varying the  $kB$  factor (solid red) to the measured quenching factors (black with hatched error band) above 300 keV nuclear recoil energy yields:  $kB = 0.0135 \text{ g MeV}^{-1}\text{cm}^{-2}$ . Additionally, curves assuming scattering off protons or off carbon nuclei only are also shown. Below this energy a clear divergence of the measurement from the Birks description can be observed.

The  $kB$  factor resulting from fitting the here presented data to the Birks formalism above 300 keV may be compared with a previous value of  $kB = 0.009 \text{ g MeV}^{-1}\text{cm}^{-2}$  reported for  $\alpha$ -particle interactions in polystyrene-based plastic scintillator ([173] and references therein). The level of agreement is good, considering the choice of data acquisition alone can produce discrepancies of a factor of two [173]. The current results exhibit a slightly steeper dependence than expected from the Birks formalism, but interestingly, the same feature is apparent in all previous measurements for organic scintillators presented in the above reference. Above about 300 keV, the present data broadly support the semi-empirical description of Birks. Below that nuclear recoil energy, a clear deviation from Birks is evident in Fig. 6.17, indicating that the fraction of scintillation generated by low energy nuclear recoils appears to decrease even more

rapidly. As mentioned above, the analysis reported here has been limited to above 5 phe, to avoid complications that might be introduced by single photoelectron level processes not included in the simulations. However, not only would inclusion of these effects increase the discrepancy further, but examination of the 3–5 phe region indicated the trend continuing, with an even stronger dependence. A physical mechanism responsible for this behaviour is unclear. It should be emphasised that none of the uncertainties studied here that could arise for this specific type of analysis method, of comparing Monte Carlo simulations to experimental data, affected the validity of the final energy dependent quenching factor result departing from Birks law at low energies.

## Chapter 7

# Backgrounds in the ZEPLIN-III Experiment

Accurate measurements and understanding of backgrounds in any rare event search detector are of utmost importance for the validation and confidence in the results. Various techniques have been developed to discriminate between electron and nuclear recoil events, such as the ratio of ionisation and scintillation signals produced in a dual-phase detection chamber. Although the design of dark matter experiments is driven by the requirement of negligible levels in neutron background, sensitivities of rare event searches to date are very often limited by the dominant electron recoil background. Leakage of electron recoil events into the signal region, caused, for example, by multiple scattering  $\gamma$ -rays with one vertex occurring in a region which yields no ionisation, or  $\beta$ -induced signals, originating from  $^{40}\text{K}$  contamination internally to the PMT, is a serious threat.

This chapter outlines the origin of the expected background, categorised as external and internal sources, complemented with a comparison of the absolute measured electron recoil background in the ZEPLIN-III detector to that of a Monte Carlo simulation. Subsequently, following the verification of component contamination levels, the expected nuclear recoil background was estimated from simulations. The majority of the work presented here is based on the publication of backgrounds in the ZEPLIN-III experiment [4].

### 7.1 Background sources

The dominant cause of detected low-energy electron recoil events is interaction of  $\gamma$ -rays and  $\beta$ -particles arising from natural radioactivity, dominated by primordial U, Th and

$^{40}\text{K}$ . Similarly, the primary production processes for neutrons, making up most of the nuclear recoil background, are spontaneous fission (predominately of  $^{238}\text{U}$ ) and  $(\alpha,\text{n})$  reactions arising from U and Th chain decays interacting with their local environment.

The levels of contamination within the individual components of the ZEPLIN-III experiment were measured with  $\gamma$ -ray spectroscopy with a high-purity germanium detector and complemented with ICP-MS measurements for several materials, in a similar way to the measurements of the veto construction materials described earlier in Chapter 5. The HPGe measurements were conducted at the Boulby low background counting facility using an ORTEC GEM detector with a 2-kg crystal, reaching  $\sim 0.5$  ppb sensitivity levels for U and Th. Additionally, available data have been taken from the UKDMC database [195].

### 7.1.1 External background sources

#### Cosmic-rays and muon-induced neutrons

Cosmic-rays entering the Earth's atmosphere collide with molecules and produce a cascade of lighter particles, which subsequently decay into muons. High energy cosmic-ray muons produce neutrons through interaction with matter. Unlike neutrons arising from radioactive decay with energies limited to a few MeV, these muon-induced neutrons can reach energies of several GeV. Consequently, while radioactivity neutrons may be effectively controlled by appropriate shielding constructions and selection of radio-pure building materials, removing cosmic-ray induced neutrons is more difficult. One effective solution is to go deep underground, where the muon flux is reduced by several orders of magnitude. Figure 7.1 shows the muon intensity as a function of depth for some of the largest underground facilities from all over the world.

The rock overburden of the Boulby Underground Laboratory reduces the cosmic-ray muon flux by  $\sim 6$  orders of magnitude to  $(3.75 \pm 0.09) \times 10^{-8}$  muons/s/cm<sup>2</sup> [5]. The production rate of muon-induced neutrons in the ZEPLIN-III experiment will be discussed in Chapter 9. Neutrons from this source did not have a significant impact on the nuclear recoil background of the ZEPLIN-III experiment, due to the given sensitivity of the detector and the effectiveness of the veto in rejecting muon events. A rate of  $\sim 0.3$  events/year is to be expected in the signal region. This estimate was based on simulation performed for the ZEPLIN-II detector [197], however analysis of simulation data generated with the ZEPLIN-III setup confirmed the level of this expectation. From a three year simulated live-time, no single-elastic nuclear recoil scatter depositing 5–50 keV<sub>nr</sub> in the fiducial xenon volume was observed; however, one hit depositing the correct energy was found to be situated just outside the fiducial volume.

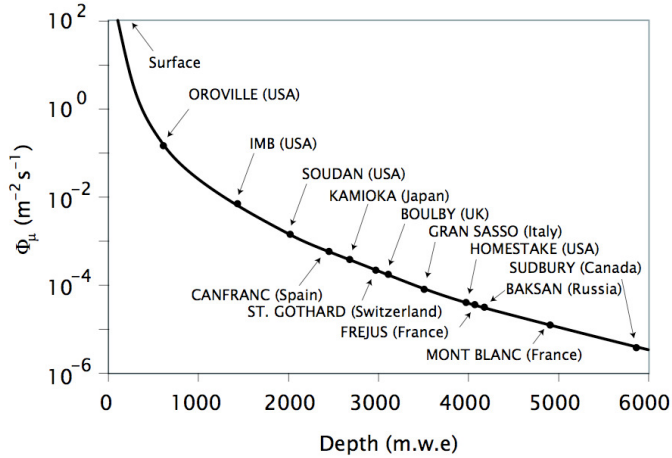


Figure 7.1: Muon intensity as a function of water equivalent depth. The muon flux for some of the largest underground facilities are indicated [196].

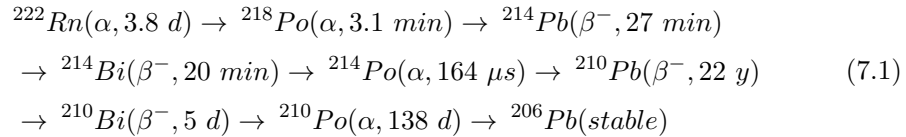
Despite the negligible impact for the ZEPLIN-III experiment, muon-induced backgrounds may become a dominant contributor to the nuclear recoil background expectations in future large scale detection systems. Interest in this field of research is evidenced by the very recent publication studying the impact of the muon-induced background in the EDELWEISS-II dark matter search and calculating a projection for the forthcoming EDELWEISS-III experiment [198]. A similar conclusion as for the ZEPLIN-III detector was reached for the EDELWEISS-II instrument, whereby muon-induced background expectations of  $<0.72$  events in the WIMP search region are only a very small contributor in comparison to other backgrounds; 5 events have been observed in the signal acceptance region in their WIMP search. Studies for the EDELWEISS-III instrument with a projected 6-months exposure of 3000 kg·day showed the possibility of background free data taking from an extrapolated expectation of  $0.6^{+0.7}_{-0.6}$  irreducible background events (90% CL). In the tonne-scale EURECA experiment a more significant contribution from muon-induced background is expected.

### Environmental background

The environmental background combines all sources outside the experimental detector setup, including the laboratory itself and more importantly the surrounding rock. Radioactive trace contamination in the rock would contribute very significantly to the neutron radiation budget of an underground experiment if no appropriate shielding construction was in place.

Experiments with a freely exposed 2-kg Ge detector in the open cavern resulted in measurements of  $67 \pm 6$  ppb U and  $127 \pm 10$  ppb of Th (secular equilibrium assumed) to be contained within the NaCl (Halite) rock of the Boulby mine [199]. Adequate shielding, in the case of ZEPLIN-III with a 20 cm thick lead castle enclosing the detector, ensures mitigation of the  $\gamma$ -ray background from this source to insignificant levels in the WIMP target (attenuation factor of  $\sim 10^5$  [200]). On the other hand, propagation of laboratory rock neutrons into the target volume needs to be carefully assessed. Despite a high overall attenuation factor of  $\sim 10^5$  through the shielding setup, any gaps for cabling or pipework might alter the expected nuclear recoil background. Hence, CPU intensive Monte Carlo simulations with an implemented detailed CAD solid model were performed. This work is presented separately in Section 7.2.

Another environmental source affecting the ZEPLIN-III experiment was air-borne radon and its metallic progeny plated on the inner walls of the lead castle.  $^{222}\text{Rn}$  is part of the uranium-radium decay chain. It bottlenecks at  $^{210}\text{Pb}$  which has a half life of  $T_{1/2} = 22.3$  years (see decay chain sequence 7.1 [181]).



Measurements with a commercial monitor inside the empty lead castle resulted in an activity of  $2.4 \text{ Bq/m}^3$ , which corresponds to an electron recoil rate observed in ZEPLIN-III of 0.03 dru.

### 7.1.2 Internal background sources

#### Photomultiplier tubes

Backgrounds originating internally from the PMTs are one of the most challenging and most intense sources due to their proximity to the target volume. The PMT array used in the FSR of ZEPLIN-III dominated the background of the experiment by a significant factor for both electron and nuclear recoils. Relatively high contamination levels of U, Th and K in the original phototubes (2-inch ETEL D730Q) resulted in a radioactivity budget of 14.5 dru electron recoil background recorded in the WIMP target of ZEPLIN-III. Therefore, a new low-background array was designed to exactly fit into the slots of the FSR PMTs to reduce and control radioactive contaminations in the SSR. The new phototube (D766Q), developed by ETEL in collaboration with the ZEPLIN-III project, achieved radioactivity levels as low as 35 mBq for  $\gamma$ -rays. With

a value of 0.4 dru in the liquid xenon target, a 40-fold improvement over the previous array was accomplished. The nuclear recoil background was reduced by a factor of 50 in comparison to the FSR PMTs, with each unit emitting just over 2 neutrons per year.

Furthermore, backgrounds that can arise from internal  $\beta$ -activity need to be carefully considered. Similar to the veto PMTs (discussed in Section 5.2.2),  $\beta$ -particles from the  $^{40}\text{K}$  generator induce, directly by transmission or via bremsstrahlung, additional electron recoil background in the xenon target. In the case of a dark matter detector these additional signals can lead to problematic event populations diminishing the discrimination capability of a dual-phase TPC. A more thorough discussion of these rare types of electron recoil events will be given in Section 7.3.1.

### Veto detector

Primary consideration, when designing the veto detector, was to minimise additional contributions to the radiation budget of ZEPLIN–III, whilst achieving high rejection efficiencies of neutron events that might have otherwise incorrectly been identified as a WIMP signal, *i.e.* the advantages of event identifications must outweigh the added background. Contamination levels and signal rates within the veto detector have already been discussed in Section 5.1.2 and 5.2.2, respectively.

The PMTs, the cabling and the electronics of the veto were located externally and as far as possible away from the sensitive target volume. As such, the hydrocarbon shielding mitigated neutrons successfully. Also, the contributions to the electron recoil background in the WIMP target were negligible. On the contrary, despite the very low radioactivity levels, the polypropylene parts and the polystyrene based plastic scintillator added significantly to the  $\gamma$ -ray background because of their very large masses. 0.25 dru of electron recoils were introduced to the xenon target from the polypropylene shielding alone. It should be noted that contributions from the scintillators were very effectively tagged by the veto (the  $Q$ -value of the radioactive decay is almost always sufficient to trigger the veto), and thus did not contribute to the final background budget of ZEPLIN–III.

Despite the additional contributions from the construction materials of the veto, an overall 20-fold improvement in the  $\gamma$ -ray background was achieved for the SSR of ZEPLIN–III in comparison to its first science run phase. The total expected contributions to the nuclear recoil rate in the signal region are 0.13 events/year (assuming unity efficiency and excluding rejection efficiency of the anti-coincidence detector).

### **$^{85}\text{Kr}$**

A well known background source for any xenon based detector is  $^{85}\text{Kr}$ , an anthropogenic  $\beta^-$ -emitter, contained within the noble gas. Pre nuclear industry, the ratio of atmospheric  $^{85}\text{Kr}/\text{Kr}$  was  $3 \times 10^{-18}$ . However it has increased since to a present day ratio of approximately  $1.3 \times 10^{-11}$  [201].  $^{85}\text{Kr}$  is produced as a fission product with a 0.3% fission yield. Very small amounts of  $^{85}\text{Kr}$  are naturally generated by high energy cosmic-rays interacting with the stable  $^{84}\text{Kr}$  isotope in the atmosphere. Since the 1940s, nuclear weapon tests and nuclear power plant accidents since released the majority of the still remanent atmospheric  $^{85}\text{Kr}$ . In addition,  $^{85}\text{Kr}$  is still produced and released today with nuclear reprocessing facilities being the dominant source [202]. The isotope primarily decays via the emission of a  $\beta$ -particle with  $\beta_{max} = 687$  keV and a half life of  $T_{1/2} = 10.76$  years [203]. Thus, great care has to be taken to select xenon that is sourced from air with low  $^{85}\text{Kr}$  content. The xenon used for the ZEPLIN-III project was extracted in the 1970s from an underground origin. In 1997 an accurate measurement of the  $^{85}\text{Kr}$  content of a 5.9-g sample was performed, from which an age-corrected  $^{85}\text{Kr}/\text{Kr}$  ratio of  $1.5 \times 10^{-12}$  was derived [204]. Subsequently, cryogenic distillation was used to reduce the overall krypton content to  $\sim 50$  ppb  $^{85}\text{Kr}$  by weight. This would correspond to an energy electron recoil background of 0.2 dru in the xenon target. However, present measurements suggest that this was still a significant overestimate.

Coincidence delayed analysis with ZEPLIN-III and the veto detector was used for estimating the current level of  $^{85}\text{Kr}$  contamination. A minor  $\beta$ -decay with a branching ratio of 0.434% and  $\beta_{max} = 173$  keV is accompanied by a 514 keV  $\gamma$ -ray from the  $^{85}\text{Rb}$   $9/2+$  level with a half life of  $T_{1/2} = 1.015$   $\mu\text{s}$  [203]. This allows delayed coincidences to be observed. The krypton contamination level measured with this technique was 150 ppt  $^{85}\text{Kr}$  resulting in an insignificant electron recoil rate of  $0.007 \pm 0.002$  dru in the target of ZEPLIN-III.

### **Other construction materials**

There are three more general construction materials that need to be considered, partly because of their increased radioactivity and partly due to their relatively large mass in the experimental setup. Firstly, copper was the main construction material of the ZEPLIN-III detector, totalling approximately 400 kg in mass. Conservative upper limits for copper (OFHC C103) of 0.5 ppb in U and Th contamination were adopted for simulations resulting in 0.35 dru in the WIMP target. However, comparison to data suggested a far less significant contribution to the electron recoil background and an upper limit of 0.1 dru for the primordial radioactivity was set. Additionally, cosmogenic activation from exposure to atmospheric muons need to be considered. Several radio-

isotopes are produced, but only  $^{60}\text{Co}$  with  $T_{1/2} = 5.3$  years (adopted production rate of  $\sim 50$  atoms/kg/day [205]) will remain a measurable contaminant after storing the copper underground for many years. Assuming secular equilibrium, and a period of at least 4 years being placed underground prior to the SSR, the electron recoil rate from all copper parts combined resulted in a negligible 0.01 dru.

Secondly, ceramic used for feed-throughs of all signal and high voltage connections, with measured contamination levels of 105 ppb U, 270 ppb Th and 880 ppm K, was the dominant source of the observed neutron background. Contributions to the electron recoil rate were marginal.

Finally, 60 tonnes of lead used as shielding around the experiment also contributed to the background. However, two decades of being placed underground ensured a very low level of  $^{210}\text{Pb}$  contamination and an overall electron recoil rate of only 0.01 dru was measured from the entire shielding castle.

## 7.2 Shielding against rock neutrons

One of the most challenging simulations in estimating the contribution to the neutron background was the correct propagation of rock neutrons to the WIMP target. Despite the high attenuation factor provided by the hydrocarbon shielding of  $\sim 10^5$ , exceptionally precise modelling of the shielding constructions were needed to ensure accurate predictions of the neutrons interacting within the liquid xenon. Minor gaps from assembling or holes for cabling and pipework might have, when not taken into account correctly, altered the final result significantly. Moreover, Monte Carlo simulations of neutron propagation in large volumes were computationally very intensive and additionally low event rates demanded simulations with very long live-times. For the results presented here a total of 250 years equivalent live-time was simulated.

Primary neutrons for subsequent propagation studies were generated in the rock at a depth of 3 m according to primordial contamination levels and recorded on a test surface in the virtual laboratory. At this stage the integrated flux was adjusted to agree with measurements at Boulby [206], including backscattered neutrons. For simulations of the full experimental setup these previously recorded neutrons were released with a cosine bias from a virtual sphere of radius 2.2 m enclosing the whole experiment.

### 7.2.1 GEANT4 simulations with CAD-based geometry modelling

Geometries created with CAD supporting software were incorporated into the ZEPLIN-III simulation [122]. This new technique was necessary to assure a realistic geometry

of the setup, especially for the recently installed veto detector, being assembled from over a thousand individual parts. Figure 7.2 shows the detailed geometrical description achieved (down to the level of individual screws) in comparison to the standard detector construction in the original ZEPLIN-III simulation. To incorporate CAD constructed geometries into GEANT4, they have to be translated into GDML (Geometry Description Markup Language) code, and the detector construction source code file of GEANT4 modified, to be able to read the respective geometry files.

The GEANT4 (version 9.2) based Monte Carlo simulation resulted in a single-elastic nuclear recoil rate in the target of ZEPLIN-III, within the limits of a WIMP search region from 5–50 keV<sub>nr</sub> and unity detection efficiency, of  $0.53 \pm 0.05$  neutrons/year. The differential energy spectrum of nuclear recoils from rock neutrons in the fiducial volume of the xenon is shown in Fig. 7.3.

Moreover, this work motivated the use of an additional polypropylene shielding sheet inserted between the veto detector and the inside of the lead castle. Simulations determined that 6 cm of extra hydrocarbon shielding reduces the expected number of neutrons by over a factor of 2. This additional layer of shielding can be seen in the beginning of its construction on the right hand side of the photograph on the very right in Fig. 5.3 in Chapter 5. Finally, this type of simulation setup allowed confirmation that the Am-Be calibration did not cause neutron activation of materials with long half lives, since the CAD model took all components and materials into account.

To summarise, using a highly detailed description of the shielding geometry (incl. the 6 cm of additional polypropylene) it was shown that the expected background from single nuclear recoils of neutrons coming from the rock of  $0.53 \pm 0.05$  neutrons/year is almost three times the rate in comparison to the result obtained when performing simulations with an idealised 30 cm hydrocarbon shielding box surrounding the detector ( $0.19 \pm 0.08$  neutrons/year). Thus, expectations of the single nuclear recoil background from rock neutrons would have been significantly underestimated.

Although for this work only the passive shielding property of the veto detector was considered, in perspective of future applications, alterations to the source code of GEANT4 have been undertaken to enable GDML based geometries to be used as sensitive detectors in these kind of simulations. This had not yet been deployed before and induced interest in the GEANT4 community. An example code of a realistically modelled PMT coupled to a plastic scintillator was provided.

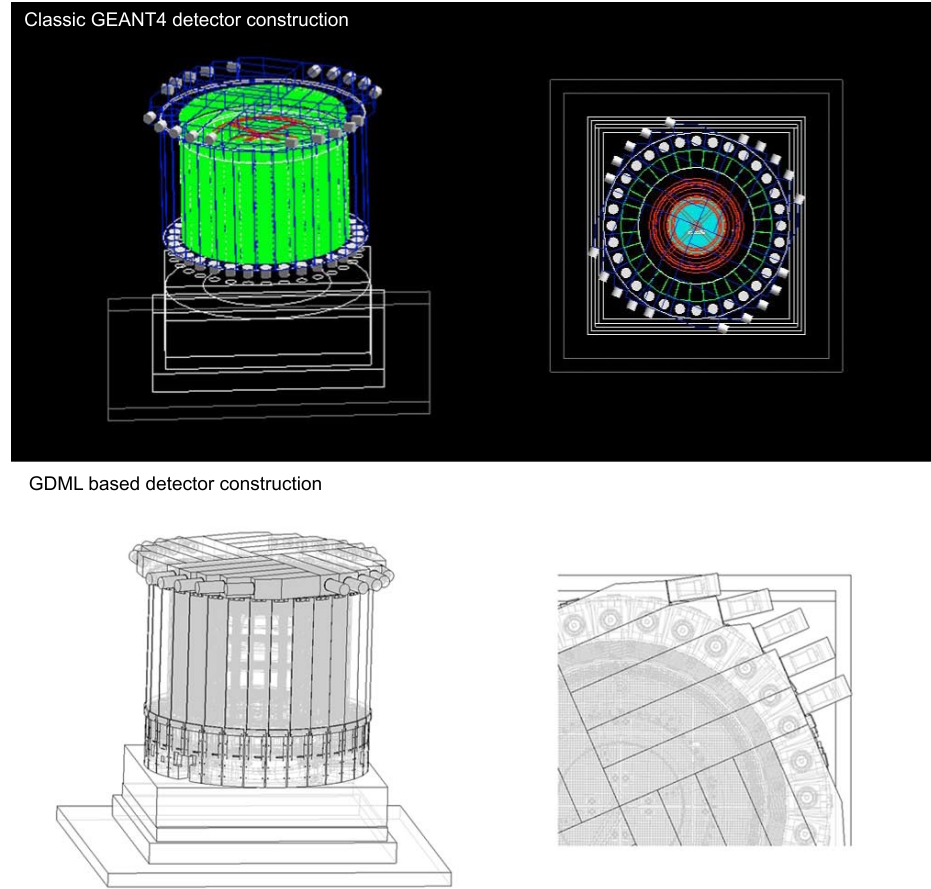


Figure 7.2: Screenshots of the ZEPLIN-III veto detector from the classical C++ detector construction, used as a standard modelling tool in GEANT4 (top), and from the same setup using CAD based geometries translated into GDML code (bottom). Note the level of details of the GDML based geometry, including cut outs for pipe work, gaps due to the assembly of 32 individual modules to form a round barrel, PMTs, clamps and screws.

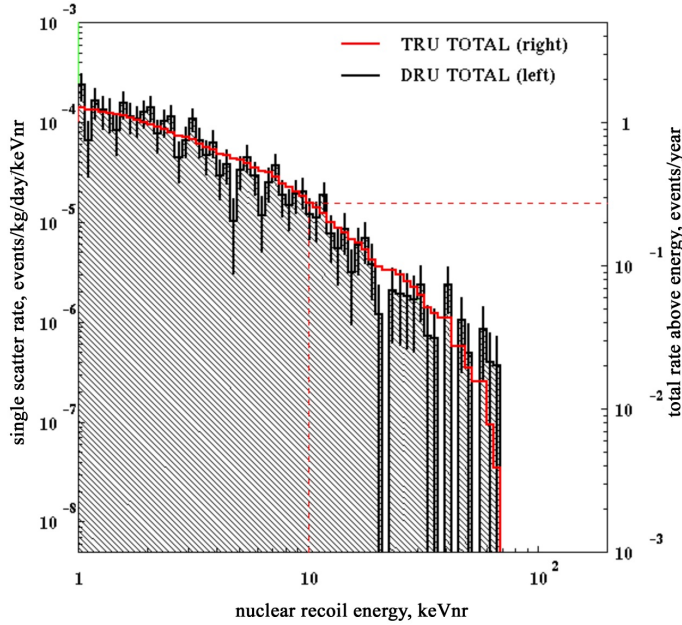


Figure 7.3: Energy differential spectrum of nuclear recoils from single-elastic scatters of rock neutrons within the fiducial volume of the xenon target.

## 7.3 Backgrounds in the second science run of ZEPLIN-III

### 7.3.1 Electron recoil background

To quantify the electron recoil background in the ZEPLIN-III detector prior to any WIMP search analysis, a dataset of 24 days with a blind nuclear recoil signal region up to 40 keV<sub>ee</sub> (to not compromise a blind analysis) was used. For the complementary simulations the 20 most intense  $\gamma$ -ray lines from each primordial decay chain (U and Th) as well as the 1,461 keV  $\gamma$ -ray from the  $^{40}\text{K}$  radioactive isotope, with intensities according to the performed component-level radio-assay measurements, were propagated.

Figure 7.4 shows the energy differential electron recoil background rate from the data (solid filled histogram) in comparison with simulations (thick blue solid line). It should be noted that there is no scaling involved in any of the comparisons of data to simulation, only absolute rates are shown. The energy scale is defined by a linear combination of S1 and S2 energy, exploiting the anti-correlation between the two response channels. Despite the dual range data acquisition tuned for WIMP search energies of 0–50 keV<sub>ee</sub>, the 8-bit dynamic range still introduced saturation of larger

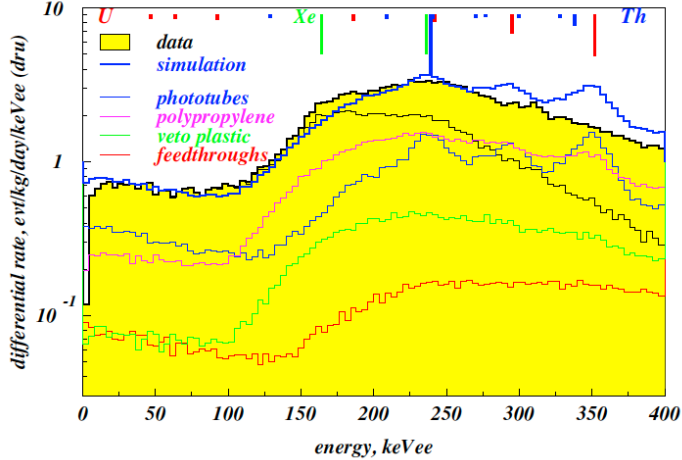


Figure 7.4: Energy differential histogram of the electron recoil background from a 24 day dataset (filled histogram) in comparison to simulations (blue thick solid lines), build up from component-level contamination measurements. All individual components from the simulations are given separately. Truncation of the data occurs at energies  $\gtrsim 150$  keV $_{ee}$ . The histogram plotted with a thin black line shows the unsaturated contributions of the data only. The energy of the most important U, Th and Xe activation  $\gamma$ -rays are indicated at the top [4].

signals. Above  $\sim 150$  keV $_{ee}$  the signals became significantly truncated and a fall-off in electron recoil rate at higher energies in the WIMP search data can be observed (see the difference in simulation to data at high energies in Fig. 7.4).

Data for this analysis was taken following a neutron calibration run only a few weeks earlier. As such, isomeric transition  $\gamma$ -rays from activation of the xenon, predominantly from  $^{129m}\text{Xe}$  with  $T_{1/2} = 8.88$  days [207] and  $^{131m}\text{Xe}$  with  $T_{1/2} = 11.8$  days [208], are still visible in the data (indicated with green lines at the top of Fig. 7.4). Despite this divergence and the discrepancy due to truncation at high energies good agreement of data to simulations was achieved in the region of interest.

Figures 7.5 and 7.6 show the same electron recoil background as a function of radius and as a function of depth in the liquid xenon disk, respectively. Again, good agreement is given between data and simulation in the spatial distributions. Figure 7.5 shows a discrepancy at small radii, which can be attributed to a higher than average contamination in the central PMT (still within expected batch variability).

The depth distribution in Fig. 7.6 is very closely reproduced by simulations except for the strongly increased rate in the data observed at approximately 37 mm. This is the location of the cathode wire grid, which has been contaminated with  $^{210}\text{Pb}$

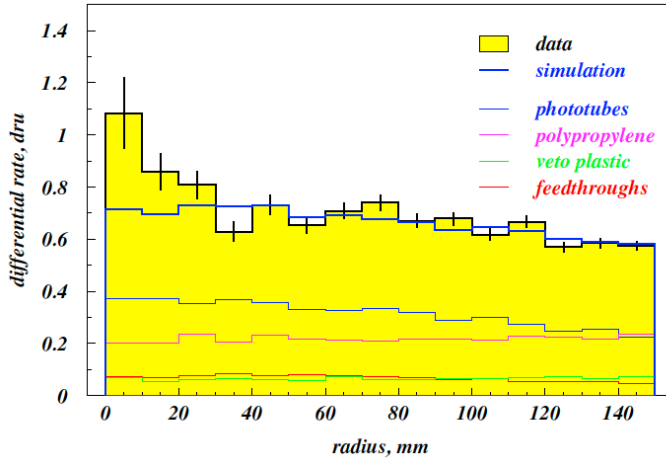


Figure 7.5: Electron recoil events as observed from the data (filled histogram) and from simulations (thick blue line) as a function of radius of the liquid xenon disk [4].

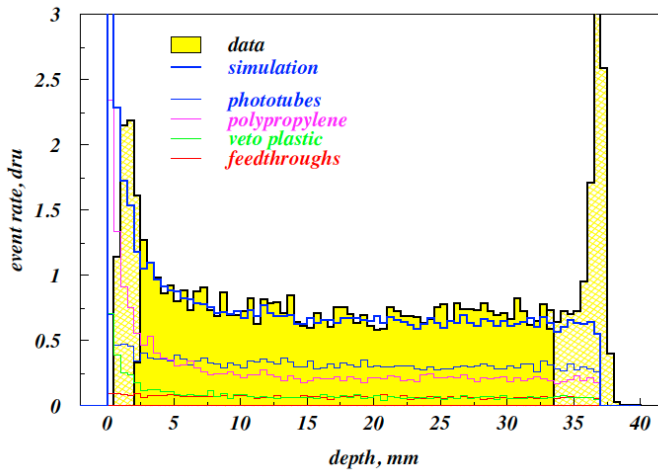


Figure 7.6: Electron recoil background from data (filled histogram) and simulations (thick blue line) as a function of depth. Good agreement between data and simulation is given for the fiducial region (dark yellow). At large depths a spike, arising from radon progeny left over from the FSR, can be observed. See text for further details [4].

Table 7.1: Component-level contributions to the electron recoil background from simulations based on individual radio-assay measurements. All rates are given in dru (at 10 keV<sub>ee</sub>). The total from simulations, labelled as ‘SSR total’ and the rate measured from the data are given below with a comparison to the electron recoil background measured in the FSR of ZEPLIN-III. On the right hand side the tagging efficiency provided by the veto detector is listed for each individual component [4].

Material	mass (kg)	e-recoil (dru)	PTAG
Krypton-85	–	0.007	~0
Ceramic feed-throughs	0.9	0.08	0.30
Photomultipliers	4.2	0.4	0.26
Rock (halite)	–	~0	~0
Polypropylene shield	1,266	0.25	0.04
Scintillator modules	1,057	0.09	~1
Copper ware	~400	(<0.1)	0.10
Lead castle	~60,000	0.01	0.54
Radon-222	1 m <sup>3</sup>	0.03	0.19
SSR total		0.86±0.05	0.28
SSR data		0.75±0.05	0.28
FSR		14.5±0.5	–

implantations from radon, arising in the xenon purification getters prior to the FSR of ZEPLIN-III. A more detailed discussion of this effect is presented in the next subsection. However, these discrepancies can be sufficiently mitigated by applying fiducial cuts.

Table 7.1 summarises the component-level contributions to the electron recoil background from simulations. Its sum equals 0.86±0.05 dru in a 6.5-kg fiducialised region of radius 150 mm and a depth of 32 mm. The measured total background in the science run data amounts to 0.75±0.05 dru, which is a 20-fold improvement over the backgrounds seen in the FSR.

As previously discussed in Section 5.2, the veto detector provided not only invaluable rejection of neutron events, but also tagged an average of 28% of the  $\gamma$ -ray background. Simulations can be used to estimate the tagging capability of the veto for each individual component. By implementation of active  $\gamma$ -ray detection by the veto in the simulations (performed previously to find the individual contributions to the background) component-level tagging was studied. The individual efficiencies are listed in Table 7.1. The weighted average adds up to a tagging fraction of 0.28±0.01 with exceptional good agreement to the measured overall prompt tagging efficiency of 28.1±0.2%.

## **$^{222}\text{Rn}$ progeny**

The contamination of the xenon gas with radon was first identified in the ZEPLIN-II project [90]. In this case the system relied on continuous gas recirculation through a purification getter (SAES PS11-MC500). Through this process,  $^{222}\text{Rn}$ , emanated from this specific getter model, entered the liquid xenon chamber. Measurements at the time identified an  $\alpha$ -activity with a half life of  $3.83 \pm 0.1$  days, fully consistent with the half life of  $^{222}\text{Rn}$  ( $T_{1/2} = 3.824$  days [209]). Unfortunately, prior to these measurements, the same getters had been used to purify the xenon for the ZEPLIN-III project and plating of radon progeny on the internal surfaces of the ZEPLIN-III detector could not be avoided. The getter has since been replaced with a new model (SAES PS4-MT3), preventing reoccurrence of this type of contamination.

The chain sequence of the  $^{222}\text{Rn}$  decay, as part of the  $^{238}\text{U}$  chain (shown in Section 7.1.1, labeled 7.1), explains the continuing presence of electron recoil background from this source. The uniformly mixed-in radon in the xenon will undergo decay. The two subsequent  $\beta$ -decays of  $^{214}\text{Pb}$  and  $^{214}\text{Bi}$  create  $^{214}\text{Bi}^+$  and  $^{214}\text{Po}^+$  ions, respectively. Transfer of their ionisation state to the noble gas is not possible, and thus the ions will drift to the negatively charged cathode. This is followed by the  $\alpha$ -decay of  $^{214}\text{Po}$ , implanting  $^{210}\text{Pb}$  isotopes within the wire grid. With a half life of 22.3 years the chain is bottlenecked at this stage. The remaining approximately stable radioactivity in the SSR has been measured by the rate of  $^{210}\text{Po}$  nuclear recoils to be  $19.4 \pm 0.3$  decays/day (per each of  $^{210}\text{Pb}$ ,  $^{210}\text{Bi}$  and  $^{210}\text{Po}$ ).

## **Rare event types**

Reduction, identification and rejection of neutron background is the main concern of any dark matter search. However, electron recoil type events producing signals with particular (unwanted) characteristics may leak into the defined signal region. These are then indistinguishable from nuclear recoil like events and might even dominate the irreducible background. Two specific event types of this kind are discussed in the following:

Firstly,  $^{40}\text{K}$  from sensitising of the internal PMT surfaces may be a substantial threat to any single- as well as dual-phase noble gas detector. Despite its contribution to the electron recoil background through the electron capture  $\gamma$ -ray at 1,461 keV,  $^{40}\text{K}$  is also a  $\beta$ -emitter (89% branching ratio and  $\beta_{max} = 1,311$  keV [167]), producing next to the  $\beta$ -particles themselves, bremsstrahlung and Cherenkov photons in the quartz window of the PMT. These additional electron recoil signals arising from within the PMT have been previously discussed and described for the veto PMTs in Chapter 5, Section 5.2.2. For the ZEPLIN-III PMTs 30 mBq of this type of background are

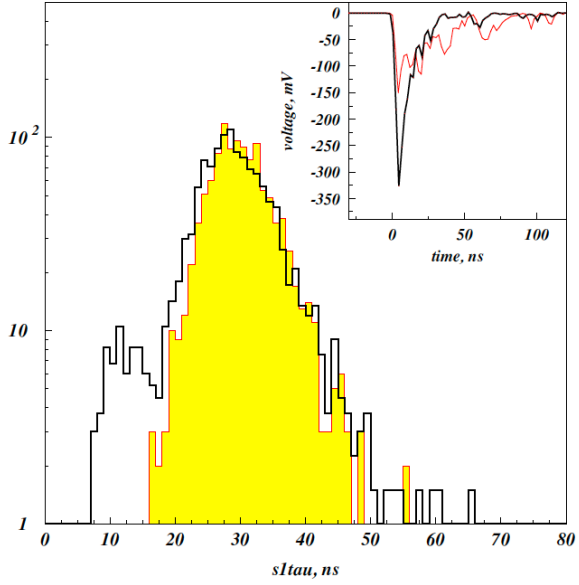


Figure 7.7: Distribution of the S1 mean arrival time sampled from the fiducial volume (filled yellow histogram) and from events below the cathode grid (empty histogram). Both distributions cover a similar apparent energy range of 30–60 keV<sub>ee</sub>. A population of very fast signals is clearly visible from the sub-cathode distribution, attributed to Cherenkov light emission. The inset shows a 30 keV<sub>ee</sub> electron recoil scintillation signal (red) with  $\tau = 35$  ns in comparison to a signal chosen from the sub-cathode population with  $\tau = 13$  ns and the same apparent reconstructed energy [4].

expected. Despite contributing 10–20% to the detector trigger rate, severe problems arise when signals of these  $\beta$ -induced events combine with single scatters in the fiducial volume. This would lead to a reduction in the observed S2/S1 ratio, the discrimination parameter of a dual-phase detector. However, accompanying Cherenkov light may not only increase the size of a time coincident scintillation pulse, but also reduce its apparent time constant, threatening not only dual-phase detectors but single-phase instruments, which depend on pulse-shape discrimination. A lower mean signal arrival time,  $\tau$ , would be generally associated with a nuclear recoil rather than an electron recoil. This effect was observed with the ZEPLIN-III detector and is shown in Fig. 7.7. The two plotted histograms represent distributions of mean S1 signal arrival times sampled from events with the same apparent energy range (30–60 keV<sub>ee</sub>) from the fiducial volume (filled yellow histogram) and from below the cathode (empty histogram), respectively. The sub-cathode events are mainly due to  $\beta$ -particles, but a small very fast contribution attributed to Cherenkov emission is also visible. Origin from nuclear recoils was ruled out from comparison to the timing spectrum from the upper grid surface, confirming

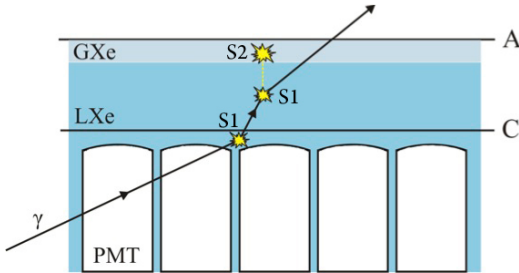


Figure 7.8: Schematic of the ZEPLIN-III detection region including the bottom PMT array immersed in the liquid xenon (LXe), the cathode grid (C) and the anode mirror (A). A possible MSSI event is shown, producing two simultaneous scintillation signals (S1), with one vertex located in a dead region of the detector. Only one of the scatters produces a secondary scintillation signal from ionisation (S2).

that pulses from this population are faster than nuclear recoils. Consequently, and as illustrated in the inset of Fig. 7.7, scintillation signals can be contaminated with Cherenkov light, lowering significantly the mean arrival time in comparison to clean electron recoil events with the same apparent reconstructed energy.

Secondly, electron recoil multiple scatter events can, under certain circumstances, diminish the effectiveness of a dual-phase detector discrimination significantly. If one vertex of a multiple scatter event occurs in a region which yields no ionisation, the first pass cut rejection will fail and the event will be accepted as a genuine single scatter event. In such Multiple-Scintillation Single-Ionisation (MSSI) events, the multiple scintillation signals are time coincident, artificially increasing the S1 signal size, and thus lowering the apparent S2/S1 ratio. In ZEPLIN-III there were two problematic regions within the liquid xenon target: the peripheral region near the side walls; and the reverse field region between the PMT windows and the cathode grid. The latter case is illustrated in Fig. 7.8 in the form of a schematic, showing a possible MSSI event constellation. To efficiently reject MSSI events and to avoid background domination in the WIMP search region, cuts based on S1 light patterns and S1-S2 vertex consistency are necessary.

### 7.3.2 Nuclear recoil background

The knowledge of expected nuclear recoils from neutron background in the WIMP search region is vital for claiming discovery of a WIMP like signal or the setting of a new upper cross-section limit on the WIMP-nucleon interaction in case of a null result. Excellent agreement of electron recoil rates observed in the fiducial volume of ZEPLIN-III between simulations and data was shown, and thus adopted contamination

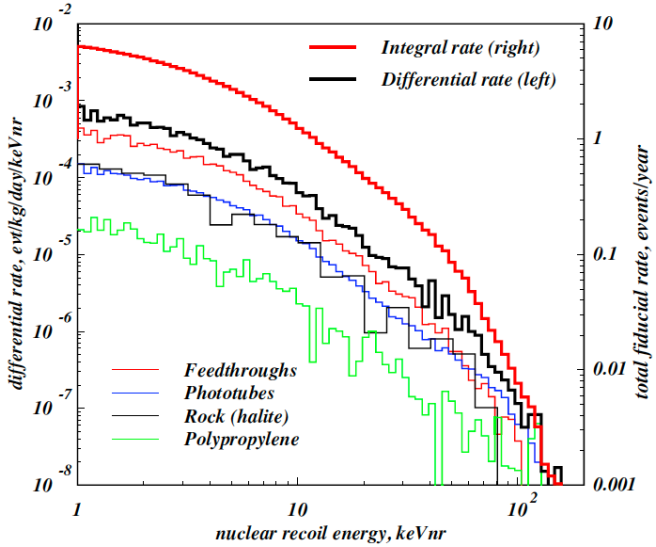


Figure 7.9: Total differential energy spectrum of single-elastic nuclear recoil energy depositions in ZEPLIN-III from simulations (black solid curve), alongside a component-level breakdown of individual contributions. The integrated rate (red solid histogram) is also shown, referring to the scale on the right hand side of the plot [4].

levels for the individual components were confirmed. Consequently, Monte Carlo simulations to estimate the expected nuclear recoil background from neutrons were performed.

The input neutron spectra for the simulations were calculated with SOURCES-4A [210] and 4C [185].  $(\alpha, n)$  cross-sections were extended to 10 MeV as described in Ref. [211] and complemented with cross-sections and branching ratios for transitions of excited states from EMPIRE2.19 [212] according to Ref. [213]. Primary generated neutrons were released isotropically and accordingly to the position of the specific component, followed by their subsequent tracking to the liquid xenon volume. Rock neutrons were propagated as described in Section 7.2.

The differential energy spectrum of single nuclear recoil scatters from neutron background is shown in Fig. 7.9. Again a component-level breakdown of the strongest contributors is plotted on the same graph. Values for the simulated neutron rates in the fiducial volume and in the energy interval of 5–50 keV<sub>nr</sub> are given in Table 7.2. A total of  $3.05 \pm 0.5$  neutrons/year are expected for the ZEPLIN-III experiment, assuming unity efficiency and excluding the veto rejection efficiency from delayed tagging. Overall a  $\sim 10$  fold improvement in the irreducible neutron background in comparison to the FSR of ZEPLIN-III has been achieved.

Table 7.2: Single-elastic nuclear recoils expectations from irreducible neutron background in the fiducial volume of ZEPLIN-III with energy depositions between 5 and 50 keV<sub>nr</sub>. The very right column shows the delayed tagging efficiency of the veto detector. The summed total is given below with a comparison to nuclear recoil expectations from the FSR of ZEPLIN-III [4].

Material	mass (kg)	neutrons/year	DTAG
Ceramic feed-throughs	0.9	1.35	0.58
Photomultipliers	4.2	0.74	0.58
Rock (halite)	–	0.53	0.58
Polypropylene shield	1,266	0.10	0.58
Scintillator modules	1,057	0.03	~1
Copper ware	~400	(<0.15)	0.58
Lead castle	~60,000	~0	0.58
Radon-222	1 m <sup>3</sup>	~0	–
Muon-induced	–	~0.3	~1
SSR total		3.05±0.5	0.58
FSR		36±18	

## Chapter 8

# The Second Science Run of ZEPLIN–III – Analysis and Results

Following the discussion on operation and calibration in Chapter 4, the focus in this chapter is the analysis procedure leading to the final result, *i.e.* the WIMP-nucleon interaction cross-section limit from the second science run data of ZEPLIN–III. This work has been presented in Ref. [2] to which the author contributed significantly.

The SSR lasted for 319 calendar days with an effective time of 265.5 days and a raw fiducial exposure of 1344 kg·days. The reduction in net time was predominately due to power interruptions at the laboratory and maintenance issues. A commissioning phase resulted in a dataset which was immediately open for analysis and proved to be very useful in improving software and analysis procedures. Data from the effective exposure were subjected to a blind analysis to prevent biasing of the signal observation in the pre-defined WIMP search region.

### 8.1 Analysis

Chapter 4 described how a corrected (golden) dataset was established. The raw waveforms were first parameterised with the bespoke pulse parameterisation software ZE3RA. Subsequently, the golden code selected valid single scatter events consisting of a single S1 followed by a single S2 signal. Selected S1 signals needed to fulfil the 3-fold requirement – that the summed waveform comprised signals from at least 3 individual PMTs. At this stage, the corrections, that are summarised in Chapter 4, Section 4.4.3, were applied and parameters booked into n-tuples. The number of events returned

by the golden code was of order 250 000 for the full effective exposure of the SSR. Next, the Mercury event reconstruction code calculated the position and energy, as well as simultaneously flat-fielding the PMT array by establishing the LRF curves for each individual PMT. Finally, the ZEPLIN-III data stream was synchronised with the events acquired using the veto DAQ.

The first step in the analysis procedure was the application of the PTAG and DTAG subroutines on the synchronised golden events, tagging  $\sim 28\%$  of electron recoil events as well as  $\sim 61\%$  of neutrons. Consistent with the extremely low neutron rate expected in the fiducial volume of ZEPLIN-III (see discussion on nuclear recoil background from neutrons in Section 8.1.3), the number of delayed tags observed agrees well with the calculated fraction of accidentally tagged events –  $\sim 0.7\%$ .

In previous studies [90, 116, 153], a fraction of at least 10% of the science run data from the blind box (broad region around the anticipated signal box – for more details see next section) was opened for inspection of events and to allow for the definition of selection cuts. As such, 10% of potential WIMP data had to be sacrificed for the analysis. However, the novelty in using an anti-coincidence device (the veto) supplies a sample of almost 30% of open events, evenly distributed in energy, for further study, without infringing on a blind analysis. In general this holds true, provided the veto samples all the event classes which can occur in the liquid xenon. Nonetheless, since the data were dominated by background, the sample of vetoed events represented a good estimate of the expected event distributions.

### 8.1.1 Defining a signal region

Neutron calibration sources were used to define the region of interest for nuclear recoil scatters, and thus for the signals expected from WIMP elastic recoil interactions. In the first instance, an initial evaluation of the energy dependent mean,  $\mu$ , and width,  $\sigma$ , of the nuclear recoil band population provided the necessary parameters to exclude events in a blind box (from 0–40 keV<sub>ee</sub> and in a range of  $\mu_{-3\sigma}^{+3\sigma}$ ) to ensure a non-biased analysis. The parameterisation was accomplished by Gaussian fits to the discrimination parameter  $\log_{10}(S2/S1)$  binned into 1 to 10 keV<sub>ee</sub> wide S1-energy slices. This corresponds to energy bins (adjusted in width to hold sufficient statistics) in the event scatter plot from an exposure to an Am-Be source as shown in Fig. 4.17 in Chapter 4 (event distribution in red) projected on to the y-axis. The plots in Fig. 8.1 show the fits to the first (left hand side) and last (right hand side) energy slice of the discrimination parameter for the final WIMP acceptance region.

Figure 8.2 shows the fits with polynomials of 4<sup>th</sup> and 3<sup>rd</sup> degree to the mean and width of the nuclear recoil band, respectively. The data points for the full energy range

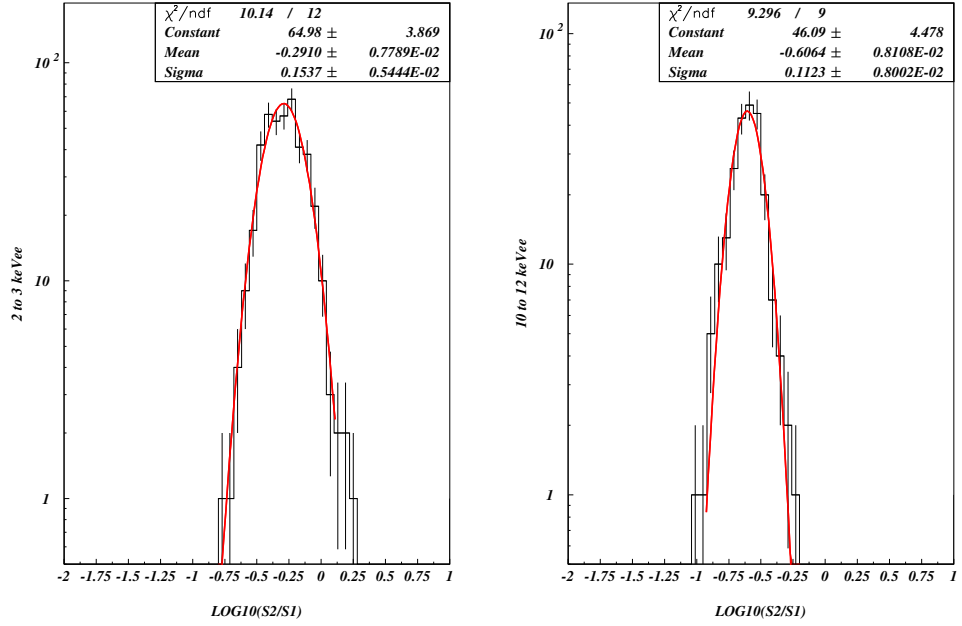


Figure 8.1: Gaussian fits to the discrimination parameter  $\log_{10}(S2/S1)$  of the nuclear recoil band populated by an Am-Be neutron source calibration run. Left: First slice in S1 energy for the final signal acceptance region from 2 to 3 keV $_{ee}$ . Right: Last slice from 10 to 12 keV $_{ee}$ .

up to 100 keV $_{ee}$  are the results from the Gaussian fits described earlier. The calculated mean (indicated by the thick line) and the region of  $\pm 2\sigma$  (thin blue lines) are shown in Fig. 8.3 superimposed on the elastic nuclear recoil distribution from the exposure to the Am-Be calibration source.

The definition of a WIMP search box, exploiting the discrimination from applying high electric fields across the liquid xenon target, is by far the most powerful cut to remove electron recoil background. Thus, great care needs to be taken in the optimisation of the region of signal acceptance. Gradual unblinding in combination with re-fitting and re-evaluation of the nuclear recoil band parameters, as well as progressive discarding of areas around the box, led to a final region of interest for the WIMP search. The procedure was as follows. After a preliminary definition of selection cuts, events with energies greater than 20 keV $_{ee}$  and  $\log_{10}(S2/S1) > \mu + \sigma$  were opened for analysis. At this stage the event reconstruction was finalised; the opened region was far enough away from a final anticipated search box such that minor redefinition of event parameters did not infringe on the blind analysis. Subsequently, all events above the mean ( $\log_{10}(S2/S1) > \mu$ ) were unblinded and selection cuts finalised (see Section 8.1.2).

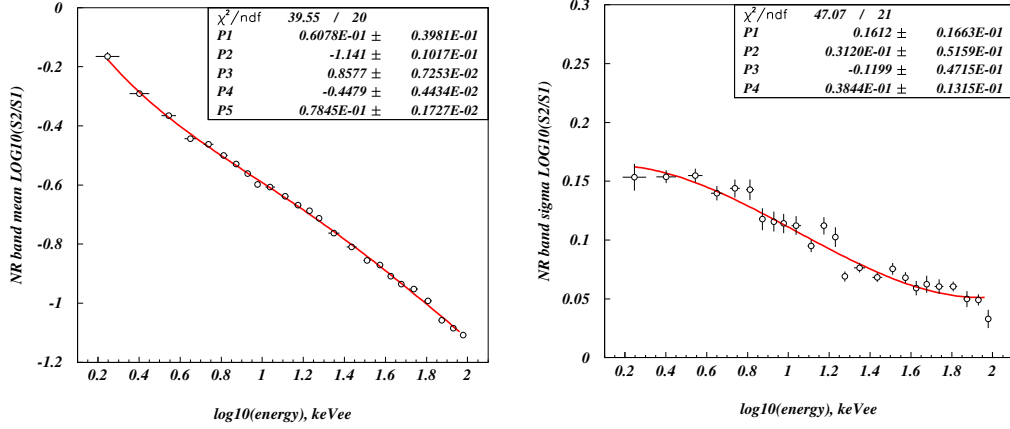


Figure 8.2: Polynomial fits to the mean,  $\mu$ , and width,  $\sigma$ , of the elastic nuclear recoil band with data points from Gaussian fits to the discrimination parameter sliced in 1 to 10 keV<sub>ee</sub> S1-energy bins (see Fig. 8.1).

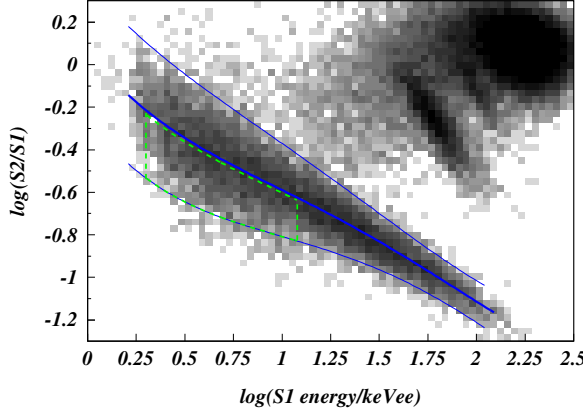


Figure 8.3: Discrimination parameter  $\log_{10}(S2/S1)$  as a function of S1 energy for an exposure to an Am-Be calibration source. The mean and  $\pm 2\sigma$  region of the nuclear recoil band are indicated by the blue lines. This event population was also selected for the analysis of the Gd fraction and neutron tagging efficiency of the veto detector presented in Chapter 5. The other populations are made up from inelastic neutron scatters and  $\gamma$ -rays released by the Am-Be source. The final WIMP search box is highlighted in green (dashed line), reaching from 2–12 keV<sub>ee</sub> [2].

Additionally, the nuclear recoil band parameters were re-calculated one last time, with the final set of selection cuts applied to the data. The ultimately selected WIMP search region reached from 2–12 keV<sub>ee</sub>, between 2.3% ( $\mu-2\sigma$ ) and 45% ( $\mu-0.126\sigma$ ) acceptance. The fine-tuning of the signal acceptance was guided by background event number expectations in various regions of the blind box from extrapolation of fits to the already opened science data (in a similar way as presented in Section 8.1.3). In the region from 50 to 45% acceptance approximately 3 events were predicted. Thus, this region was discarded and opened to help in refining analysis cuts.

It is worth emphasising, again, that the final definition of the acceptance region was performed whilst the WIMP search region was still blind.

### 8.1.2 Selection cuts and efficiencies

Although the SSR PMTs met their radioactivity goals, under-performance of the full array, such as large variability in quantum efficiency and gains of the individual PMTs, caused large systematic uncertainty in the reconstruction of events. Additionally, the observed poor electrical and optical performance increased cross-talk artefacts. These negative effects led to a greater than anticipated leakage of electron recoil events into the region below the nuclear recoil median – a measure of the discrimination power. As highlighted by the number of observed events in the signal acceptance region (see Section 8.2), the discrimination power dramatically decreased, from 1:7800 achieved in the FSR, to a ratio of only 1:280. The behaviour of the PMTs therefore demanded a set of sophisticated selection cuts. These can be generally split into two main categories: cuts acting on the quality of reconstruction; and cuts designed to remove well reconstructed background events.

The two most powerful cuts in the latter class were the already discussed definition of a WIMP search box, actively rejecting electron recoil events, as well as the fiducialisation of the physical xenon volume in all three dimensions. By selecting an inner target region, enclosed within the liquid xenon, the self-shielding property of the noble gas can be exploited. From the restriction of the liquid xenon disc to a radius of 140 mm and the drift time (*i.e.* the z-coordinate) to 1–13  $\mu$ s, translating to 2.4–30.8 mm below the liquid surface, an effective target volume of 5.1 kg of liquid xenon could be retained. Pulse shape discrimination (as presented earlier in Chapter 4, Section 4.2) was explored in an S1 signal timing cut. The FWHM of the S1 pulse was limited to 19 ns. The efficiency of this cut is shown as an individual curve in Fig. 8.12, labeled  $\eta_3$ . This cut becomes most effective at energies  $\gtrsim 10$  keV<sub>ee</sub>, where pulses are constructed from a sufficient number of photoelectrons to obtain better pulse-shape resolution. Finally, the identification of event particle species by the veto detector provided another layer

of rejection for  $\gamma$ -ray and neutron events.

The second type of selection cuts targeted the quality of the reconstructed events. In the first instance, events that were correlated with large changes in any of the environmental parameters were excluded from the analysis. For example, the external temperature variations may alter the detector response, and thus measured outliers in the laboratory temperature were removed. Secondly, an array of cuts aimed at removing mis-reconstructed events (*e.g.* events that were incorrectly identified as a single scatter) from the dataset – the so-called quality cuts. These cuts were developed to effectively target the outliers of the electron recoil distribution. The following plots show each individual quality cut which was applied to the golden dataset of the SSR. Fiducialised golden events are shown in black. Events from a small box (including the final signal acceptance region) from 0–20 keV<sub>ee</sub> and between  $\mu$  and  $\mu - 2\sigma$  in log<sub>10</sub>(S2/S1) acceptance are plotted in red. Data from below the nuclear recoil band median are printed in blue. The superimposed events in green are from the  $\mu_{-2\sigma}^{+0\sigma}$  region of the Am-Be calibration dataset. The imposed cuts are indicated by the red lines and the mathematical definition is given in the caption of each individual figure. Efficiencies are plotted on the right hand side. Due to the very challenging PMT array, a blind analysis could not be followed through to its ultimate conclusion (for more details see Section 8.2). As such, the quality cuts had to be re-tuned after the final opening of the WIMP search region. It should be emphasised that this unforeseen necessity did not affect the data-blind definition of the signal acceptance region, which was kept from the stage before the final unblinding. Furthermore, only small changes have been made to the previously defined quality cut parameters, such that the general shape of the cuts have not been altered retrospectively; also, no new cuts have been added. The following plots show the full open dataset, which was not available for the primary definition of these cuts; only vetoed events were open for analysis below the nuclear recoil median at this stage. The cuts have been developed in an iterative procedure to optimise effectiveness and (energy independent) efficiency. The efficiencies were calculated using the nuclear recoil band ( $\mu_{-2\sigma}^{+0\sigma}$ ) from the Am-Be calibration. The first three cuts proved to be very powerful in mitigating events which were incorrectly identified as single scatters. The spatial RMS of the secondary signal ( $s2rmsm$ ) is plotted in Fig. 8.4. Signals that are spread very widely across the PMT array may indicate a possible multiple-vertex event or effects due to a noise contribution. Similarly, cuts on large distances between the individually reconstructed S1 and S2 position ( $s12dism$  – see Fig. 8.5) and highly asymmetric S2 pulse shapes ( $s2symm$  – see Fig. 8.6) mitigate for potential MSSI events.

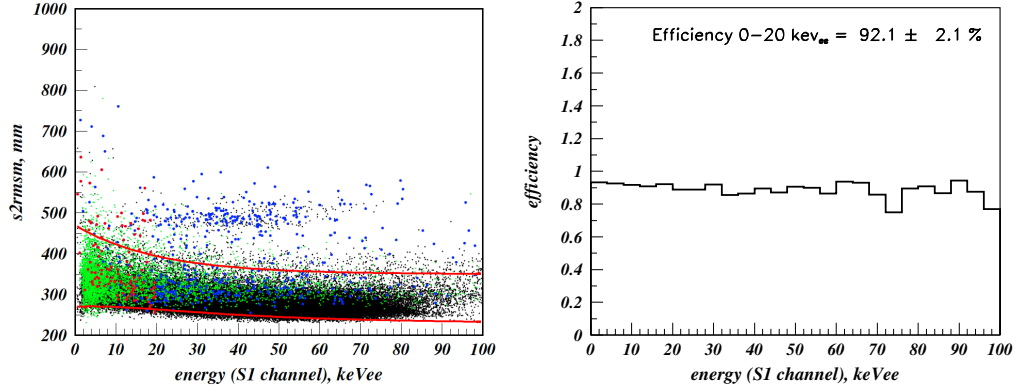


Figure 8.4: Spatial RMS of S2 (multiplied by a constant scaling factor),  $s2rmsm$ , as a function of S1 energy with the quality cut applied to the SSR data indicated by the red lines. The left plot shows all fiducialised golden data (black), events below the nuclear recoil median (blue), events in the small box from 0–20 keV<sub>ee</sub> and between  $\mu$  and  $\mu - 2\sigma$  (red), and the elastic nuclear recoil events from the Am-Be calibration run restricted to the  $\mu^{+0\sigma}_{-2\sigma}$  region (green). The efficiency calculated from the Am-Be data is shown on the right hand side. Cut definition:  $s2rmsm < 120 * e^{-0.05*S1} + 350 \ \&\& s2rmsm > -30 * e^{-0.09*S1} + 70 * e^{-0.03*S1} + 230$ .

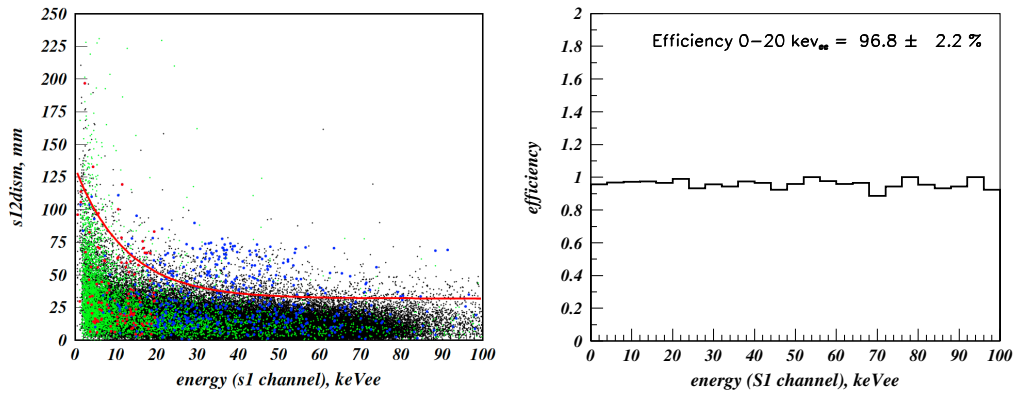


Figure 8.5: Left: Horizontal distance between reconstructed S1 and S2 position,  $s12dism$ , as a function of S1 energy with the quality cut indicated by the red line. Previous colour codes apply. Right: Efficiency calculated from Am-Be data. Cut definition:  $s12dism < 100 * e^{-0.08*S1} + 32$ .

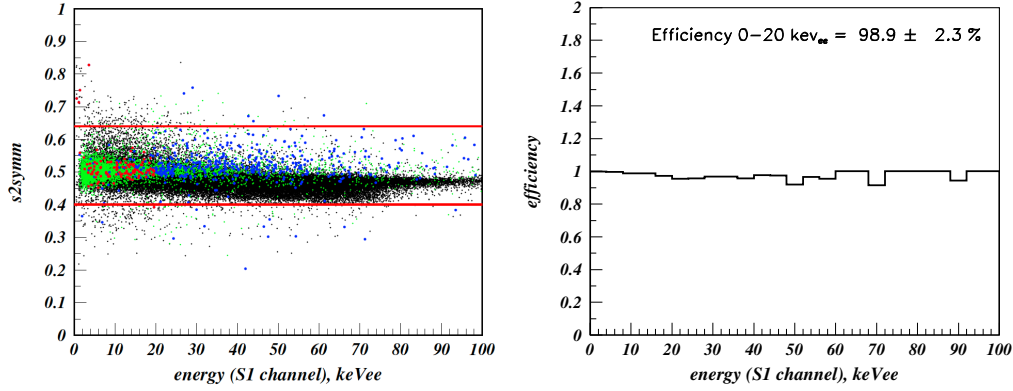


Figure 8.6: Left: S2 pulse symmetry ( $s2symm$ ), i.e. the area fraction in the first half-width of the pulse, as a function of S1 energy with quality cuts indicated by the red lines. Previous colour codes apply. Right: Efficiency calculated from Am-Be data. Cut definition:  $0.40 < s2symm < 0.64$ .

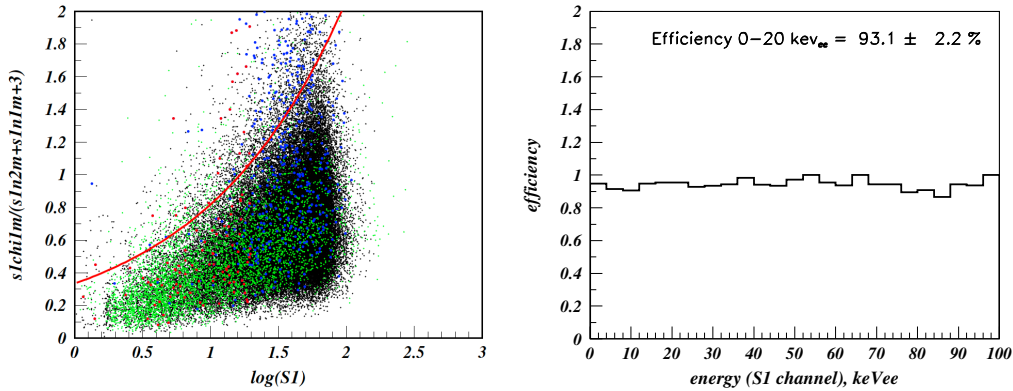


Figure 8.7: Left: Reduced  $\chi^2$  for the reconstructed S1 energy with the WLS method for the S2 position ( $s1chi1m$ ) divided by the sum of PMTs with exactly 1 phe ( $s1n1m$ ) and 2 or more phe ( $s1n2m$ ) in the S1 pulse as a function of  $\log_{10}(S1)$  energy. The cut is indicated by the red line. Previous colour codes apply. Right: Efficiency calculated from Am-Be data. Cut definition:  $s1chi1m/(s1n2m + s1n1m + 3) < e^{0.95*\log_{10}(S1)-1.1875} + 0.03$ .

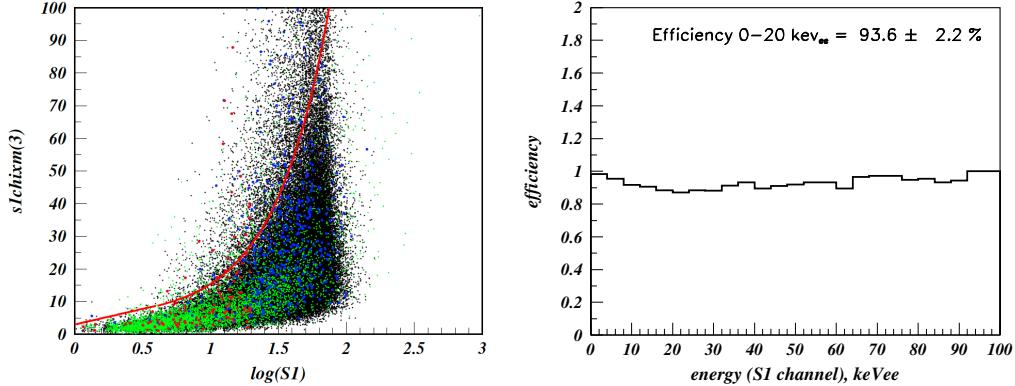


Figure 8.8: Left: ML value (opposite sign of log likelihood) from the S1 energy reconstruction using two separate PMT groups (PMTs with 0 phe and PMTs with non-zero contributions),  $s1chixm(3)$ , as a function of  $\log_{10}(S1)$  energy. The quality cut is indicated by the red line. Previous colour codes apply. Right: Efficiency calculated from Am-Be data. Cut definition:  $S1 < 4 \&\& s1chixm(3) < 9.58 * \log_{10}(S1) + 3.0 \mid\mid S1 > 4 \&\& s1chixm(3) < e^{2.5 * \log_{10}(S1) - 0.125} + 4.7$ .

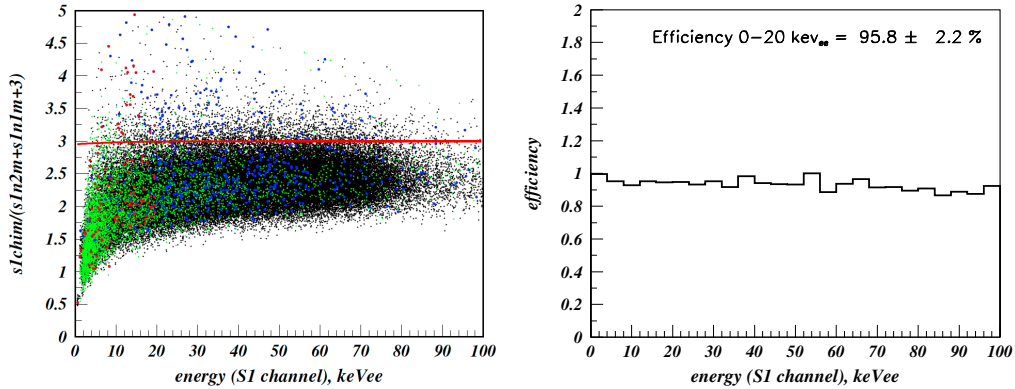


Figure 8.9: Left: ML value (opposite sign of log likelihood) of S1 energy reconstruction at S1 position ( $s1chim$ ) divided by the sum of PMTs with non-zero contributions to the S1 pulse as a function of S1 energy. The quality cut is indicated by the red line. Previous colour codes apply. Right: Efficiency calculated from Am-Be data. Cut definition:  $s1chim/(s1n1m + s1n2m + 3) < 3.0 - 0.5 * e^{-0.1 * S1}$ .

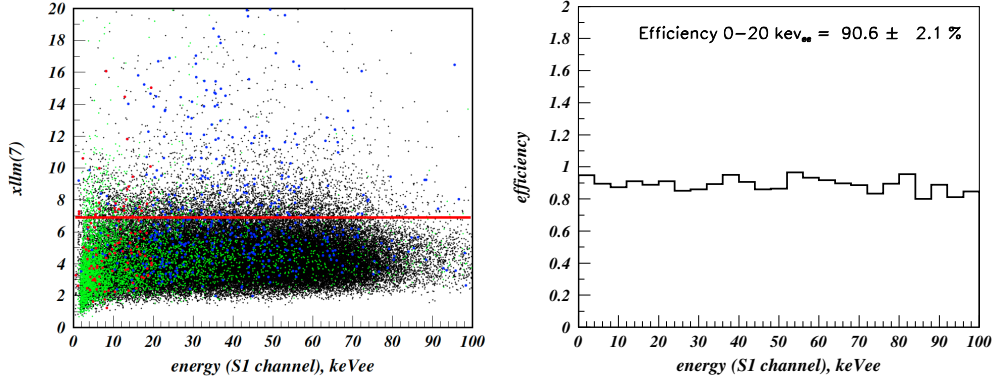


Figure 8.10: Left: Log likelihood (opposite sign) of PMT of least-likely response to have the observed amount of light or more on this particular PMT,  $xllm(7)$ , as a function of S1 energy. The quality cut is indicated by the red line. Previous colour codes apply. Right: Efficiency calculated from Am-Be data. Cut definition:  $xllm(7) < 6.9$ .

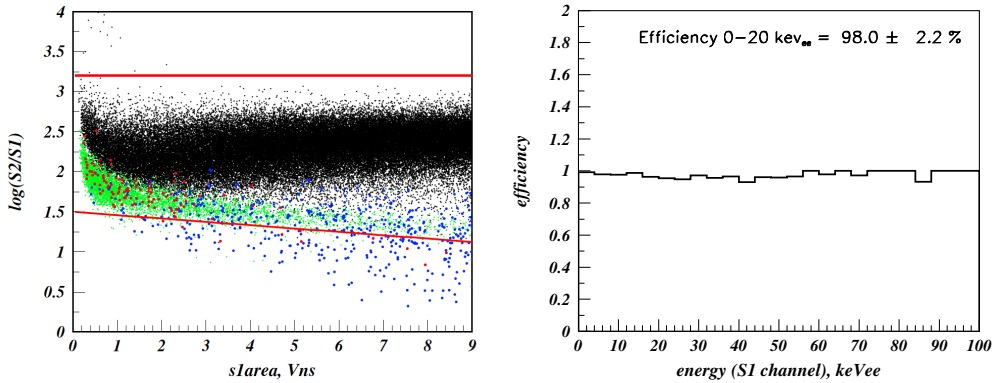


Figure 8.11: Left: Variation of the discrimination parameter,  $\log_{10}(s2area/s1area)$ , as a function of the flat-fielded summed area of the S1 pulse,  $s1area$ , with the cuts indicated by the red lines. Previous colour codes apply. Right: Efficiency calculated from Am-Be data. Cut definition:  $1.5 - 0.0418 * s1area < \log_{10}(s2area/s1area) \&& \log_{10}(s2area/s1area) < 3.2$ .

A second set of quality cuts, to remove outliers in the electron recoil distribution, accessed the parameters that quantify the goodness-of-fit in the Mercury reconstruction. The reduced  $\chi^2$  (see Fig. 8.7) and various ML values (see Figs. 8.8 and 8.9) of the fits to

the signals for different types of energy reconstructions proved to be the most effective measures. Additionally, the cut shown in Fig. 8.10 used the log likelihood value for the least-likely PMT to ‘see’ the measured number of photoelectrons. A variation of the discrimination parameter in terms of the raw (flat-fielded) summed area provided complementary cutting power (see Fig. 8.11).

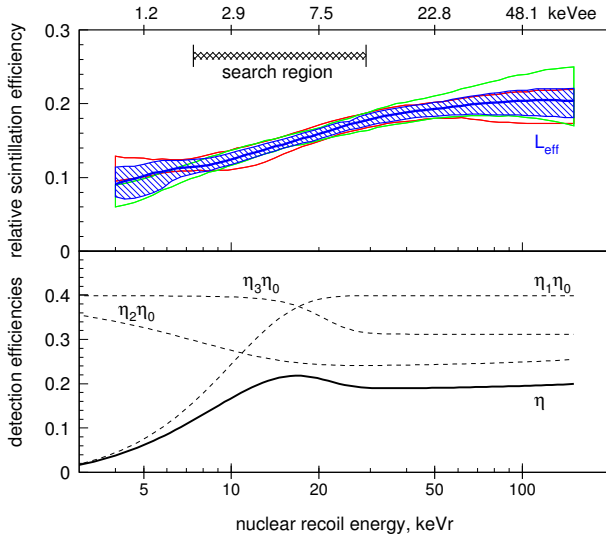


Figure 8.12: Top panel: Relative scintillation efficiency of nuclear recoils at zero field. The combination of the FSR (red) and SSR curve (green) is shown by the thick blue line. The hatched area represents the combined error, calculated from the 68% confidence regions from the two individual curves. The WIMP search box from 2–12 keV<sub>ee</sub> (7.4–29 keV<sub>nr</sub>) is indicated at the top. Bottom panel: Total nuclear recoil detection efficiency,  $\eta$ , comprised from a combination of a flat factor,  $\eta_0 = 39.8\%$ , and three energy-dependent components:  $\eta_1$  – 3-fold requirement of S1 pulse;  $\eta_2$  – quality cuts; and  $\eta_3$  – S1 pulse timing cut [2].

In Fig. 8.12 the total nuclear recoil detection efficiencies are summarised. To convert energies from electron equivalent units to nuclear recoil energies the two relative scintillation efficiency curves, derived independently for the FSR and the SSR (presented previously in Chapter 4, Section 4.2), were combined with each other. Consistency between the two curves and agreement (within experimental errors) with recent neutron beam measurements give confidence in the results. The individual and combined  $L_{\text{eff}}$  values are shown in the top panel of Fig. 8.12. The WIMP search region from 2–12 keV<sub>ee</sub> corresponds to a nuclear recoil energy of 7.4–29 keV<sub>nr</sub>. The lower panel of the same figure shows the total detection efficiency,  $\eta$ , a combination of three separate energy-dependent components,  $\eta_{1-3}$ , and a constant factor,  $\eta_0$ . The latter

consists of a set of constant factors such as the DAQ live-time fraction (99.2%), the veto accidental/random coincidences (PTAG: 99.6%, DTAG: 99.0%) and the predominant contributor, the signal acceptance region, with an efficiency of 42.7%. Additional minor efficiency losses from cuts of outliers in environmental parameters, as discussed earlier, as well as cuts regarding the quality and robustness of waveform parameterisation, *e.g.* when large discrepancies between pulse areas clustered by different algorithms were observed (possibly indicator for pick-up), resulted in a combined value of  $\eta_0 = 39.8\%$ . The energy-dependent curves  $\eta_{1-3}$  represent: the detection efficiency of the 3-fold PMT requirement for an S1 pulse (implemented in the golden code),  $\eta_1$ ; the combined efficiency of the event reconstruction quality cuts,  $\eta_2$ ; and the efficiency from the S1 timing cut for modest pulse shape discrimination,  $\eta_3$ . Taking the overall detection efficiency into account, an effective exposure of 251 kg·days for a WIMP with a mass of 50 GeV/c<sup>2</sup> was achieved.

### 8.1.3 Background estimations

To evaluate the statistical significance of a signal, or to calculate a cross-section limit from the number of observed events in a defined signal region, the expected backgrounds have to be carefully evaluated. Single-elastic nuclear recoil scatters from neutrons are indistinguishable from a genuine WIMP signal. The simulated expected nuclear recoil background from neutrons in ZEPLIN-III, previously presented in Chapter 7, Section 7.3.2, is  $3.05 \pm 0.5$  events/year for a fiducial volume of 6.5 kg and in an energy range from 5–50 keV<sub>nr</sub>. By taking the final effective exposure from the SSR, the reduced fiducial volume of 5.1 kg and the reduced size of the WIMP search box (7.4–29 keV<sub>nr</sub>, 42.7% acceptance in  $\log_{10}(S2/S1)$ ) into account, the number of single-elastic neutron scatters expected in the defined signal region and in anti-coincidence with the veto detector reduces to  $0.06 \pm 0.01$  events [2].

An independent but weaker constraint for the expected neutron background rate was found from the number of observed DTAG events in the signal acceptance region. Consistency of delayed tagged events with random coincidences with the electron recoil background was confirmed by looking at limited regions around the WIMP search box. Figure 8.13 shows the rate of DTAG events for the full dataset with all quality cuts applied (top panel) and for two regions around the nuclear recoil band (two bottom panels). In all cases, the number of observed DTAG events agree (within error) with the predictions. The DTAG event in the bottom plot appears at 84% acceptance in  $\log_{10}(S2/S1)$ ; the signal acceptance region does not hold any DTAG events. From the absence of delayed tags in the WIMP box and the confirmation of the statistical consistency of DTAGs with random coincidences in the vicinity of the signal region,

an upper limit of 0.75 neutron events (90% CL) can be inferred. Together with expectations from simulation, the successful mitigation of neutron backgrounds was confirmed.

Consequently, the background of events observed in the WIMP signal region will be dominated by electron recoil events. The significant amount of leakage from the electron recoil band to below the median of nuclear recoil acceptance was already clear from the large number of prompt tagged events observed (not subject to blindness) before the application of any quality cuts. Here, initially the region between 0–20 keV<sub>ee</sub> revealed 38 events in the fiducial volume. Influenced by an under-performing PMT array, dispersion of electron recoil events was far greater than expected and is demonstrated by the reduced discrimination power in comparison to the FSR.

An additional component of spurious electron recoil background arises from rare event topologies, leading, for example, to reconstruction of MSSI events under the assumption that they are genuine single scatter events. Other events may have pick-up or accompanying Cherenkov light produced in the PMT that adds to the S1 pulse and, as such, the apparent  $\log_{10}(S2/S1)$  discrimination parameter is lowered (see also Chapter 7, Section 7.3.1). Such effects are particularly problematic for single-phase noble gas detectors [86].

Two approaches have been adopted to estimate the remaining background of electron recoil events after the application of the pre-defined selection cuts: a calibration with  $\gamma$ -rays from a  $^{137}\text{Cs}$  source exposure; and an extrapolation of the fitted electron recoil distribution into the signal acceptance region. Results of both methods agree within errors.

Firstly, a run with an exposure to a  $^{137}\text{Cs}$  calibration source (for more details on the used source see Chapter 4, Section 4.4.3) was analysed in a similar manner to the science data and with the same selection cuts applied. Figure 8.14 shows the  $^{137}\text{Cs}$  data (blue crosses) normalised to the acceptance of the nuclear recoil band. Nine events have been observed within the signal region (indicated in red) after the application of a small cathode charging correction in S2/S1 ratio of order 6%, which reduced the total number by one. The origin of the cathode charging is understood as follows. From an increased trigger rate (in this case  $\sim$ 350 times the rate of the WIMP search data) systematic effects in the detector response are expected to occur. Rate dependent increasing resistivity of the photocathode enhances the charging of the photocathode. Consequently, the electric field lines become distorted and the collection efficiency of photoelectrons on the first dynode decreases [214]. Therefore, the mean value of the S2/S1 ratio may be reduced due to the higher fractional effect on the larger S2 signal relative to the S1. From a relative exposure of the  $^{137}\text{Cs}$  calibration run (in comparison to the WIMP search data) of 96%, an electron-recoil background expectation value of

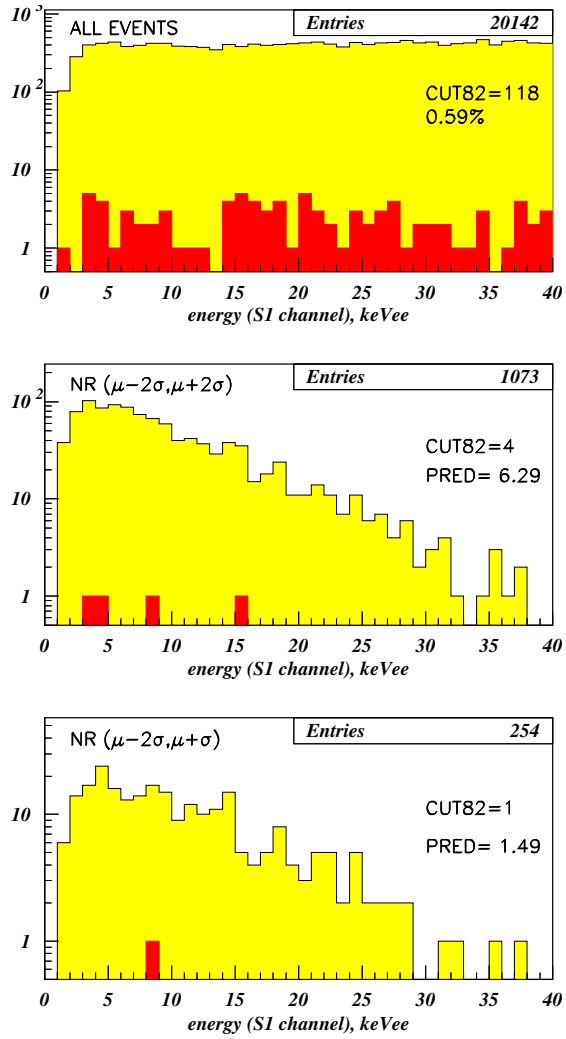


Figure 8.13: Golden events as a function of S1 energy with fiducial and quality cuts applied (yellow) for the full region (top), the nuclear recoil band between  $\mu-2\sigma$  and  $\mu+2\sigma$  (middle) and between  $\mu-2\sigma$  and  $\mu+\sigma$  (bottom). The number of DTAG events (red) are consistent with predictions for accidentally tagged electron recoil events.

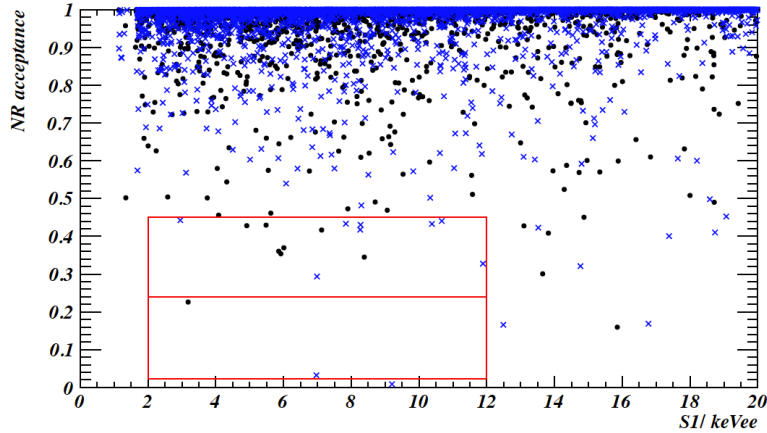


Figure 8.14: Nuclear recoil acceptance as a function of S1 energy for data from the  $^{137}\text{Cs}$  calibration run (blue crosses) with all selection cuts applied for the evaluation of the electron recoil background expectation in the WIMP search region (indicated in red). The partition of the search box will be discussed in Section 8.2. Golden WIMP search data are plotted in black (for further details see also Section 8.2).

$9 \pm 3$   $\gamma$ -ray events in the signal region was found.

The second method used to estimate the electron recoil leakage into the defined signal region was the extrapolation of skew-Gaussian (SG) fits to the electron recoil band distribution into the WIMP search box. Consistency of the electron recoil distributions with SG functions for fixed S1 energies had previously been found in the analysis of the FSR data [153] and was confirmed in the SSR for  $^{137}\text{Cs}$  data and the vetoed events. The un-vetoed search data, binned into 2 keV $_{ee}$  energy slices, was fitted by SG functions as given in Eq. (8.1):

$$f(x; x_c, \omega, \alpha) = \frac{1}{\omega \sqrt{2\pi}} e^{-\frac{(x-x_c)^2}{2\omega^2}} \left[ 1 + \operatorname{erf} \left( \frac{\alpha}{\sqrt{2}} \frac{x - x_c}{\omega} \right) \right], \quad (8.1)$$

where  $x$  represents the discrimination parameter  $\log_{10}(\text{S2}/\text{S1})$ , and  $x_c$ ,  $\omega$  and  $\alpha$  are the position, width and skewness, respectively. Figure 8.15 shows the SG fits to the data from the first and last bin of the WIMP search box. The summed background expectations in the signal region from extrapolations of the individual fits result in a value of  $6.5 \pm 3.4$  events. Despite the assumption that the electron recoil distribution shows functional dependency, as well as the possibility of contamination from real signal, consistency with the result from the independent measurement with the  $^{137}\text{Cs}$  calibration source gives confidence in the calculated background.

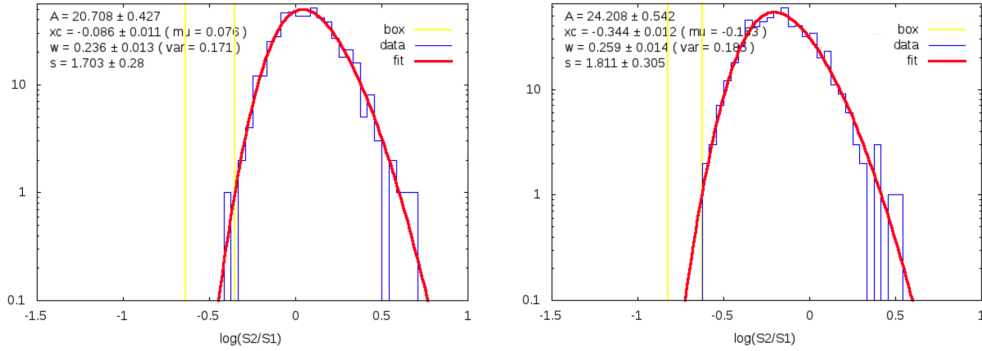


Figure 8.15: Skew-Gaussian fits (red) to the un-vetoed science data (blue) from the first (2–4 keV<sub>ee</sub> - left hand side) and last (10–12 keV<sub>ee</sub> - right hand side) S1 energy slice. Extrapolations into the WIMP search region (indicated in yellow) allow to estimate the expected background from leakage of the electron recoil band.

## 8.2 WIMP search results from the ZEPLIN-III SSR

Despite the absence of any vetoed events following the definition and subsequent application of quality cuts for box blind data, the opening of the pre-defined signal acceptance region revealed 12 additional un-vetoed events. Following a detailed inspection of waveforms, greater than anticipated cross-talk effects, resulting from the poor electrical performance of the SSR PMT array, were discovered. At this stage, it was decided to proceed with an open dataset. Minor re-tuning of some of the quality cut parameters, especially the ones targeting the goodness-of-fit of the Mercury reconstruction, provided sufficient rejection of spurious events; no additional cuts had to be defined. The golden data set from the final non-blind analysis is shown in Fig. 8.16. Eight events remain in the WIMP search box.

The number of observed events in the pre-defined signal region is consistent with both predictions of the electron recoil background. Results are summarised in Table 8.1. One of the 8 events appears fairly separated from the tail of the electron recoil distribution, with a reconstructed S1 energy of 3.2 keV<sub>ee</sub> and 1.11 keV<sub>ee</sub> in S2. The Poisson expectation probability for an event with this given S2 signal to produce the observed log<sub>10</sub>(S2/S1) value is 0.8%. Thus, given the rate of detected electron recoils one such low-lying event is fully consistent with the background.

Given the SG distribution of background, it is expected that the electron recoil background experiences a steep decrease in density when going to lower values of log<sub>10</sub>(S2/S1). Consequently, to maximise the sensitivity, the WIMP search region has been partitioned as follows. Skew-gaussian ML fits to the data above the search region

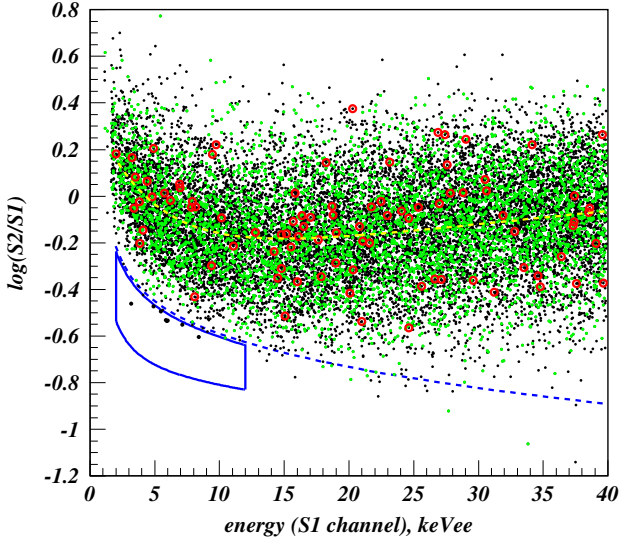


Figure 8.16: Discrimination parameter  $\log_{10}(S2/S1)$  as a function of S1 energy, showing the full SSR data (black) after the final non-blind analysis. There are 8 un-vetoed events in the signal acceptance region (indicated in blue). The median of the electron and nuclear recoil distributions are represented by the blue and yellow dashed lines, respectively. Promptly tagged events (PTAG) are highlighted in green and delayed tagged events (DTAG – consistent with accidental coincidences) are marked in red [2].

Table 8.1: Number of events observed,  $n_{obs}$ , in the partitioned signal acceptance region from SSR data. Background estimates from neutrons,  $\mu_{b1}$ , and electron recoils,  $\mu_{b2}$ , from both applied methods are given alongside the limit on the signal expectation,  $\mu_s$ .

Acceptance keV <sub>nr</sub>	fraction	$n_{obs}$	Neutrons, $\mu_{b1}$ $^{137}\text{Cs}$	Electron recoils, $\mu_{b2}$ SG fit	$\mu_s$ , 90% CL
7–29	24–45%	7	$0.03 \pm 0.005$	$8.3 \pm 2.9$	$5.5 \pm 2.2$
	2–24%	1	$0.03 \pm 0.005$	$1.0 \pm 1.0$	$1.0 \pm 1.2$

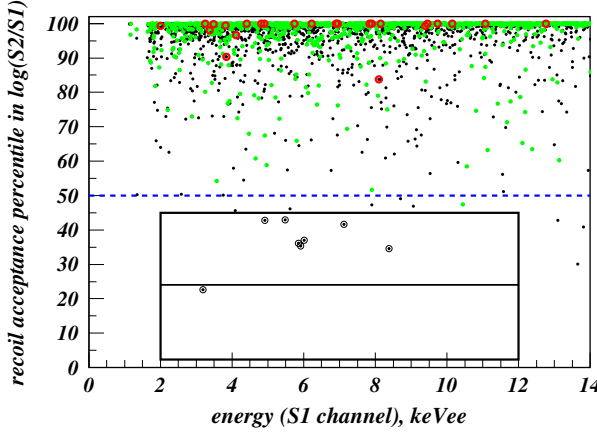


Figure 8.17: Signal acceptance as a function of S1 energy for unblinded SSR WIMP search data. The partitioned WIMP search box is indicated by the black lines. Seven and one events are observed in the upper and lower half of the signal acceptance region, respectively. Previous colour codes apply [2].

in 2-keV<sub>ee</sub> bins were used to estimate the background for different partitions of the box. The search data inside the signal box were not considered for this calculation. A two-bin Feldman-Cousins method [215] was applied to derive simulated upper limits with the best sensitivity achieved using a division line at 24% acceptance in log<sub>10</sub>(S2/S1). Figure 8.17 shows the unblinded search data as a function of signal acceptance in percentiles with the two parts of the signal acceptance region indicated. Seven and one events are observed in the upper and lower bin, respectively.

For the calculation of the confidence interval of signal expectation, the method of Profile Likelihood Ratio (PLR), which accounts for the uncertainty in the background predictions [169], was chosen. The likelihood ratio test performed has the form:

$$R_{PLR} = \frac{L\left(\mu_{test}, \hat{\beta}\right)}{L\left(\hat{\mu}, \hat{\beta}\right)}, \quad (8.2)$$

where  $L(\hat{\mu}, \hat{\beta})$  is the ML of the observation under any signal,  $\mu$ , and background,  $\beta$ , and  $L(\mu_{test}, \hat{\beta})$  is the likelihood maximised over  $\beta$  for a given test hypothesis of the expected signal,  $\mu_{test}$ . The likelihood function  $L(\mu, \beta)$  is built up from the probability density functions of the distribution of observed events and estimated backgrounds, including three parts:  $L_{box}(\mu, \beta)$ , a Poisson likelihood for the observed number of events,  $n$ ,

given the background,  $\beta$ , and signal,  $\mu$ ;  $L_{Cs}(\beta)$ , a Poisson likelihood for the observed background events from the  $^{137}\text{Cs}$   $\gamma$ -ray calibration,  $m$ , with a relative exposure  $\tau$  (in comparison to the WIMP search data) given the  $\gamma$ -ray background,  $\beta_\gamma$ ; and  $L_{extrap.}(\beta)$ , an approximated Gaussian likelihood for the electron recoil background estimated from SG fits,  $b_{SG}$ , and the expected neutron rate,  $b_n$ , given the total background,  $\beta = \beta_\gamma + \beta_n$ :

$$\begin{aligned} L(\mu, \beta) &= L_{box}(\mu, \beta) \cdot L_{Cs}(\beta) \cdot L_{extrap.}(\beta) \\ &= \prod_{i=1}^2 Pr(n_i; \mu_i + \beta_i) \cdot Pr(m_i; \tau \beta_{i,\gamma}) \\ &\quad \times \frac{1}{\sigma_i \sqrt{2\pi}} e^{\frac{(\beta_i - (b_{i,SG} + b_{i,n}))^2}{2\sigma_i^2}}, \end{aligned} \quad (8.3)$$

where  $i$  is the counter for the two bins of the partitioned box and  $\sigma_i$  reflects the uncertainty of the Gaussian estimates. It is conventional and convenient to calculate the  $R_{PLR}$  in terms of  $q$ :

$$q \equiv -2 \log R_{PLR}, \quad (8.4)$$

which has the form of a  $\chi^2$  distribution. To build up the confidence interval,  $q$  was computed for random values (drawn from the corresponding distributions by Monte Carlo) of  $n_i$ ,  $m_i$  and  $b_{i,SG}$ . The estimated background from neutrons in the SSR was too small to be of any real impact, and thus was implicitly included in the values for  $b_{i,SG}$ . The Gaussian for the SG background predictions were treated to be truncated at zero. A signal rate,  $\mu_{test}$ , was rejected when its observed value for  $q$  lay above the critical 90<sup>th</sup> percentile of all simulated trials. Thus, an expected signal,  $\mu_s$  (equivalent to  $\mu_{test}$  for the Monte Carlo), was rejected when  $q$ , calculated for the observed number of events and background estimates in the SSR, exceeded the 90<sup>th</sup> percentile of the Monte Carlo trials. The 90% confidence interval was found to be  $\mu_s = 0\text{--}5.1$  events in the WIMP search box.

### 8.3 The final dark matter search result from the ZEPLIN–III project

Experimental dark matter searches try to constrain the properties of the WIMP dark matter particle in terms of interaction cross-section and the most probable mass. In the case of a null result, *i.e.* the number of observed events is consistent with background expectations, as was the case for both the FSR and SSR of ZEPLIN–III, upper limits

on the cross-sections for a range of different WIMP masses are found. As outlined in Chapter 3, Section 3.3, for ease of comparison to other experiments, featuring for example different target materials, the parameter of interest for any direct dark matter search is the WIMP-nucleon scattering cross-section,  $\sigma_n$ . It is directly proportional to the expected signal,  $\mu_s$ , in a given search region.

In this section, the calculation of a scalar and spin-dependent WIMP-nucleon cross-section limit is discussed, followed by results obtained from the SSR data. A revised limit for the FSR data is also presented. Finally I conclude with a combined result from the two science runs of ZEPLIN-III, published in Ref. [2].

### 8.3.1 Cross-section limit calculations and SSR results

To calculate the WIMP-nucleon cross-section, the limit on the total event rate has to be found. This is achieved by comparing the integrated rate of the predicted spectrum of WIMP interactions to the limit on the signal rate, *i.e.* integrating the normalised spectrum in the energy range of the signal region and subsequently scaling it to the observed rate (the limit on the signal rate divided by the final exposure).

The predicted energy differential WIMP recoil spectrum can be calculated from Eq. (3.1) given in Chapter 3, Section 3.3. Although this already includes the nuclear form factor, which especially influences interactions with targets of heavier mass, it describes the spectrum expected for a perfect detector with 100% efficiency. To obtain a realistic spectrum, energy resolution and efficiency losses have to be accounted for. First, the measured scintillation yield was applied to convert from nuclear recoil energies to electron equivalent units. Next, the energy resolution, found to be of order  $\sigma_{S1[\text{keV}_{ee}]} \approx 1.0\sqrt{S1[\text{keV}_{ee}]}$ , was convolved with the predicted spectrum. Finally, all detection efficiencies described earlier in Section 8.1.2 were applied. Standard galactic halo parameters have been used in the calculations ( $\rho_0 = 0.3 \text{ GeV}/c^2/\text{cm}^3$ ,  $v_c = 220 \text{ km/s}$ ,  $v_{esc} = 544 \text{ km/s}$ , and  $v_E = 232 \text{ km/s}$ ) along with the Helm form factor [76] as given in Eq. (3.10) and parameterised in Ref. [77].

The limit on the total predicted signal rate,  $R_0$ , is obtained by scaling the predicted spectrum, integrated over the energy range of the signal region, to the observed rate.  $R_0$  is related to the WIMP-nucleus cross-section,  $\sigma_0^{SI}$ , through Eq. (8.5) [77]:

$$\frac{R_0}{r} = \frac{D\sigma_0^{SI}}{\mu_N^2}, \quad (8.5)$$

where  $\mu_N$  is the reduced mass of the WIMP-nucleus system,  $D$  is a constant factor accounting for the dark matter density and  $r$  is a kinematic factor given in Eq. (8.6), with  $m_\chi$  and  $m_N$  representing the mass of the WIMP and nucleus, respectively:

$$r = \frac{4m_\chi m_N}{(m_\chi + m_N)^2}. \quad (8.6)$$

Substituting Eq. (3.9) into Eq. (8.5) the WIMP-nucleon cross-section,  $\sigma_n$ , can be found:

$$\sigma_n = \frac{\mu_n^2}{A^2 D} \frac{R_0}{r}. \quad (8.7)$$

In the above equation,  $A$  denotes the mass number of the target and  $\mu_n$  the reduced mass of the WIMP-nucleon system.

The minimum of the spin-independent WIMP-nucleon cross-section limit for the SSR data of  $4.8 \times 10^{-8}$  pb (90% CL, double sided) was reached at a WIMP mass of 51 GeV/c<sup>2</sup>. The full limit curve is plotted in Fig. 8.20 at the end of this chapter. For the elastic scattering of light WIMPs, the confidence in the upper limit of the WIMP-nucleon cross-section at low masses is significant; this is directly influenced by the precision of the  $L_{eff}$  measurement. Varying the applied  $L_{eff}$  curve by  $\pm 1\sigma$  changes the cross-section limit in a range from  $(2.2\text{--}9.3) \times 10^{-6}$  pb at a WIMP mass of 10 GeV/c<sup>2</sup>, whilst having no significant effect on the result at the curve minimum.

Although xenon shows higher sensitivity in the spin-independent channel, it is of great interest to also calculate the cross-section limit for spin-dependent interactions as these may dominate particular regions in some SUSY scenarios [216]. As previously mentioned in Chapter 3, Section 3.3, the proton interaction is highly suppressed in xenon, due to its isotopic composition. However, xenon targets show good sensitivity to the WIMP-neutron interactions since approximately half of the natural abundance in xenon consists of the odd-neutron isotopes <sup>129</sup>Xe (total nuclear spin  $J = 1/2$ ) and <sup>131</sup>Xe ( $J = 3/2$ ). The xenon used in ZEPLIN-III was depleted in heavy isotopes and as such the abundance of <sup>129</sup>Xe and <sup>131</sup>Xe were boosted to 29.5% and 23.7%, respectively.

The calculation of the SD cross-section limit followed the description in Ref. [154]. The WIMP-neutron cross-section was calculated for each individual isotope from Eq. (8.8):

$$\frac{\sigma_{neutron}}{\sigma_0^{SD}} = \frac{3}{4} \frac{\mu_n^2}{\mu_N^2} \frac{1}{\langle S_n \rangle^2} \frac{J}{J+1}. \quad (8.8)$$

Here, the WIMP-nucleus elastic scattering cross-section,  $\sigma_0^{SD}$ , (given in Eq. (3.11)) is first obtained from the experimental limits on the predicted nuclear recoil spectrum, similar to the SI case. However, SD descriptions of the form factors have to be adopted (see Eq. (3.12) and Section 3.3 in Chapter 3). These are calculated in Ref. [217] using the Bonn-CD nucleon-nucleon potential [218]. In the same reference estimates for the

spin matrix elements,  $\langle S_{p,n} \rangle$ , for the two different xenon isotopes are also presented. The total cross-section was derived by combining the results from the individual isotopes:

$$(\sigma_{neutron})^{-1} = (\sigma_{neutron}^{129})^{-1} + (\sigma_{neutron}^{131})^{-1}. \quad (8.9)$$

A SD cross-section limit has only been calculated from the combined result of FSR and SSR data and is presented at the end of this chapter in Fig. 8.21.

### 8.3.2 A revised limit for the first science run of ZEPLIN-III

An unaccounted efficiency loss in the FSR data was discovered during the SSR analysis. Motivated by the new  $L_{eff}$  measurement with data from an Am-Be calibration run in the SSR, a revised WIMP-nucleon cross-section limit, using analysis codes developed for the SSR, has been calculated. This section will describe the changes made and present the newly obtained FSR result.

An implemented first pass cut waveform check in the original FSR golden code, testing the consistency of high and low sensitivity channels, led to a significant loss in the number of low energy events. Noise was picked up in the low sensitivity by ZE3RA and parameterised as genuine pulses; at the same time no signal was recorded in the high sensitivity. When retaining only the 10 largest pulses in each timeline, these spurious signals will predominately show up in the pulse arrays of very low energy events. In the case of high energy events, the array will instead be filled up by artefacts, such as afterpulsing, which are accompanying large energy depositions. Adopting the updated SSR software, a 16% relative change in the overall acceptance from the golden event selection code was observed. Crucially, this previous deficiency affected almost exclusively low energy events. New quality cuts have been defined, targeting similar goodness-of-fit parameters as in the SSR (produced by the application of the updated Mercury event reconstruction code), yielding an efficiency of  $\sim 76\%$ . In this instance, the previously mentioned  $\chi^2$  spatial maps (see Chapter 4, Section 4.4.4) were explicitly used to remove mis-reconstructed multiple-vertex events. Figure 8.18 shows an example of an event originally observed in the signal region, which was rejected on the grounds of a clearly visible multiple-vertex hit pattern of the S1 signal.

Fiducial cuts reduced the target volume to 6.52 kg, leading to a net effective exposure of 437 kg·days for a WIMP mass of 50 GeV/c<sup>2</sup>. The definition of the WIMP search box (2–16 keV<sub>ee</sub> and 2–50% in log<sub>10</sub>(S2/S1) acceptance) was kept from the original FSR analysis. Using the result from the newly measured  $L_{eff}$  curve (FSR and SSR combined – see Fig. 8.12) this translates to 7.4–35 keV<sub>nr</sub> nuclear recoil energy. The previously calculated scintillation efficiency from FSR neutron calibration data showed a significantly steeper dependency at low energies [153]. Five events are observed within

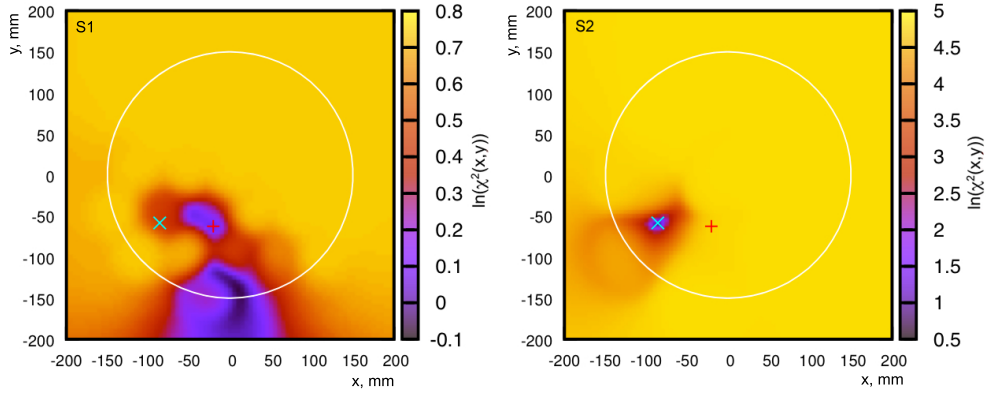


Figure 8.18: Spatial  $\chi^2$  map in  $x$  and  $y$  of the target volume (left: S1, right: S2) showing an event rejected due to its multiple-vertex hit pattern visible in the map of the S1 signal. The reconstructed position of the S1 (red) and the S2 (blue) signal are marked by the crosses.

the pre-defined signal region as shown in Fig. 8.19. An excellent discrimination power of 1:7,800 was achieved.

The background expectation from electron recoil events was estimated from extrapolations of SG fits to the data. Estimates from a  $^{137}\text{Cs}$  calibration led to a significant over-prediction of leakage into the box by a factor of  $\sim 5$ . The observed discrepancy may have been caused by more effective rate-dependent photocathode charging effects or other unknown systematic differences in comparison to the SSR  $\gamma$ -ray calibration. The total expected background was  $7.9 \pm 4.8$  events, including  $1.2 \pm 0.6$  neutrons. These and the observed number of events binned in two separate acceptance regions are given in Table 8.2. The horizontal division of the WIMP search box was found using the same data-blind optimisation procedure as in the SSR. From statistical analysis, a double-sided 90% confidence interval for the expected signal  $\mu_s$  of 0–4.2 events was found. The minimum WIMP-nucleon cross section limit of  $8.4 \times 10^{-8}$  pb was reached at 55 GeV/c $^2$  WIMP mass. This result is similar to the original published cross-section limit for the FSR of  $8.1 \times 10^{-8}$  pb at 60 GeV/c $^2$  [153]. The corresponding cross-section curve is shown in Fig. 8.20 at the end of this chapter.

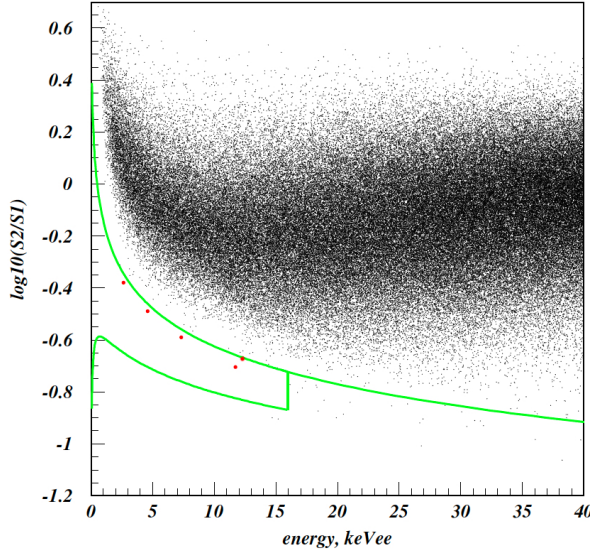


Figure 8.19: Event scatter plot of re-analysed FSR data (black). Five events (red) are located within the WIMP search box (green) extending from the mean of the nuclear recoil band acceptance to  $\mu-2\sigma$ .

Table 8.2: Number of events observed,  $n_{obs}$ , in the partitioned signal acceptance region from re-analysed FSR data. Background estimates from simulation for neutrons,  $\mu_{b1}$ , and electron recoils,  $\mu_{b2}$ , from extrapolation of SG fits are given alongside the limit on the signal expectation,  $\mu_s$ .

Acceptance keV <sub>nr</sub>	$n_{obs}$	Neutrons, $\mu_{b1}$	Electron recoils, $\mu_{b2}$	$\mu_s$ , 90% CL
fraction		SG fit		
7–35	29–50%	4	0.5±0.3	5.2±3.1
	2–29%	1	0.7±0.3	1.5±1.7

### 8.3.3 Combined cross-section limits

To conclude the ZEPLIN science programme at the Boulby Underground Laboratory, results from both science runs of ZEPLIN-III were combined to find the best WIMP-nucleon elastic scattering cross-section limit achieved from this series of steadily evolving direct dark matter search experiments.

A combined limit was found from a four-bin PLR analysis, resulting in a 90% confidence interval for  $\mu_s = 0\text{--}6.0$  events, for the full exposure of both science runs. The minimum in the SI upper cross-section limit is located at  $52 \text{ GeV}/c^2$  with a value of  $3.9 \times 10^{-8} \text{ pb}$ . The full curve is shown in Fig. 8.20 (black solid line) alongside the cross-section limit curves from the individual runs and from other direct dark matter search experiments. The characteristic shape of the left ascent of these limit curves is governed by the detector limitations in efficiencies, energy resolution and threshold. The increase in the cross-section limits going towards higher WIMP masses comes from the mass difference of the target with respect to the increasingly heavier WIMP and its decreasing number density.

The presented result strongly disfavours (along with other experiments) the interpretation of the signal reported from the DAMA and CRESST-II experiment in terms of a signal from WIMP elastic nuclear recoils scatters. Models favouring the allowed parameter regions constrained by the CoGeNT dark matter search cannot exclusively be ruled out with the ZEPLIN-III data.

The combined FSR and SSR curve for the SD cross-section analysis is shown in Fig. 8.21. The minimum of the WIMP-neutron cross-section of  $8.0 \times 10^{-3} \text{ pb}$  is reached at a WIMP mass of  $50 \text{ GeV}/c^2$ . At the time of publishing this was the world leading limit. The corresponding WIMP-neutron cross section limit from the XENON10 experiment [228] is not included in Fig. 8.21 since this analysis assumed a constant scintillation efficiency and the more favourable Bonn-A potential (by approximately a factor of 2 [154]). An equal comparison of the results would raise the reported limit above the ZEPLIN-III result. Only very recently, the XENON100 collaboration published a limit on the SD WIMP-nucleon cross-section from the 225 live days dataset, setting the most stringent upper limit on the WIMP-neutron cross-section to date for WIMP masses above  $6 \text{ GeV}/c^2$  [229]. The minimum of  $3.5 \times 10^{-4} \text{ pb}$  is found for a WIMP mass of  $45 \text{ GeV}/c^2$ , over an order of magnitude below the ZEPLIN-III result. However, the more recent calculations of the spin matrix elements by Menéndez *et al.* [230] were adopted for the XENON100 results, with values very close to those calculated with the Bonn-A potential [231], but rather different from the ones using the Bonn-CD potential (used for the ZEPLIN-III SD result).

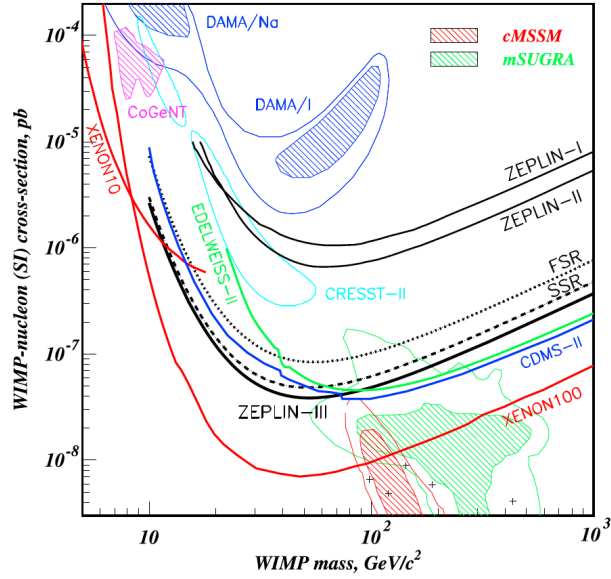


Figure 8.20: Spin-independent WIMP-nucleon cross-section limit curves (90% CL) from the FSR (black dotted line), SSR (black dashed line) and the combination from FSR and SSR data (black solid line). Additional limits from the following dark matter search experiments are shown: XENON100 [219], XENON10 (low energy analysis [95]), CDMS-II [93] and EDELWEISS-II [94]. Moreover, previous results from the ZEPLIN programme are indicated [116, 90]. The 3- and 5- $\sigma$  contours of the DAMA/LIBRA experiment (2008 data, no ion channelling [220]) interpreted in [221] are plotted in blue. The contours of fits to the CoGeNT data under the light WIMP hypothesis [222] and the 2- $\sigma$  region favoured by the CRESST-II data [92] are shown in magenta and cyan, respectively. The favoured regions in parameter space from a 2008 Bayesian analysis in mSUGRA [157] (green) and the likelihood analysis of LHC data within cMSSM [223] (red) are also indicated. This plot represents the status quo of the field at the time of publication of the ZEPLIN-III SSR results [2]. The cross-section limit plot including most recent results is shown in Fig. 3.6 in Chapter 3.

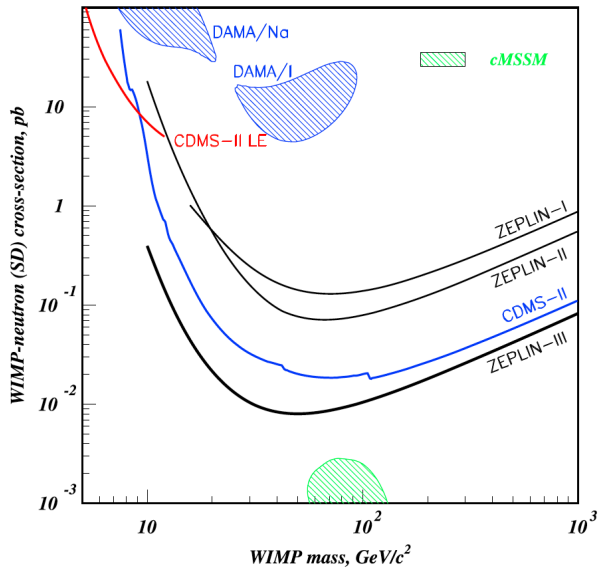


Figure 8.21: Spin-dependent pure neutron coupling (assuming no proton interaction) WIMP-nucleon cross-section limit curve from the combined FSR and SSR data of ZEPLIN-III (thick black solid line). Limit curves from the previous ZEPLIN experiments are indicated [224, 225]. Additionally, the SD cross-section results from the CDMS-II experiment (2004-09 data [156, 93] and low energy (LE) analysis [226]) are shown. The  $3\sigma$  contour of the DAMA experiment (2008 data, no ion channelling [220]) interpreted in [221] is plotted in blue. The tip of the 95% probability region for cMSSM neutralinos [227] is indicated by the green hatched area [2].



## Chapter 9

# Measurement and Simulation of the Muon-induced Neutron Yield in Lead

Rare signal searches, such as those performed for direct dark matter detection ([232, 82, 72] and references therein), are typically carried out in deep underground laboratories. The rock over-burden of such facilities removes or dramatically reduces many of the background signals that would be present if the experiments were conducted in surface laboratories (see Section 7.1.1, Chapter 7). As improved sensitivity is achieved, the need to characterise and mitigate remaining backgrounds becomes ever more important. One of the most problematic backgrounds that still remains is that of cosmic-ray muon-induced neutrons with the potential of becoming a limiting factor for next-generation rare event searches. This specific type of background already shows its impact in current dark matter experiments, with XENON100 reporting it to be the dominant contributor to their nuclear recoil background expectation [69].

In this chapter, I will present a measurement of the neutron production rate in lead induced by high energy cosmic-ray muons using data accrued with the ZEPLIN-III veto detector. The measurement was conducted in parallel to the 319-day long SSR of the experiment. The text and figures follow closely the work presented in Ref. [5] (submitted for publication by the author); an extended introduction and additional information of the analysis process are given. Finally, alternative shielding materials and their consequences for rare events searches are discussed briefly.

## 9.1 Introduction

Neutrons arising from radioactive decays, for example as part of a fission process or produced in  $(\alpha, n)$  reactions following  $\alpha$ -decays of trace contaminations of heavy radio-isotopes, have energies limited to a few MeV (for a discussion of the specific sources for radioactivity neutrons please refer to Chapter 7). In contrast, neutrons produced through interaction of high energy cosmic-ray muons with matter can reach energies of several GeV. Consequently, while radioactivity neutrons may be effectively controlled by appropriate shielding constructions and selection of radio-pure building materials, removing cosmic-ray induced neutrons is more difficult, with the most effective solution being to go deep underground where the muon flux is reduced by several orders of magnitude compared to that at the surface. Passive shielding constructions, installed around the detectors to shield from ambient electron and nuclear recoil type background radiation, can easily be penetrated by high energy muon-induced neutrons. Moreover, these sophisticated layered shielding constructions may in fact even act as a target themselves, leading to an increased background due to the production of neutrons in muon collisions with the shielding material itself. Furthermore, the interacting muon can initiate cascades and showers, generating large number of neutrons. Therefore, further mitigation of this background involves large active muon vetoes, such as large instrumented water tanks, to efficiently detect far away muon tracks and actively reject correlated neutron events.

As previously discussed in Chapter 7, for current relatively small detectors, such as ZEPLIN-III, which feature only several (tens of) kilograms of active scintillator in the fiducialised target volume, the expected rates associated with this type of background are very low and insignificant in comparison to neutron backgrounds from other sources. However, in next generation projects, with target volumes scaled to several tonnes of active scintillator and improved radio-pure construction materials, it may become one of the limiting factors, dominating the nuclear recoil background rate. As such, a precise knowledge of the expected muon and muon-induced neutron flux, in conjunction with the ability to model it correctly, becomes paramount for guiding the design of the detectors and their accompanying obligatory veto systems. Moreover, it is crucial for the correct evaluation of expected background rates (by reducing systematic errors), not only for future experiments, but also in currently pursued rare event searches.

### 9.1.1 Cosmic-rays and muons underground

Primary cosmic-rays interact with the Earth's atmosphere producing fluxes of secondary (tertiary, etc.) particles in cascades, also called air showers, which ultimately lead to the production of cosmic-ray muons. Cosmic-rays are defined as the spectrum

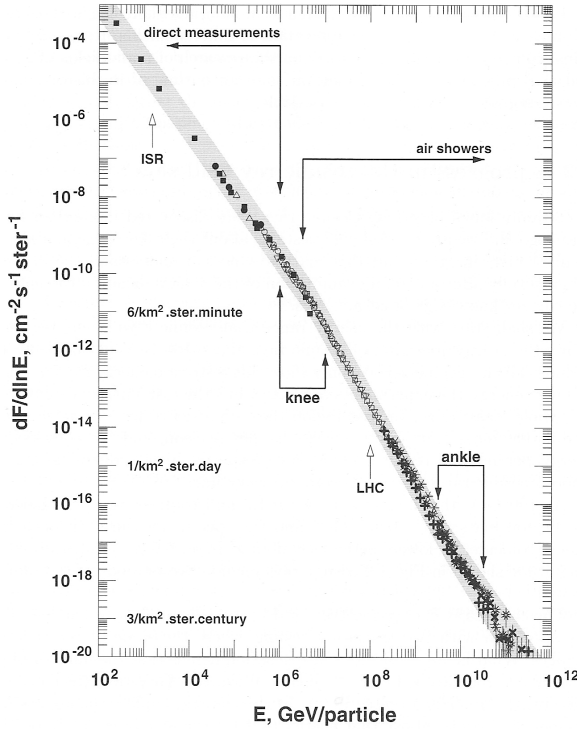


Figure 9.1: Energy spectrum of cosmic-ray nuclei with energies above 100 GeV [233].

of charged particles from interstellar space reaching the Earth's atmosphere. Primary charged particles, sourced in stellar explosions, are accelerated to energies that allow escape from the accelerating medium. The flux of primary cosmic-rays is believed to consist of a menagerie of particles, including almost all stable nuclei in various degrees of abundance, dominated by fully charged H and He particles, a steady flux of electrons, and of a very minor fraction of anti-matter. An energy spectrum of all cosmic-ray nuclei above an energy of 100 GeV is shown in Fig. 9.1. Particles with energies below the 'knee' are thought to be predominantly accelerated within supernova remnants, via processes such as stochastic acceleration and, the much more efficient, acceleration by astrophysical shocks. At energies between the 'knee' and the 'ankle' other galactic sources, such as non-standard supernova remnants, may be responsible for the acceleration of the charged particles. Cosmic-rays above the 'ankle' are believed to originate from extra-galactic sources. A detailed description of cosmic-ray sources, acceleration and secondary particle production is given in Ref. [233].

Once accelerated, cosmic-rays have to propagate through the interstellar medium before reaching our solar system. Interactions of cosmic-rays in the ISM lead, next to

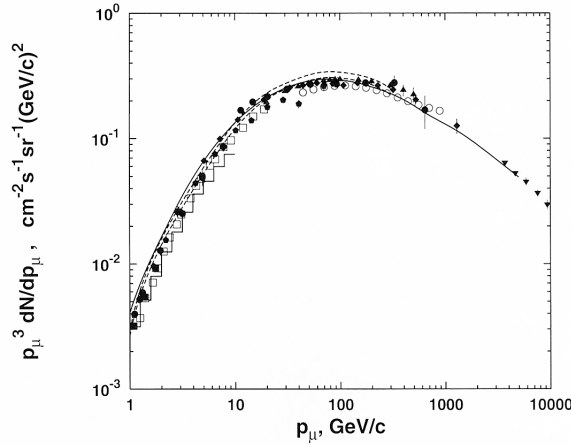


Figure 9.2: Differential muon momentum spectrum weighted by  $p_\mu^3$  as measured at ground level by a number of experiments and from theoretical predictions (dashed lines) [233] (individual references can be found therein).

the production of an array of secondary particles, to an almost perfectly isotropic flux with no correlation or memory of the position of their primary sources (directionality of cosmic-rays with greatest energies may not be completely lost [233]). Upon reaching the atmosphere, cascades of secondary particles are produced in interactions of the cosmic-rays with the atmosphere, including nuclei and mesons. The subsequent decays of these mesons produce the flux of atmospheric muons, with the predominant part coming from charged pion decays (see Eq. (9.1)); contributions from kaon decays are approximately an order of magnitude smaller.

$$\pi^+ \rightarrow \mu^+ + \nu_\mu \text{ and } \pi^- \rightarrow \mu^- + \bar{\nu}_\mu \quad (9.1)$$

At sea level, muons are the most abundant charged particles with a mean energy of  $E_\mu \approx 4$  GeV [234] (primary cosmic-rays almost never reach sea level). Produced high in the atmosphere, they lose about 2 GeV in energy through ionisation processes before reaching the ground. Their characteristic energy spectra are shaped by the production process, energy loss and decay. At low energies the shape of the primary cosmic-ray spectrum is preserved; while at high energies ( $E_\mu > 1$  TeV) the energy spectrum of atmospheric muons is one power steeper than the primary spectrum. At these energies, the atmosphere is not thick enough for pions to decay. For muons with  $E_\mu \approx 3$  GeV the overall angular distribution at ground level is proportional to  $\cos^2\theta$ , where  $\theta$  represents the zenith angle. Figure 9.2 shows the differential energy (momentum) spectrum of atmospheric muons at ground level.

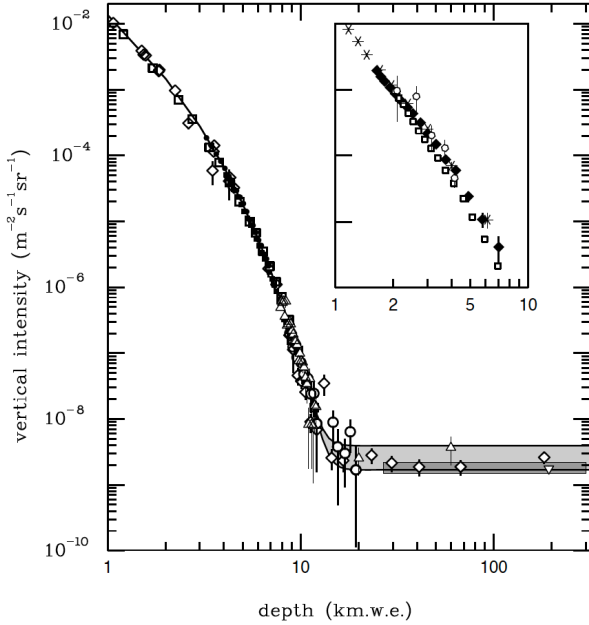


Figure 9.3: Compilation of vertical muon intensity measurements as a function of depth (individual references can be found in Ref. [234]). For better comparison, the experimental measurements, at various depths and from rock overburden of different chemical composition, are converted to standard rock (artificial material with  $A = 22$ ,  $Z = 11$  and density of  $2.65 \text{ g/cm}^3$ ). The depth is given in km w.e., which corresponds to a column depth of  $10^5 \text{ g/cm}^2$  of standard rock. The flat tail of the curve (grey shaded area) represents the locally neutrino-induced muon flux with muons of energies above 2 GeV. The inset shows the vertical intensity curve measured for water and ice. The shallower decrease of the intensity is due to the lower muon energy loss in water [234].

Considering cosmic-ray related fluxes propagating into the ground, secondary particles, such as hadrons, electrons and  $\gamma$ -rays, are absorbed very quickly in the first few meters of rock. Only high energy muons,  $E_\mu > 500 \text{ GeV}$  (and neutrinos), may penetrate deep into the Earth's crust and remaining fluxes can be measured in underground laboratories. While muons in the atmosphere almost exclusively lose energy via ionisation, muons penetrating through rock lose energy through an additional number of different radiation processes, with intensities dependent on the muon energy: bremsstrahlung; direct pair-production, where the muon emits a virtual photon which in turn produces an  $e^-e^+$  pair; and photo-production, again a virtual photon is emitted by the muon, this time interacting hadronically with matter generating secondary hadrons. Figure 9.3 shows the depth intensity curve of the muon flux as a function of penetrated rock.

### 9.1.2 Muon-induced neutrons

A penetrating cosmic-ray muon may produce neutrons via four main processes: muon spallation – *i.e.* muon-nuclear interaction via the exchange of a virtual photon, resulting in nuclear disintegration; muon capture, which is only dominant for low energies and therefore at shallow depths,  $\lesssim 100$  m w.e.; photo-nuclear interactions in muon-triggered electromagnetic showers; and hadron-production in hadronic cascades initiated by the muon. These secondary cascades make up most of the muon-induced neutron production in deep sites. Specifically, neutrons are predominately created by photo-nuclear interactions of  $\gamma$ -rays produced in electromagnetic showers, neutron inelastic scattering, pion spallation and pion absorption at rest. The rate of neutron production by direct muon nuclear interaction is significantly smaller than for the other processes listed [197, 235, 236, 237, 238].

Measuring the flux of these high energy muon-induced neutrons is a non-trivial task. The necessary requirements are very similar to those for a low-background rare event search. Measurements are preformed (predominantly) in deep underground laboratories with detectors that are sensitive to neutrons and which feature large target masses. Moreover, it is crucial to maintain stability of the detection system during the full duration of the experiment, lasting typically for a couple of months up to a year. The task has been pursued by a number of underground experiments (see [236, 237, 238, 239] for a compilation of such results). Most recently, a study on the impact of the muon-induced background in the EDELWEISS dark matter search, alongside estimates for future large scale experiments, has been published [198]. Also recently, the KamLAND collaboration has presented muon-induced neutron rates for a number of target isotopes [240]. Additional work from other groups is ongoing [235]. While for low-A targets, agreement between the different measurements and simulation toolkits (GEANT4 [121], FLUKA [241, 242]) is reasonable, studies of heavy targets are somewhat controversial and inconsistent [243]. Some results from older measurements for lead targets are  $1.75 \times 10^{-3}$  neutrons/muon/(g/cm<sup>2</sup>) [244] and  $1.16 \times 10^{-2}$  neutrons/muon/(g/cm<sup>2</sup>) [245] for a mean muon energy of  $\simeq 110$  GeV and  $\simeq 310$  GeV, respectively. Using an approximation for the muon energy dependency of the neutron yield ( $\propto E^{0.79}$  in hydrocarbon [236]) these values can be converted to a neutron production yield induced by muons with an average energy of 260 GeV (mean muon energy at a depth of 2850 m w.e.), resulting in  $\sim 3.5 \times 10^{-3}$  neutrons/muon/(g/cm<sup>2</sup>) and  $\sim 1.0 \times 10^{-2}$  neutrons/muon/(g/cm<sup>2</sup>). These old lead target measurements, as well as beam measurements [246], without Monte Carlo simulation of neutron production, transport and detection, show much larger neutron yields than expected from simulations [236, 237, 238, 247]. On the contrary, measurements with the veto

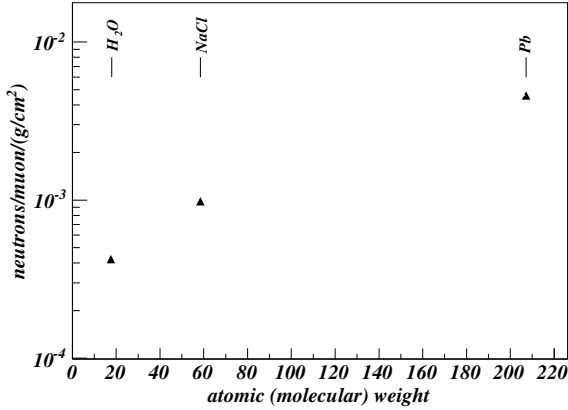


Figure 9.4: Simulated muon-induced neutron yields as a function of the atomic (molecular) weight of some common target materials: rock, water and lead. The rock is represented by  $NaCl$ , which is making up the predominant part of the Boulby rock composition.

of the ZEPLIN-II experiment at the Boulby Underground Laboratory showed an over-production in the simulation by  $\sim 80\%$  [248].

The neutron production cross-section for high energy muons is very large in high-A materials and increases with increasing atomic (molecular) weight. Figure 9.4 demonstrates this behaviour, showing neutron production yields for three different materials, most commonly used for shielding purposes: rock, water and lead. The latter exhibits the greatest yield of them all. Despite this, several rare event search projects utilise large amounts of lead to provide shielding against ambient  $\gamma$ -rays. Thus, the accurate knowledge of the production rate of neutrons by cosmic-ray muons in this material is very important for assessing and planning the capability of these projects, present and future.

## 9.2 Experimental apparatus

Data for this measurement were accrued with the ZEPLIN-III anti-coincidence detector in parallel to the coincidence data taking for the dark matter search in the SSR, by operating the veto in slave and master mode simultaneously. In the master mode the system was triggered when the sum of simultaneously occurring pulses in the roof modules exceeded a set threshold (summed in a dedicated hardware unit), providing high detection efficiencies for cosmic-ray muons. The performance of the veto is well understood through data and validated Monte Carlo simulations [4, 1] (see Chapter 5).

It should be emphasised at this stage that the veto detector was primarily designed to be used as a tool for the tagging of background events in dark matter search data. As such, some parts were specifically developed to enhance its performance as an anti-coincidence device. For example, the addition of Gd-epoxy in the polypropylene part of the veto system results in high detection efficiencies for the radiative neutron capture through the emission of 3–4  $\gamma$ -rays (totalling  $\sim$ 8 MeV) and with a mean delay of only  $\sim$ 11  $\mu$ s [1]. This is of great advantage for detecting and identifying radioactivity neutrons from internal detector components. For the more energetic muon-induced neutrons, which are mostly produced externally, a slower capture on hydrogen in the plastic scintillator is expected. Moreover the energy range of the DAQ was adjusted and tuned especially for background coincidence measurements, thus high saturation of signals are to be expected for the highly energetic muons and neutrons in this specific analysis.

### 9.3 Monte Carlo simulations

Simulated primary muon energy spectra and angular distributions were obtained by propagation of atmospheric muons from the Earth’s surface through an appropriate depth of rock (2850 m w.e. for the Boulby Undergound Laboratory, where 1 m w.e. corresponds to a column depth of  $10^2$  g/cm<sup>2</sup> of standard rock) using the MUSIC code [249, 250]; this distribution was then sampled with the MUSUN code [236, 250]. Both are Monte Carlo based software packages specifically designed for the simulation of muons. The former code, MUSIC, is used for propagating muons through large thicknesses of rock, modelling muon transportation through matter. The latter uses the results from MUSIC to generate muons around the underground laboratory by taking their energy spectrum and angular distribution into account. The energy, momentum, position and charge of each muon was recorded at the point where it intersected the surface of a cuboid, fully enclosing the main cavern of the laboratory. The cuboid included an extra 5 m of rock on each side, except for the top which enclosed a total of 7 m of additional rock. Figures 9.5 and 9.6 show the energy spectrum and the angular distribution, respectively, of primary simulation input muons located on the surface of the virtual cuboid, which were then released for propagation with the GEANT4 Monte Carlo frame work; already propagated muons, crossing the veto detector, are also displayed. The mean energy of the muon distribution was  $\sim$ 260 GeV and 20 million of these muons were generated. The equivalent live-time of the final simulation for the present study amounts to  $\sim$ 3.1 years ( $\sim$ 4.5 times the runtime of the data).

The comprehensive simulation that was developed for the ZEPLIN-III experiment has already been well established in previous studies [122, 4, 145, 164, 1]. This

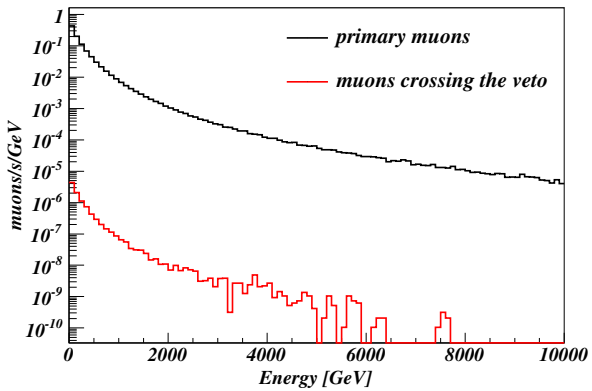


Figure 9.5: Energy spectra of primary muons released from the surface of a virtual cuboid in the rock surrounding the laboratory (black histogram) and muons propagated through the rock and the laboratory crossing the veto detector (red histogram).

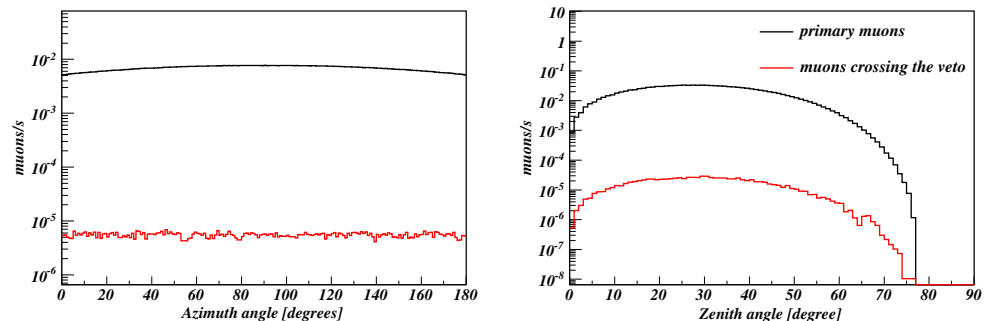


Figure 9.6: Primary muons released from the surface of a virtual cuboid in the rock surrounding the laboratory (black histogram) and muons propagated through the rock and laboratory crossing the veto detector (red histogram); left: azimuth angular distributions; right: zenith angular distributions.

simulation was updated to run with version 9.5 (patch 01) of GEANT4 for this work.

To model the physical processes for this setup the modular physics list `Shielding`, currently recommended for shielding applications at high energies, was implemented. It uses the Fritiof string model (FTF) and the Bertini cascade (BERT) for the high and low energy ranges (up to 5 GeV), respectively, similar to the `FTFP_BERT` reference list but with different neutron cross-section data (JENDL-HE-2007 [251] up to 3 GeV and evaluated cross-sections [252] above 3 GeV) [253]. Neutron interactions below 20 MeV are described by high-precision data-driven models with data obtained from the ENDF/B-VII library [254]. Additionally, thermal scattering off chemically bound atoms was implemented for neutron energies below 4 eV, which is especially important to model thermalisation in the plastics [186]. Secondary particle production thresholds ('cuts') were set to 0.1 mm for  $\gamma$ -rays and  $e^-/e^+$  which, in lead, translate to  $\sim 30$  keV and  $\sim 250$  keV, respectively. This is safely below photo- and electro-nuclear reaction thresholds.

The output generated by the simulation has been designed to recreate that of the experiment, *i.e.* a waveform-like readout with a resolution of  $0.1\ \mu s$  for all 52 individual channels separately. Thus, direct comparison to data as well as the use of similar analysis cuts for experimental and simulated data was possible.

## 9.4 Event selection

During the SSR, it was required that the veto be maximally sensitive to the low energy deposits expected from multiply scattering radioactivity neutrons and  $\gamma$ -rays. Consequently, bias voltages for each PMT were adjusted to deliver a dynamic range in the region of 1–70 phe, corresponding to approximately 20–1300 keV at the far end of the scintillator. A minimum-ionising muon crossing the full thickness of a scintillator bar deposits at least  $\sim 20$  MeV, and thus muon signals, together with a greater number of MeV energy deposits from ambient  $\gamma$ -ray background, result in heavily saturated pulses. Given a single range data acquisition, recording of non-saturated muon events simultaneously with the signal expected from captured neutrons would not be possible. Selection of muons from this data set was therefore non-trivial, but was achieved by searching for coincident saturated signals in roof and barrel scintillators, due to the optical separation of the modules.

Figure 9.7 shows the greatest energy deposition observed in a roof module plotted against the largest corresponding (coincident) signal in a barrel module for each event, occurring within  $\pm 0.2\ \mu s$  around the trigger point. This is similar to the prompt coincidence window used for tagging  $\gamma$ -ray events in ZEPLIN-III (see Section 5.2.3, Chapter 5). A well separated population is observed, with a graphical selection criterion

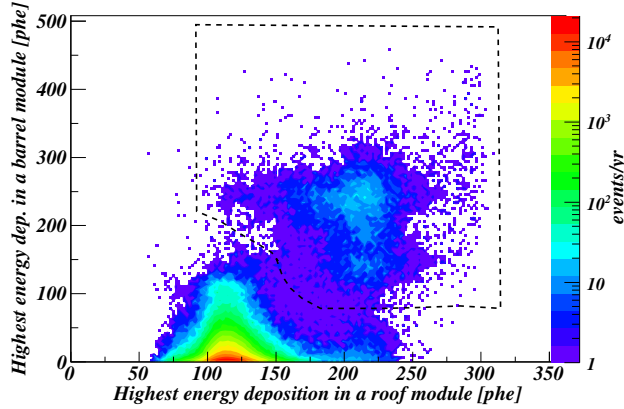


Figure 9.7: Highest energy deposition observed in one of the roof scintillator modules versus the time-coincident highest energy deposition in a barrel scintillator module. The dashed line indicates the graphical cut used to select the muons. Note that energy depositions  $\gtrsim 100$  phe are saturated.

indicated. Here, the photoelectron scale is defined by using a constant conversion factor between the pulse area and the pulse height parameter, which was utilised for the single photoelectron calibration. Given that the pulse area is less affected by saturation than the pulse height (due to the abrupt cutoff in the latter), the impact of saturation can be pushed to higher energies ( $> 100$  phe), and so improve separation of event populations.

Selection of muons in the simulation followed a very similar procedure. Firstly, events with a minimum energy deposition observed from the summed signal of the veto roof, analogous to the trigger function of the veto detector, were selected (see Fig. 9.8). Additionally, as in the data, a cut on time coincidence ( $0\text{--}0.4 \mu\text{s}$ ) between roof and barrel was applied. In Fig. 9.9 the region selected, corresponding to muon signals, is indicated by the dashed line. Figure 9.10 shows the projection of Fig. 9.9 on to the y-axis. Here, the Monte Carlo data are plotted as a function of the largest energy deposition in the (coincident) barrel module only. Separate curves are shown for all events satisfying the coincidence condition, and for only those events corresponding to energy depositions directly resulting from muon traversal of scintillator modules. The difference between the two curves is predominantly due to the energy depositions from particles generated in showers as muons pass nearby. A simple cut at the position indicated by the dashed line selects a population which is composed of  $\sim 93\%$  muon energy depositions with the required coincidence, *i.e.* at least one roof and one barrel module firing within the defined coincidence window.

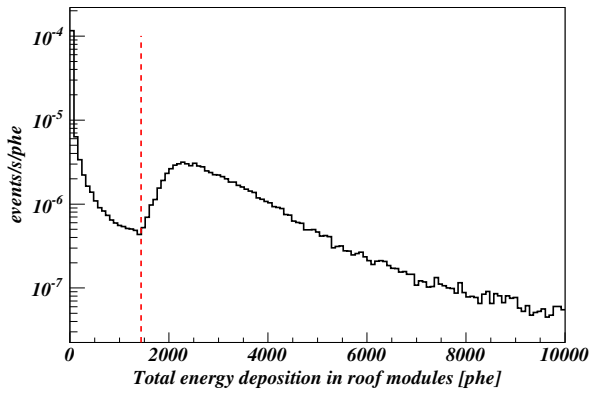


Figure 9.8: Energy depositions summed over all roof modules in a coincidence window around the trigger time from simulations. The red dashed line indicates the applied cut.

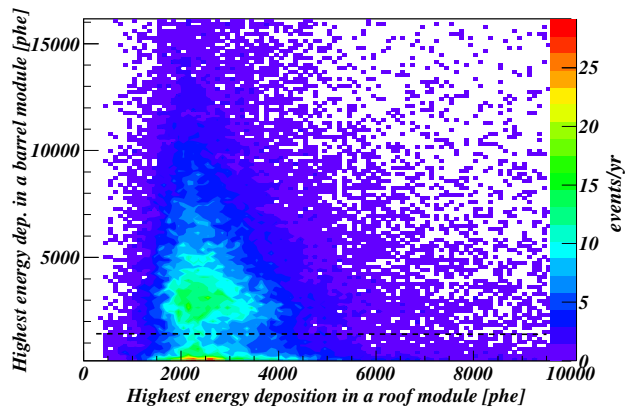


Figure 9.9: Muon event scatter plot from simulations, showing the highest energy deposition observed in one of the roof scintillator modules versus the time-coincident highest energy deposition in a barrel scintillator module. The dashed line indicates the applied selection cut.

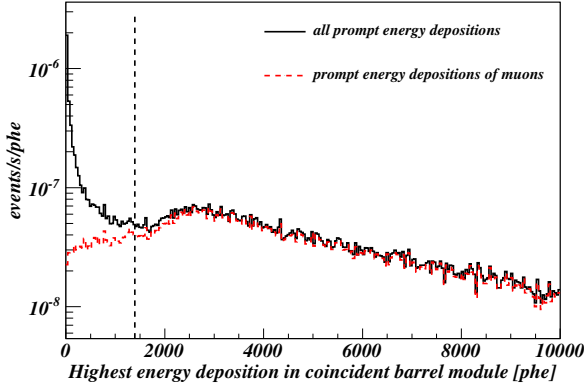


Figure 9.10: The plot shows the highest energy deposition observed in a barrel scintillator module when measured in coincidence with a roof module for all prompt energy depositions in the simulation (black solid). The red dashed spectrum shows the same but for muon hits only, *i.e.* the muon crosses both the roof and the coincident barrel module. The cut used to select muon events is indicated by the thick dashed vertical line.  $\sim 88\%$  of muons with a roof – barrel coincidence have energies above this threshold.

Confirmation that the identified region in the experimental data corresponds to the muon event region in the Monte Carlo was provided by comparing the event distributions between pairs of roof modules and barrel modules, as shown in Fig. 9.11. Here, the two upper panels show the distribution of roof modules (numbered 32–51) registering a coincidence with a specific barrel module (modules 3 and 19, as indicated). Similarly, the lower panels show which barrel modules were in coincidence with which roof modules (39 and 46). A schematic of the veto detector (viewed from above) indicating the number assigned to each individual scintillator bar, is shown in Fig. 9.12. The combination of the relative orientations of the modules with respect to each other, their individual response functions, and the asymmetric impact of the surrounding laboratory geometry, resulted in a complex distribution of coincidences between modules. However, the Monte Carlo reproduced the experimental data reasonably well (the average reduced  $\chi^2$  value of these 51 coincidence contributions is  $\sim 1.9$ ), confirming that the selected experimental data correspond to cosmic-ray muon events.

The overall efficiency for the detection of pure muon events, including previously mentioned effects and the (geometric) requirement for coincidence between barrel and roof is  $36.8 \pm 0.6\%$ , where the error includes uncertainties due to the precise choice of the location of the selection cuts. A total number of 7979 muons was selected from the

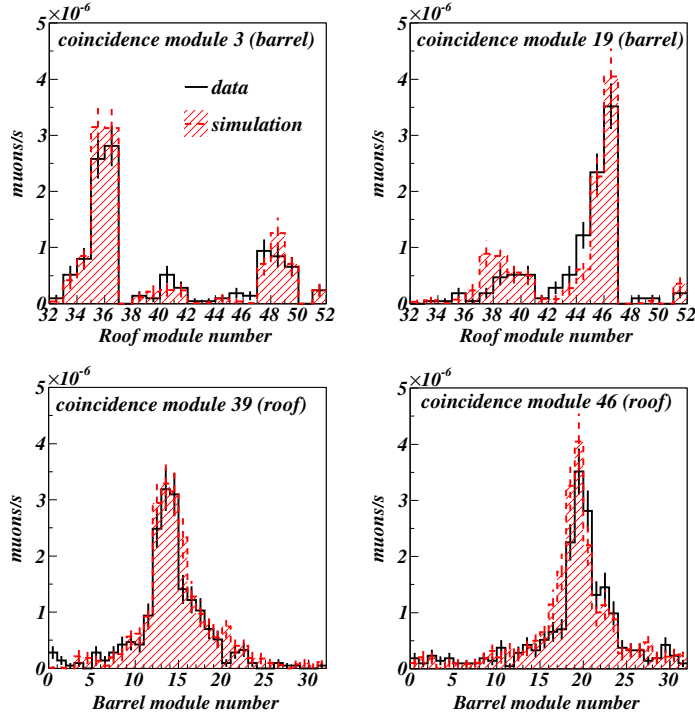


Figure 9.11: Sample of coincident channels from two barrel slabs (top, module 3 and 19) and two roof slabs (bottom, module 39 and 46) with all modules (channels) of the roof and the barrel, respectively. The simulation, scaled to the total muon rate observed in the data, is shown by the red dashed hatched histogram in comparison to the data (black histogram).

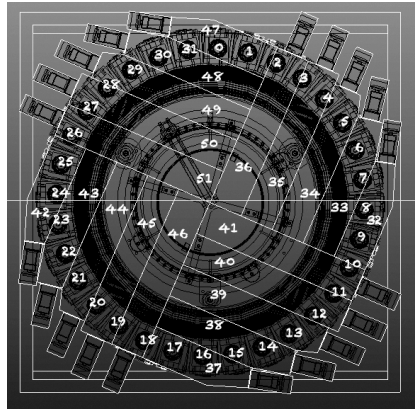


Figure 9.12: Schematic of the ZEPLIN-III veto detector viewed from above indicating the number assigned to each individual scintillator module: barrel modules 0–31 and roof modules 32–51.

full dataset translating to a rate of  $32.3 \pm 0.4$  muons/day. By comparing the measured rates to the Monte Carlo predictions, using the normalised flux through a sphere in the simulation in a similar way to [248], a muon flux of  $(3.75 \pm 0.09) \times 10^{-8}$  muons/s/cm<sup>2</sup> was deduced. This result is in excellent agreement with the last reported value for the muon flux in the Boulby Underground Laboratory of  $(3.79 \pm 0.15) \times 10^{-8}$  muons/s/cm<sup>2</sup> [248], measured in the cavern hosting both the ZEPLIN-II and ZEPLIN-III detectors, and  $\sim 8\%$  lower than the value obtained for another cavern in Boulby reported in [255].

As an additional check, the muon flux was also calculated following the method in Ref. [255] by determining the effective area, including all geometrical factors and applied analysis cuts, of the veto detector. Robinson *et al.* calculated the proportion of muons passing through a 2 m sided cube in the Boulby Underground Laboratory, and subsequently determined its effective area,  $\langle S \rangle$ , using Eq. 9.2.

$$\langle S \rangle = \frac{\int I_\mu(\theta, \Phi) S_\perp(\theta, \Phi) d\Omega}{\int I_\mu(\theta, \Phi) d\Omega}, \quad (9.2)$$

where  $I_\mu(\theta, \Phi)$  is the flux of muons as a function of zenith angle,  $\theta$ , and azimuth angle,  $\Phi$ , in the laboratory, and  $S_\perp(\theta, \Phi)$  is the area of the cube perpendicular to the muon flux as a function of zenith and azimuth angle. In a very similar manner, a virtual cube, enclosing the whole detector setup, was constructed for the present simulation and muons passing through it counted. An effective area of  $10100 \pm 200$  cm<sup>2</sup> was determined for the ZEPLIN-III veto for this specific application and analysis, resulting in a muon flux of  $(3.70 \pm 0.09) \times 10^{-8}$  muons/s/cm<sup>2</sup> (assuming no error on the effective area calculation in Ref. [255]). Good agreement with previous results is demonstrated.

## 9.5 Muon-induced neutron yield

The vast majority of detected neutrons produced by muons in this set-up originated in the  $\sim 60$ -tonne lead shield (20 cm thick, with a side length of  $\sim 2.3$  m and a height of  $\sim 2.4$  m), which protected the experiment from ambient  $\gamma$ -rays. To determine the muon-induced neutron yield in lead from the present data the number of neutrons captured in the veto following a recorded muon event were counted. This was compared with simulations performed using the same analysis cuts. It should be noted that a data set with single photoelectron resolution is a real asset: at the expense of a small increase in background rate, the low threshold analysis increases the number of detected neutrons substantially in comparison with previous works.

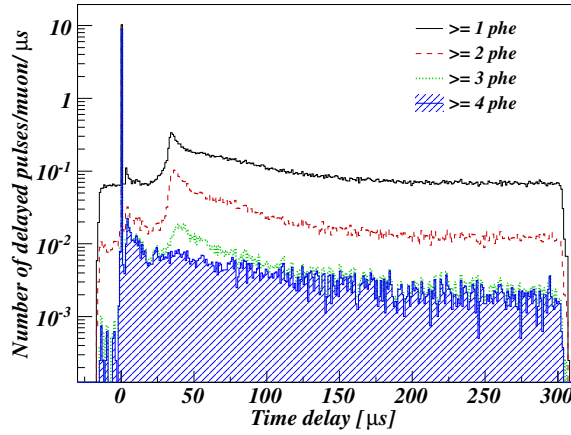


Figure 9.13: Time delay distribution for all recorded pulses above given thresholds relative to the muon.

### 9.5.1 Experiment

As described previously, neutrons were identified through signals occurring in one or more of the 51 scintillators as a result of the  $\gamma$ -rays emitted following their capture. These signals were delayed relative to the muon's passage due to the time for thermalisation and capture to occur. Ideally, the data would have been searched for the signatures of neutron captures over the entire period in which these signals may have arrived. However, the PMT response to a large energy deposition was such that the timelines became at first heavily saturated, and then were followed by a large signal overshoot. For extreme energy depositions the overshoots persisted for up to 40  $\mu$ s. The effect of these ‘dead’ waveform periods can be seen in Fig. 9.13, showing a significantly reduced pulse rate for the first  $\sim$ 40  $\mu$ s after the muon trigger. Thus, the timeline for detecting delayed neutrons was restricted to the region of 40–300  $\mu$ s relative to the observed muon. An efficiency of  $\sim$ 47% was retained from this timeline selection cut (calculated from simulations, recording neutron events up to 1 ms after the muon trigger). Furthermore, the maximum number of recorded pulses was restricted to 300 entries per event (an equivalent cut was implemented in the analysis of the simulation). The impact of this restriction is discussed in Section 9.5.2.

For the detection of muon-induced neutrons, as compared to internally-generated radioactivity neutrons, which are of predominant concern in dark matter searches, one expects an increased importance of neutrons capturing on hydrogen. In the dark matter veto case, the neutrons have scattered within the ZEPLIN-III device, and thus have a high geometrical likelihood of being captured in the Gd-loaded polypropylene shielding

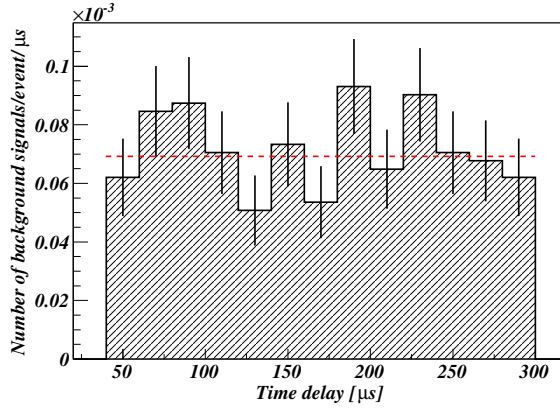


Figure 9.14: Time delay distribution of channel multiplicity one events (threshold of  $\geq 10$  phe) in ZEPLIN–III coincident background data. The dashed (red) line indicates the constant fit to the background.

immediately surrounding the target. Most muon-induced neutrons come from outside of the setup and will more likely be captured in the hydrocarbon scintillator material surrounding the Gd-loaded shielding. A single  $\sim 2.2$  MeV  $\gamma$ -ray is emitted following capture on hydrogen, and therefore signals observed in a single scintillator module are more likely to occur – in contrast to the several  $\gamma$ -ray signature from Gd capture, which can be recorded simultaneously in several scintillator modules. Due to the relatively long capture times of neutrons on hydrogen in comparison to captures on gadolinium, the rejection of the first  $40\ \mu\text{s}$  of the waveforms reduced the probability of detection with single scintillator signals by only  $\sim 26\%$ .

Single scintillator events are more exposed to backgrounds, and careful consideration of thresholds and a good knowledge of those backgrounds are required. Since available statistics of the limited pre-trigger timeline fraction were very scarce, an additional data set from the same run with similar trigger conditions was used to estimate the background correctly. The dataset of synchronised (with ZEPLIN–III) slave triggered veto events (see Section 5.1.3, Chapter 5) was considered to calculate the background. Optimisation of the number of neutron captures observed in the muon triggered data, with respect to the number of false events due to background, resulted in a threshold of  $\geq 10$  phe being chosen for single scintillator events. Figure 9.14 shows the rate of background events with a threshold of  $\geq 10$  phe applied. The rate is approximately constant, *i.e.* it is independent of the time since the trigger occurred.

Following the methodology used in the analysis of the dark matter search data, coincident signals in multiple scintillators can also be searched for, detecting

multiple scatters and  $\gamma$ -rays following neutron capture on gadolinium at later times. Coincidences were defined as occurring within  $\pm 0.2 \mu\text{s}$  of each other. To optimise efficiency, different signal size thresholds have been required depending on the number of signals in coincidence, balanced against the rate of false signals arising from non-neutron related sources (background and induced noise). Noise from the PMTs can be intrinsic, *i.e.* from thermionic emission and internal radioactive decays, or directly induced. Especially after larger signals, such as resulting from muons, positive ions generated from ionisation of residual gases in the PMTs lead to secondary signals. These create afterpulsing at short time scales of up to several  $\mu\text{s}$  dependent on the ion transit time (see [172, 256] and references therein). In the present data, afterpulsing of small amplitudes were suppressed at short decay times due to the large pulse overshoots observed following a muon energy deposit (see Fig. 9.13). A second noise component observed at longer time scales, visible in Fig. 9.13 between  $\sim 30\text{--}50 \mu\text{s}$  after the start of the muon signal, with sizes of 4 phe and below, may be attributed to the organic scintillator. Luminescence with long time constants is expected from phosphorescence and delayed fluorescence processes in the plastic scintillator (see *e.g.* [172, 257, 258]).

These additional signals could lead to false coincidences between scintillators, generating spurious neutron detections. Based on the event rates, the probability of false coincidences can be calculated. It was found that for neutron capture events with a channel multiplicity of two, *i.e.* two scintillator bars firing within  $\pm 0.2 \mu\text{s}$  of each other, a signal size requirement of threshold  $\geq 4$  phe (in each pulse) was sufficient to remove afterpulses. For three-fold coincidences between scintillators, a threshold of  $\geq 2$  phe per signal was found to be appropriate, and for four or more scintillators, a threshold at the level of a single photoelectron was sufficient. For consistency, a global requirement was set that regardless of the number of scintillators fired in coincidence, all events must have a total signal size of at least 8 phe. Despite the lower threshold for multiple scintillator events, accidental rates arising from background were substantially smaller due to the required coincidences of pulses. The same dataset as used earlier to estimate the background rate in the single scintillator case has thence been utilised to calculate the contribution from background to the yields of neutron captures from the multiple scintillator requirements. Background rates found were at the level of statistical uncertainties. Table 9.1 summarises the results. Each instance in which the designated criteria were met was interpreted as indicating a neutron capture. Most muon-induced neutron captures were observed through events seen in single scintillators only, despite the higher threshold required. However, a significant number also generated energy depositions observed in coincidence in several scintillators. Overall, a mean of  $0.346 \pm 0.007$  neutrons (including background corrections) were observed for every muon detected.

Table 9.1: Measured number of neutrons per muon from the data in comparison to neutron rates extracted from simulations using the same requirements and cuts as in the experimental data analysis. Background rates, for correction of the data, are listed individually for the different channel multiplicities (their required thresholds for the individual pulses are also indicated). The errors given for the data are the sum of statistical errors and the rate coming from random accidental coincidences of pulses calculated from the average observed pulse rate for a given threshold. Errors of simulated rates are statistical only.

Channel mult.	Threshold	Data		Simulation	
		Events/muon	Background rate	n/muon (bkg.corr.)	n/muon
1	$\geq 10$	$0.216 \pm 0.005$	$0.019 \pm 0.001$	$0.197 \pm 0.005$	$0.145 \pm 0.002$
2	$\geq 4$	$0.088 \pm 0.003$	$0.0049 \pm 0.0005$	$0.083 \pm 0.003$	$0.076 \pm 0.001$
3	$\geq 2$	$0.039 \pm 0.002$	$0.0019 \pm 0.0003$	$0.037 \pm 0.002$	$0.0321 \pm 0.0009$
$\geq 4$	$\geq 1$	$0.029 \pm 0.002$	$0.0008 \pm 0.0002$	$0.028 \pm 0.002$	$0.0231 \pm 0.0008$
Total		$0.372 \pm 0.007$	$0.026 \pm 0.001$	$0.346 \pm 0.007$	$0.275 \pm 0.003$

### 9.5.2 Comparison with simulations

Monte Carlo simulations of the experiment have been performed as described in Section 9.3. The dimensions and parameters of the apparatus have been previously measured and documented [164, 145, 3] (see also Chapter 5), including signal gains and attenuation lengths of the scintillators so that photoelectron spectra could be generated. This allowed Monte Carlo pseudo-data to be analysed using identical routines as used for the real data. The overall agreement on the rate of detected neutrons between data and simulation obtained is good, at the level of 25%. For the initial discussion the total number of neutrons has been normalised to the data.

Figure 9.15 compares the time delay distributions for detected neutrons from data (solid black) and simulation (red dashed). Excellent agreement between the two distributions was found. Moreover, the module (channel) multiplicity per neutron event was used as an additional consistency check, beyond the initial muon identification, taking advantage of the segmented nature of the detector. Figure 9.16 shows the number of channels with coincident signals involved in each individual neutron event. The data were corrected for the contributions from background coincidences, as given in Table 9.1. Again, excellent agreement, over the full range of channel multiplicities, is demonstrated.

In Fig. 9.17 the energy depositions associated with the observed (captured) neutrons are given in the region before the onset of saturation, with excellent agreement between simulation and data obtained. Importantly, here, for the comparison of detected neutrons in the data with simulations the original single photoelectron calibration

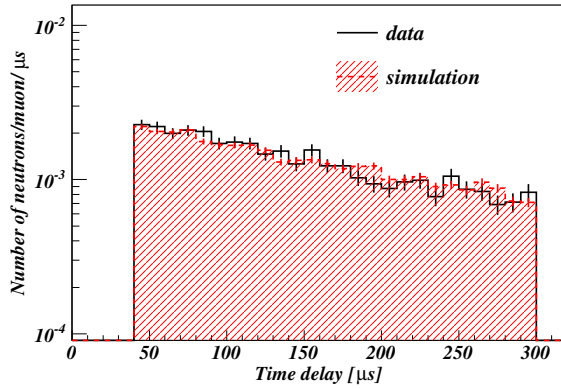


Figure 9.15: Time delay distribution of detected captured neutrons from experimental data (black solid histogram) and simulations (red dashed hatched histogram). The constant background has been subtracted from the data histogram. Results from simulation are normalised to the total number of neutrons observed in the data.

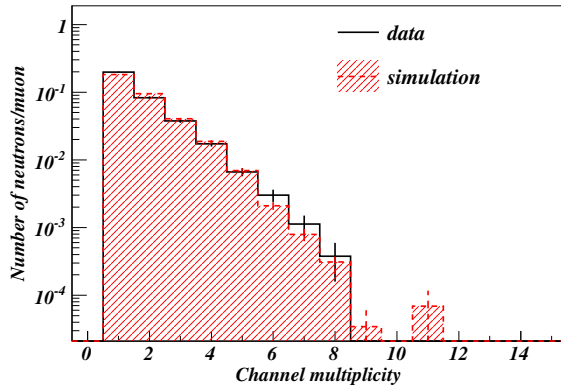


Figure 9.16: Comparison of channel (scintillator module) multiplicities per detected neutron in the data (black solid) to simulations (red dashed hatched histogram). The data are background corrected according to Table 9.1. Results from simulation are normalised to the total number of neutrons observed in the data.

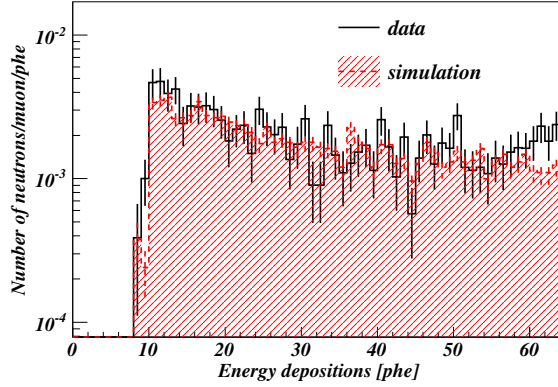


Figure 9.17: Energy depositions of detected neutrons from background corrected data (black solid) and simulations (red dashed hatched histogram) below the saturation point in the data, *i.e.* the energy scale is given in absolute number of photoelectrons (1 phe  $\simeq$  20 keV). Results from simulation are normalised to the total number of neutrons observed in the data.

defined via the pulse height parameter (accessing the database described previously in Section 5.2.1, Chapter 5) was used to ensure highest possible accuracy for the region of interest (energy depositions of only a few phe) for neutron detections (*cf.* the thresholds used for the neutron identification). Calibration of the simulation has been carried out in a similar way to that performed for the quenching factor study in Chapter 6. Although the energy calibration was only known to within  $\sim 10\%$  due to, amongst other factors, the saturation of the data, tests in varying the energy scale by this amount resulted in only small neutron rate differences and were considered in the systematic error of the simulated rate.

A muon may produce more than one fast neutron in a cascade, resulting in several neutron capture signals at different times and in different locations in the veto. Figure 9.18 shows the relative fraction of observed neutrons per muon for data and simulation. When exploring neutron multiplicities, rather than scaling the simulation to the total number of neutrons observed in the data, a simple normalisation to the number of detected muons was applied. For background corrections even distribution of background events was assumed. As such, most non-neutron signals would have occurred in one of the empty waveforms following a muon trigger, making up almost 90% of all observed muon events. Generally, good agreement is observed.

When scaled to the number of neutrons detected, the simulations reproduce well the time distributions, the energy depositions and the number of scintillators involved in each event. The absolute numbers of neutrons expected to be observed per muon,

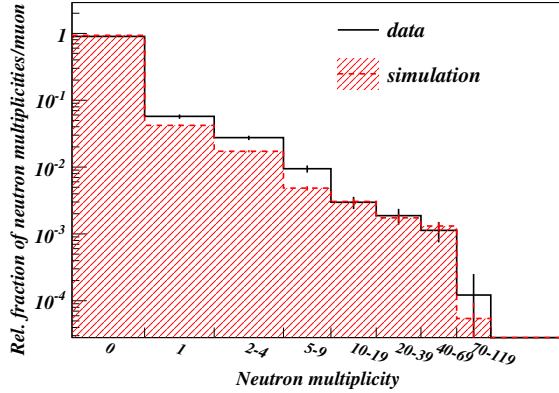


Figure 9.18: Relative fraction of neutron multiplicities per muon, *i.e.* the number of delayed signals observed after a muon trigger in the defined time window, for background corrected data (black solid) and simulation (red dashed hatched histogram) normalised to the total number of observed muons in each case.

as determined from the simulation for each individual channel multiplicity, are also summarised in Table 9.1, showing an overall reduced neutron rate from simulations of  $\sim 20\%$  (*i.e.* the total yield from the data exhibits an increase over the simulation by  $\sim 26\%$ ). Discrepancies are largest for single scintillator events. At higher multiplicities absolute agreement between simulation and data is of order 10–20% (*cf.*  $\sim 36\%$  for single scintillator events). The expected total muon-induced neutron rate calculated from simulations is  $0.275 \pm 0.003$  (stat.)  $^{+0.004}_{-0.007}$  (syst.) neutrons/muon. Systematic errors were calculated from the variability in the energy calibration.

Regarding the discrepancy for single channel neutron events, the agreement between data and simulation for the spectrum of energy deposits for single scintillator events does not differ significantly from the one shown for all multiplicities in Fig. 9.17. Increasing the analysis threshold to  $\geq 14$  phe for channel multiplicity one events reduced the absolute disagreement between simulation and data only marginally from  $\sim 36\%$  to  $\sim 33\%$ . Moreover, tests in limiting the chosen time window further, *i.e.* going from 40–300  $\mu$ s to 80–300  $\mu$ s, did not show any improvement, whilst the data suffered a great loss in statistics.

As previously mentioned, a restriction on the maximum number of recorded pulses was applied to the data, and similarly in the analysis of the simulation. Importantly, the number of selected muon events, in both data and simulation, affected by this limitation are in excellent agreement with each other, further supporting the good performance of the Monte Carlo simulation. In the data 11 events were counted; the number in the simulation (scaled to the data) amounts to  $11 \pm 2$  events. When including all energy

depositions in the simulation a higher absolute neutron rate was observed ( $\sim 30\%$ ). This increase can be connected with only a few muon events (approximately 1 in 1700, counting only events exceeding the highest multiplicity observed in the data) featuring exceptionally high neutron multiplicities. For example, one simulated event was found to be correlated with up to 323 delayed coincidences (in the restricted time window of 40–300  $\mu$ s). Moreover, it was shown that this specific event was associated with over 2000 neutron captures on H alone. Thus, due to the finite bin width, overlaps of unrelated capture  $\gamma$ -rays are very likely to occur for these exceptional events, artificially decreasing the number of observed neutrons; at the same time the channel multiplicities for some of the neutrons are artificially increased. Crucially, one such extreme event was also observed in the experimental data, affirming that these were not artefacts of the simulation only. Figure 9.19 shows a snapshot of this event (in fact the event lasted for 3 ‘events’ in a row, *i.e.* up to  $\sim 1$  ms) displayed in the RaVen event viewer. Each of the lines corresponds to a waveform of one of the 52 scintillator modules. The extremely low rate of these events (1 in 10 months of data taking) highlights the importance of very high statistics for future muon-induced neutron studies. However, it is worth noting that these high multiplicity events are less significant for dark matter searches due to the generally high veto efficiencies expected for these.

Table 9.2 shows the relative production of neutrons in different materials for all neutrons generated in the simulation, and for detected neutrons only. As expected, nearly all neutrons were produced in the rock cavern of the underground laboratory, reflecting that the simulation included sufficient volume to remove edge effects. Importantly, less than 1.5% of detected neutrons were produced in the rock, confirming the effectiveness of the shielding setup of the ZEPLIN-III detector. On the other hand, the lead component of the shielding enclosure evidently provided an effective target for neutron production by high energy cosmic-ray muons, with  $\sim 95\%$  of all detected neutrons having been created there.

Table 9.3 lists the specific elements involved in the capture of the neutrons, both for detected neutrons and for all the neutrons in the simulation. As previously mentioned, the vast majority of detected muon-induced neutrons were captured on hydrogen, emphasising the importance of measuring the single  $\sim 2.2$  MeV  $\gamma$ -ray from this process. The captures on Gd amount to only  $\sim 7.0\%$  for this configuration at these neutron energies (being much more effective for internal radioactivity neutrons due to the detector geometry).

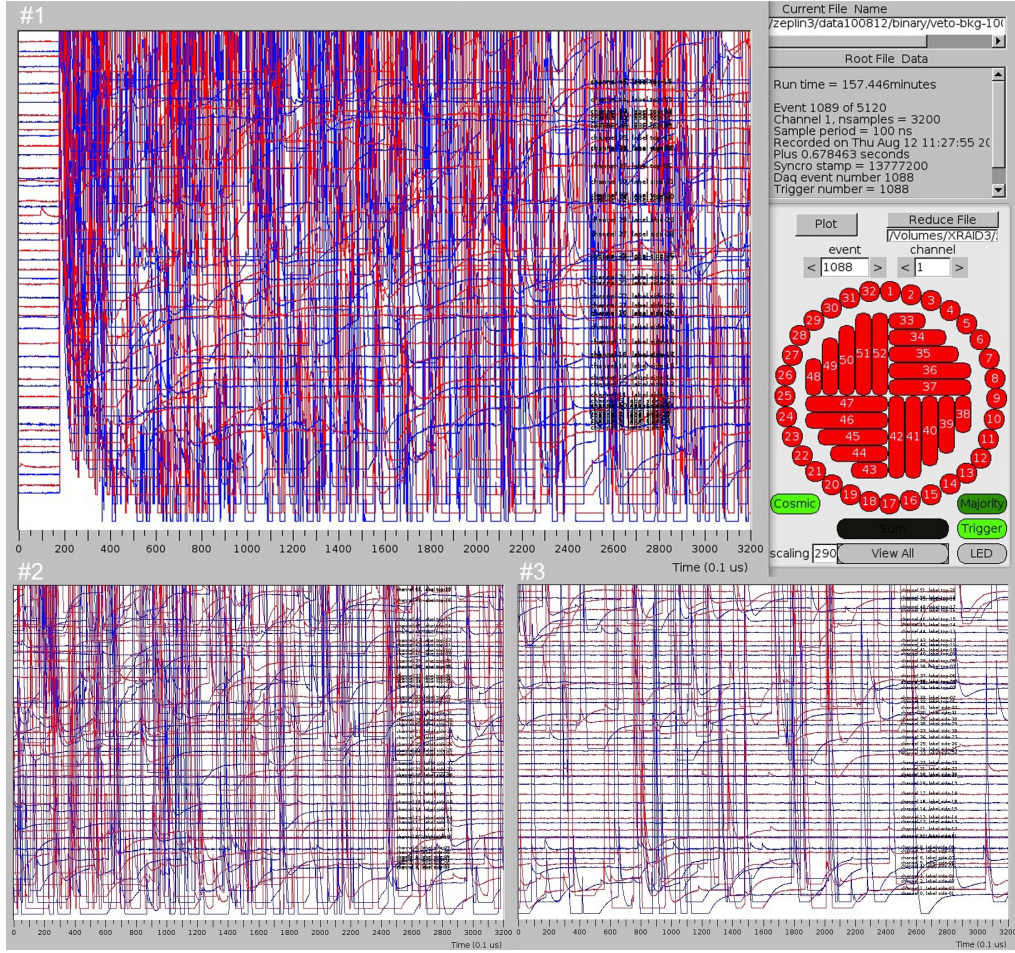


Figure 9.19: Screenshot from RaVen showing an extreme high neutron multiplicity event recorded with the ZEPLIN-III veto DAQ. Numbers at the top of each display indicate the order of the sequentially recorded waveforms associated with the same event number identifier.

Table 9.2: Fractions of neutrons produced in different materials for all generated neutrons in the simulation and for detected neutrons only.

Material	Production material of	
	all neutrons	detected neutrons
Lead	0.2%	95.0%
Rock	99.8%	1.4%
Steel	-	1.2%
C <sub>8</sub> H <sub>8</sub>	-	0.9%
Copper	-	0.8%
CH <sub>2</sub>	-	0.5%
Gd-epoxy	-	0.1%
Liquid Xe	-	0.1%

Table 9.3: Fractions of neutrons captured on different elements for all and for detected neutrons only.

Element	Capture element of	
	all neutrons	detected neutrons
H	-	71.1%
Fe	-	11.5%
Cl	94%	7.0%
Gd	-	7.0%
Pb	-	1.3%
C	-	1.1%
Cu	-	0.6%
Na	6%	0.2%
Mn	-	0.2%

### 9.5.3 Muon-induced neutron yield in lead

As shown in Table 9.2, the detected neutrons have predominantly been produced in lead. Thus, the observed neutron rate may be used to derive an absolute neutron production yield in this material. The methodology used follows that of Refs. [197, 248], and is essentially to scale an idealised simulation of neutron production by a mono-energetic beam of muons in pure lead by the ratio in rate observed between the present data and the full detector simulation (assuming that the fraction of detected neutrons produced in lead ( $\sim 95\%$ ) is well described by the simulation).

The simulation of a mono-energetic muon beam in lead was conducted as follows. Neutron production was recorded for a mono-energetic 260 GeV  $\mu^-$  beam (mean muon energy at Boulby), incident on the centre of a lead block of 3200 g/cm<sup>2</sup> thickness. Figure 9.20 shows the differential energy spectrum of neutrons produced. Only neutrons from the central half length of the lead block were considered to avoid surface/edge

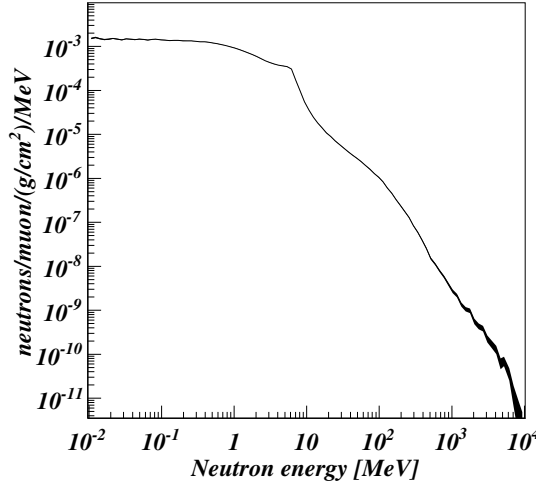


Figure 9.20: Differential energy spectrum of muon-induced neutrons produced in lead by  $\mu^-$  of 260 GeV.

effects. To prevent double counting of neutrons in neutron inelastic processes, the first neutron produced in each reaction was dismissed independent of its energy. A neutron production rate of  $(4.594 \pm 0.004) \times 10^{-3}$  neutrons/muon/(g/cm<sup>2</sup>) was obtained for the physics list and version of GEANT4 used for this particular work (`Shielding` with version 9.5). However, since the experimental muon-induced neutron rate was found to be a factor of  $1.26 \pm 0.03$  (stat.)  $^{+0.04}_{-0.03}$  (syst.) higher, the results suggest a true production rate by 260 GeV muons of  $(5.8 \pm 0.1 \text{ (stat.)} ^{+0.2}_{-0.1} \text{ (syst.)}) \times 10^{-3}$  neutrons/muon/(g/cm<sup>2</sup>), assuming neutron transport and detection were modelled accurately.

In this analysis, uncorrelated arrival of muons was assumed, as opposed to muon bundles produced together by primary cosmic-rays in the atmosphere. A study based on a simple approximation to find the survival probability of muons at a given depth showed the effect to be negligible and the error to be very small for the measurement performed with the ZEPLIN-III veto detector [259].

### Changes in the neutron production yield from simulations

It is also of interest to explore the evolution of the neutron production yield with successive versions of GEANT4. To do this further simulations of a mono-energetic  $\mu^-$ -beam focused on a lead block have been performed. Table 9.4 summarises the results, including the yield obtained with version 8.2 from Ref. [197]. In addition, combination of different physics lists and GEANT4 versions are listed, also linking the

custom list used in [197] to the current high energy reference lists. The bespoke physics list is very similar to `QGSP_BIC_HP`, featuring the Quark-Gluon String (QGS) theoretical model at high energies coupled to nuclear de-excitation with a pre-compound model, the intra-nuclear Binary Cascade (BIC) model below 6 GeV and a data-driven high-precision neutron package (`NeutronHP`) to transport neutrons below 20 MeV down to thermal energies. Reasonable variation of change-over energies between the BIC and QGS models in the custom physics list in comparison to the reference one have little impact (<3%) on the overall neutron yield. A steady increase with every new version of GEANT4 is demonstrated.

Table 9.4: Muon-induced production yields for neutrons for different versions of GEANT4 and physics lists (for 260 GeV muons). The neutron yield from version 8.2 is based on the value reported in Ref. [197]. A small modification has been applied to correct for a previously unaccounted error in the rejection of neutrons produced in neutron inelastic processes to avoid double counting (referred to as ‘stars’ in that work).

GEANT4 version	physics list	muon-induced neutron yield [neutrons/muon/(g/cm <sup>2</sup> )]
8.2	custom built	(2.846±0.006)×10 <sup>-3</sup>
9.4	custom built	(3.304±0.003)×10 <sup>-3</sup>
9.4	<code>QGSP_BIC_HP</code>	(3.376±0.003)×10 <sup>-3</sup>
9.4	<code>Shielding</code>	(3.682±0.003)×10 <sup>-3</sup>
9.5	<code>QGSP_BIC_HP</code>	(3.993±0.004)×10 <sup>-3</sup>
9.5	<code>QGSP_BERT_HP</code>	(4.369±0.004)×10 <sup>-3</sup>
9.5	<code>FTFP_BERT</code>	(4.467±0.004)×10 <sup>-3</sup>
9.5	<code>Shielding</code>	(4.594±0.004)×10 <sup>-3</sup>

The `Shielding` physics list shows not only the largest muon-induced neutron production yield in comparison to other reference lists, but is also subject to the highest increase in going from version 9.4 to 9.5. This is explored in detail in Fig. 9.21, showing the individual contributions from the most important neutron creation processes for muons in lead. The main difference lies in the increased neutron production in inelastic scattering of hadrons, and in particular, neutrons: A ∼38% higher production yield for this process is observed. Part of the increase observed between versions 9.4 and 9.5 of the toolkit (applicable to all standard lists used in this study) can be attributed to the muon-nucleus interaction model (`G4VDMuonNuclearModel`); as in previous versions, this still relies on the Kokoulin mu-nuclear cross-sections [260], but the final state of the hadronic vertex is now replaced by a  $\pi^0$  interacting further through the Bertini intra-nuclear cascade. The previous model (`G4MuNuclearInteraction`) replaced the virtual photon with  $\pi^{+-}$  instead, which would then interact through the low/high energy parameterised models (LEP/HEP) – these are known to yield fewer neutrons. There

has also been increased neutron production in the FTF model, which may account for some of the enhanced yields in the `Shielding` and `FTFP_BERT` lists; The addition of the Reggeon cascade [261], which can cause more nucleon secondaries, is a possible explanation, but further study is required [262].

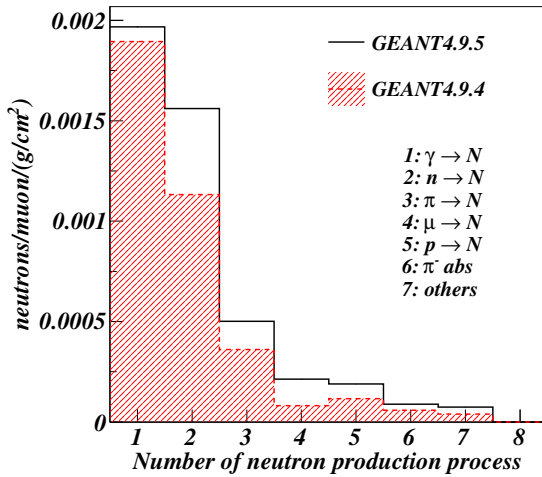


Figure 9.21: Absolute neutron yields of the most important production processes for muon-induced neutrons generated from firing 260 GeV  $\mu^-$  on lead using the `Shielding` physics list and GEANT4 version 9.5 (black histogram) and version 9.4 (red dashed histogram). The neutron creation processes are: 1: photo-nuclear interaction of  $\gamma$ -rays ( $\gamma \rightarrow N$ ), 2: neutron inelastic scattering ( $n \rightarrow N$ ), 3: pion spallation ( $\pi \rightarrow N$ ), 4: muon spallation ( $\mu \rightarrow N$ ), 5: proton spallation ( $p \rightarrow N$ ), 6: pion absorption ( $\pi^- \text{ abs}$ ) and 7: all other neutron production processes.

## 9.6 Discussion

For the development of future rare-event searches, especially in the context of direct dark matter experiments, accurate data on muon-induced neutron yields in several materials is of great importance, as is the ability to simulate these processes using modern Monte Carlo toolkits. Complex models inform the design of large and expensive shielding and veto systems around these experiments, as well as the interpretation of their data (background expectations). There exists significant uncertainty in the simulated muon-induced neutron rate, as evidenced by the steady change in the total neutron yield with every new version of GEANT4 and physics list and available data have been inconclusive.

In this study, the dataset from 319 days of operation of the ZEPLIN-III anti-coincidence detector has been analysed for high energy cosmic-ray muons. The number of muon-induced neutrons has been evaluated by detecting delayed  $\gamma$ -ray signals following radiative captures. A muon flux in the Boulby Underground Laboratory of  $(3.75 \pm 0.09) \times 10^{-8}$  muons/s/cm<sup>2</sup> has been determined, consistent with and improving upon previous measurements. The muon-induced neutron detection rate was measured to be  $0.346 \pm 0.007$  neutrons/muon traversing the ZEPLIN-III scintillator veto. Monte Carlo simulations, using GEANT4 (version 9.5) and the **Shielding** physics list with the same cuts and thresholds applied as used for the analysis of the data, resulted in a detected neutron rate of  $0.275^{+0.005}_{-0.008}$  neutrons/muon (quadratically combined statistical and systematic errors), which is  $\sim 20\%$  lower than the experimentally measured value. However, absolute rates aside, the simulation reproduced very well all tested parameters, strengthening confidence in the results. The ratio of neutron rates between data and simulation have been used to evaluate a muon-induced neutron yield in pure lead of  $(5.8 \pm 0.2) \times 10^{-3}$  neutrons/muon/(g/cm<sup>2</sup>) for a mean muon energy of 260 GeV. Additional simulations exploring previous versions of the GEANT4 simulation packages confirm the trend of an increasing neutron production rate in lead with every successive distribution of GEANT4 (also shown in other simulation studies [237, 263]). A further increase by 25% is encouraged by the results presented here.

A similar comparison between simulation and experiment was performed for the ZEPLIN-II anti-coincidence system [197, 248]. In that work a muon-induced neutron yield in lead of  $(1.31 \pm 0.06) \times 10^{-3}$  neutrons/muon/(g/cm<sup>2</sup>) was reported. A collaborator revisited the simulation, now using GEANT4 version 9.5 and the **Shielding** physics list, including thermal scattering cross-sections, and a significantly larger sample of primary muons. This resulted in a new estimate for the neutron yield in lead of  $(3.4 \pm 0.1) \times 10^{-3}$  neutrons/muon/(g/cm<sup>2</sup>) in that setup. Even though an increase of the neutron production rate from the change over to a more recent version of GEANT4 and physics list was to be expected (see Table 9.4), the simulated neutron rate is now lower than originally obtained, bringing experimental observation and simulation closer together (from a factor of  $\sim 1.8$  to  $\sim 1.3$ ); thus, increasing the inferred neutron yield in lead. This may indicate that recent changes in GEANT4 concern not only neutron production but also also the modelling of neutron interaction processes. While it is clear that a significant contribution of the newly obtained ZEPLIN-II yield comes from the updated simulation (note that the data analysis of the experimental measurements with the ZEPLIN-II veto has not been revisited), there remains a significant discrepancy with the present result. One possible explanation for this is that the angular distribution of emitted neutrons may not be accurately modelled.

The virtually complete geometrical enclosure of the ZEPLIN-III veto with respect to the lead shielding would be expected to make the present results less susceptible to such effects than in ZEPLIN-II.

The previously mentioned work from the EDELWEISS collaboration, published very shortly after the work presented here, emphasises the current interest in this field of research. The publication includes a similar study of muons, comparing data with Monte Carlo simulated muon tracks. However, the paper does not report on an absolute muon-induced neutron yield in lead (or other production materials) by studying neutron propagation and detection via Monte Carlo simulations. On the other hand, the study concentrates on the impact of irreducible muon-induced nuclear recoil background on the current EDELWEISS-II experiment and also gives important expectation values for future large scale direct dark matter search instruments [198].

Finally, as the results presented here confirm the very significant contribution of lead in the production of muon-induced neutrons, the use of lead-based shielding to prevent  $\gamma$ -rays from the environment to propagate into the sensitive volume of the detector should be carefully assessed for any future rare event search. Alternative shielding compositions, such as large water tanks surrounding the detectors, have the potential to significantly decrease the muon-induced neutron rates; the neutron yield is reduced by approximately an order of magnitude due to the use of a lighter shielding material (see Fig. 9.4). Moreover, the greater volumes of the shielding constructions, in conjunction with the possibility of instrumenting these (*e.g.* with PMTs to detect the produced Cherenkov light), allow to detect far away muon tracks much more efficiently, thus, rejecting correlated neutron events. Shielding constructions like these are already being used in some current dark matter searches [119, 87, 86], and as well are being discussed for near future next generation experiments [103, 106].

# Chapter 10

## Conclusions

A vast number of astronomical observation point towards the existence of an unknown (dark) component dominating the matter content of our Universe. One of the currently favoured dark matter particle candidates, the WIMP, has great potential to be detected in deep underground low background experiments, which are looking for direct interactions of WIMPs with dedicated target materials. In this thesis, the results achieved with the ZEPLIN-III detector in its second science run configuration have been presented.

ZEPLIN-III was based in the Boulby Underground Laboratory at a vertical depth of  $\sim 1100$  m (2850 m w.e.), reducing the atmospheric muon flux by approximately 6 orders of magnitude. It featured a dual-phase liquid/gas xenon time projection chamber, recording recoils via two signals generated from the same interaction – scintillation and ionisation. The ratio of these two signal channels provides a mechanism to discriminate between nuclear recoils and the dominant background – electron recoils. The second science run of the instrument profited from a new array of very low background PMTs and the incorporation of an active tonne-scale plastic scintillator veto device, enclosing the dark matter detector. By tagging and rejecting  $\sim 61\%$  of the nuclear recoil background, and an additional fraction of  $\sim 28\%$  of the detected electron recoils, the veto was a crucial element in achieving a competitive result. The background in the xenon target was dramatically improved by the implementation of the new set of PMTs with a reduction by a factor  $\sim 20$  and  $\sim 10$  for electron recoils and neutrons, respectively. However, the demand of such low levels of radioactivity caused unanticipated problems in the production of the PMTs, resulting in large gain variabilities and poor single photoelectron responses. Consequently, the new PMT performance was poor, leading to a significant drop in discrimination power to only 1:280 (*cf.* 1:7800 in the first science run).

The minima of the experimental upper limits on the WIMP-nucleon elastic scattering cross-section obtained from the combined science run results are  $3.9 \times 10^{-8}$  pb and  $8.0 \times 10^{-3}$  pb near a WIMP mass of 50 GeV/c<sup>2</sup> for the spin-independent and spin-dependent (WIMP-neutron) case, respectively. Both results represent today the world's second best limits. A plot showing the most recent results from direct dark matter searches, including the currently world leading spin-independent cross-section curve from the XENON100 experiment is given in Chapter 3, Fig. 3.6.

The present results are only a temporary reflection of the current state of direct dark matter searches, a fast progressing field of research. To date, a number of next-generation experiments are being planned, built or even already in the stage of commissioning. With exceptional sensitivities expected by these future experiments the majority of the favoured parameter space will soon be explored. Direct dark matter searches may be on the door step of a discovery. Figure 10.1 shows projected WIMP-nucleon cross-section limits for two of the future dual-phase liquid xenon detectors – LUX and LZ. Although this thesis concentrated in particular on the detection with liquid noble gas systems (specifically xenon), it should be emphasised that it is of utmost importance to study WIMP interactions with a variety of different target materials and detection mechanisms for the reduction of systematic errors and, in the case of a discovery, to conduct research into the properties of the newly found particle. Tonne-scale cryogenic solid state detectors currently under development are the EURECA and SuperCDMS projects.

To achieve these high sensitivities, detectors are scaled up to be able to hold tonnes of active target material. The increase in volume and the required sensitivities give rise to new challenges, such as controlling and predicting expected background rates. This includes not only the demand for construction materials featuring extremely low radioactivity levels, but more accurate knowledge of ‘new’ background sources, suddenly becoming dominant contributors to the nuclear recoil background budget of these big detectors at these level of sensitivities.

One of these backgrounds is cosmic-ray muon-induced neutrons. This thesis reported a new measurement of the muon-induced neutron yield in lead (used to shield experiments from ambient  $\gamma$ -rays). By performing complementing Monte Carlo simulations a production yield of  $(5.8 \pm 0.2) \times 10^{-3}$  neutrons/muon/(g/cm<sup>2</sup>) was inferred for a mean muon energy of 260 GeV. Absolute agreement between experimental measured and simulated rates are of order  $\sim 25\%$ . The resulting high muon-induced neutron rate in lead encourages the use of alternative shielding compositions, such as large instrumented water tanks.

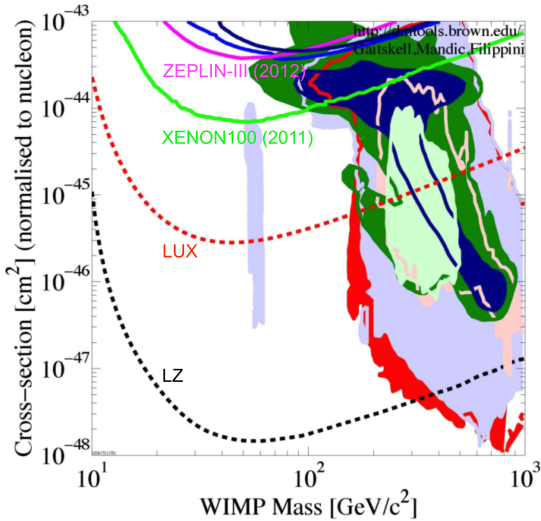


Figure 10.1: Projection of WIMP-nucleon cross-section upper limits to be reached (aimed for) by the LUX (red dashed line) and LZ (black dashed line) experiments. For comparison cross-section limits from XENON100 (2011 data), ZEPLIN-III (combined first and second science run), CDMS-II (blue solid line) and EDELWEISS II (dark blue solid line) are shown as well [264].

Comprehensive simulation packages guide the design of next-generation experiments and, as such, accurate modelling of background rates from these newly arising sources are of utmost importance. These results are not only crucial for future rare event searches, but for the prediction of the expected background in current experiments, reducing systematic errors.

Moreover, and again critical for the accuracy of Monte Carlo simulations, it is very important to have sufficient knowledge about the response of all detection instruments. While studies for liquid noble gases into their response to nuclear recoils are comprehensive, research into the detection properties of plastic scintillators, often used in veto system applications, are scarce. In this thesis I presented a new measurement of the nuclear recoil quenching factor for polystyrene based plastic scintillators for recoil energies between 125 and 850 keV, correlating nuclear recoil energy depositions and the resulting scintillation output. A strong dependence (steep decrease in scintillation light produced) at low energies is observed. Relevance for this work is not restricted to dark matter searches alone, but to a variety of other fields in industry and science, such as medical physics or muon tomography, where plastic scintillator detectors are commonly used.

The second scientific deployment of the ZEPLIN-III detector successfully concluded the series of ZEPLIN dark matter experiments. However, the ZEPLIN-III team together with the LUX collaboration is currently developing a next generation tonne-scale liquid noble gas detector – the LUX-ZEPLIN instrument. The 7 tonne dual-phase xenon detector will attempt to push sensitivities down by more than three orders of magnitude further than the current world best limit. At this level, the capability of an instrument becomes sensitive to, and perhaps ultimately limited by, solar  $p$ - $p$  chain neutrinos. Furthermore, the challenges of multiple-scintillation single-ionisation events, Cherenkov contributions, two neutrino double beta decay, and perhaps other new, as yet unknown background sources, will also have to be addressed. The detailed measurement, simulation and, most important of all, understanding, of rare interaction sources and types still has some way to go.

# Glossary

<b>2dFGRS</b>	Two degree Field Galaxy Redshift Survey
<b>ADC</b>	Analoge to Digital Converter
<b>AMANDA</b>	Antarctic Muon And Neutrino Detector Array
<b>ArDM</b>	Argon Dark Matter
<b>ATLAS</b>	A Toroidal LHC ApparatuS
<b>BAO</b>	Baryonic Acoustic Oscillations
<b>BBN</b>	Big-Bang Nucleosynthesis
<b>BERT</b>	BERTini cascade
<b>BIC</b>	BIrary Cascade
<b>CAD</b>	Computer-Aided Design
<b>CDM</b>	Cold Dark Matter
<b>CDMS</b>	Cryogenic Dark Matter Search
<b>CL</b>	Confidence Level
<b>CLEAN</b>	Cryogenic Low Energy Astrophysics with Noble gases
<b>CMB</b>	Cosmic Microwave Background
<b>CMS</b>	Compact Muon Solenoid
<b>cMSSM</b>	constrained Minimal Supersymmetric Standard Model
<b>CoGeNT</b>	Coherent Germanium Neutrino Technology
<b>COUPP</b>	Chicagoland Observatory for Underground Particle Physics
<b>CP-symmetry</b>	combination of Charge conjugation and Parity symmetry
<b>CRESST</b>	Cryogenic Rare Event Search with Superconducting Thermometers
<b>CSISRS</b>	Cross-Section Information Storage and Retrieval System
<b>DAMA/LIBRA</b>	DArk MAtter/Large sodium Iodide Bulk for RAre processes
<b>DAQ</b>	Data Acquisition
<b>DEAP</b>	Dark matter Experiment using Argon Pulse-shape discrimination
<b>DRIFT</b>	Directional Recoil Identification From Tracks

<b>dru</b>	events/kg/day/keV
<b>DTAG</b>	Delayed Tag
<b>EDELWEISS</b>	Expérience pour DEtecter Les Wimps En SIté Souterrain
<b>ENDF</b>	Evaluated Nuclear Data File
<b>EURECA</b>	European Underground Rare Event Calorimeter Array
<b>Fermi-LAT</b>	Fermi Large Area Telescope
<b>FLUKA</b>	FLUktuierende KAskade
<b>FSR</b>	First Science Run of ZEPLIN-III
<b>FTF</b>	Fritiof string model
<b>FWHM</b>	Full Width at Half Maximum
<b>GDML</b>	Geometry Description Markup Language
<b>GEANT</b>	GEometry ANd Tracking
<b>HDM</b>	Hot Dark Matter
<b>HEP</b>	High Energy Parameterised model
<b>HESS</b>	High Energy Stereoscopic System
<b>HP</b>	High Precision
<b>HPGe</b>	High-Purity Germanium
<b>HS</b>	High Sensitivity
<b>HST</b>	Hubble Space Telescope
<b>ICM</b>	Intra Cluster Medium
<b>ICP-MS</b>	Inductively Coupled Plasma Mass Spectrometry
<b>ICP-OES</b>	Inductively Coupled Plasma Optical Emission Spectrometry
<b>ISM</b>	Interstellar Medium
<b>JENDL</b>	Japanese Evaluated Nuclear Data Library
<b>keV<sub>ee</sub></b>	electron-equivalent unit of energy
<b>keV<sub>nr</sub></b>	nuclear recoil energy
<b>KIMS</b>	Korea Invisible Mass Search
<b>ΛCDM</b>	Lambda Cold Dark Matter Model (standard cosmological model)
<b>L<sub>eff</sub></b>	relative scintillation efficiency
<b>LEP</b>	Low Energy Parameterised model
<b>LHC</b>	Large Hadron Collider
<b>LHCb</b>	Large Hadron Collider beauty experiment
<b>LN2</b>	Liquid Nitrogen
<b>LNGS</b>	Gran Sasso National Laboratory
<b>LRF</b>	Light Response Function
<b>LS</b>	Low Sensitivity

---

<b>LSP</b>	Lightest Supersymmetric Particle
<b>LUX</b>	Large Underground Xenon detector
<b>LZ</b>	LUX-ZEPLIN
<b>ML</b>	Maximum Likelihood
<b>MSSI</b>	Multiple Scintillation Single Ionisation
<b>MSSM</b>	Minimal Supersymmetric Standard Model
<b>mSUGRA</b>	minimal SUper GRAvity
<b>MUSIC</b>	MUon SImulation Code
<b>MUSUN</b>	MUon Simulations UNderground
<b>MW</b>	Milky Way
<b>NIST</b>	National Institute of Standards and Technology
<b>NLSP</b>	Next-to-Lightest Supersymmetric Particle
<b>PAMELA</b>	Payload for Antimatter Matter Exploration and Light-nuclei Astrophysics
<b>phe</b>	photoelectron
<b>PLR</b>	Profile Likelihood Ratio
<b>PMT</b>	Photo Multiplier Tube
<i>PQ</i>	Peccei-Quinn
<b>PTAG</b>	Prompt Tag
<b>QCD</b>	Quantum Chromodynamics
<b>QGS</b>	Quark-Gluon String theoretical model
<b>RaVen</b>	Reduction and Analysis of Veto signals software package
<b>RMS</b>	Root Mean Square
<b>S1</b>	prompt scintillation signal
<b>S2</b>	secondary electroluminescence signal
<b>SD</b>	Spin-Dependent
<b>SDSS</b>	Sloan Digital Sky Survey
<b>SG</b>	Skew Gaussian
<b>SHM</b>	Standard Halo Model
<b>SI</b>	Spin-Independent
<b>SM</b>	Standard Model
<b>SNe</b>	Type Ia Supernovae
<b>SNO</b>	Sudbury Neutrino Observatory
<b>SPE</b>	Single Photoelectron
<b>SRIM</b>	Stopping and Range of Ions in Matter
<b>SSR</b>	Second Science Run of ZEPLIN-III
<b>STAGES</b>	Space Telescope A901/902 Galaxy Evolution Survey

<b>Super-K</b>	Super-Kamioka neutrino detection experiment
<b>SUSY</b>	SUperSYmmetry
<b>TPC</b>	Time Projection Chamber
<b>VUV</b>	Vacuum UltraViolet
<b>WArp</b>	Wimp Argon Programme
<b>WDM</b>	Warm Dark Matter
<b>w.e.</b>	water equivalent
<b>WIMP</b>	Weakly Interacting Massive Particle
<b>WLS</b>	Weighted Least Square
<b>WMAP</b>	Wilkinson Microwave Anisotropy Probe
<b>ZE3RA</b>	ZEPLIN-III Reduction and Analysis software
<b>ZEPLIN</b>	ZonEd Proportional scintillation in LIquid Noble gases

# Bibliography

- [1] C. Ghag et al. Performance of the veto detector incorporated into the ZEPLIN-III experiment. *Astroparticle Physics*, 35:76–86, 2011.
- [2] D. Yu. Akimov et al. WIMP-nucleon cross-section results from the second science run of ZEPLIN-III. *Physics Letters B*, 709:14–20, 2012.
- [3] L. Reichhart et al. Quenching factor for low energy nuclear recoils in a plastic scintillator. *Physical Review C*, 85:065801, 2012.
- [4] H. M. Araújo et al. Radioactivity backgrounds in ZEPLIN-III. *Astroparticle Physics*, 35:495–502, 2012.
- [5] L. Reichhart et al. Measurement and simulation of the muon-induced neutron yield in lead. *arXiv:1302.4275v1 [physics.ins-det]*, submitted to *Astroparticle Physics*, 2013.
- [6] G. Efstathiou, W.J. Sutherland, and S.J. Maddox. The cosmological constant and cold dark matter. *Nature*, 348:705–708, 1990.
- [7] “The Nobel Prize in Physics 2011”. Nobelprize.org. 22 Oct 2012 [http://www.nobelprize.org/nobel\\_prizes/physics/laureates/2011/](http://www.nobelprize.org/nobel_prizes/physics/laureates/2011/).
- [8] J. Peacock. *Cosmological Physics*. Cambridge University Press, 1999.
- [9] J. Peacock and C. Heymans. *Lecture Notes to Advanced Cosmology*. University of Edinburgh, 2009–2010.
- [10] N. Jarosik et al. Seven-year Wilkinson Microwave Anisotropy Probe (WMAP) Observations: Sky Maps, Systematic Errors, and Basic Results. *The Astrophysical Journal Supplement Series*, 192(2):article 14, 2011.
- [11] N. Suzuki et al. The Hubble Space telescope Cluster Supernova Survey: V. Improving the dark energy constraints above  $Z>1$  and building an early-type-hosted supernova sample. *Astrophysical Journal*, 746(1):85, 2012.
- [12] F. Zwicky. Republication of: The redshift of extragalactic nebulae. *General Relativity and Gravitation*, 41(1):207–224, 2009.
- [13] E.L. Lokas and G.A. Mamon. Dark matter distribution in the Coma cluster from galaxy kinematics: breaking the mass-anisotropy degeneracy. *Monthly Notices of the Royal Astronomical Society*, 343(2):401–412, 2003.
- [14] T. Van Albada et al. Distribution of dark matter in the sprial galaxy NGC-3198. *Astrophysical Journal*, 295(2):305–313, 1985.
- [15] F. Zwicky. On the masses of nebulae and of clusters of nebulae. *The Astrophysical Journal*, 83(3):217–246, 1937.

## BIBLIOGRAPHY

---

- [16] P. Simon et al. Spatial matter density mapping of the STAGES Abell A901/2 supercluster field with 3D lensing. *Monthly Notices of the Royal Astronomical Society*, 419:998–1016, 2012.
- [17] D. Clowe et al. A direct empirical proof of the existence of dark matter. *The Astrophysical Journal*, 648:L109–L113, 2006.
- [18] D.J. Fixsen. The temperature of the cosmic microwave background. *The Astrophysical Journal*, 707:916–920, 2009.
- [19] V. Springel et al. The large-scale structure of the Universe. *Nature*, 440:1137–1144, 2006.
- [20] M. Colless et al. The 2dF Galaxy Redshift Survey: spectra and redshifts. *Monthly Notices of the Royal Astronomical Society*, 328:1039–1063, 2001.
- [21] J.R. Gott et al. A map of the Universe. *The Astrophysical Journal*, 624:463–484, 2005.
- [22] M.J. Geller and J.P. Huchra. Mapping the Universe. *Science*, 246(4932):897–903, 1989.
- [23] V. Springel et al. Simulation of the formation, evolution and clustering of galaxies and quasars. *Nature*, 435:629–636, 2005.
- [24] K.A. Olive, G. Steigman, and T.P. Walker. Primordial nucleosynthesis: theory and observations. *Physics Reports*, 333–334:389–407, 2000.
- [25] M. Taoso, G. Bertone, and A. Masiero. Dark matter candidates: a ten-point test. *Journal of Cosmology and Astroparticle Physics*, 03(022), 2008.
- [26] G. Bertone, editor. *Particle Dark Matter: observations, models and searches*. Cambridge University Press, 2010.
- [27] S. Cole et al. The 2dF Galaxy Redshift Survey: power-spectrum analysis of the final data set and cosmological implications. *Monthly Notices of the Royal Astronomical Society*, 362:505–534, 2005.
- [28] S.D.M. White and C.S. Frenk. Galaxy formation through hierarchical-clustering. *Astrophysical Journal*, 379(1):52–79, 1991.
- [29] M.R. Lovell et al. The haloes of bright satellite galaxies in a warm dark matter universe. *Monthly Notices of the Royal Astronomical Society*, 420:2318–2324, 2012.
- [30] J. Wang et al. The missing massive satellites of the Milky Way. *Monthly Notices of the Royal Astronomical Society*, 424:2715–2721, 2012.
- [31] C.A. Baker et al. Improved Experimental Limit on the Electric Dipole Moment of the Neutron. *Physical Review Letters*, 97:131801, 2006.
- [32] R.D. Peccei and H.R. Quinn. CP Conservation in the Presence of Pseudoparticles. *Physical Review Letters*, 38(25):1440–1443, 1977.
- [33] R.D Peccei and H.R. Quinn. Constraints imposed by CP conservation in the presence of pseudoparticles. *Physical Review D*, 16(6):1791–1797, 1977.
- [34] P. Sikivie (G. Bertone, editor). *Axions. in: Particle Dark Matter: observations, models and searches*, chapter 11, pages 204–227. Cambridge University Press, 2010.
- [35] S.J. Asztalos et al. SQUID-Based Microwave Cavity Search for Dark-Matter Axions. *Physical Review Letters*, 104:041301, 2010.
- [36] G. Jungman, M. Kamionkowski, and K. Griest. Supersymmetric dark matter. *Physics Reports*, 267:195–373, 1996.

- [37] J.F. Feng. Dark Matter Candidates from Particle Physics and Methods of Detection. *Annual Review Astrophysics*, 48:495–545, 2010.
- [38] G. Gelmini and P. Gondolo (G. Bertone, editor). *DM production mechanisms. in: Particle Dark Matter: observations, models and searches*, chapter 7, pages 121–141. Camebridge University Press, 2010.
- [39] ATLAS Collaboration. Observation of a new particle in the search for the Standard Model Higgs boson with the ATLAS detector at the LHC. *Physics Letters B*, 716:1–29, 2012.
- [40] CMS Collaboration. Observation of a new boson at a mass of 125 GeV with the CMS experiment at the LHC. *Physics Letters B*, 716:30–61, 2012.
- [41] J. Ellis and K.A. Olive (G. Bertone, editor). *Supersymmetric dark matter candidates. in: Particle Dark Matter: observations, models and searches*, chapter 8, pages 142–163. Camebridge University Press, 2010.
- [42] T. Falk, K.A. Olive, and M. Srednicki. Heavy sneutrinos as dark matter. *Physics Letters B*, 339(3):248–251, 1994.
- [43] A.H. Chamseddine, R. Arnowitt, and P. Nath. Locally Supersymmetric Grand Unification. *Physical Review Letters*, 49(14):970–974, 1982.
- [44] J. Ellis, K.A. Olive, and Y. Santoso. Constraining supersymmetry. *New Journal of Physics*, 4:32.1–32.17, 2002.
- [45] T. Burgess et al. Finding viable Models in SUSY Parameter Spaces with Signal Specific Discovery Potential. *arXiv:1210.7020v1 [hep-ph]*, 2012.
- [46] G. Servant (G. Bertone, editor). *Dark matter at the electroweak scale: non-supersymmetric candidates. in: Particle Dark Matter: observations, models and searches*, chapter 9, pages 164–189. Camebridge University Press, 2010.
- [47] A. Giuliani (S. Matarrese, M. Colpi, V. Gorini and U. Moschella, editors). *Dark Matter Direct and Indirect Detection. in: Dark Matter and Dark Energy: A Challenge for Modern Cosmology*, chapter 7, pages 295–328. Springer, 2011.
- [48] O. Adriani et al. An anomalous positron abundance in cosmic rays with energies 1.5–100 GeV. *Nature*, 458:607–609, 2009.
- [49] A.A. Abdo et al. Measurement of the Cosmic Ray  $e^+ + e^-$  Spectrum from 20 GeV to 1 TeV with the Fermi Large Area Telescope. *Physical Review Letters*, 102:181101, 2009.
- [50] F. Aharonian et al. Energy Spectrum of Cosmic-Ray Electrons at TeV Energies. *Physical Review Letters*, 101:261104, 2008.
- [51] F. Aharonian et al. Probing the ATIC peak in the cosmic-ray electron spectrum with H.E.S.S. *Astronomy and Astrophysics*, 508(2):561–564, 2010.
- [52] A. Strumia. Dark matter interpretations of the cosmic-ray  $e^\pm$  excess. *Theoretical and Mathematical Physics*, 170(2):203–210, 2012.
- [53] D. Grasso et al. On possible interpretations of the high energy electron-positron spectrum measured by the Fermi Large Area Telescope. *Astroparticle Physics*, 32:140–151, 2009.
- [54] M. Ackermann et al. Constraining Dark Matter Models from a Combined Analysis of Milky Way Satellites with the Fermi Large Area Telescope. *Physical Review Letters*, 107:241302, 2011.
- [55] M. Ackermann et al. Search for dark matter satellites using the FERMI-LAT. *Astrophysical Journal*, 747(2):121, 2012.

## BIBLIOGRAPHY

---

- [56] D. Hooper and L. Goodenough. Dark matter annihilation in the Galactic Center as seen by the Fermi Gamma Ray Space Telescope. *Physics Letters B*, 697:412–428, 2011.
- [57] K.N. Abazajian. The consistency of Fermi-LAT observations of the galactic center with a millisecond pulsar population in the central stellar cluster. *Journal of Cosmology and Astroparticle Physics*, (3):010, 2011.
- [58] M. Chernyakova et al. The high-energy, arcminute-scale galactic center gamma-ray source. *The Astrophysical Journal*, 726(60):1–8, 2011.
- [59] R. Abbasi et al. Multiyear search for dark matter annihilations in the Sun with the AMANDA-II and IceCube detectors. *Physical Review D*, 85:042002, 2012.
- [60] E. Andres et al. The AMANDA neutrino telescope: principle of operation and first results. *Astroparticle Physics*, 13:1–20, 2000.
- [61] T. Tanaka et al. An indirect search for weakly interacting massive particles in the sun using 3109.6 days of upward-going muons in Super-Kamiokande. *The Astrophysical Journal*, 742(2):78, 2011.
- [62] H.S. Lee et al. Limits on Interactions between Weakly Interacting Massive Particles and Nucleons Obtained with CsI(Tl) Crystal Detectors. *Physical Review Letters*, 99:091301, 2007.
- [63] E. Behnke et al. Improved Limits on Spin-Dependent WIMP-Proton Interactions from a Two Liter CF<sub>3</sub>I Bubble Chamber. *Physical Review Letters*, 106(021303), 2011.
- [64] G. Redlinger. Searches for supersymmetry with the ATLAS detector. *Modern Physics Letters A*, 27(32):1230033, 2012.
- [65] S. Chatrchyan et al. Inclusive search for squarks and gluinos in  $pp$  collisions at  $\sqrt{s}=7$  TeV. *Physical Review D*, 85:012004, 2012.
- [66] R. Aaij et al. Strong Constraints on the Rare Decays  $B_s^0 \rightarrow \mu^+ \mu^-$  and  $B^0 \rightarrow \mu^+ \mu^-$ . *Physical Review Letters*, 108:231801, 2012.
- [67] T. Li et al. Correlating LHCb  $B_s^0 \rightarrow \mu^+ \mu^-$  Results with the ATLAS-CMS Multijet Supersymmetry Search. *Europhysics Letters*, 100(2):21001, 2012.
- [68] O. Buchmueller et al. The CMSSM and NUHM1 in Light of 7 TeV LHC,  $B_s \rightarrow \mu^+ \mu^-$  and XENON100 Data. *The European Physical Journal C*, 72:2243, 2012.
- [69] E. Aprile et al. Dark Matter Results from 225 Live Days of XENON100 Data. *Physical Review Letters*, 109:181301, 2012.
- [70] O. Buchmueller et al. Supersymmetry in light of 1/fb of LHC data. *The European Physical Journal C*, 72:1878, 2012.
- [71] O. Buchmueller et al. Higgs and supersymmetry. *The European Physical Journal C*, 72:2020, 2012.
- [72] V. Chepel and H.M. Araújo. Liquid noble gas detectors for low energy particle physics. *arXiv:1207.2292 [physics.ins-det]*, 2012.
- [73] A.M. Green. Astrophysical uncertainties on direct detection experiments. *Modern Physics Letters A*, 27(3):1230004, 2012.
- [74] D.G. Cerdeño and A.M. Green (G. Bertone, editor). *Direct detection of WIMPs*. in: *Particle Dark Matter: observations, models and searches*, chapter 17, pages 347–369. Cambridge University Press, 2010.

- [75] C. Savage et al. Compatibility of DAMA/LIBRA dark matter detection with other searches. *Journal of Cosmology and Astroparticle Physics*, 04:010, 2009.
- [76] R.H. Helm. Inelastic and Elastic Scattering of 187-MeV Electrons from selected Even-Even Nuclei. *Physical Review*, 104(5):1466–1475, 1956.
- [77] J.D. Lewin and P.F. Smith. Review of mathematics, numerical factors, and corrections for dark matter experiments based on elastic nuclear recoil. *Astroparticle Physics*, 6:87–112, 1996.
- [78] J. Engel. Nuclear form factors for the scattering of weakly interacting massive particles. *Physics Letters B*, 264(1,2):114–119, 1991.
- [79] A. Benoit et al. Measurement of the response of heat-and-ionization germanium detectors to nuclear recoils. *Nuclear Instruments and Methods in Physics Research A*, 577:558–568, 2007.
- [80] D. Akimov. Techniques and results for the direct detection of dark matter (review). *Nuclear Instruments and Methods in Physics Research A*, 628:50–58, 2011.
- [81] R.J. Gaitskell. Direct Detection of Dark Matter. *Annual Review of Nuclear and Particle Science*, 54:315–359, 2004.
- [82] E. Figueroa-Feliciano. Direct detection searches for WIMP dark matter. *Progress in Particle and Nuclear Physics*, 66:661–673, 2011.
- [83] E. Aprile and T. Doke. Liquid xenon detectors for particle physics and astrophysics. *Reviews of Modern Physics*, 82:2053–2097, 2010.
- [84] P. Benetti et al. Measurement of the specific activity of  $^{39}\text{Ar}$  in natural argon. *Nuclear Instruments and Methods in Physics Research A*, 574:83–88, 2007.
- [85] D. Acosta-Kane et al. Discovery of underground argon with low level of radioactive  $^{39}\text{Ar}$  and possible applications to WIMP dark matter detectors. *Nuclear Instruments and Methods in Physics Research A*, 587:46–51, 2008.
- [86] H. Sekiya, for the XMASS collaboration. XMASS. *Journal of Physics: Conference Series*, 308:012011, 2011.
- [87] M. G Boulay for the DEAP Collaboration. DEAP-3600 Dark Matter Search at SNOLAB. *Journal of Physics: Conference Series*, 375:012027, 2012.
- [88] J. Monroe. Recent Progress from the MiniCLEAN Dark Matter Experiment. *Journal of Physics: Conference Series*, 375:012012, 2012.
- [89] K. Abe et al. Light WIMP search in XMASS. *arXiv:1211.5404v3 [astro-ph.CO]*, 2013.
- [90] G.J. Alner et al. First limits on WIMP nuclear recoil signals in ZEPLIN-II: A two-phase xenon detector for dark matter detection. *Astroparticle Physics*, 28:287–302, 2007.
- [91] G.E. Aalseth et al. Search for an Annual Modulation in a p-Type Point Contact Germanium Dark Matter Detector. *Physical Review Letters*, 107:141301, 2011.
- [92] G. Angloher et al. Results from 730 kg days of the CRESST-II Dark Matter search. *The European Physical Journal C*, 72:1971, 2012.
- [93] Z. Ahmed et al. Dark Matter Search Results from the CDMS II Experiment. *Science*, 327:1619–1622, 2010.
- [94] E. Armengaud et al. Final results of the EDELWEISS-II WIMP search using a 4-kg array of cryogenic germanium detectors with interleaved electrodes. *Physics Letters B*, 702:329–335, 2011.

## BIBLIOGRAPHY

---

- [95] J. Angle et al. Search for Light Dark Matter in XENON10 Data. *Physical Review Letters*, 107:051301, 2011.
- [96] M. Felizardo et al. Final Analysis and Results of the Phase II SIMPLE Dark Matter Search. *Physical Review Letters*, 108:201302, 2012.
- [97] E. Behnke et al. First dark matter search results from a 4-kg CF<sub>3</sub>I bubble chamber operated in a deep underground site. *Physical Review D*, 86:052001, 2012.
- [98] E. Armengaud et al. Search for low-mass WIMPs with EDELWEISS-II heat-and-ionization detectors. *Physical Review D*, 86:051701, 2012.
- [99] A. Wright for the DarkSide Collaboration. The DarkSide Program at LNGS. *arXiv:1109.2979v1 [physics.ins-det]*, *Proceedings of the DPF-2011 Conference, Providence, RI*, 2011.
- [100] A. Marchionni et al. ArDM: a ton-scale LAr detector for direct Dark Matter searches. *Journal of Physics: Conference Series*, 308:012006, 2011.
- [101] D.S. Akerib et al. The Large Underground Xenon (LUX) Experiment. *Nuclear Instruments and Methods in Physics Research A*, 704:111–126, 2013.
- [102] E. Aprile. The XENON1T Dark Matter Search Experiment. *arXiv:1206.6288v1 [astro-ph.IM]*, 2012.
- [103] D.C. Malling et al. After LUX: The LZ Program. *arXiv:1110.0103v2 [astro-ph.IM]*, 2011.
- [104] A. Brown et al. Extending the CRESST-II commissioning run limits to lower masses. *Physical Review D*, 85:021301, 2012.
- [105] D.S. Akerib et al. The SuperCDMS proposal for dark matter detection. *Nuclear Instruments and Methods in Physics Research A*, 559:411–413, 2006.
- [106] H. Kraus. EURECA – the European Future of Dark Matter Searches with Cryogenic Detectors. *Nuclear Physics B (Proc. Suppl.)*, 173:168–171, 2007.
- [107] R. Bernabei et al. New results from DAMA/LIBRA. *The European Physical Journal C*, 67:39–49, 2010.
- [108] E. Fernandez-Martinez and R. Mahbubani. The Gran Sasso muon puzzle. *Journal of Cosmology and Astroparticle Physics*, 07:029, 2012.
- [109] D.Yu. Akimov et al. Limits on inelastic dark matter from ZEPLIN-III. *Physics Letters B*, 692:180–183, 2010.
- [110] E. Aprile et al. Implications on inelastic dark matter from 100 live days of XENON100 data. *Physical Review D*, 84:061101, 2011.
- [111] Z. Ahmed et al. Search for annual modulation in low-energy CDMS-II data. *arXiv:1203.1309v2 [astro-ph.CO]*, 2012.
- [112] R. Foot. Mirror dark matter interpretation of the DAMA, CoGeNT, and CRESST-II data. *Physical Review D*, 86:023524, 2012.
- [113] D. Daw et al. Spin-dependent limits from the DRIFT-II directional dark matter detector. *Astroparticle Physics*, 35:397–401, 2011.
- [114] S. Archambault et al. Constraints on low-mass WIMP interactions on <sup>19</sup>F from PICASSO. *Physics Letters B*, 711:153–161, 2012.
- [115] T.J. Sumner. The ZEPLIN-III dark matter project. *New Astronomy Reviews*, 49:277–281, 2005.

- [116] G.J. Alner et al. First limits on nuclear recoil events from the ZEPLIN I galactic dark matter detector. *Astroparticle Physics*, 23:444–462, 2005.
- [117] D.Yu. Akimov. The ZEPLIN-III dark matter detector: Instrument design, manufacture and comissioning. *Astroparticle Physics*, 27:46–60, 2007.
- [118] A.C. Hollis Hallet (editor G.A. Cook). *Argon, Helium and the Rare Gases: The Elements of the Helium Group. Vol. 1, History Occurrences and Properties*. Interscience, New York, 1961.
- [119] D.N. McKinsey et al. The LUX dark matter search. *Journal of Physics: Conference Series*, 203:012026, 2010.
- [120] E. Aprile et al. The XENON100 dark matter experiment. *Astroparticle Physics*, 35:573–590, 2112.
- [121] S. Agostinelli et al. GEANT4 – a simulation toolkit. *Nuclear Instruments and Methods in Physics Research A*, 506:250–303, 2003.
- [122] H. M. Araújo et al. The ZEPLIN-III dark matter detector: Performance study using an end-to-end simulation tool. *Astroparticle Physics*, 26:140–153, 2006.
- [123] P. Benetti et al. Detection of energy deposition down to the keV region using liquid xenon scintillation. *Nuclear Instruments and Methods in Physics Research A*, 327:203–206, 1993.
- [124] P. Majewski et al. Performance data from the ZEPLIN-III second science run. *Journal of Instrumentation*, 7:C03044, 2012.
- [125] J. Jortner et al. Localized Excitations in Condensed Ne, Ar, Kr, and Xe. *The Journal of Chemical Physics*, 42(12):4250–4253, 1965.
- [126] S. Kubota et al. Recombination luminescence in liquid argon and liquid xenon. *Physical Review B*, 17(6):2762–2765, 1978.
- [127] A. Hitachi and T. Takahashi. Effect of ionization denisty of the time dependence of luminescence from liquid argon and xenon. *Physical Review B*, 27(9):5279–5285, 1983.
- [128] S. Kubota, M. Hishida, and J. Raun. Evidence for a triplet state of the self-trapped exciton states in liquid argon, krypton and xenon. *Journal of Physics C: Solid State Physics*, 11(12):2645–2651, 1978.
- [129] G.J. Davies et al. Liquid xenon as a dark matter detector. Prospects for nuclear recoil discrimination by photon timing. *Physics Letters B*, 320:395–399, 1994.
- [130] S. Kubota et al. Dynamical behaviour of free electrons in the recombination process in liquid argon, krypton, and xenon. *Physcial Review B*, 20(8):3486–3496, 1979.
- [131] M. Szydagis et al. NEST: a comprehensive model for scintillation yield in liquid xenon. *Journal of Instrumentation*, 6:P10002, 2011.
- [132] J. Lindhard et al. Integral equations governing radiation effects (Notes on atomic collisions, III). *Mat. Fys. Medd. Dan. Vid. Selsk.*, 33(10):1–42, 1963.
- [133] A. Hitachi. Properties of liquid xenon scintillation for dark matter searchers. *Astroparticle Physics*, 24:247–256, 2005.
- [134] A. Manzur et al. Scintillation efficiency and ionization yield of liquid xenon for monoenergetic nucer recoils down to 4 keV. *Physical Review C*, 81:025808, 2010.
- [135] D.-M. Mei et al. A model of nuclear recoil scintillation efficiency in noble liquids. *Astroparticle Physics*, 30:12–17, 2008.

## BIBLIOGRAPHY

---

- [136] J. B. Birks. Scintillations from organic crystals: Specific fluorescence and relative response to different radiations. *Proceedings of the Physical Society. Section A*, 64(10):874–877, 1951.
- [137] T. Doke et al. Absolute scintillation yields in liquid argon and xenon for various particles. *Japanese Journal of Applied Physics*, 41(3A):1538–1545, 2002.
- [138] G. Plante et al. New measurements of the scintillation efficiency of low-energy nuclear recoils in liquid xenon. *Physical Review C*, 84:045805, 2011.
- [139] E. Aprile et al. New measurements of the relative scintillation efficiency of xenon nuclear recoils below 10 keV. *Physical Review C*, 79:045807, 2009.
- [140] F. Arneodo. Scintillation efficiency of nuclear recoil in liquid xenon. *Nuclear Instruments and Methods in Physics Research A*, 449:147–157, 2000.
- [141] D. Akimov et al. Measurements of scintillation efficiency and pulse shape for low energy recoils in liquid xenon. *Physics Letters B*, 524:245–251, 2002.
- [142] V. Chepel et al. Scintillation efficiency of liquid xenon for nuclear recoils with the energy down to 5 keV. *Astroparticle Physics*, 26:58–63, 2006.
- [143] E. Aprile et al. Simultaneous measurement of ionization and scintillation from nuclear recoils in liquid xenon for a dark matter experiment. *Physical Review Letters*, 97:081302, 2006.
- [144] P. Sorensen et al. The scintillation and ionization yield of liquid xenon for nuclear recoils. *Nuclear Instruments and Methods in Physics Research A*, 601:339–346, 2009.
- [145] M. Horn et al. Nuclear recoil scintillation and ionisation yield in liquid xenon from ZEPLIN-III data. *Physics Letters B*, 705:471–476, 2011.
- [146] E. Aprile et al. Scintillation response of liquid xenon to low energy nuclear recoils. *Physical Review D*, 72:072006, 2005.
- [147] R.L. Platzman. Total ionization in gases by high-energy particles - an appraisal of our understanding. *The International Journal of Applied Radiation and Isotopes*, 10(2-3):116–127, 1961.
- [148] L.S Miller, S. Howe, and W.E. Spear. Charge Transport in Solid and Liquid Ar, Kr, and Xe. *Physical Review*, 166(3):871–878, 1968.
- [149] E. Santos et al. Single electron emission in two-phase xenon with application to the detection of coherent neutrino-nucleus scattering. *Journal of High Energy Physics*, 12:115, 2011.
- [150] T. Takahashi et al. Emission spectra from Ar-Xe, Ar-Kr, Ar-N<sub>2</sub>, Ar-CH<sub>4</sub>, Ar-CO<sub>2</sub> and Xe-N<sub>2</sub> gas scintillation proportional counters. *Nuclear Instruments and Methods in Physics Research*, 205(3):591–596, 1983.
- [151] P. Sorensen et al. Lowering the low-energy threshold of xenon detectors. *Proceedings of Science IDM 2010*, page 017, 2010.
- [152] H.M. Araújo et al. Low-temperature study of 35 photomultiplier tubes for the ZEPLIN III experiment. *Nuclear Instruments and Methods in Physics Research A*, 521:407–415, 2004.
- [153] V. N. Lebedenko et al. Results from the first science run of the ZEPLIN-III dark matter search experiment. *Physical Review D*, 80(5):052010, 2009.
- [154] V.N. Lebedenko et al. Limits on the Spin-Dependent WIMP-Nucleon Cross Sections from the First Science Run of the ZEPLIN-III experiment. *Physical Review Letters*, 103:151302, 2009.

- [155] J. Angle et al. First Results from the XENON10 Dark Matter Experiment at the Gran Sasso National Laboratory. *Physical Review Letters*, 100:021303, 2008.
- [156] Z. Ahmed et al. Search for Weakly Interacting Massive Particles with the First Five-Tower Data from the Cryogenic Dark Matter Search at the Soudan Underground Laboratory. *Physical Review Letters*, 102:011301, 2009.
- [157] R. Trotta et al. The impact of priors and observables on parameter inferences in the constrained MSSM. *Journal of High Energy Physics*, 12:024, 2008.
- [158] ETEL. <http://www.et-enterprises.com>.
- [159] F. Neves et al. ZE3RA: the ZEPLIN-III Reduction and Analysis package. *Journal of Instrumentation*, 6:P11004, 2011.
- [160] P. Scovell. *Results from the ZEPLIN-III Dark Matter Search Experiment*. PhD thesis, University of Edinburgh, 2011.
- [161] M.R. Bhat. Nuclear Data Sheets 85, 415 (1998), National Nuclear Data Center, NuDat 2.6 database: [www.nndc.bnl.gov/nudat2](http://www.nndc.bnl.gov/nudat2).
- [162] V.N. Solovov et al. Position Reconstruction in a Dual Phase Xenon Scintillation Detector. *IEEE Transactions on Nuclear Science*, 59(6):3286–3293, 2012.
- [163] E. Browne and J.K. Tuli. Nuclear Data Sheets 108, 2173 (2007), National Nuclear Data Center, NuDat 2.6 database: [www.nndc.bnl.gov/nudat2](http://www.nndc.bnl.gov/nudat2).
- [164] D. Yu. Akimov et al. The ZEPLIN-III anti-coincidence veto detector. *Astroparticle Physics*, 34:151–163, 2010.
- [165] Amcrys-H Corp. [www.amcrys-h.com](http://www.amcrys-h.com).
- [166] M.B. Chadwick et al. ENDF/B-VII.0: Next generation evaluated nuclear data library for nuclear science and technology. *Nuclear Data Sheets*, 107(12):2931–3059, 2006.
- [167] J.A. Cameron and B. Singh. Nuclear Data Sheets 102, 293 (2004), National Nuclear Data Center, NuDat 2.6 database: [www.nndc.bnl.gov/nudat2](http://www.nndc.bnl.gov/nudat2).
- [168] A.G. Wright. An investigation of photomultiplier background. *Journal of Physics E-scientific Instruments*, 16(4):299–307, 1983.
- [169] W.A. Rolke, A.M. Lopez, and J. Conrad. Limits and confidence intervals in the presence of nuisance parameters. *Nuclear Instruments and Methods in Physics Research A*, 551:493–503, 2005.
- [170] R. Brun and F. Rademakers. ROOT – An object oriented data analysis framework. *Nuclear Instruments and Methods in Physics Research A*, 389:81–86, 1997.
- [171] A. Wright et al. A highly efficient neutron veto for dark matter experiments. *Nuclear Instruments and Methods in Physics Research A*, 644:18–26, 2011.
- [172] J. B. Birks. *The Theory and Practice of Scintillation Counting*. Pergamon Press Limited, London, 1964.
- [173] V. I. Tretyak. Semi-empirical calculation of quenching factors for ions in scintillators. *Astroparticle Physics*, 33:40–53, 2010.
- [174] G. V. O’Rielly, N.R. Kolb, and R.E. Pywell. The response of plastic scintillator to protons and deuterons. *Nuclear Instruments and Methods in Physics Research A*, 368(745-749), 1996.

## BIBLIOGRAPHY

---

- [175] R. L. Craun and D.L. Smith. Analysis of response data for several organic scintillators. *Nuclear Instruments and Methods*, 80:239–244, 1970.
- [176] R. A. Cecil, B.D. Anderson, and R. Madey. Improved predictions of neutron detection efficiency for hydrocarbon scintillators from 1 MeV to about 300 MeV. *Nuclear Instruments and Methods*, 161:439–447, 1979.
- [177] R. Madey et al. The response of NE-228A, NE-228, NE-224 and NE-102 scintillators to protons from 2.43 to 19.55 MeV. *Nuclear Instruments and Methods*, 151:445–450, 1978.
- [178] D. L. Smith, R.G. Polk, and T.G. Miller. Measurements of the response of several organic scintillators to electrons, protons and deuterons. *Nuclear Instruments and Methods*, 64:157–166, 1968.
- [179] E. Simon et al. Sicane: a detector array for the measurement of nuclear recoil quenching factors using a monoenergetic neutron beam. *Nuclear Instruments and Methods in Physics Research A*, 507:643–656, 2003.
- [180] Th. Jagemann, J. Jochum, and F.V Feilitzsch. Neutron scattering facility for the measurement of nuclear recoil quenching factors. *Nuclear Instruments and Methods in Physics Research A*, 551:245–260, 2005.
- [181] Nuclear structure and decay data: [www.nndc.bnl.gov/nudat2](http://www.nndc.bnl.gov/nudat2).
- [182] P. Benetti et al. First results from a dark matter search with liquid argon at 87 K in the Gran Sasso underground laboratory. *Astroparticle Physics*, 28:495–507, 2008.
- [183] Cross Section Evaluation Working Group: [www.nndc.bnl.gov/csewg/](http://www.nndc.bnl.gov/csewg/). ENDF/B-VI data files may be accessed at national nuclear data center [www.nndc.bnl.gov](http://www.nndc.bnl.gov).
- [184] International Organization for Standardization 56. CH-1211 Geneva. Iso 8529-1, 2001. reference neutron radiations - part 1: Characteristic and methods of productions: [www.iso.org/iso/catalogue\\_detail.htm?csnumber=25666](http://www.iso.org/iso/catalogue_detail.htm?csnumber=25666).
- [185] E. F. Shores. SOURCES 4C: A code for calculating ( $\alpha$ ,n), spontaneous fission, and delayed neutron sources and spectra, LA-UR-02-1839, April 2002.
- [186] S. Garry et al. GEANT4 transport calculations for neutrons and photons below 15 MeV. *IEEE Transactions on Nuclear Science*, 56(4):2392–2396, 2009.
- [187] ENDF. Angular distributions for elastic neutron scattering:  
<http://t2.lanl.gov/data/data.html>.
- [188] Experimental Nuclear Reaction Data (EXFOR/CSISRS):  
<http://www.nndc.bnl.gov/exfor/exfor00.htm>.
- [189] G. Cowan. *Statistical data analysis*. Clarendon Press, Oxford, 1998.
- [190] R. J. Barlow. *Statistics: A Guide to the Use of Statistical Methods in the Physical Sciences*. John Wiley and Sons, reprint 1999.
- [191] J.W. Marsh, D.J. Thomas, and M. Burke. High resolution measurements of neutron energy spectra from Am-Be and Am-B neutron sources. *Nuclear Instruments and Methods in Physics Research A*, 366:340–348, 1995.
- [192] R. Barlow. Asymmetric errors. *eConf C030908, WEMT002*, 2003.
- [193] M. J. Berger et al. Stopping-power and range tables for electrons, protons, and helium ions: [www.nist.gov](http://www.nist.gov).
- [194] J. F. Ziegler, J. P. Biersack, and M. D. Ziegler. SRIM, The Stopping Range of Ions in Matter, SRIM Co., 2008, SRIM Version 2008.04: [www.srim.org](http://www.srim.org).

- [195] D. Lewin et al. UKDMC: [hepwww.rl.ac.uk/ukdmc/Radioactivity/](http://hepwww.rl.ac.uk/ukdmc/Radioactivity/).
- [196] J. Morales et al. The canfrac underground laboratory present and future. *Proceedings of the Fifth International Workshop on the Identification of Dark Matter*, World Scientific, pages 447–452, 2005.
- [197] A. Lindote et al. Simulation of neutrons produced by high-energy muons underground. *Astroparticle Physics*, 31:366–375, 2009.
- [198] B. Schmidt et al. Muon-induced background in the EDELWEISS dark matter search. *arXiv:1302.7112v1 [astro-ph.CO]*, 2013.
- [199] P.F. Smith et al. Simulation studies of neutron shielding, calibration and veto systems for gaseous dark matter detectors. *Astroparticle Physics*, 22:409–420, 2005.
- [200] M. Carson. Veto performance for large-scale xenon dark matter detectors. *Nuclear Instruments and Methods in Physics Research A*, 548:418–426, 2005.
- [201] P. Collon et al. Measurements of  $^{81}\text{Kr}$  in the atmosphere. *Nuclear Instruments and Methods in Physics Research B*, 123:122–127, 1997.
- [202] J. Ahlswede et al. Update and improvement of the global krypton-85 emission inventory. *Journal of Environmental Radioactivity*, 115:34–42, 2013.
- [203] H. Sievers. Nuclear Data Sheets 62, 271 (1991), National Nuclear Data Center, NuDat 2.6 database: [www.nndc.bnl.gov/nudat2](http://www.nndc.bnl.gov/nudat2).
- [204] J. Gavrilyuk et al. Searches for  $2\text{K}(2\nu)$ -capture mode of  $^{78}\text{Kr}$  and  $^{124}\text{Xe}$  decays with wall-less proportional counters. *in: Proceedings of First International Workshop on Nonaccelerator New Physics (NANP 97)*, 1997, *Physics of Atomic Nuclei*, 61(8):1287–1292, 1998.
- [205] D.-M. Mei, Z.-B. Yin, and S.R. Elliot. Cosmogenic production as a background in searching for rare physics processes. *Astroparticle Physics*, 31:417–420, 2009.
- [206] E. Tziaferi et al. First measurement of low intensity fast neutron background from rock at the Boulby Underground Laboratory. *Astroparticle Physics*, 27:326–338, 2007.
- [207] Y. Tendow. Nuclear Data Sheets 77, 631 (1996), National Nuclear Data Center, NuDat 2.6 database: [www.nndc.bnl.gov/nudat2](http://www.nndc.bnl.gov/nudat2).
- [208] Yu. Khazov, I. Mitropolsky, and A. Rodionov. Nuclear Data Sheets 107, 2751 (2006), National Nuclear Data Center, NuDat 2.6 database: [www.nndc.bnl.gov/nudat2](http://www.nndc.bnl.gov/nudat2).
- [209] A.K. Jain and B. Singh. Nuclear Data Sheets 107, 1027 (2006), National Nuclear Data Center, NuDat 2.6 database: [www.nndc.bnl.gov/nudat2](http://www.nndc.bnl.gov/nudat2).
- [210] W.B. Wilson et al. SOURCES 4A: A code for calculating  $(\alpha,n)$ , spontaneous fission and delayed neutrons sources and spectra. Tech. Rep. LA-13693 LANL, 1999.
- [211] M.J. Carson et al. Neutron background in large-scale xenon detectors for dark matter searches. *Astroparticle Physics*, 21:667–687, 2004.
- [212] M. Herman et al. EMPIRE: nuclear reaction model code system for data evaluation. *Nuclear Data Sheets*, 108:2655–2715, 2007.
- [213] V. Tomasello, V.A. Kudryavtsev, and M. Robinson. Calculation of neutron background for underground experiments. *Nuclear Instruments and Methods in Physics Research A*, 595:431–438, 2008.
- [214] F. Neves et al. Calibration of photomultiplier arrays. *Astroparticle Physics*, 33:13–18, 2010.

## BIBLIOGRAPHY

---

- [215] G.J. Feldman and R.D. Cousins. Unified approach to the classical statistical analysis of small signals. *Physical Review D*, 57:3873–3889, 1998.
- [216] V.A. Bednyakov, F. Simkovic, and I.V. Titkova. Nuclear spin in direct dark matter search. *arXiv:hep-ph/0412067v1*, 2004.
- [217] P. Toivanen et al. Large-scale shell-model calculations of elastic and inelastic scattering rates of lightest supersymmetric particles (LSP) on  $^{127}\text{I}$ ,  $^{129}\text{Xe}$ ,  $^{131}\text{Xe}$ , and  $^{133}\text{Cs}$  nuclei. *Physical Review C*, 79:044302, 2009.
- [218] M. Hjorth-Jensen, T.T.S. Kuo, and E. Osnes. Realistic effective interactions for nuclear systems. *Physics Reports*, 261:125–270, 1995.
- [219] E. Aprile et al. Dark Matter Results from 100 Live Days of XENON100 Data. *Physical Review Letters*, 107:131302, 2011.
- [220] R. Bernabei et al. First results from DAMA/LIBRA and the combined results with DAMA/NaI. *The European Physical Journal C*, 56:333–355, 2008.
- [221] C. Savage et al. Compatibility of DAMA/LIBRA dark matter detection with other searches in light of new galactic rotation velocity measurements. *Journal of Cosmology and Astroparticle Physics*, 09:036, 2009.
- [222] C.E. Aalseth et al. Results from a Search for Light-Mass Dark Matter with a  $p$ -Type Point Contact Germanium Detector. *Physical Review Letters*, 106:131301, 2011.
- [223] O. Buchmueller et al. Implications of initial LHC searches for supersymmetry. *The European Physical Journal C*, 71:1634, 2011.
- [224] G.J. Alner et al. (N. Spooner and V. Kudryavtsev, editors). *ZEPLIN I: First Limits on Nuclear Recoil Rate*. in: *Identification of Dark Matter*, pages 218–223. World Scientific Pub Co Inc, 2005.
- [225] G.J. Alner et al. Limits on spin-dependent WIMP-nucleon cross-sections from the first ZEPLIN-II data. *Physics Letters B*, 653:161–166, 2007.
- [226] Z. Ahmed et al. Results from a Low-Energy Analysis of the CDMS II Germanium Data. *Physical Review Letters*, 106:131302, 2011.
- [227] L. Roszkowski, R.R. de Austri, and R. Trotta. Implications for the Constrained MSSM from a new prediction for  $b \rightarrow s\gamma$ . *Journal of High Energy Physics*, 07:075, 2007.
- [228] J. Angle et al. Limits on Spin-Dependent WIMP-Nucleon Cross Sections from the XENON10 Experiment. *Physical Review Letters*, 101:091301, 2008.
- [229] E. Aprile et al. Limits on spin-dependent WIMP-nucleon cross-sections from 225 live days of XENON100 data. *arXiv:1301.6620v1 [astro-ph.CO]*, 2013.
- [230] J. Menéndez, d. Gazit, and A. Schwenk. Spin-dependent WIMP scattering off nuclei. *Physical Review D*, 86:103511, 2012.
- [231] M.T. Ressell and D.J. Dean. Spin-dependent neutralino-nucleus scattering for  $A \sim 127$  nuclei. *Physical Review C*, 56:535–546, 1997.
- [232] D. Akimov. Techniques and results for the direct detection of dark matter (review). *Nuclear Instruments and Methods in Physics Research A*, 628:50–58, 2011.
- [233] T. Stanev. *High Energy Cosmic Rays*. Springer in association with Praxis Publishing Ltd, Chichester, UK, second edition, 2010.

- [234] T.K. Gaisser and T. Stanev. Cosmic Rays. in: K Nakamura et al. (Particle Data Group) Review of Particle Physics. *Journal of Physics G: Nuclear and Particle Physics*, 37(075021):269–276, 2010.
- [235] V.Yu. Kozlov et al. A detection system to measure muon-induced neutrons for direct dark matter searches. *Astroparticle Physics*, 34:97–105, 2010.
- [236] V.A. Kudryavtsev, N.j.C Spooner, and J.e. McMillan. Simulations of muon-induced neutron flux at large depths underground. *Nuclear Instruments and Methods in Physics Research A*, 505:688–698, 2003.
- [237] H.M. Araújo, V.a. Kudryavtsev, N.J.C. Spooner, and T.j. Sumner. Muon-induced neutron production and detection with GEANT4 and FLUKA. *Nuclear Instruments and Methods in Physics Research A*, 545:398–411, 2005.
- [238] Y.-F. Wang et al. Predicting neutron production from cosmic-ray muons. *Physical Review D*, 64:013012, 2001.
- [239] D.-Mei and A. Hime. Muon-induced background study for underground laboratories. *Physical Review D*, 73:053004, 2006.
- [240] S. Abe et al. Production of radioactive isotopes through cosmic muon spallation in KamLAND. *Physical Review C*, 81:025807, 2010.
- [241] G. Battistoni et al. The FLUKA code: Description and benchmarking. *Proceedings of the Hadronic Shower Simulation Workshop 2006, Fermilab 6–8 September 2006, M. Albrow, R. Raja eds., AIP Conference Proceeding*, 896:31–49, 2007.
- [242] A. Ferrari, P.R Sala, A. Fasso, and J. Ranft. FLUKA: a multi-particle transport code. *CERN-2005-10 (2005), INFN/TC\_05/11, SLAC-R-773*.
- [243] V.A. Kudryavtsev, L. Pandola, and V. Tomasello. Neutron- and muon-induced background in underground physics experiments. *The European Physical Journal A*, 36:171–180, 2008.
- [244] G.V. Gorshkov, V.A. Zyabkin, and R.M. Yakovlev. Production of neutrons in Pb, Cd, Fe and Al by high-energy muons. *Soviet Journal of Nuclear Physics-USSR*, 18:57–61, 1974.
- [245] L. Bergamasco, S. Costa, and P. Picchi. Experimental results on neutron production by muons at 4300 m we. *Nuovo Cimento della Societa Italiana di Fisica A-Nuclei Particles and Fields*, A 13:403–412, 1973.
- [246] V. Chazal et al. Investigations of fast neutron production by 190 GeV/c muon interactions on different targets. *Nuclear Instruments and Methods in Physics Research A*, 490:334–343, 2002.
- [247] M.G. Marino et al. Validation of spallation neutron production and propagation within GEANT4. *Nuclear Instruments and Methods in Physics Research A*, 582:611–620, 2007.
- [248] H.M. Araújo et al. Measurements of neutrons produced by high-energy muons at the Boulby Underground Laboratory. *Astroparticle Physics*, 29:471–481, 2008.
- [249] P. Antonioli et al. A three-dimensional code for muon propagation through the rock: MUSIC. *Astroparticle Physics*, 7:357–368, 1997.
- [250] V.A. Kudryavtsev. Muon simulation codes MUSIC and MUSUN for underground physics. *Computer Physics Communications*, 180:339–346, 2009.
- [251] JENDL High Energy File 2007, <http://wwwndc.jaea.go.jp/ftpnd/jendl/jendl-he-2007.html>.

## BIBLIOGRAPHY

---

- [252] V.S. Barashenkov. Reprint: Nucleon - Nucleus Cross-sections. *Joint Institute for Nuclear Research*, pages P2–89–770, 1990.
- [253] Tatsumi Koi. A GEANT4 Physics List for Shielding Calculations. At the SATIF10 at CERN, June 2010.
- [254] Cross Section Evaluation Working Group. ENDF/B-VII data files may be accessed through the national nuclear data center [www.nndc.bnl.gov](http://www.nndc.bnl.gov).
- [255] M. Robinson et al. Measurements of muon flux at 1070 m vertical depth in the Boulby underground laboratory. *Nuclear Instruments and Methods in Physics Research A*, 511:347–353, 2003.
- [256] L. Campbell. Afterpulse measurement and correction. *Review of Scientific Instruments*, 63:5794–5798, 1992.
- [257] U. Kawada, J. Ito, and Q.-W. Wang. Temperature dependence of spurious pulses in use of plastic scintillation detectors. *Applied Radiation and Isotopes*, 60:403–407, 2004.
- [258] T.P. Marvin. Single-Photoelectron Noise Reduction in Scintillation Detectors. *IEEE Nuclear Science Symposium and Medical Imaging Conference Record*, 1-3:764–767, 1996.
- [259] J. Quenby (ICL, ZEPLIN-III Collaboration), private communication.
- [260] A.G. Bogdanov et al. Geant4 Simulation of Production and Interaction of Muons. *IEEE Transactions on nuclear science*, 53(2):513–519, 2006.
- [261] V. Uzhinsky. Development of the Fritiof Model in Geant4. *Joint International Conference on Supercomputing in Nuclear Applications and Monte Carlo 2010 (SNA + MC2010)*, Tokyo, Japan, 2010.
- [262] D. Wright (SLAC, GEANT4 Collaboration), private communication.
- [263] V. Tomasello. *Background Simulations for a Large-scale Cryogenic Dark Matter Experiment*. PhD thesis, University of Sheffield, High Energy Physics Group, November 2009.
- [264] R. Gaitskell, V. Mandic, and J. Filippini. <http://dmtools.brown.edu>.

*BIBLIOGRAPHY*

---

*BIBLIOGRAPHY*

---

# Publications

- D. Yu. Akimov *et al.*, The ZEPLIN-III Anti-Coincidence Veto Detector. In *Astroparticle Physics* 34:151-163, 2010.
- D. Yu. Akimov *et al.*, Limits on inelastic dark matter from ZEPLIN-III. In *Physics Letters B* 692:180-183, 2010.
- C. Ghag *et al.*, Performance of the veto detector incorporated into the ZEPLIN-III experiment. In *Astroparticle Physics* 35:76-86, 2011.
- M. Horn *et al.*, Nuclear recoil scintillation and ionisation yields in liquid xenon from ZEPLIN-III data. In *Physics Letters B* 705:471-476, 2011.
- F. Neves *et al.*, ZE3RA: The ZEPLIN-III Reduction and Analysis Package. In *Journal of Instrumentation* 6:P11004, 2011.
- D. C. Malling *et al.*, After LUX: The LZ Program. In *arXiv:1110.0103v2*, 2011.
- E. Santos *et al.*, Single electron emission in two-phase xenon with application to the detection of coherent neutrino-nucleus scattering. In *Journal of High Energy Physics* 12:115, 2011.
- H. M. Araujo *et al.*, Radioactivity Backgrounds in ZEPLIN-III. In *Astroparticle Physics* 35:495-502, 2012.
- D. Yu. Akimov *et al.*, WIMP-nucleon cross-section results from the second science run of ZEPLIN-III. In *Physics Letters B* 709:14-20, 2012.
- P. Majewski *et al.*, Performance data from the ZEPLIN-III second science run. In *Journal of Instrumentation* 7:C03044, 2012.
- L. Reichhart *et al.*, Quenching Factor for Low Energy Nuclear Recoils in a Plastic Scintillator. In *Physical Review C* 85:065801, 2012.
- V. N. Solovov *et al.*, Position Reconstruction in a Dual Phase Xenon Scintillation Detector. In *IEEE Transactions on Nuclear Science* 59:3286-3293, 2012.
- L. Reichhart *et al.*, Measurement and simulation of the muon-induced neutron yield in lead. In *arXiv:1302.4275v1, submitted to Astroparticle Physics*, 2013.